



HAL
open science

Numerical simulation of woodwind dynamics:investigating nonlinear sound production behavior in saxophone-like instruments

Tom Colinot

► **To cite this version:**

Tom Colinot. Numerical simulation of woodwind dynamics:investigating nonlinear sound production behavior in saxophone-like instruments. Acoustics [physics.class-ph]. Aix-Marseille Université (AMU), 2020. English. NNT: . tel-03122454

HAL Id: tel-03122454

<https://theses.hal.science/tel-03122454>

Submitted on 27 Jan 2021

HAL is a multi-disciplinary open access archive for the deposit and dissemination of scientific research documents, whether they are published or not. The documents may come from teaching and research institutions in France or abroad, or from public or private research centers.

L'archive ouverte pluridisciplinaire **HAL**, est destinée au dépôt et à la diffusion de documents scientifiques de niveau recherche, publiés ou non, émanant des établissements d'enseignement et de recherche français ou étrangers, des laboratoires publics ou privés.

AIX-MARSEILLE UNIVERSITÉ
ÉCOLE DOCTORALE SCIENCES POUR L'INGÉNIEUR 353
Mécanique, Physique, Micro et Nanoélectronique

Laboratoire de Mécanique et d'Acoustique, UMR7031 AMU CNRS Centrale Marseille

Thèse présentée pour obtenir le grade universitaire de docteur

Discipline : Sciences pour l'ingénieur
Spécialité : Acoustique

Tom COLINOT

**Numerical simulation of woodwind dynamics:
investigating nonlinear sound production behavior in
saxophone-like instruments**

Simulation numérique de la dynamique des instruments à anche : étude des comportements non linéaires de production du son dans les instruments de type saxophone

Soutenue le 19 novembre 2020 devant le jury composé de :

Jose ANTUNES	Professeur, ADL, Sacavém, Portugal	Rapporteur
Joël GILBERT	Directeur de Recherche CNRS, LAUM, Le Mans, France	Rapporteur
Brigitte D'ANDREA-NOVEL	Professeur, Sorbonne Université, Paris, France	Examinatrice
Sébastien OLLIVIER	Maitre de conférences, LMFA, Ecully, France	Examinateur
Philippe GUILLEMAIN	Directeur de Recherche CNRS, LMA, Marseille, France	Directeur de thèse
Jean-Baptiste DOC	Maitre de Conférence, LMSSC, Paris, France	Co-encadrant de thèse
Christophe VERGEZ	Directeur de Recherche CNRS, LMA, Marseille, France	Co-encadrant de thèse
Michael JOUSSERAND	Ingénieur, Buffet-Crampon, Mantes-la-Ville, France	Invité

Numéro national de thèse/suffixe local : 2020AIXM0518/028ED353

Affidavit

I, undersigned, Tom Colinot, hereby declare that the work presented in this manuscript is my own work, carried out under the scientific supervision of Philippe Guillemain, Jean-Baptiste Doc and Christophe Vergez, in accordance with the principles of honesty, integrity and responsibility inherent to the research mission. The research work and the writing of this manuscript have been carried out in compliance with both the French national Charter for Research Integrity and the Aix-Marseille University Charter on the fight against plagiarism.

The work presented in this manuscript has not been submitted previously either in France or in another country in the same or in a similar version as part of another examination or defense process.

Marseille, December 17, 2020

Signature

Abstract

This work links features of sound production in woodwinds to the action of the musician, through numerical simulation of a physical model supported by experiments. It focuses on the nonlinear dynamics of the model, as one of the missing links between the acoustical features of the instrument, and how easy it is to play. The results are intended to facilitate future instrument development endeavors that would use a physical model as a virtual prototype.

Two fundamentally different simulation methods are used conjointly to provide a robust understanding of the mechanisms governing sound production in woodwind instruments. On the one hand, time-domain synthesis allows large-scale direct investigations into the transients and steady-state oscillations, with the advantage of being interpretable directly in terms of musician actions. On the other hand, the Harmonic Balance Method associated with continuation (Asymptotic Numerical Method) provides a precise, in depth investigation of stable and unstable periodic solution branches throughout the parameter space. This method highlights bifurcations which signal the apparition or disappearance of oscillation regimes: Neimark-Sacker, period doubling, Hopf and fold. These last two are followed by continuation, in codimension 2.

Experimental results constitute the initial foundation and final validation of numerical simulations. Input impedance measurements allow simulations to be based on the acoustical parameters of real saxophones. This justifies subsequent comparisons of simulated dynamics with phenomena observed in playing situation using an instrumented saxophone mouthpiece. Archetypes of oscillating regimes are explored and connected to musician control parameters, such as the blowing pressure and action on the reed. The so-called standard, inverted and double two-step regimes are revealed and analyzed both experimentally and numerically.

The influence of geometrical and modal parameters of the resonator on the instrument's dynamics is detailed. The dynamic system is characterized globally, by mapping out its oscillation thresholds and regime production regions. Maps representing types of oscillation regimes produced depending on the control parameters constitutes a more detailed way to compare two instruments or fingerings. They are applied to compare two alto saxophones, demonstrate the effect of the register key, and assess sound production on a virtual prototype of bicylindrical resonator. This virtual prototype's geometry is optimized based on the input impedance of a saxophone, using a differentiable cost function well-suited to gradient-based optimization procedures.

A more fundamental investigation of woodwind dynamics tackles multistability (different regime being stable for the same control parameter values), which is shown to be ubiquitous on saxophones. The initial conditions leading to different regimes are grouped as attraction basins. Multistability is also characterized in a more musically interpretable way, via a variable blowing pressure transient affecting the obtained steady-state regime. These considerations are applied to improve the regime maps and avoid bias that may be due to overlooking multistable regimes. Improved regime maps are used to demonstrate that the ratio between the first two resonance frequencies leading to the most first register production is not exactly 2, but a slightly higher value.

The results of this dissertation and the related analysis tools further the understanding of a complex dynamic, that of the saxophone, and open the door to quantitative studies and direct application in virtual prototyping.

Résumé

Cette thèse lie la production de son par les instruments à anches aux actions du musicien, à travers des simulations numériques appliquées à un modèle physique et soutenues par des expériences. On se concentre sur la dynamique non linéaire du modèle, comme l'un des chaînons manquants entre les caractéristiques acoustiques de l'instrument et sa jouabilité. Les résultats doivent faciliter de futurs projets de développement d'instrument qui utiliseraient un modèle physique en tant que prototype virtuel.

Deux méthodes de simulation fondamentalement différentes sont utilisées conjointement pour améliorer notre compréhension des mécanismes régissant la production du son dans les instruments à anches. D'un côté, la synthèse temporelle permet des études à grande échelle des phénomènes transitoires et des régimes établis, avec l'avantage d'être interprétable directement en termes d'actions du musicien. D'un autre côté, la Méthode d'Équilibrage Harmonique associée avec la continuation (Méthode Asymptotique Numérique) permet d'explorer l'espace des paramètres de contrôle en suivant les branches de solutions périodiques stables et instables. Cette méthode met en évidence des bifurcations qui marquent l'apparition ou la disparition de régimes oscillants : Neimark-Sacker, doublement de période, Hopf et fold. Ces deux dernières sont suivies par continuation, en codimension 2.

Les résultats expérimentaux constituent à la fois un préalable et une validation finale des simulations numériques. Des mesures d'impédance d'entrée permettent de fonder les simulations sur les paramètres acoustiques de vrais saxophones. Ceci justifie les comparaisons ultérieures entre la dynamique simulée et les phénomènes observés en situation de jeu effectués à l'aide d'un bec instrumenté.

Des formes archétypales de régimes d'oscillations sont étudiés et liés aux paramètres de contrôle du musicien que sont la pression d'alimentation et l'appui de la lèvre sur l'anche. Les régimes à deux états dits standard, inversé, et double, sont exhibés et analysés expérimentalement et numériquement. L'influence des paramètres géométriques et modaux du résonateur sur la dynamique de l'instrument est détaillée. Le système dynamique est caractérisé de manière globale, en cartographiant les seuils d'oscillations et les régions de production de régimes. Des cartes représentant les types de régimes oscillants permettent de comparer en détail deux instruments ou deux doigtés d'un même instrument. Ainsi, on compare deux saxophones altos, on illustre l'effet de la clé de registre, et on évalue un prototype virtuel de résonateur bicylindre. La géométrie de ce prototype virtuel est optimisée à partir de l'impédance d'entrée d'un saxophone, à l'aide d'une fonction de coût dérivable adaptée aux méthodes d'optimisations basée sur le gradient.

Une étude plus fondamentale de la dynamique des instruments à anches traite du phénomène de multistabilité (plusieurs régimes stables pour une seule valeur des paramètres de contrôle). Sur les saxophones, ce phénomène s'avère très important. Les conditions initiales menant à chaque régime sont regroupées en bassins d'attraction. La multistabilité est aussi caractérisée d'une manière plus proche du jeu musical, via un transitoire variable de pression d'alimentation qui affecte le régime final obtenu. Ces considérations sont appliquées à l'amélioration des cartographies de régimes afin d'éviter les biais qui peuvent apparaître si la multistabilité est négligée. Ces cartographies améliorées démontrent que le rapport entre les deux premières fréquences de résonance du saxophone qui mène à la production la plus importante de premier registre ne vaut pas exactement 2 mais une valeur légèrement plus élevée.

Les résultats de cette thèse et les outils d'analyse afférents permettent d'avancer dans la compréhension d'une dynamique complexe, celle du saxophone, et ouvrent la porte à des études quantitatives et à des applications directes de prototypage virtuel.

Remerciements

Trois ans de thèse, c'est trois ans de science, mais pas que (heureusement !).

Mais c'est quand même d'abord trois ans de science, de science passionnante, qui filent au rythme des échanges d'idées, des erreurs de syntaxe, des relectures et des répétées. Merci à Philippe pour sa confiance sans faille, et de m'avoir fait commencer à rêver d'acoustique musicale et de synthèse sonore. À JB Doc, pour sa bienveillance depuis Paris et son œil avisé, pour des visios trop rarement remplacées par une bonne vieille discussion à bâtons rompus, devant un écran rempli de lignes de codes ou deux verres remplis de bière. À Christophe, enfin, un allié de taille pour pourfendre du système dynamique, mais surtout un inestimable soutien – du bureau à la salle de manip, en passant (toujours !) par la salle café.

C'est justement trois ans de cafés, et de discussions, de petits dessins et de *punchlines* au tableau, de panbagnats et de gâteaux à partager. Tout ça dans une ambiance au beau fixe, grâce à la faune disparate et débonnaire qui constitue l'équipe SONS du LMA. Pour commencer, je salue Patrick, qui entre deux *buffers* nous éduque sur Marseille, ses coutumes, son vocabulaire, ses vanes (toujours de bon goût) et ses spécialités culinaires, dégustation à l'appui. Clin d'œil appuyé, bien sûr, aux psychopâtes, même si leur café est meilleur que le nôtre, dont *Jack Chatron* – mine de savoir et de bonne humeur. Je remercie Jean, pilier scientifique, présence inspirante, le sourire en coin et la mèche au vent. C'est ici que je tire mon chapeau à mes illustres co-thésards, à commencer par Louis Guillot clarinettiste, acolyte des premières heures, qui sut ressusciter et sublimer le saxophone neutre et m'initier au monde merveilleux de ¹MANLAB. Bien évidemment, il ne sera pas dit que j'ai oublié Ana 'la croate d'à côté', ni Mémé – et son plaid, son thé, et son tube qui bien que court nous étonne toujours. Merci à Tim, que tes bulles soient toujours homogènes et que PIPO s'accorde à ton diapason. I thank Erik "Petersen" Petersen, knight of the toneholes, connoisseur of peppers², and the most solid purveyor of weird music and classy sayings. Nod to G, for making me realize there's much more to contemporary music than a bunch of stuck-up dudes, and for a refreshing turkey-based choreography.

C'est, évidemment, trois ans de musique. Le blues rock bien de chez nous d'Hustle Bustle avec Bapt notre leader adoré, Flore – la plus belle, parce qu'on a beau essayer nous on est pas belles – et Emi mon virtuose préféré, qui a eu la superbe idée de me pêcher dans un boeuf du Red Lion. C'était mon premier CD physique (vrai de vrai) avec des copains ! Et le punk rock bien gras des VZ, avec Nic et ses excellentes leçons d'italien accéléré, Jess et le baptême de l'os péruvien sans oublier nos reprises punk/country/coldwave, Castaldjjjji et sa créativité tant aux baguettes qu'au volant. Je n'oublie pas non plus les musiciens du labo, à commencer par les stagiaires : les morceaux choisis du Kintett Onirik, dont Baptiste qui m'a initié à l'improvisation libre, suivi de Romane et Rémi (*a.k.a.* Nidhögg *a.k.a.* N le R) qui ont continué mon éducation – je comprends toujours rien mais c'est quand même marrant –, Marmion sans doute le stagiaire le plus funky du LMA (de mémoire de thésard en tout cas), et Alexandra, Adrien et Justin avec qui on a tapé le boeuf comme il se doit. Peti anj parti tro to, et pour des raisons moralement douteuses, je remercie PYB³ pour bien trop peu de black métal atmosphérique, une passionnante hésitation guitaristique (c'était bien la peine de se casser la tête pour la fabriquer à l'envers !) et au moins un délicieux macaron. Merci à Natacha, pour les jams au didgeridoo, et son exploration courageuse de mes codes pas toujours très propres. Merci aussi à tous ceux qui ont partagé une scène semi-improvisée (ou une jam carrément préparée, ou un simple moment de musique) au LMA, dont Marc à la trompette, Vincent au trombone, Mouze à la batterie, Olivier à la basse, Alex à la guitare, Hector à la clarinette, Martin au violoncelle, Régis à la contrebasse, Ossen à la basse, Jérôme à la basse, Geoffroy au tuba, *Rodger* à la guitare, Clément à la batterie, et Cédric à la basse.

C'est trois ans de vie, simplement. Je remercie ma famille pour son soutien indéfectible, bien avant le début de cette histoire de saxophones – Papa, Maman, Max, toujours présents, prêts à casser la croûte, faire une partie de jeu de société, charger du matos, décharger du matos, jouer du funk pendant 4h, boire un coup, dormir et recommencer. En dernier, et avec tout mon cœur, je remercie Laura qui m'a accompagné à tous les instants.

¹Nana-nana-nana-nana-Nana-nana-nana-nana-

²*Ça pique pas du tout !*

³Lire Pi-Why-Bi, sur l'air de PYT.

À toute ma famille.

Contents

Affidavit	iii
Abstract	iv
Résumé	v
Remerciements	vii
Introduction	1
1 Fundamentals concepts and basic applications	5
1.1 Physical model of reed instrument	5
1.1.1 Structure of the physical model, main variables and parameters	5
1.1.2 The reed model	7
1.1.2.1 Model of contact with the lay	8
1.1.2.2 The reed flow	9
1.1.3 The reed channel	10
1.1.3.1 Nonlinear characteristic deduced from Bernoulli's law	10
1.1.3.2 Regularizations	11
1.1.4 The resonator	12
1.1.4.1 Modal analysis of the input impedance	13
1.1.4.2 Reflection coefficient and reflection function	15
1.2 Numerical simulation	16
1.2.1 Time-domain synthesis	17
1.2.1.1 Discretization of the equations	18
1.2.1.2 Application: effect of the cutoff frequency on the produced signals for a cylindrical resonator with clear cutoff behavior	23
1.2.2 The Harmonic Balance Method associated with the Asymptotic Numerical Method of continuation: MANLAB	25
1.2.2.1 Harmonic Balance Method	26
1.2.2.2 Asymptotic Numerical Method	27
1.2.2.3 Some bifurcation theory	29
1.3 Numerical optimization	34
1.3.1 Typical optimization problem	35
1.3.2 Optimization algorithms	37
1.3.2.1 Trust-region algorithm	37
1.3.2.2 Genetic algorithms	39
1.4 Experimental tools	41
1.4.1 The instrumented mouthpiece	41
1.4.1.1 Structure of the instrumented saxophone mouthpiece	41
1.4.1.2 Calibration of the optical displacement sensor (internship A. Goloubkov)	42
1.4.2 Measuring impedances with the CTTM impedance sensor	43
1.4.2.1 Presentation of the CTTM impedance sensor	44
1.4.2.2 Repeatability measurements applied to the oboe (internship R. Buttard)	44
1.4.2.3 Measuring the impedance of the saxophone family (internship C. Marmion)	46

2	Optimizing a bicylindrical resonator	49
2.1	Motivation and summary	49
2.2	Introduction	51
2.3	Input impedance of the saxophone and the bicylindrical resonator	52
2.3.1	Saxophone impedance measurement: target and control	52
2.3.2	Impedance of a bicylindrical resonator	53
2.3.3	Initial geometrical parameters of the optimization	54
2.4	Optimization procedure	55
2.4.1	Optimization method	55
2.4.2	Choice of the cost function	55
2.4.3	Robustness of the optimization procedure	56
2.5	Differences between the bicylindrical resonator and the saxophone resonators	59
2.5.1	Optimization results	59
2.5.2	Comparison between characteristics of the impedances	60
2.6	Conclusion	63
2.7	Appendices	64
2.7.1	Derivability and derivatives of the cost function	64
2.7.2	Optimization of a bicylindrical resonator with tone holes	64
2.8	Supplementary results	65
2.8.1	Another optimum	65
2.8.2	Another cost function, based on $\log(Z)$	65
2.8.3	Details on comparing the cost functions	65
2.8.4	Preliminary optimization tests: using a noisy bicylindrical impedance as target	68
2.8.5	Global inharmonicity descriptor	69
3	Oscillation regimes and bifurcation diagrams	71
3.1	Foreword	71
3.2	Treble: standard and inverted regimes	73
3.2.1	Standard and inverted two-step motion	73
3.2.2	Continuous transition between standard and inverted motion in a saxophone model	73
3.2.3	Fold continuation	75
3.2.3.1	Tracking folds: the augmented system	75
3.2.3.2	Toy problem: Dessi's 5 th order Van der Pol oscillator	76
3.2.3.3	Application to the saxophone	77
3.3	Low: multiple two-step regimes	81
3.3.1	Introduction	81
3.3.2	Experimental observation of double two-step motions on a saxophone	82
3.3.2.1	Experimental apparatus	82
3.3.2.2	Observation of single and double two-step oscillating regimes	82
3.3.3	Numerical study of the regimes using a physical model	84
3.3.3.1	Saxophone model	84
3.3.3.2	Numerical resolution with harmonic balance method	86
3.3.3.3	Results	87
3.3.4	Conclusion	91
3.4	Medium: effect of the "ghost reed"	92
3.4.1	Introduction	92
3.4.2	Mathematical model of reed instrument	92
3.4.3	Comparison between the ghost reed simplification and the impact model	94
3.4.3.1	Waveforms	94
3.4.3.2	Bifurcation diagrams	96
3.4.4	Conclusion	97
3.5	Bifurcations of an idealized model	98
3.6	Introduction	98
3.7	Model and numerical methods	99
3.7.1	Model	99
3.7.2	Sound synthesis	99

3.7.3	Continuation with harmonic balance method	100
3.8	Results	101
3.9	Conclusions	101
4	Sound production cartography	103
4.1	Introduction	103
4.2	Cartography	104
4.2.1	Computing descriptors	106
4.2.2	Effect of the register key on regime production	106
4.2.3	Comparison between two alto saxophones	107
4.2.4	Comparison between the alto saxophone and bicylindrical resonator	109
4.3	Emergence of regimes: Hopf bifurcation continuation	110
4.3.1	Preliminary: simple analytical formulas for instability thresholds	111
4.3.2	Principle of the Hopf continuation	112
4.3.3	Effect of varying modal parameters on Hopf bifurcations	112
4.3.3.1	Modal residue and damping	113
4.3.3.2	Inharmonicity	114
4.3.4	Comparing oscillation thresholds in the saxophone family	114
4.3.4.1	Preliminary: modal parameters in the saxophone family	115
4.3.4.2	Location of the first, second and third Hopf bifurcation for the saxophones	117
5	Multistability and attraction basins	121
5.1	Foreword	121
5.2	Introduction	123
5.3	Numerical simulation framework	124
5.3.1	Saxophone model	124
5.3.1.1	The reed model	124
5.3.1.2	The reed channel	125
5.3.1.3	The resonator	125
5.3.2	Time-domain synthesis	126
5.3.3	Harmonic balance and numerical continuation	126
5.4	Multistability	126
5.4.1	Overlapping stability zones on the bifurcation diagram	127
5.4.2	Time-domain synthesis with blowing pressure ramps	129
5.5	Effect of the rising time of the blowing pressure	130
5.5.1	Control scenario: increasing blowing pressure	130
5.5.2	Attraction basins in the phase space	132
5.6	Effect of the resonator's inharmonicity on regime production	133
5.6.1	Regime production regions	134
5.6.2	Rate of produced regimes: influence of the rise time on global regime production	135
5.6.3	Inharmonicity of the saxophone	137
5.7	Conclusion	137
	General conclusion	141
A	First-order quadratic saxophone model	145
A.1	Quadractic recast	145
A.2	Jacobian matrix	145
B	Estimation of control parameters (internship A. Pillet, co-supervised)	147
	Bibliography	151

List of Figures

1	Graphical layout of the concepts and descriptions applicable to a woodwind model explored in this dissertation.	2
1.1	Elements of a saxophone model	6
1.2	Elements and variables of a saxophone model	7
1.3	Saxophone reed and mouthpiece	8
1.4	Saxophone mouthpiece	9
1.5	Reed channel and mouthpiece rails	9
1.6	Contact force, raw and regularized	10
1.7	Regularizations of the ramp and absolute value	11
1.8	Static characteristic of Eq. (1.14), raw and regularized	12
1.9	Modal fit, first peak of a cylinder and a saxophone	14
1.10	Reconstruction of the impedance modulus from modal coefficients	15
1.11	High frequency reconstruction of the input impedance after truncation of the reflection function	17
1.12	Effect of the reflection function truncation on the reconstructed input impedance	19
1.13	Modal time-domain synthesis pressure signals	22
1.14	Reflection function time-domain synthesis pressure signals	23
1.15	Comparison of time-domain synthesis signals: modal and reflection function	23
1.16	Input impedance of resonators designed for cutoff frequencies of 1 and 2 kHz	24
1.17	Internal pressure spectra obtained with time-domain synthesis for resonators with designed cutoff frequencies	25
1.18	Oscillations of the Van der Pol oscillator.	26
1.19	Phase diagram and harmonic coefficients, Van der Pol oscillator.	27
1.20	Continuation, Van der Pol oscillator.	29
1.21	Hopf bifurcation schema	30
1.22	Hopf bifurcation, Van der Pol oscillator.	31
1.23	Fold bifurcation schema	31
1.24	Pitchfork bifurcation schema	32
1.25	Neimark-Sacker bifurcation schema	32
1.26	Period-doubling phase diagrams	33
1.27	Period-doubling bifurcation schema	33
1.28	Cusp and Bautin bifurcation schema	34
1.29	Cost function	36
1.30	Geometrical design parameters of a woodwind resonator	36
1.31	Trust-region algorithm example	38
1.32	Trust-region algorithm example, with ‘wrong’ point	39
1.33	Principle of a genetic algorithm	40
1.34	Instrumented mouthpiece	42
1.35	Optical sensor calibration apparatus	43
1.36	Static calibration of the optical sensor for a dry and a wet reed	44
1.37	Schema of the CTTM impedance sensor	44
1.38	Oboe	45
1.39	Oboe impedance with and without artifact	45
1.40	Alto saxophone	46
1.41	Schema of the adaptation piece between impedance sensor and saxophone	47
1.42	Measured impedance for four saxophones: two altos, a soprano and a tenor	47
1.43	Comparisons in the saxophone family: L^2 -norm and transition frequency band (indicator of the cutoff)	48

2.1	Coaxial saxophone	50
2.2	Yamaha Venova	50
2.3	Optimized resonator layout	54
2.4	Norms between initial impedance and target impedance	56
2.5	Cost function evolution	57
2.6	Cost function around the optimum, long cylinder length L_b	58
2.7	Cost function around the optimum, radii r_a and r_b	59
2.8	Cost function around the optimum, lengths L_a and L_m	59
2.9	Optimized impedance and target impedance	61
2.10	First impedance peak frequency for the optimum, target and control	61
2.11	Harmonicity of the target, control, and optimum	62
2.12	Peak height ratio for the target, control and optimum	63
2.13	Impedances of the optimum with toneholes and the target	65
2.14	Impedance of the undesirable optimum, optimum and target	66
2.15	Impedance of the optimum with cost function based on $\log(Z)$ and target	66
2.16	Optimal parameters for several exponent in the cost function	67
2.17	First impedance peak frequency: discrepancy in cents versus the corresponding notes in the tempered scale.	68
2.18	Height of the impedance peaks for the target and optimums with several cost functions	68
2.19	Second impedance peak frequency for the target and optimums with several cost functions	69
2.20	Impedance of a target which is a bicylindrical resonator impedance with added noise and associated optimum	69
2.21	Global inharmonicity descriptor	70
3.1	Standard and inverted two-step, time-domain pressure	73
3.2	Bifurcation diagrams showing continuous and discontinuous transition between standard and inverted two-step	74
3.3	Bifurcation diagram of the fifth-order Van der Pol oscillator, with a fold bifurcation	76
3.4	Analytical 3D bifurcation diagram of the fifth order Van der Pol and fold continuation	77
3.5	3D bifurcation diagram of the saxophone model with fold continuation, with the cusp bifurcation acting on the transition between standard and inverted two-step	78
3.6	Bifurcation diagram of the saxophone model with three fold bifurcations	79
3.7	3D bifurcation diagram of the saxophone model with fold continuation outlining the existence of oscillations	79
3.8	Instrumented mouthpiece	82
3.9	Input impedance of the low B fingering	83
3.10	Measured reed position for simple standard and inverted two-step	83
3.11	Measured reed position for double standard and inverted two-step	84
3.12	Multimedia file: Sound recorded outside the resonator for the standard two-step motion, corresponding to the measured displacement shown in figure 3.10, (a).	84
3.13	Multimedia file: Sound recorded outside the resonator for the inverted two-step motion, corresponding to the measured displacement shown in figure 3.10, (b).	84
3.14	Multimedia file: Sound recorded outside the resonator for the double two-step motion, corresponding to the measured displacement shown in figure 3.11, (a).	85
3.15	Multimedia file: Sound recorded outside the resonator for the inverted double two-step motion, corresponding to the measured displacement shown in figure 3.11, (b).	85
3.16	Regimes appearing during a blowing pressure increase with the instrumented mouthpiece	85
3.17	Synthesized and measured time-domain pressure for all two-step regimes	88
3.18	Multimedia file: Animation: evolution of the acoustic pressure waveform and spectrum following the stable branches of the bifurcation diagram in figure 3.19.	88
3.19	Bifurcation diagram with two-step regime types for the low B fingering	89

3.20	Bifurcation diagrams with two-step regime types for the low B fingering for other values of ζ	90
3.21	Multimedia file: Animation: evolution of the acoustic pressure waveform and spectrum during a continuous transition between double two-step regime and second register for the low C fingering of an alto saxophone, following branches of the bifurcation diagram in figure 3.22.	90
3.22	Bifurcation diagram with two-step regime types for the low C fingering	90
3.23	Regularization of the static nonlinear characteristic	93
3.24	Waveform and spectrum of oscillations with and without impact force, $\gamma = 0.5$	95
3.25	Waveform and spectrum of oscillations with and without impact force, $\gamma = 1.5$	95
3.26	Bifurcation diagrams with and without impact force	96
3.27	Zoom on the bifurcation diagrams with and without impact force	97
3.28	Amplitude cartography of the idealized model with respect to γ and the length ℓ	100
3.29	Bifurcation diagram, idealized model, long length $\ell = 1$	101
3.30	Bifurcation diagram, idealized model, short and medium length $\ell = 0.4$ and 0.6	102
4.1	Example of regime maps, with superposition	105
4.2	Impedance for fingerings $D\sharp$, $F\sharp$ and middle C of the Senzo with register hole closed and open	106
4.3	Regime map, with register hole closed and open	107
4.4	Impedance for fingerings $D\sharp$, $F\sharp$ and middle C of the Senzo and YAS-280	108
4.5	Regime maps, Senzo and YAS-280	108
4.6	Pitch map, Senzo and YAS-280	109
4.7	Regime maps, Senzo and bicylindrical optimum	110
4.8	Pitch map, Senzo and bicylindrical optimum	110
4.9	Numerical Hopf bifurcation continuation and analytical approximations	113
4.10	Effect of modal damping on Hopf bifurcations	114
4.11	Effect of the modal residue on Hopf bifurcations	115
4.12	Effect of the inharmonicity on Hopf bifurcations	115
4.13	Modal parameters of the four saxophones	116
4.14	Hopf continuation for the four saxophones	118
4.15	Hopf continuation comparison: Senzo and YAS (alto)	118
4.16	Hopf continuation comparison: Senzo and YTS (tenor)	119
4.17	Hopf continuation comparison: Senzo and YSS (soprano)	119
5.1	Time-domain synthesis of a transien: envelope and spectrogram	127
5.2	Bifurcation diagram with multistability zones	128
5.3	Hysteresis in the amplitude of the synthesized signal, overlaid with the bifurcation diagram	129
5.4	Blowing pressure control scenario (fast and slow attack)	131
5.5	Regime maps with respect to the blowing pressure and the attack time	131
5.6	2D projection of the attraction basins	133
5.7	Multimedia file: Animation: evolution of a 3D projection of the attraction basins along the bifurcation diagram.	133
5.8	3D projection of the attraction basins	134
5.9	Regime map with respect to the blowing pressure, lip action parameter ζ and attack time, for null and positive inharmonicity	135
5.10	Rate of regime production depending on inharmonicity and attack time, $B\flat$ fingering	136
5.11	Rate of regime production depending on the inharmonicity and attack time, D and $D\sharp$ fingerings	137
5.12	Rate of regime production depending on inharmonicity, lowest fingerings of the saxophone	138
5.13	Graphical layout of the numerical tools and representations explored throughout this dissertation. Compare with the introduction diagram Figure 1.	141
B.1	Beating reed displacement signal, schema	148
B.2	Correspondance between blowing pressure and mean reed position, in synthesis	148

B.3	Detection of the reed closure on instrumented mouthpiece signals	149
B.4	Estimation of the blowing pressure parameter γ for a blowing pressure ramp .	150

List of Tables

2.1	Optimized geometrical parameters of the designed bicylindrical resonator. . .	60
2.2	Mean resonance frequency discrepancy between target and optimum or control	62
2.3	Resonance frequency discrepancies for several exponents in the cost function .	67
3.1	Parameters of the model	94
4.1	Parameters of the model	105
5.1	Parameters of the model	125

List of Abbreviations

HBM	H armonic B alance M ethod
ANM	A symptotic N umerical M ethod
YAS	Y amaha A lto S axophone
YTS	Y amaha T enor S axophone
YSS	Y amaha S oprano S axophone

List of Symbols

MAIN VARIABLES

x	Reed displacement from equilibrium	1
p	Acoustic pressure at resonator input	1
u	Acoustic flow at resonator input	1

INDEPENDANT VARIABLES

t	Continuous time	s
n	Discrete time	samples
ω	Angular frequency	rad/s
f	Frequency	Hz

CONTROL PARAMETERS

γ	Blowing pressure parameter	1
ζ	Lip action parameter, related to the reed opening at rest	1

OTHER VARIABLES

F_c	Contact force between reed and lay	1
u_r	Acoustic flow due to reed speed ("reed flow")	1
u_b	Acoustic flow through reed channel	1
ω	Angular frequency	rad/s
p_k	Modal pressure component	1
p^+	Forward pressure wave	1
p^-	Backward pressure wave	1
V	Strictly causal part of the pressure (in synthesis)	1

MODEL PARAMETERS

ω_r	Reed angular eigenfrequency	rad/s
q_r	Reed damping coefficient	1
K_c	Nonlinear contact stiffness	1
α	Nonlinear contact exponent	1
β	Nonlinear contact damping coefficient	s
S_r or λ	Effective reed surface giving the reed flow	m ² or 1
O_a	Reed opening regularization parameter	1
V_a	Pressure equilibrium regularization parameter	1
η	Absolute value regularization parameter	1
N_m	Number of modes	1
C_k	Complex modal residues (k^{th} mode)	1
s_k	Complex modal poles (k^{th} mode)	rad/s
ω_k	Real modal eigenfrequency (k^{th} mode)	rad/s
α_k	Real modal damping coefficient (k^{th} mode)	1
A_k	Real modal amplitude factor (k^{th} mode)	1
F_s	Sampling rate	Hz
r	Reflection function	1
D_t or D	Truncation duration or index of the reflection function	s or samples

OTHER CONTINUOUS MODEL ELEMENTS

F	Characteristic giving flow through reed channel	1
Z	Input impedance	1
R	Reflection coefficient	1

VARIABLES FOR HBM AND ANM

X_i	i^{th} time-dependent variable	1
N_v	Number of variables	1
\mathbf{X}	Vector of variables	1
ω_0	Fundamental angular frequency	rad/s
$X_{i,h}$	Complex amplitude of the h^{th} harmonic of the i^{th} variable	1
H	Number of harmonics for each variable	1
R	Function calculating the residue of system after HBM	1
\mathbf{U}	Variables (harmonic amplitudes, frequency, continuation parameter)	[multiple]
λ	Continuation parameter	1
ϵ_r	Tolerance on the residue	1
$\mathbf{J}_{\mathbf{X}_0}$	Jacobian of the linearized system at \mathbf{X}_0	s^{-1}
β_i	i^{th} eigenvalue of the jacobian	s^{-1}
\mathbf{p}_i	i^{th} eigenvector of the jacobian	1

SYMBOLS FOR OPTIMIZATION

Φ	Cost function	1
Θ	Optimization parameters	[multiple]
h_i	i^{th} inequality optimization constraint	1
\bullet_{tar}	Target value in optimization of variable \bullet	1

*With my feet upon the ground
I lose myself between the sounds.*

...
*And following our will and wind
We may just go where no one's been.*

MJK

Introduction

Where could science intervene in the process of designing a musical instrument – and especially a woodwind? A well designed instrument is made to meet the needs of the musician – for instance, it can play in tune, and notes are easy to produce. To achieve these characteristics means to give the musician control over the complex physical phenomena involved in the production of sound. The essential human element of this challenge has lead instrument manufacture somewhere between an art and a craft. The field has forever been driven by expert luthiers, who improved instruments step by careful step. However, making an instrument includes a technical aspect, in understanding and conditioning its physical mechanisms. This is where science comes in. Through objective tools and concepts, a scientific point of view has the potential to facilitate some steps in the design process. In particular, in today’s numerical age, precise physical modeling of the instrument may be used to simulate its behavior. Then, there would be no need to physically build a prototype for each step of the development process. In particular, early exploratory stages stand to be greatly accelerated, by exploiting the simulation to dimension a first prototype that plays roughly in tune for all notes.

The field of scientific assistance to instrument making has been subject to a lot of attention lately, especially since the 2000s. Founding works such as [Dal+95] have offered general rules as to how changing the geometry of an instrument influences its sound, thus laying the groundworks for more applicative results. Since then, scientific methods have been added to the instrument maker’s toolbox of a portion of the new generation of makers, as instantiated in France by ITEM’s *Plate-forme d’Aide à la Fabrication Instrumentale* [Dou12; Fer+14]. In parallel, the academia has used computerized optimization to suggest novel geometries for the trombone [Kau01] or the clarinet [Nor+13; Gui15]. The newest generation of optimization methods uses numerical tools to their full potential, with works like [Tou+17] synthesizing sounds to assess the design criteria.

The present thesis aims at identifying the scientific challenges that must be met to optimize a saxophone-like instrument, and tackling them using numerical and experimental tools. This document can be read with two main interests in mind. First, an objective description of the characteristics of existing saxophones, to best match these characteristics when designing a new instrument. Secondly, a more fundamental exploration into the dynamics of self-oscillating instruments, to develop new methods of assessment of a virtual (numerical) prototype based on the sounds it produces. Figure 1 represents the global thought process underlying this thesis. Black double arrows represent the scientific tools, which can calculate the acoustical features of a resonator from its geometry as well as simulate the production of sound by an instrument. Then, as displayed by the solid blue arrows, we infer more general rules about how sound production is influenced by the acoustical characteristics, and indirectly by the geometry. Two dashed arrows materialize the ultimate motivation behind the present Ph. D., as it pertains to instrument design: directly knowing how to adjust geometrical parameters to obtain certain sound production characteristics.

To experience some of the challenges of scientific instrument design first-hand, the thesis starts by exploring the computerized development of a novel resonator, based on the acoustics of the saxophone. This new instrument is to be played with a single-reed, most likely a saxophone or clarinet mouthpiece. This first task is primarily about determining the resonator’s geometry, which would not be based on a single (mostly) conical bore like usual saxophones. Instead, it would be comprised of two cylinders, as per an academic approximation of a saxophone’s acoustics. This approximation, sometimes called *transverse saxophone*⁴ relies on the two cylinders being placed in derivation after the mouthpiece. Note that, before being applied to novel instruments, the transverse saxophone approximation had not been limited to an academic use as a convenient analytical framework for the saxophone [Iro31; DGK00]. It also

⁴*Saxophone traversier* in French.

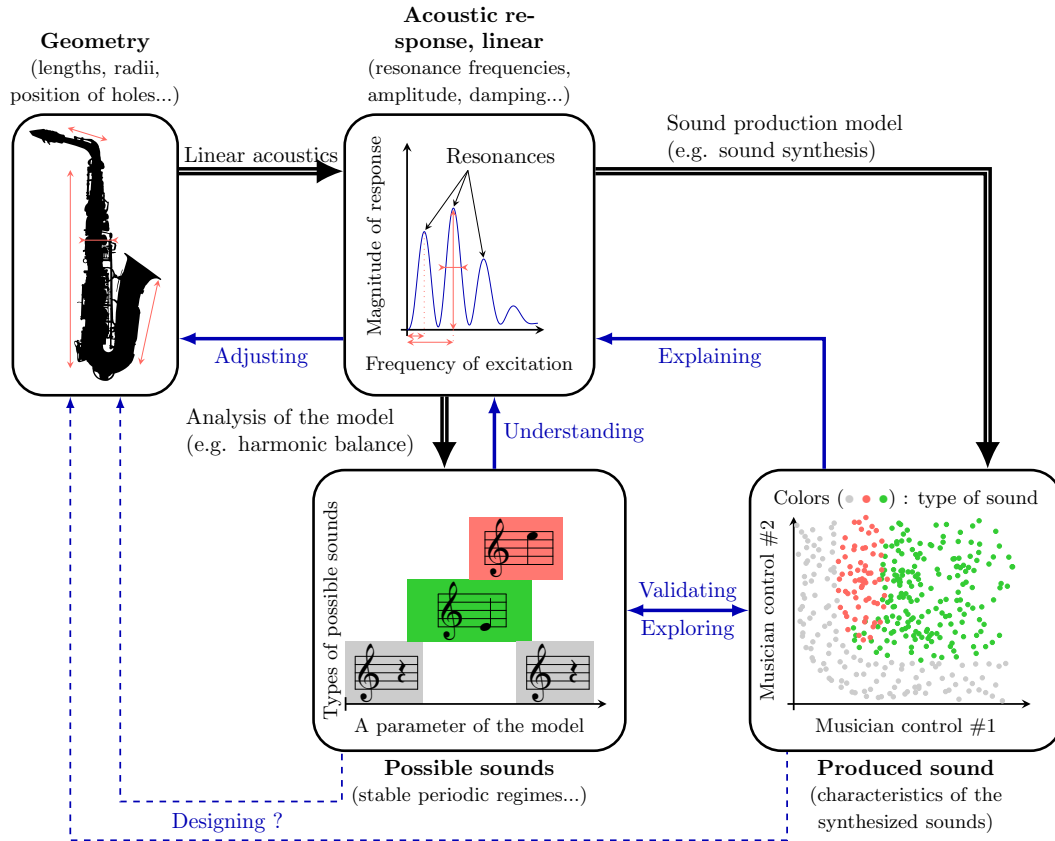


FIGURE 1: Graphical layout of the concepts and descriptions applicable to a woodwind model explored in this dissertation.

plays a part in commercial keyboards featuring real-time synthesis, such as the Yamaha VL-1 [MK95; Mas18].

Before the beginning of this Ph. D., a functioning proof of concept for a woodwind based on this geometry had been built and tested in the LMA [Doc+16]: to our knowledge, the only working implementation of a cylindrical saxophone geometry⁵, thanks to clever positioning of the short cylinder around the other (see chapter 2 for more detail). However, this prototype is capable of producing only a handful of notes, and is not particularly tuned to any scale whatsoever. Therefore, at this point, the stakes were high on developing and realizing a full cylindrical saxophone prototype, capable of playing a chromatic scale, and numerical optimization seemed a viable and scientifically motivating way of designing its geometry. It is at this moment, in 2017, that the Yamaha Corporation released the Venova (YVS-100), a saxophone-like instrument based on two branched cylinders. This drastically changed perspective on what would qualify as a "novel" saxophone-like instrument, as well as the requirements such instrument would have to fulfill.

Since a playable cylindrical saxophone instrument already exists, there is now an incentive for a new instrument of the same kind to not only be able to produce sound, but also be relatively in tune and easy to play. This incentive adds to the challenge posed to the numerical optimization procedure. In particular, it calls for an evolution of the optimization criteria, towards predicting the optimized instrument's "ease of playing" based on its physical model. As a consequence, the work orientation shifts, from merely optimizing a resonator geometry based on linear acoustics considerations, to exploring and qualifying the dynamics of a saxophone model, with an intimate link with the musician's control. Many fundamental building blocks for this are lacking. Notably, the overall knowledge on which signals the saxophone can

⁵More precisely, this prototype was the only cylindrical saxophone using a normal saxophone reed and mouthpiece. The south-american *caña de millo* [Lis83] and the west african transverse clarinets [GB04] constitute transverse saxophones, but their reeds are carved directly into the side of the resonator body, making the playing technique very different from that of the saxophone or the clarinet.

produce depending on the musician's actions is very limited. Although some work exists, it is often confined to small amplitudes [GGL97] near the thresholds [Ric+09], or uses geometrical approximations [ODK04; Tak+09].

The exploration of the dynamics of the saxophone is approached from a specific angle: qualitative classification of the oscillation regimes, as represented by the red and green colors on Figure 1. The objective of this approach is to explore as wide a range of control parameters as possible, and qualitatively sorting the results depending on broad archetypes of the steady-state oscillations. All through this document, the steady-state patterns of evolution of the mechanical and acoustical variables in the instrument are called *regimes*.

The first distinction, far from uninteresting as it continues to frustrate many a wind instrument beginner, lies between oscillating and non-oscillating regimes. Clearly, an instrument will not be considered playable if producing any sound at all is already tedious. This first distinction, simplistic as it may seem, has the potential to yield a first indicator of "ease of playing". Then, when dealing with oscillating regimes, one can distinguish between periodic regimes (which correspond directly to musical pitch) or other kinds of sound, such as raucous or unpitched sounds. This separation can lead to a slightly more evolved indicator of ease of playing: how easy it is to produce a pitched tone, that can correspond to a musical note. Generally, throughout this work, refinements of the regime classification point to the same objective of quantifying the ease of playing. To this end, classifications are applied to numerical simulations of a saxophone's dynamics, to show which action of the (virtual) musician leads to which type of regime. The finality of such study would be to assess whether a regime is easy or hard to play, based on how it appears in numerical simulations – often, rarely, only for extreme control parameter values... This branch of the work also serves to introduce practical visual representations of the model's behavior, and reflect on their possible use. These visual representations can be assimilated to maps, displaying intervals of the control parameter leading to each regime as a region in the parameter space. This process provides an occasion to reflect on the traps intrinsic to studying the dynamics of a strongly nonlinear system such as the saxophone, and many comments throughout this work aim at identifying and compensating certain bias due to the unpredictability and the complexity of the model.

The dynamic behavior of the saxophone is explored by applying numerical simulation tools to a physical model. This model's oscillating regimes are studied using two methods. The first is time-domain synthesis, which directly gives the sound produced by the model. The second is the harmonic balance method (HBM) which instead indicates the possible sounds – that is, the stable periodic oscillations of the model. These two fundamentally different methods are used in order to widen the perspective on the results, as well as make them more robust by validating each other's results. As often as possible, experimental work supports the numerical studies. Measurements of the passive acoustical characteristic of saxophone resonator provide the value of many parameters of the model. Moreover, an instrumented mouthpiece ties the dynamic phenomena observed numerically to real playing situations involving a musician, whose control of the instrument is monitored. The experimental aspect of the work is intimately linked to its original objective being practical instrument design: the result should stay as close as possible to the musician's experience with a real instrument.

This dissertation is organized as follows. Chapter 1 lays the foundations to understand the tools used in the next chapters. Its objective is to provide a more pedagogical and detailed approach to the mathematical concepts, numerical methods and experimental tools than what is offered in the introductory sections of each reproduced paper. Chapter 2 presents the optimization of a bicylindrical resonator, based on the acoustical characteristics of a saxophone. Much of the discussion concerns the optimization procedure, the validity and unicity of the optimum, and its differences with the target saxophone. Chapter 3 initiates the discussion about the dynamics of the saxophone by collecting, organizing and finding links between the oscillation regimes produced by the saxophone. This chapter separates the study of high and low fingerings, and also study the effect of a well-known simplification employed in saxophone models, the so-called *ghost reed*. Taking the study of the dynamics further, and somewhat circling back to the idea of a design criterion closer to playability, chapter 4 studies a two-dimensional representation of the saxophone behaviors as regime maps in the control parameter space. The final chapter 5 tackles a phenomenon with great impact on the understanding and description of the behavior of a saxophone: multistability. This focus on simultaneously stable regimes is the occasion to discuss how initial conditions and control

parameter transients can affect the steady-state signal, as well as introduce a refinement to the regime maps.

Chapter 1

Fundamental concepts and basic applications: woodwind models, analysis and optimization tools

Introduction

This chapter introduces the elements used in this work to explore the problem of scientifically informed instrument design. The starting point (Section 1.1) defines a physical model of saxophone, meaning the equations governing all the interacting parts of the instrument their parameters. Among the various existing representations of each element, this work does not always present and use the most recent or the most detailed. This is due to a concern on our behalf to limit the number of parameters as much as possible, with a twofold objective: to facilitate reproducibility of the results, and to be able to keep track of which phenomenon and behavior can be attributed to each element of the model. Once the physical model is constructed, Section 1.2 details the two methods used to solve the model's equations and thus the sound produced by the saxophone model. These two methods, namely time-domain synthesis and a combination of the Harmonic Balance Method (HBM) and the Asymptotic Numerical Method (ANM), are intrinsically different. As such, throughout this document, they provide two complimentary approaches to the complex problem of the model's dynamic behavior. Each method tempers the other's results, to give nuanced conclusions on the observed phenomena. The next Section 1.3 outlines a numerical tool omnipresent in scientifically-based design across all fields: optimization. Section 1.3, in addition to giving a general definition of an optimization problem, explains the principle of two types of optimization algorithm mentioned in Chapter 2. The last Section 1.4 concerns the experimental investigations carried out alongside the thesis, to reinforce the conclusions drawn using the physical model. It describes two experimental devices: the impedance sensor that characterizes the instrument's resonator to inform the model, and the instrumented mouthpiece that allows monitored exploration of the instrument's dynamics while played by a musician.

Some of these elements are directly put into context by presenting a straightforward application case. Synthesized sound examples complete the description of numerical time-domain synthesis and illustrate the effect of some important parameters. The instrumented mouthpiece is presented alongside a discussion pertaining to its calibration and its limitations. Similarly, after describing the impedance sensor, we mention the results of work aiming to estimate its inherent uncertainties, and show input impedances measured in the saxophone family that exhibit some interesting common features.

1.1 Physical model of reed instrument

1.1.1 Structure of the physical model, main variables and parameters

Woodwind physical models are traditionally constituted of three main elements forming a feedback loop: the reed, the reed channel, and the resonator (see Fig. 1.1). The musician presses on the reed, mainly with their lower lip, and blows into the reed channel. When

oscillation is triggered, the reed vibrates: it moves mainly up and down, thus varying the height of the reed channel. When the reed channel height varies, the flow circulating through it is modulated. This modulated flow excites the entrance of the resonator, the air column contained in the tube. This air column, due to its geometry, has resonant properties: it responds more strongly to certain frequencies of excitation. The response of the resonator can be seen as pressure, that acts upon the movement of the reed. When it so happens that the modulated flow wave coming from the reed channel excites the resonator at a resonance, meaning a frequency to which it responds strongly, it reinforces the movement of the reed at this particular frequency, thus amplifying the flow through the reed channel. This process leads to self-sustained oscillation at said frequency: a note is produced.

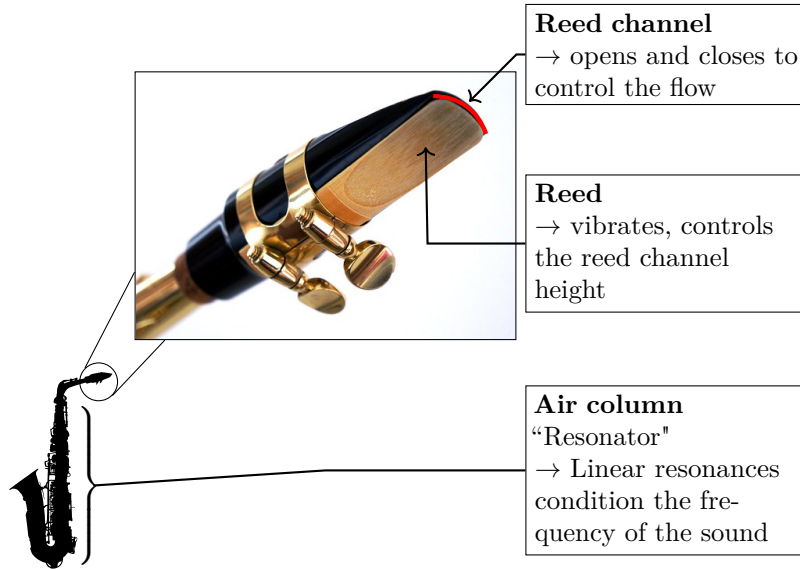


FIGURE 1.1: Schema and graphical representation of the different elements of a saxophone model.

The main physical variables of this model are the reed displacement from equilibrium x , the acoustic flow rate entering the mouthpiece u , and the acoustic pressure in the mouthpiece p . Through the present document, dimensionless variables are used [WB74; Gok79; Hir95]. In numerical applications, they contribute to prevent ill-conditioning and rounding issues that can arise when variables are several orders of magnitude apart. They are also used to formulate the analytical results which provide unambiguous references to most numerical studies carried out in the present work. Dimensionless models also facilitate comparisons, say between saxophone and clarinet, or between alto and tenor saxophone, by eliminating some irrelevant scaling effects. The dimensionless variables are defined by

$$x = \frac{\hat{x}}{H} \quad ; \quad p = \frac{\hat{p}}{p_M} \quad ; \quad u = Z_c \frac{\hat{u}}{p_M} \quad (1.1)$$

where the hat denotes the physical variable with its dimension, H is the distance between the reed at rest and the mouthpiece lay, p_M is the static pressure necessary to bring the reed to the mouthpiece lay and Z_c is the characteristic impedance at the input of the resonator. For a cylinder, $Z_c = \frac{\rho c}{S}$, where S is the cross-section at the input, ρ is the density of air and c is the speed of sound. Under normal conditions, $\rho = 1.2 \text{ kg/m}^3$ and $c = 343 \text{ m/s}$. Note that \hat{x} is the physical reed displacement relative to equilibrium, which is distinct from the height \hat{h} (physical) and h (dimensionless) of the reed channel. The two variables are linked in physical and dimensionless form by

$$\hat{x} = \hat{h} - H, \quad h = x + 1. \quad (1.2)$$

The rest of this work uses the notation x as often as possible.

The dimensionless control parameters γ and ζ are used throughout this work to represent the musician’s action, through the blowing pressure they apply (γ) and the strength applied by their lip to control the opening of the reed channel at rest (ζ). The parameters are defined as

$$\zeta = wHZ_c\sqrt{\frac{2}{\rho p_M}}, \quad \gamma = \frac{\hat{\gamma}}{p_M}, \quad (1.3)$$

where w is the effective width of the reed channel and $\hat{\gamma}$ is the physical value of the blowing pressure. A null value of the blowing pressure parameter ($\gamma = 0$) corresponds to the musician not blowing into the instrument, while $\zeta = 0$ corresponds to the reed channel being closed at rest. Note that both situations prevent any self-sustained oscillations. Another important value is $\gamma = 1$, above which the pressure in the mouth of the musician is sufficient to close the reed channel completely in the static regime. Therefore, when $\gamma \geq 1$, an equilibrium can appear where the reed channel stays closed. Another reference value of the blowing pressure is the instability threshold $\gamma = 1/3$ of the simple woodwind model (the lossless Raman model, see [Wor71; GGL97; KOG00]), above which the equilibrium becomes unstable. Figure 1.2 represents a simplified block diagram featuring the elements of the model and the variables through which they interact.

Representing the action of the musician using only two control parameters is obviously a gross simplification. Technique guides designed for musicians such as [Tea63] regroup under the term *embouchure* or *face mask* the combined action of all facial muscles controlling the jaws, lips, cheeks and tongue. Some saxophone control techniques beyond those that can be described using γ and ζ are the object of scientific studies: we mention the adjustment of the vocal tract [CTH82; SLS08; CSW08; Gui+10; Li+16] or the use of the tongue [HG14; LCL17; PVHC18]. In the present document, these effects are ignored for several reasons. Firstly, having more than two parameters hinders the visual representation of the results. Second, γ and ζ have a clearly defined effect on the nonlinear characteristic, which is the element of the model necessary for self-sustained oscillations and on which there is a consensus in the scientific community after thorough studies. Finally, as the rest of this document shows, several complex phenomena can be exhibited using only these two control parameters.

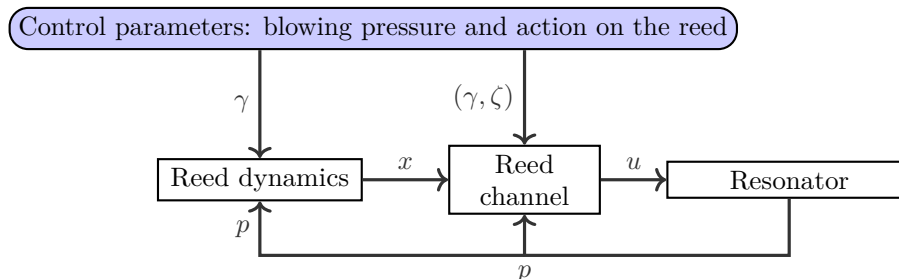


FIGURE 1.2: Block diagram of the three main elements of a saxophone model, along with dimensionless control parameters and physical variables.

1.1.2 The reed model

The reed is a very sensitive element of woodwind instruments. Often made of cane, it can also be totally or partially made of plastic. As shown in Figure 1.3, it is carved in a very specific fashion, with a thick butt and stock held against the mouthpiece by the ligature, thinning progressively until the tip. The thin portion of the reed is flexible and its role is to control the opening section that exists between the mouthpiece and the mouth of the musician. In fact, the reed constitutes the one moving mechanical element that renders possible the ‘valve effect’ leading to oscillations. Moreover, the reed is in direct contact with the musician’s lower lip, making it a privileged vector of musician control. Conveying all the subtle characteristics of the reed would require a very complex model. In the present work, we rather focus on a simple model fit for fast numerical synthesis, with only two to four parameters.

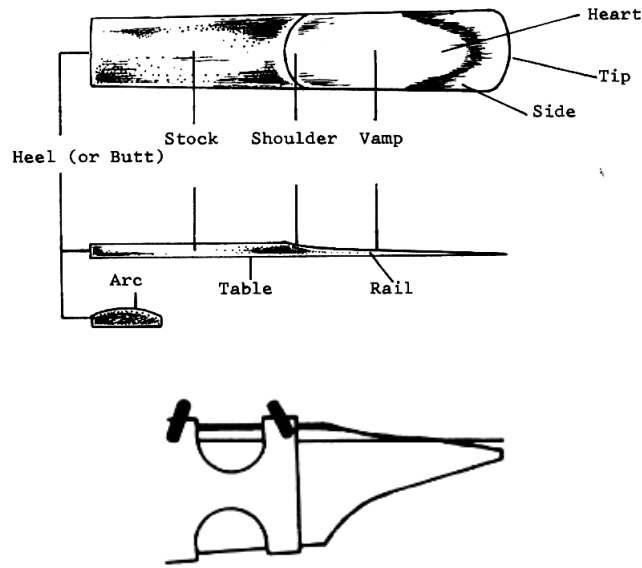


FIGURE 1.3: Saxophone reed and mounting on the mouthpiece (adapted from [Tea63]).

The reed, as a three-dimensional mechanical oscillator, has several modes of vibration, associated with different modal shapes and resonance frequencies [FBC00; AVW04; Tai+14]. However, it is often represented as a single degree of freedom oscillator [Das31; Gho38; Bac63; Tho79; VWA07]. In the simplest approximation, the reed can be considered a mere spring without dynamics [Ker+16], instantaneously following the pressure difference between the inside of the mouthpiece and the mouth of the musician, leading to the dimensionless equation:

$$x = p - \gamma. \quad (1.4)$$

Note that this equation can be applied to studying static cases.

In a dynamic setting, a single degree of freedom oscillator equation is often employed, accounting for only one mode of the reed. The governing equation is

$$\frac{1}{\omega_r^2} \ddot{x} + \frac{q_r}{\omega_r} \dot{x} + x = p - \gamma + F_c(x), \quad (1.5)$$

where the modal parameters of the reed are the angular frequency ω_r and the damping coefficient q_r , and $F_c(x)$ is the force accounting for the contact between the reed and the lay, detailed in Subsection 1.1.2.1. A common refinement of this model includes a varying stiffness and damping, for instance discussed in [MA+16]. For the sake of simplicity, but most of all for the sake of reducing the number of parameters of the model, the value of the modal parameters is $\omega_r = 4224$ rad/s (672.3 Hz), and $q_r = 1$ through this document, unless otherwise specified. These values are empirically determined in [MA+16], by fitting signals synthesized with a linear model to experimental data.

1.1.2.1 Model of contact with the lay

As the reed progressively closes the channel, it curls onto the mouthpiece lay and rails (see Figure 1.4 for an annotated view of the mouthpiece). Figure 1.5 shows that a closed reed channel implies contact between the reed and the mouthpiece, and thus the limitation of the reed displacement. Therefore, a complete reed model should include an element accounting for the action of the lay. The process of contact between the reed and the mouthpiece lay and rails is complex, as it involves multiple point of contact between two deformable surfaces

[Oll02]. The present work chooses to model contact as a force acting on the reed following recent work [CW12; BTC15]. This force increases when the reed channel closes.



FIGURE 1.4: Side and below schematic views of a saxophone mouthpiece, adapted from [Tea63].

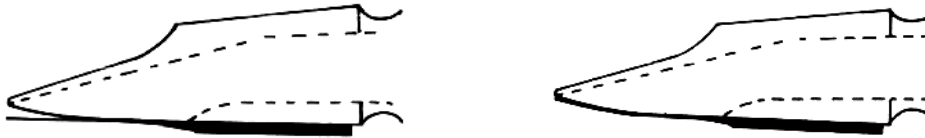


FIGURE 1.5: Side schema of an open reed channel and closed reed channel, with reed pressed against the mouthpiece rails, adapted from [Tea63].

The contact force $F_c(x)$ relies on a polynomial stiffness depending on the penetration of the reed into the lay [CW12], to which a nonlinear damping term can be added [BTC15]. The dimensionless expression depending on the distance from reed to lay $x + 1$ is

$$F_c(x) = K_c([x + 1]^-)^\alpha - \beta K_c([x + 1]^-)^\alpha \dot{x}, \quad (1.6)$$

where K_c is the nonlinear stiffness of the mouthpiece lay, α is a stiffness exponent and β is a dimensionless coefficient that controls the nonlinear damping term, and the notation $[.]^- = (. - |.|)/2$ denotes the negative part of a variable. In the rest of this work, unless otherwise specified, we fix $K_c = 100$ and $\alpha = 2$. The value $K_c = 100$ is based on [BTC15] and $\alpha = 2$ facilitates the quadratic recast necessary to implement the system into MANLAB (see Subsection 1.2.2). This models a barrier with some penetration [Tai18]. The phenomenon of penetration due to a regularized contact law is actually better interpreted as progressive increase of the contact surface and some squishing between the reed on the mouthpiece. Interpreted as such, a regularized contact may be in better agreement with the physics of the system than a stiff limitation of the reed displacement. Studies based on finite element simulations [VWA07] actually suggest a variable stiffness as a lumped approximation for the behavior of the reed, accounting for the progressive contact with the lay. The nonlinear contact damping coefficient is set to $\beta = 0.001$ s, so that the nonlinear damping is strong enough to dampen spurious rebounds on the lay but weak enough not to trap the reed whenever it penetrates the lay. The contact force is represented in Figure 1.6, along with the force due to the linear reed stiffness for reference. It can be seen that the contact force surpasses the linear stiffness for $x < -1.1$ and grows very rapidly. Note that the contact force $F_c(x)$ may be ignored ($F_c(x) = 0$), following the so-called *ghost reed* simplification, often used in analytical studies or work focused around the equilibrium state [Das31; Gho38; GKN89; DGK00]. The question of the effect this rather drastic simplification has on the dynamics of the system is addressed in more detail in Chapter 3 Section 3.4.

1.1.2.2 The reed flow

In addition to the flow induced in the reed channel, the reed movement can introduce a flow into the mouthpiece because the reed displaces air as it moves. According to [Sch81] it is proportional to the speed of the reed

$$u_r = -S_r \dot{x}, \quad (1.7)$$

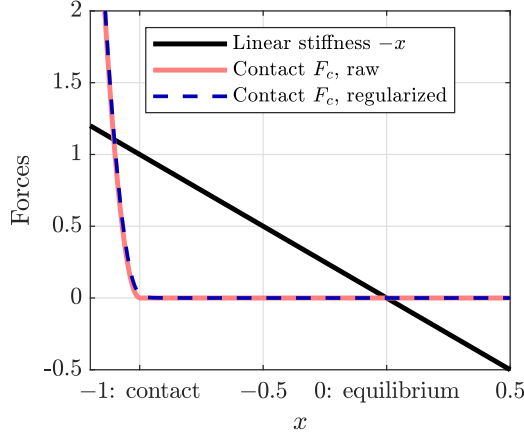


FIGURE 1.6: Contact force between the reed and the lay: raw version and version regularized using Eq. (1.17), with the force due to linear reed stiffness intended as reference.

where the coefficient S_r is proportional to the surface area of the reed. Its value $S_r = 6.5 \times 10^{-5} \text{ m}^2$ is estimated experimentally in [Dal+95].

1.1.3 The reed channel

1.1.3.1 Nonlinear characteristic deduced from Bernoulli's law

The total flow u entering the instrument can be expressed as the sum of the flow due to the movement of the reed u_r and the flow through the reed channel u_b :

$$u = u_b + u_r. \quad (1.8)$$

The flow u_b actually constitutes the main excitation mechanism of the model : contrary to u_r , it is not linear, and thus makes self-sustained oscillations possible in the model. The nonlinear characteristic described in [WB74] gives the flow going through the channel formed between the reed and the mouthpiece lay, depending on the position of the reed and the pressure on both sides of the channel: in the mouth of the musician and in the mouthpiece. The characteristic is deduced from Bernoulli's law

$$\hat{v} = \text{sign}(\hat{p}_m - \hat{p}) \sqrt{\left| \frac{2(\hat{p}_m - \hat{p})}{\rho} \right|}. \quad (1.9)$$

The flow \hat{u}_b is then deduced by multiplying the speed \hat{v} by the cross-section of the reed channel, which is assumed to be proportional to the opening of the reed $[\hat{x} + H]^+$. The proportionality factor is the effective channel width w . This hypothesis can also be seen as the reed channel cross-section being a rectangle of height $[\hat{x} + H]^+$ and width w . Although this hypothesis may seem very simplistic, experimental evidence [Hir+90; VZ+90; DGO03] support that it is reasonable for a large range of reed positions. This yields

$$\hat{u}_b = w[\hat{x} + H]^+ \hat{v} = w[\hat{x} + H]^+ \text{sign}(\hat{p}_m - \hat{p}) \sqrt{\left| \frac{2(\hat{p}_m - \hat{p})}{\rho} \right|}. \quad (1.10)$$

Introducing the dimensionless variables from Eq. (1.1) and the dimensionless blowing pressure γ of Eq. (1.3), we get

$$u_b \frac{p_M}{Z_c} = wH \sqrt{\frac{2}{\rho}} [x + 1]^+ \text{sign}(\gamma - p) \sqrt{p_M |\gamma - p|}, \quad (1.11)$$

$$u_b = wHZ_c \sqrt{\frac{2}{\rho p_M}} [x + 1]^+ \text{sign}(\gamma - p) \sqrt{|\gamma - p|}. \quad (1.12)$$

The multiplicative constant in front of this expression defines the reed opening control parameter ζ , previously introduced at Eq. (1.3), such that the dimensionless flow is

$$u_b = F(p, x) = \zeta[x + 1]^+ \text{sign}(\gamma - p) \sqrt{|\gamma - p|}. \quad (1.13)$$

In the case where reed dynamics are ignored and the reed position follows Eq. (1.4), the nonlinear characteristic only depends on the variable p and writes

$$u_b = F(p) = \zeta[p - \gamma + 1]^+ \text{sign}(\gamma - p) \sqrt{|\gamma - p|}. \quad (1.14)$$

This characteristic is the main point at which the musician control parameters γ and ζ act on the model's behavior (in addition to the intervention of γ in the reed movement equation 1.5). The blowing pressure parameter γ translates the characteristic and the point of null flow at $p = \gamma$ that corresponds, for instance, to the long episode of the standard Helmholtz motion approximation. The reed opening at rest parameter ζ controls the value of the maximum flow (occurring at $p = \gamma - 1/3$ when ignoring reed dynamics) and the steepness of the slopes.

1.1.3.2 Regularizations

The raw nonlinear characteristic of Eq. (1.14) has two singular points which can cause issues in numerical applications, for instance by introducing high-frequency artifacts. Two types of regularizations of these two points are used throughout this work.

The first version is used in the time-domain synthesis method, derived from Guillemain [Coy+15], uses trigonometric functions and is described in [Ker+16]. The correspondance between the two irregular functions and the regularized versions is depicted in Figure 1.7. The regularization of the reed opening uses the arctan function and O_a as a regularization parameter,

$$[\bullet]^+ \leftrightarrow \frac{O_a}{\pi} + \bullet \times \left(\frac{1}{2} + \frac{\arctan(\bullet/O_a)}{\pi} \right). \quad (1.15)$$

The regularization of the vertical tangent at the pressure equilibrium point $p = \gamma$ uses a hyperbolic tangent and another regularization parameter V_a , replacing the absolute value by

$$|\bullet| \leftrightarrow \bullet \times \tanh(\bullet/V_a). \quad (1.16)$$

Unless otherwise specified, the values of these regularization parameters are $O_a = 0.1$ and $V_a = 0.05$ [Ker+16].

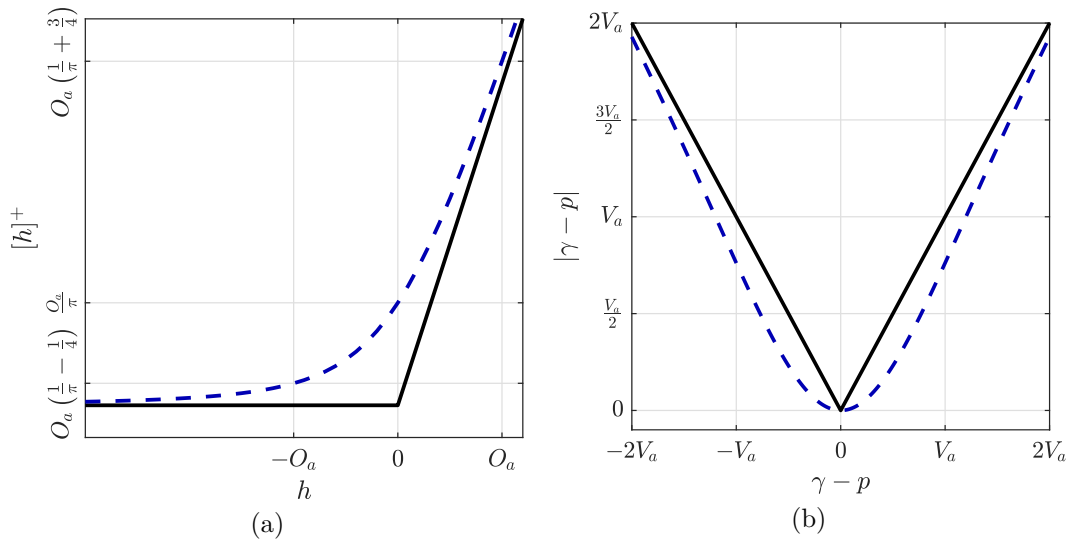


FIGURE 1.7: Representation of the regularizations, raw in solid black and regularization in dotted blue. (a) Eq. (1.15): ramp $[\bullet]^+$ and (b) Eq. (1.16): absolute value $|\bullet|$.

The second regularization is used for the quadratic formulation required by MANLAB (see 1.2.2). It involves replacing all the absolute values functions

$$|\bullet| \leftrightarrow \sqrt{\bullet^2 + \eta}, \quad (1.17)$$

using the value $\eta = 0.001$ as default. Both regularizations entail minimal changes on the nonlinear characteristic, as can be seen on Figure 1.8: they just serve to smooth out irregularities of the raw characteristic without significantly altering the behavior or the solutions of the model.

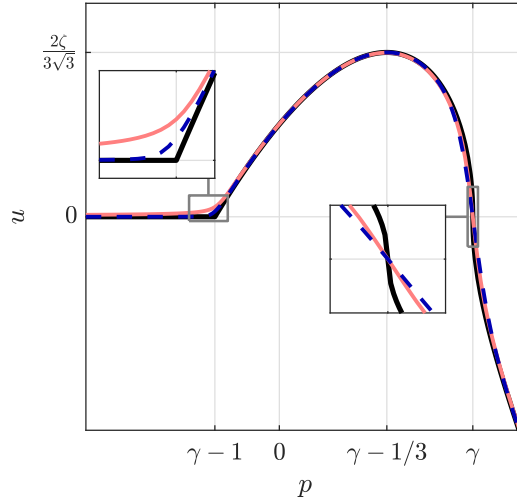


FIGURE 1.8: Representation of the static characteristic of Eq. (1.14) (black) and the regularized versions using Eqs. (1.15) and (1.16) (blue) due to Guillemain with $O_a = 0.1$ and $V_a = 0.05$, and Eq. (1.17) (red) used for MANLAB with $\eta = 0.001$.

1.1.4 The resonator

The instrument's resonator is the air column contained inside the main bore. The resonator is excited by the vibrations of the reed, and its response conditions the production of a periodic sound. In particular, the resonances of the air column conditions the possible pitches of the produced sound, while its overall acoustical response to excitation shapes the spectrum of the sound. This response is formalized by the quantity called *input impedance*, which is the ratio between the acoustic flow and pressure at the input of the resonator. The input impedance is defined in the frequency domain as

$$Z(\omega) = \frac{P(\omega)}{U(\omega)}. \quad (1.18)$$

Note that since P and U are dimensionless, the notation Z refers to the dimensionless input impedance. The relation with the input impedance \hat{Z} (with its dimension) is

$$Z(\omega) = \frac{\hat{Z}(\omega)}{Z_c}. \quad (1.19)$$

Recall that Z_c is the characteristic impedance of the resonator. The simulations carried out in this work are entirely based on input impedance measurements performed on saxophone resonators. However, the impedance is quite impractical to use as is in the simulations – notably, its time-domain equivalent obtained *via* inverse Fourier transform is very long (see [Sch81]). In order to be usable, it must be processed, for instance using the modal decomposition or the reflection function formalism. These two approaches are presented in continuous time in subsections 1.1.4.1 and 1.1.4.2. Subsection 1.2.1 then details their discrete implementation in the time-domain synthesis routine.

1.1.4.1 Modal analysis of the input impedance

The most important features of the resonator's response are its resonances. To simplify the representation of the response and include it in simulations more easily, the impedance is decomposed in modes, each of which can be associated with a resonance. Variants of this method have been used in [AR85; MA93; AFL12; Ter+12; KVC12a; Sil+14; Vel+17]. The impedance writes

$$Z(\omega) = \sum_{k=1}^{N_m} \frac{C_k}{j\omega - s_k} + \frac{C_k^*}{j\omega - s_k^*}, \quad (1.20)$$

where $*$ denotes the complex conjugate and N_m is the number of modes. The choice of N_m determining the modal truncation will vary throughout the document, depending on each study's requirements. Eventhough a large N_m accounts for high-frequency characteristics of the resonator, limiting N_m to two or three provides results that are much more readable, by limiting the number of parameters of the model. Modal fitting [Coy+15] is used to determine the modal dimensionless residues C_k and poles s_k . The modal formulation translates immediately to the continuous time-domain formulation by inverse Fourier transform, giving the evolution of each complex modal component p_k as first order ODE including the flow as the source term and the pressure p as a sum of those components

$$\dot{p}_k(t) - s_k p_k(t) = C_k u(t), \quad p(t) = 2 \sum_{k=1}^{N_m} \text{Re}(p_k(t)). \quad (1.21)$$

Some applications presented hereafter will use the formalism of real modes, that involves three real parameters rather than two complex parameters:

$$Z(\omega) = \sum_{k=1}^{N_m} \frac{4\omega_k}{\pi A_k} \frac{\alpha_k + j\omega}{\omega_k^2 + \alpha_k^2 + 2j\alpha_k\omega - \omega^2}, \quad (1.22)$$

where the modal amplitude coefficient A_k , damping coefficient α_k and angular eigenfrequency ω_k are linked to the corresponding modal poles and residues by

$$C_k = \frac{2\omega_k}{\pi A_k}, \quad s_k = -\alpha_k + j\omega_k. \quad (1.23)$$

Note that the real mode formulation is less general than the complex mode formulation, since it only includes three real parameters instead of four (real and imaginary parts of two complex coefficients). Eq. (1.22) also translates to the temporal domain and yields a second order differential equation:

$$\ddot{p}_k + 2\alpha_k\omega_k\dot{p}_k + (\omega_k^2 + \alpha_k^2)p_k = \frac{4\omega_k}{\pi A_k}(\alpha_k u + \dot{u}) \quad p(t) = 2 \sum_{k=1}^{N_m} \text{Re}(p_k(t)). \quad (1.24)$$

Real modal coefficients are extracted using a fit of the impedance around the peaks. The first step of the method is a simple peak detection performed by finding the frequencies f_p for which

$$|Z_s[f_p]| > |Z_s[f_p - \Delta f]| \quad \text{and} \quad |Z_s[f_p]| > |Z_s[f_p + \Delta f]| \quad \text{and} \quad |Z_s[f_p]| > H_t \times \max_f(|Z_s[f]|), \quad (1.25)$$

where Z_s is the impedance Z smoothed by a gaussian moving average, Δ_f is the discrete frequency step of the impedance measurement, and H_t is an arbitrary peak height threshold fixed at 1/20. The next step occurs on intervals around these frequencies f_p defined as $I_\omega = 2\pi \times [f_p - f_p^{(1)}/4; f_p + f_p^{(1)}/4]$, where $f_p^{(1)}$ is the frequency of the first peak (which is approximately the distance between two consecutive peaks for instruments overblowing to the octave).

The modal frequency is estimated as

$$\omega_k = \operatorname{argmax}_{\omega \in I_\omega} |Z(\omega)|. \quad (1.26)$$

The modal residue A_k is given by

$$A_k = \frac{k}{|Z(\omega_k)|} \frac{1 + r_m}{1 - r_m}, \quad (1.27)$$

where

$$r_m = \frac{1/(4\omega_1) - \sqrt{1/(4\omega_1)^2 + \tau_m^2}}{\tau_m}, \quad (1.28)$$

$$\tau_m = \min_{\omega \in I_\omega} (\tau_g(\omega)), \quad (1.29)$$

using the group delay defined by

$$\tau_g(\omega) = -\Im \left(\frac{d\angle Z}{d\omega} \right). \quad (1.30)$$

Note that the group delay deduced in this manner from a measured impedance is subject to strong additive noise due to the derivative. Therefore, an inverse second order polynomial is fitted in the region as a way to approximate the group delay. The minimum search is then done on the adjusted inverse second order polynomial. The modal damping α_k is then estimated as

$$\alpha_k = \frac{\omega_k}{\pi} \log \left(-\frac{1 - A_k |Z(\omega_k)|}{1 + A_k |Z(\omega_k)|} \right). \quad (1.31)$$

Figure 1.9 illustrates the fit obtained on a simulated cylinder input impedance, as well as a measured saxophone impedance. The differences can be noticed in that the asymmetry of the peak is neglected by the real mode formalism, which produces only symmetrical peaks. The method works best at the top of the peak, as the differences in modulus of Figure 1.9 exhibit.

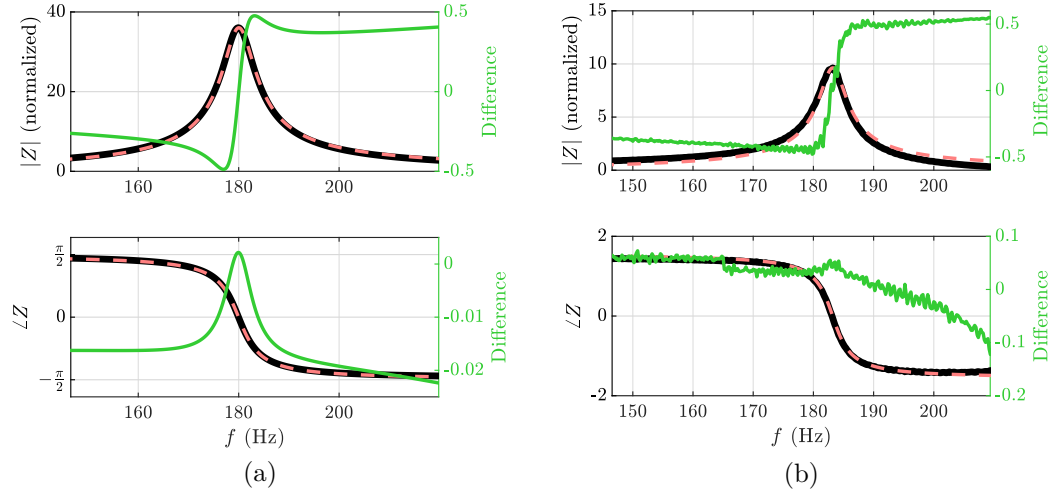


FIGURE 1.9: Modal fit according to Eqs. (1.26), (1.27), (1.31) of the first peak of (a) a cylinder (b) a saxophone (same fingering as figure 1.10). **Thick black**: measured impedance, **red** reconstructed impedance according to Eq. (1.22). The right **green** axis displays the difference between the two other curves.

Figure 1.10 shows the impedance reconstructed from 3, 6 or 12 modes. The modal analysis method applied here takes into account one peak at a time, separately. It is thus vulnerable to modal overlap in high frequency, where damped peaks that are close together occasion an overall rise of the modal impedance from the reference. This effect is visible in the figure on

the reconstructed impedance for $N_m = 12$ starting at about 1500 Hz. The main advantage of this method is that it requires no curve fitting, which makes it extremely fast.

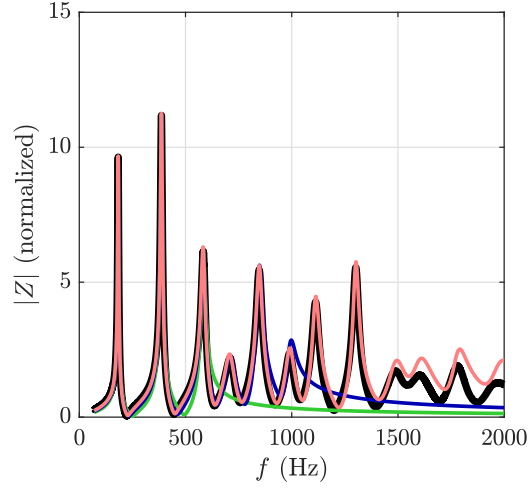


FIGURE 1.10: Reconstruction of the impedance modulus from modal coefficients. **Thick black**: measured impedance before modal decomposition, **green**: $N_m = 3$, **blue**: $N_m = 6$, **red**: $N_m = 12$.

Another way to represent the resonator, which is not subject to the modal overlap problem that arises in high frequency, is based on the reflection coefficient.

1.1.4.2 Reflection coefficient and reflection function

1.1.4.2.a Definition

The following calculations use the dimensionless variables of Eq. (1.1). The acoustic pressure inside the resonator is assumed to follow a wave equation [CK08] such as

$$\Delta p - \frac{1}{c^2} \frac{\partial^2 p}{\partial t^2} = 0, \quad (1.32)$$

where $\Delta = \nabla^2$ is the laplacian operator. Assuming plane waves with a single space parameter x , the general solution of this equation writes

$$p(x, t) = p^+(x - ct) + p^-(x + ct), \quad (1.33)$$

where p^+ is the dimensionless forward travelling wave and p^- is the dimensionless backward travelling wave. The flow inside the tube is linked to the pressure by the linearized Euler's equation:

$$\frac{\rho}{SZ_c} \frac{\partial u}{\partial t} = -\frac{\partial p}{\partial x}, \quad (1.34)$$

which we transform using Eq. (1.33) to give u as a function of the travelling waves

$$u(x, t) = p^+(x - ct) - p^-(x + ct). \quad (1.35)$$

Therefore the travelling waves at the input of the resonator write

$$p^+ = \frac{p + u}{2} \quad p^- = \frac{p - u}{2}, \quad (1.36)$$

The reflection coefficient is defined as the ratio between the forward and backward travelling waves in the frequency domain, that is

$$R(\omega) = \frac{P^-(\omega)}{P^+(\omega)} = \frac{Z(\omega) - 1}{Z(\omega) + 1}. \quad (1.37)$$

The reflection function r is obtained by inverse Fourier transform of the reflection coefficient

$$r(t) = \mathcal{F}^{-1}(R)(t) \quad (1.38)$$

and gives the backward wave at the input of the resonator as a function of the forward wave as

$$p^-(t) = (r * p^+)(t), \quad (1.39)$$

where $*$ denotes the convolution product. The reflection function is used in synthesis [MSW83; AS95] as an alternative to a full waveguide simulations .

1.1.4.2.b Computing the reflection function from a measured impedance

The input impedances on which the simulations are based are measured over a finite frequency range, from about 50 Hz up to a few thousand Hertz. However, applying the inverse Fourier transform from Eq. 1.38 requires reflection coefficient values, and therefore impedance values, all the way from frequency 0 to infinity in continuous time. For discrete time applications, reflection coefficient values must at least be supplied from 0 to the Nyquist frequency, which is half the sampling rate. For a typical audio sample rate like $F_s = 44100$ Hz, the Nyquist frequency is well above the upper frequency limit of the measurements. Before being processed into a time-domain reflection function, the impedance must be expanded in the frequency domain, both in high and low frequency (see [GGA95]). Naive zero padding adds undesirable rippling effects and is not physically valid in high frequency, where the impedance should tend to one (which corresponds to the characteristic impedance Z_c for the physical input impedance). In our case, the low-frequency prolongation consists in a simple linear interpolation from $Z = 0$ at frequency 0 to the first value of the measured impedance. More complicated expansion methods based on higher order polynomials were tested, such as the one presented in [Tai+18], with minimal effect on the synthesized signals compared to the added number of arbitrary synthesis parameters.

In higher frequency, a simple padding approach can be adopted, by appending ones above the high frequency limit of the measurement. This approach causes a discontinuity and possible rippling in high frequency as Figure 1.11 shows. A smooth expansion using an exponential function as a continuously derivable transition between the last measured impedance value and the characteristic impedance is adopted to eliminate unwanted ripples. Precisely, the impedance above the truncation at f_{max} is given by

$$Z(f) = 1 + (Z(f_{max}) - 1) \exp(\delta_Z(f_{max} - f)) \quad (1.40)$$

where the coefficient δ_Z ensures the continuity of the derivative and is given by

$$\delta_Z = \frac{Z'(f_{max})}{Z(f_{max}) - 1}. \quad (1.41)$$

In this expression $Z'(f_{max})$ denotes the value of the derivative of the impedance with respect to frequency at the truncation frequency f_{max} . Note that the impedance modulus must be decreasing at f_{max} for $Z(f)$ expression to converge to 1.

1.2 Numerical simulation

Throughout this manuscript, two main simulation methods are used complementarily to study the behavior of the physical model. The first method is time-domain synthesis, which consists of a step-by-step resolution of the equations of the model. With this method, the operator of the code acts very similarly to the musician, by imposing certain values of the control parameters, and then observing the signal that is produced by the model. This signal can attain steady-state periodic regime, provided the control parameters stay constant for a long period of time. It can also be complicated by transient phenomena, such as note onsets and offsets, as well as any type of quasi-periodic or chaotic regime the model may produce. These signals can hold a lot of information, and it is sometimes hard to categorize and interpret them clearly.

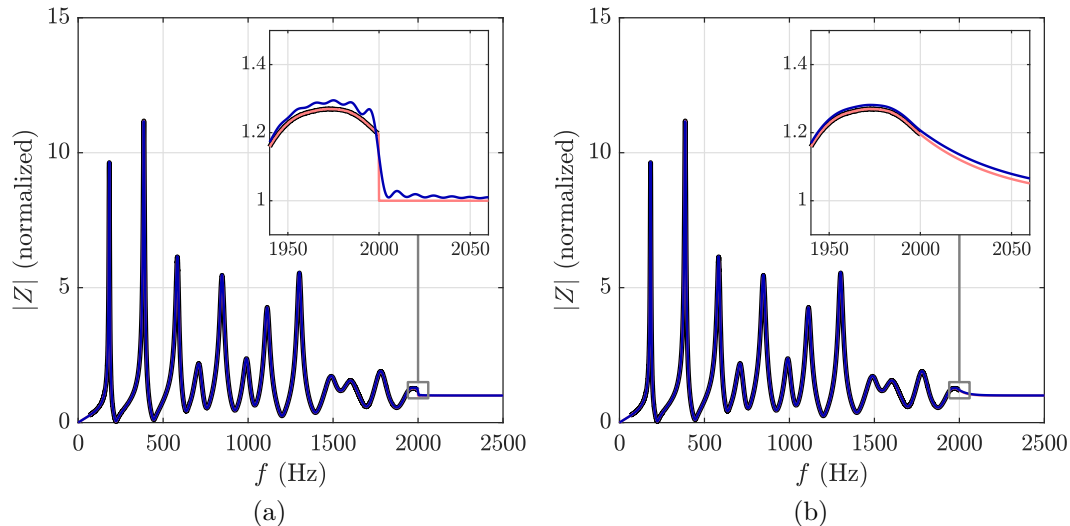


FIGURE 1.11: High frequency expansion of the measured input impedance by (a) padding (b) exponential transition. Moduli of the measured impedance in **thick black**, expanded impedance in **red** and reconstructed impedance after truncation of the reflection function in **blue** (see paragraph 1.2.1.1.c, $D_t = 100$ ms).

The second method, the Harmonic Balance Method (HBM) associated with continuation by the Asymptotic Numerical Method (ANM) [CV09], makes the strong assumption that this solution is periodic. In the HBM, the equations are simplified by solving for the amplitude of the harmonics of a solutions, instead of the complete solution. Once a periodic solution of the equations of the model is known for a given value of the control parameters, continuation by the ANM shows how it changes when progressively varying a control parameter.

Note that continuation yields sets of solutions along branches spanning continuous intervals of control parameter values, whereas any time-domain synthesis result is discrete in the control parameter space: one synthesis run will correspond to, for instance, a given couple (γ, ζ) . This approach, focused on the solution and its evolution, gives considerable insight into the functioning of the model. For instance, it can show one regime evolving into another or outline their limits of existence. This information can only be guessed when using time-domain synthesis: failure to converge to a solution does not necessarily mean this solution doesn't exist. The HBM also allows the determination of the stability of the solution and can treat unstable solutions, that do not appear in time-domain synthesis. However, all the possibilities offered follow from a strong hypothesis on the searched solutions: they must be periodic. Periodic solutions hold great interest in musical instruments, as periodic sounds will correspond to the musical notes the instrument can produce. However, this intrinsically prevents the HBM to be applied to the study of transient phenomena. For this last point, time-domain synthesis is particularly adapted.

1.2.1 Time-domain synthesis

Time-domain synthesis relies on solving the equations of the model step-by-step in the temporal domain. Here, we focus on real-time methods with uniform time step, because many of the applications presented afterwards give importance to the speed of the synthesis implementation. Two types of representation of the resonator are used: a modal decomposition of the impedance, as presented in continuous time in Subsection 1.1.4.1, and the reflection function of the resonator linking forward and backward travelling waves (subsection 1.1.4.2). Note that both formalisms for the resonator can be used in the synthesis without modifying the other equations.

1.2.1.1 Discretization of the equations

The continuous-time equations, (1.13) for the reed channel, (1.5) for the reed motion and (1.21) or (1.39), corresponding respectively to a modal or reflection function formalism for the resonator, can be discretized conjointly to give the state of the system at the next temporal step depending on the current and past states.

1.2.1.1.a Reed movement

The discretization proposed in [Gui04] yields

$$x[n] = \frac{1}{a_{0r}} (p[n-1] - \gamma[n] + F_c[n]) - \frac{a_{1r}}{a_{0r}} x[n-1] - \frac{a_{1r}}{a_{0r}} x[n-2], \quad (1.42)$$

where

$$a_{0r} = \frac{F_s^2}{\omega_r^2} + \frac{F_s q_r}{2\omega_r}, \quad a_{1r} = 1 - \frac{2F_s^2}{\omega_r^2}, \quad a_{2r} = -\frac{F_s q_r}{2\omega_r} - \frac{F_s^2}{\omega_r^2}, \quad (1.43)$$

and F_s is the sampling rate of the synthesis. Note that the pressure $p[n-1]$ in Eq. (1.42) is known, as it is the pressure at the previous instant. The contact force $F_c[n]$ is determined depending on previous values of x

$$F_c[n] = K_c([x[n-1] + 1]^+)^\alpha \times (1 - \beta F_s (x[n-1] - x[n-2])), \quad (1.44)$$

using a simple backward Euler approximation for the speed of the reed. Consequently, the stability of the synthesis method for $\beta \neq 0$ is not guaranteed, especially for low sampling rates. This is why in certain applications we will ignore the nonlinear damping term and set $\beta = 0$. Expressing F_c as a function of the current reed position would require iterative search of a fixed point, which is not a real-time process since the number of iterations is uncertain. Another possibility would be using an analytical expression of x , including F_c , but none was found. Note that once the reed position is computed, the reed flow is deduced using a backwards Euler approximation of the reed speed

$$u_r = \lambda(x[n] - x[n-1]), \quad (1.45)$$

where the constant λ is -0.7 [Coy+15].

1.2.1.1.b Resonator: modal decomposition

The modal representation of the resonator under the real modes formalism, described in continuous time in Eq. (1.24), can be discretized under the form

$$p_k[n] = b_{c0,k} u[n] + b_{c1,k} u[n-1] + b_{c2,k} u[n-2] + a_{c1,k} p_k[n-1] + a_{c2,k} p_k[n-2], \quad (1.46)$$

$$p[n] = \sum_{k=1}^{N_m} p_k[n]. \quad (1.47)$$

The coefficients $b_{c0,k}, b_{c1,k}, b_{c2,k}, a_{c1,k}, a_{c2,k}$ are obtained using the impulse invariance method [Jac00]

$$b_{c0,k} = N_o + Z_0, \quad b_{c1,k} = -N_o e_a c_w - 2Z_0 c_w e_a, \quad b_{c2,k} = Z_0 e_a^2 \quad (1.48)$$

$$a_{c1,k} = 2e_a c_w, \quad a_{c2,k} = -e_a^2 \quad (1.49)$$

with

$$N_o = \frac{4\omega_k}{\pi A_k F_s}, \quad c_w = \cos\left(\frac{\omega_k}{F_s}\right) \quad (1.50)$$

$$e_a = \exp\left(-\frac{\alpha_k}{F_s}\right), \quad Z_0 = 4 \frac{\alpha_k \omega_k}{\pi A_k (\alpha_k^2 + \omega_k^2)} - N_o \frac{1 - e_a c_w}{1 - 2e_a c_w + e_a^2}. \quad (1.51)$$

Thus, the current pressure $p[n]$ writes

$$p[n] = u[n] \sum_{k=1}^{N_m} b_{c0,k} + \sum_{k=1}^{N_m} b_{c1,k} u[n-1] + b_{c2,k} u[n-2] + a_{c1,k} p_k[n-1] + a_{c2,k} p_k[n-2]. \quad (1.52)$$

Note that this expression is not strictly causal, because there is an instantaneous relations between $p[n]$ and $u[n]$. It cannot be used without modification in real-time synthesis. This problem is discussed and a solution is proposed below in the current section, as it concerns both the modal and the reflection function formalism.

1.2.1.1.c Resonator: discrete reflection function

For the reflection function, the backward pressure wave is given by

$$p^- [n] = (r * p^+) [n] = \sum_{i=0}^{\infty} r[i] p^+ [n-i], \quad (1.53)$$

using the discrete convolution product formulation. The practical implementation of the convolution product cannot be infinite: the reflection function r must be truncated to its first D samples, giving the expression

$$p^- [n] = \sum_{i=0}^D r[i] p^+ [n-i]. \quad (1.54)$$

The truncation index D must be large enough, as it affects the low frequency content of the resonator's response. As an illustration, Figure 1.12 shows different truncated reflection functions. They are designed after the physical duration of the truncated reflection function $D_t = D/F_s$, because it is easier to connect to the frequency of the peaks than the number of samples D . The low D fingering is used for this illustration, with a first resonance at about 183 Hz and a second resonance at about 387 Hz.

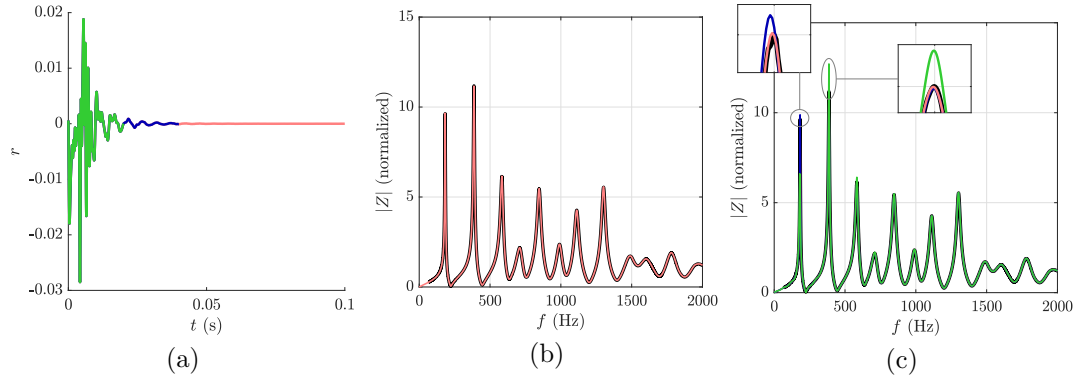


FIGURE 1.12: Effect of the reflection coefficient truncation. Graph (a) shows the reflection function r truncated at instants $D_t = 20$ ms (green), $D_t = 40$ ms (blue) and $D_t = 100$ ms (red). Graphs (b) and (c) superimposes the impedance modulus reconstructed from these truncations (using the same colors) with the measured impedance modulus in **thick black line**. Graph (b) superimposes only the impedance reconstructed with the longest truncation with the reference.

Recalling that $p^+[n]$ is unknown at this stage, the right-hand side of Eq. (1.54) must be separated into a strictly causal part and an instantaneous part, where we show p and u

$$\frac{1}{2} (p[n] - u[n]) = \frac{1}{2} r[0] (p[n] + u[n]) + \frac{1}{2} \sum_{i=1}^D r[i] (p[n-i] + u[n-i]). \quad (1.55)$$

Therefore we get $p[n]$ as a function of $u[n]$ and strictly previous instants

$$p[n] = \frac{1+r[0]}{1-r[0]}u[n] + \frac{1}{1-r[0]} \sum_{i=1}^D r[i](p[n-i] + u[n-i]). \quad (1.56)$$

This does not suffice to incorporate the equation into real-time synthesis, as $u[n]$ in the last expression prevents it from being strictly causal. A solution is proposed below.

1.2.1.1.d Resonator: instantaneous and strictly causal part

Both the modal formalism and the reflection function formalism lead to an equation giving the current pressure $p[n]$ as a function of the current flow $u[n]$ and a variable V deduced from past states, of the form

$$p[n] = b_0 u[n] + V, \quad (1.57)$$

with an instantaneous coefficient b_0 and a strictly causal part V written:

- in the reflection function formalism

$$b_0 = \frac{1+r[0]}{1-r[0]} \quad (1.58)$$

$$V = \frac{1}{1-r[0]} \sum_{i=1}^D r[i](p[n-i] + u[n-i]). \quad (1.59)$$

- in the modal formalism

$$b_0 = \sum_{k=1}^{N_m} b_{c0,k} \quad (1.60)$$

$$V = \sum_{k=0}^{N_m} b_{c1,k} u[n-1] + b_{c2,k} u[n-2] + a_{c1,k} p_k[n-1] + a_{c2,k} p_k[n-2]. \quad (1.61)$$

1.2.1.1.e Determining the flow

This paragraph decomposes and details the derivation between Eqs. (25) and (26) in [GKV05], which is a crucial part of the synthesis method. Eq. (1.8) decomposes the flow u between u_r , flow due to the reed speed, and u_b , flow through the reed channel. This decomposition is introduced into Eq. (1.57), and the pressure then writes

$$p = b_0(u_b + u_r) + V. \quad (1.62)$$

Note that from here, b_0 is assumed to be positive. This must be verified in the simulations for the following development to be valid. By definition, V is known and b_0 is a constant, and u_r is known via Eq. (1.45). Reformulating the static characteristic from Eq. (1.13), the flow u_b can be expressed depending on p and x as

$$\begin{cases} u_b^2 = W^2(\gamma - p) & \text{if } p < \gamma \\ u_b^2 = -W^2(\gamma - p) & \text{if } p > \gamma \end{cases} \quad (1.63)$$

introducing $W = \zeta[x+1]^+$ to lighten the notations. Both cases are treated very similarly, so the development is only written for the case $p < \gamma$. First, p is replaced by its expression in terms of u_b and the known variables u_r and p^- , yielding the second degree polynomial

$$u_b^2 + W^2 b_0 u_b + W^2(V + b_0 u_r - \gamma) = 0. \quad (1.64)$$

This equation admits two solutions,

$$u_{b,1,2}^+ = \frac{1}{2} \left(-W^2 b_0 \pm W \sqrt{W^2 b_0^2 + 4(\gamma - V - b_0 u_r)} \right). \quad (1.65)$$

We know that the unique solution is positive because according to Eq. (1.13), $u_b > 0$ for $p < \gamma$. Here, we know that $(\gamma - V - b_0 u_r) > 0$, because $\gamma > p$:

$$\gamma - V - b_0 u_r > p - V - b_0 u_r = b_0 u_b > 0., \quad (1.66)$$

therefore

$$W \sqrt{W^2 b_0^2 + 4(\gamma - V - b_0 u_r)} > W^2 b_0. \quad (1.67)$$

Thus the admissible positive solution is

$$u_b^+ = \frac{1}{2} \left(-W^2 b_0 + W \sqrt{W^2 b_0^2 + 4(\gamma - V - b_0 u_r)} \right). \quad (1.68)$$

For the second case $p > \gamma$, a similar development yields a negative flow

$$u_b^- = \frac{1}{2} \left(W^2 b_0 - W \sqrt{W^2 b_0^2 - 4(\gamma - V - b_0 u_r)} \right). \quad (1.69)$$

Therefore, in the general case, u_b writes

$$u_b = \text{sign}(\gamma - V - b_0 u_r) \frac{1}{2} \left(-W^2 b_0 + W \sqrt{W^2 b_0^2 + 4|\gamma - V - b_0 u_r|} \right). \quad (1.70)$$

Reading guidelines

For the sake of clarity, we summarize the time-domain synthesis here, along with the important equations. Note that the so-called *modal* formalism represents the impedance as a sum of modes, as in Eq. (1.22), which translates to continuous time as Eq. (1.24) while the *reflection function* formalism uses a time-domain convolution approach, Eq. (1.39), based on the reflection coefficient of Eq. (1.37). The time-domain synthesis loop is comprised of:

- Eq. 1.42 to compute the reed position $x[n]$;
- Eq. 1.45 to deduce the reed flow $u_r[n]$;
- Eq. (1.61) (modal) or (1.59) (reflection function) to compute the strictly causal resonator response V ;
- Eq. (1.70) to obtain the flow through the reed channel $u_b[n]$;
- Eq. (1.8) to have the flow $u[n]$;
- Eq. (1.52) (modal) or Eq. (1.56) (reflection function) to actualize the value of the pressure and its modal components $p_k[n]$ or the travelling waves $p^+[n]$ and $p^-[n]$.

1.2.1.1.f Comparison between resonator representations

Both representations of the resonator necessarily constitute a simplification. To refine this approximation, one will tend to increase the number of modes N_m in the modal formalism, or the duration D_t of the truncated reflection function. Both parameters control the accuracy of the resonator's representation while impacting the computational cost. For the modal formalism, N_m determines the number of modal components p_k actualized in Eq. (1.52). Note that the cost of applying the harmonic balance method (see Subsection 1.2.2) is also affected by the number of modes N_m . With the reflection function, D_t influences the number of multiplication-additions in the convolution product of Eq. (1.56). For this reason, when the application requires a minimization of the computation time, it is helpful to reduce these parameters as much as possible. However, a drastic simplification of the resonator will affect the phenomena that can be observed in synthesis. All the signals synthesized as illustrations in this section are produced using a standard audio sampling rate of 44100 Hz.

As an illustration, internal pressure signals are produced using time-domain synthesis with the same parameters except for the number of modes N_m (3, 6 and 12). The reasons for picking out these numbers is that $N_m = 12$ is the total number of modes under 2 kHz for this particular fingering, $N_m = 6$ is half these modes and $N_m = 3$ illustrates the effect of a drastic simplification. Figure 1.10 shows the impedance reconstructed with these truncated modal representations. The signals shown in Figure 1.13 are classified as first register regimes (whose fundamental frequency is around the first modal frequency). The transients of the three signals are shown. Notable differences appear in the transient, that can be noticed by examining (for instance) the envelope of the signal or the progressive variation of shape of each pseudo-period. However, these differences fade when looking at the steady-state regime, where the three waveforms are close together.

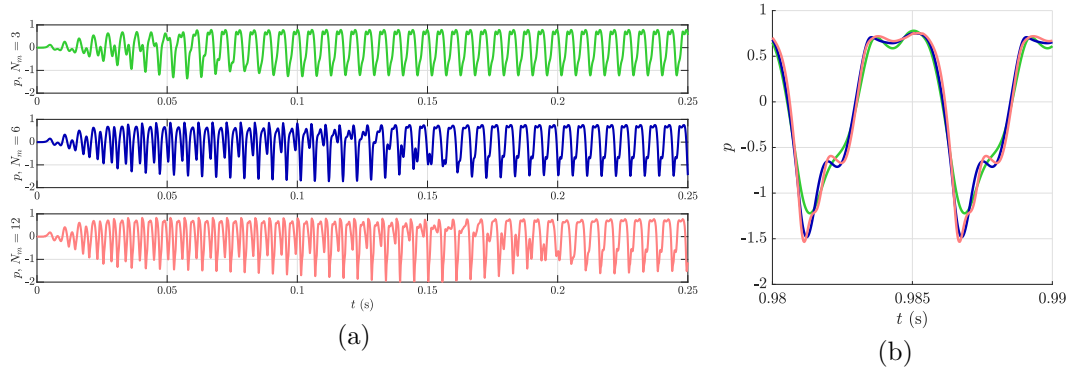


FIGURE 1.13: Time-domain synthesis pressure signals (a) transient and (b) steady state oscillations, produced using the modal decomposition with number of modes $N_m = 3$ (green), $N_m = 6$ (blue) and $N_m = 12$ (red). The steady-state signals (b) are shifted in post-processing so their maxima occur at the same time.

Figure 1.14 illustrates the effect of truncating the reflection function. The truncation durations are the same as in Figure 1.12, $D_t = 20, 40$ and 100 ms. In this case, it is interesting to notice that the first few pseudo-periods of the transient are very similar. This is understandable: the computation of the first 20 ms of the signal is strictly identical for the three examples, since only the first 20 ms of the reflection function come into play. However, it can be seen that the regime that is maintained until the steady-state for the shortest reflection function (which we call *double two-step*, see Section 3.3) transforms into a standard two-step regime [ODK04] when the reflection function is long enough. Then steady state signals obtained for $D_t = 40$ and 100 ms are almost superimposed. This demonstrates that oversimplification of the resonator can even change the qualitative steady-state behavior of the model. It also illustrates the convergence of the results by showing that taking into account more than twice the duration of the reflection function can leave the obtained signals barely changed.

The last illustration for this section is the comparison of both methods in their most detailed implementation with the highest number of modes $N_m = 12$ and the longest reflection function $D_t = 100$ ms, presented in Figure 1.15. The signals are quite different, more so than the last two of Figure 1.14. This is expected as modal overlap in high frequencies entails that the modal impedance is not the same as the measured impedance. However, many features are found in both signals: they correspond very well at the beginning of the transient, which has a comparable structure in both cases, and the differences in periodic regime are high frequency details. These kind of discrepancies call for a careful use of the time-domain synthesis tool. This is why most applications presented in this work do not rely on time-domain synthesis alone, but use measurements or another synthesis method to validate it according to the studied phenomena. At the very least, if it is used alone, it should be in a comparative study, to exhibit a difference or discrepancy between two objects in terms of produced signals. This approach is demonstrated in Subsection 1.2.1.2.

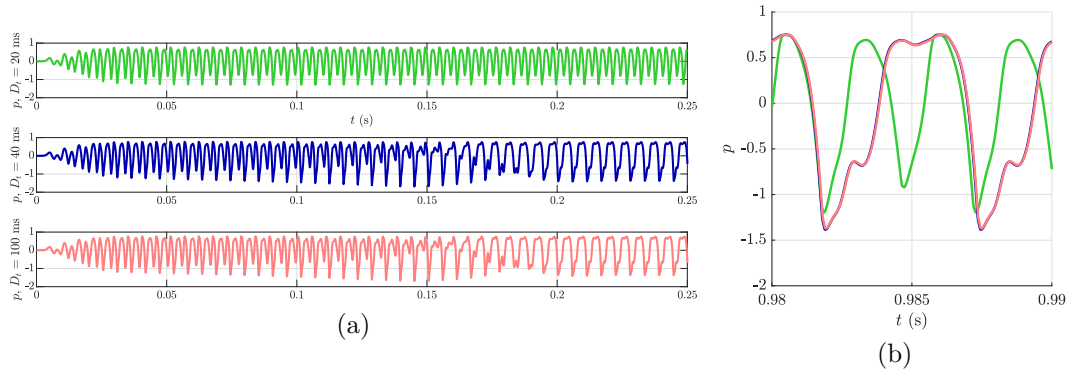


FIGURE 1.14: Time-domain synthesis pressure signals (a) transient and (b) steady state oscillations, produced using the reflection function formalism with truncation durations $D_t = 20$ ms (green), $D_t = 40$ ms (blue) and $D_t = 100$ ms (red). The steady-state signals (b) are shifted in post-processing so their maxima occur at the same time.

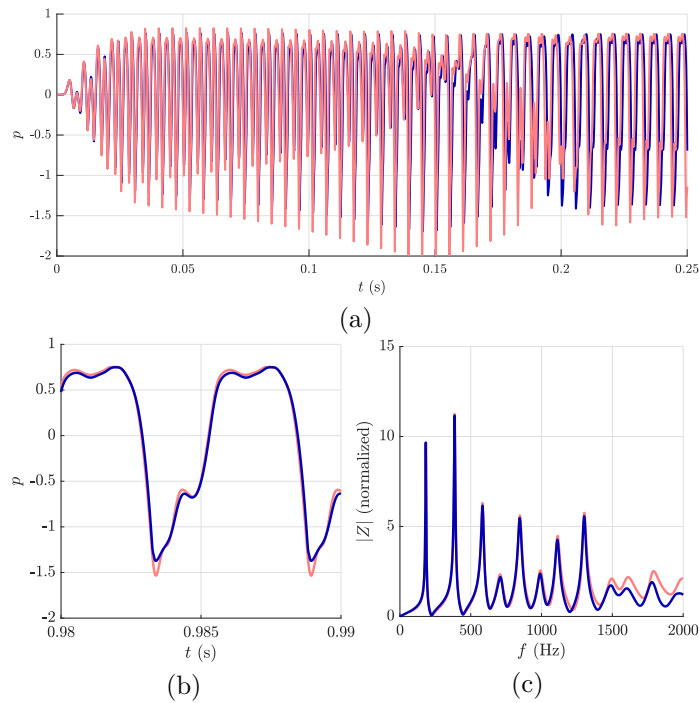


FIGURE 1.15: Time-domain synthesis pressure signals (a) transient and (b) steady state oscillations, produced using the reflection function formalism $D_t = 100$ ms (red) and the modal decomposition $N_m = 12$ (blue). The steady-state signals (b) are shifted in post-processing so their minima occur at the same time. (c) presents the corresponding reconstructed impedances.

1.2.1.2 Application: effect of the cutoff frequency on the produced signals for a cylindrical resonator with clear cutoff behavior

These results were obtained as part of a collaboration with Erik Petersen, Ph. D. student at the LMA. They were published in Acta Acustica united with Acustica as part of [Pet+19a].

Time-domain synthesis can be used as a simple tool to observe the effect of certain characteristics of the resonator on the properties of internal signals. A global characteristic of woodwind resonator is the cutoff due to the tonehole lattice [Ben90]. There are a lot of details and nuance to be discussed on this complicated topic, which is in many ways connex to the present manuscript (the interested reader is directed to [Pet+20; Pet+19b; Pet20]). Here, we present only a short introduction to the concept of cutoff and one effect it has on internal signals obtained using numerical synthesis.

The cutoff of the tonehole lattice can be defined as the separation between two types of behavior of the waves propagating into it. Below the cutoff, at low frequency, the waves are reflected and partially radiate at the first open tonehole: they do not propagate further into the lattice (they become evanescent). Above cutoff, the waves may propagate further into the lattice, they are subject to multiple reflections and radiate out of the termination of the resonator and its many open toneholes. The exact cutoff frequency separating these behaviors is well-defined in the case of a infinite periodic lattice, where all the holes are of the same dimensions and subsequent holes are separated by the same length and losses are ignored. Note that the concept of cutoff in periodic lattices is general to ondulatory physics, and not just acoustic waveguides [Bri53].

In the present case, resonators with periodic tonehole lattices were designed to have predetermined cutoff frequencies of 1.0, 1.5 and 2.0 kHz and realized using plastic tubes (see [Pet+19a] for details). These cutoff values are chosen because they bound the nominal cutoff frequencies observed on usual B♭ clarinets. Figure 1.16 represents the input impedance of the three resonators, computed by the transfer matrix method [CK08] and a variant (TMMI) including external interaction, and measured using the CTTM impedance sensor (see Subsection 1.4.2). Here the cutoff is denoted by a drastic change in the structure of the impedance peaks, which become irregularly spaced and much lower above cutoff.

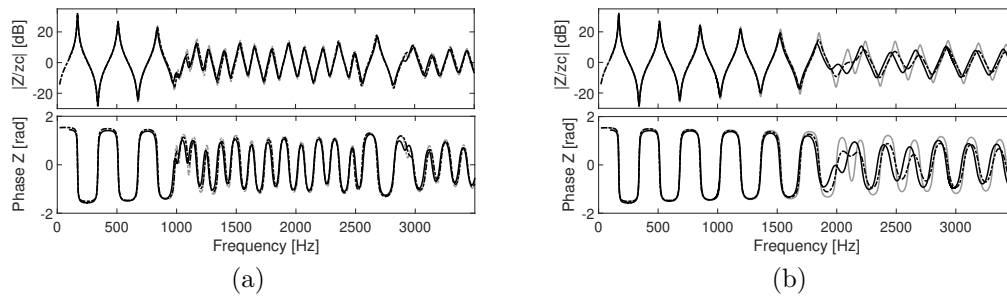


FIGURE 1.16: Input impedance of two resonators with cylindrical main bores and tonehole lattices designed for a cutoff frequency of (a) 1.0 kHz and (b) 2.0 kHz. Solid black: measurement, gray: calculated using the classic Transfer Matrix Method, dashed: calculated using the Transfer Matrix Method with external tonehole Interaction (TMMI).

Figure 1.17 represents the spectrums of internal pressure signals p synthesized using resonators with the 3 different tonehole lattices described. The length of the main bore (before the lattice) is varied to obtain, with each lattice, fundamental frequencies spanning an octave and a half. The synthesis is then applied to the impedances computed with TMMI, using the reflection function formalism to retain all the high frequency characteristics of the impedance ($D_t = 68$ ms). The synthesis parameters are $\gamma = 0.55$, $\zeta = 0.45$, $\omega_r = 2\pi \times 1500$ Hz, $q_r = 0.4$ and $F_s = 44.1$ kHz. The amplitude of the harmonics follow the same qualitative trend : even harmonics increase until their amplitude become approximately equal to that of odd harmonics, around the cutoff frequency of each lattice.

This shows the cutoff frequency determines the internal spectral content of woodwinds. This result prompted further work, to show that it stays valid for the external sound, both in numerical simulation and experiments [Pet+19b].

This illustration of a result obtained via time-domain synthesis illustrates the necessity for this method to be used comparatively. In the present case, synthesized signals were compared between several resonators, specifically designed to exhibit only one variable acoustic feature. These methodological precautions are what gives the simulation results some weight: for lack of a commonly accepted quantitative link between synthesized signals and sounds produced by real instruments, presenting only one graph out of the three in Figure 1.17 would be rather inconclusive. Since time-domain synthesized signals acquire scientific potential whenever they are compared to something else, this work also makes use of the HBM, a completely different simulation method. This enables informative comparisons, for instance by better separating between phenomena due to the physical model from numerical artifacts, due to the complementary properties of both methods.

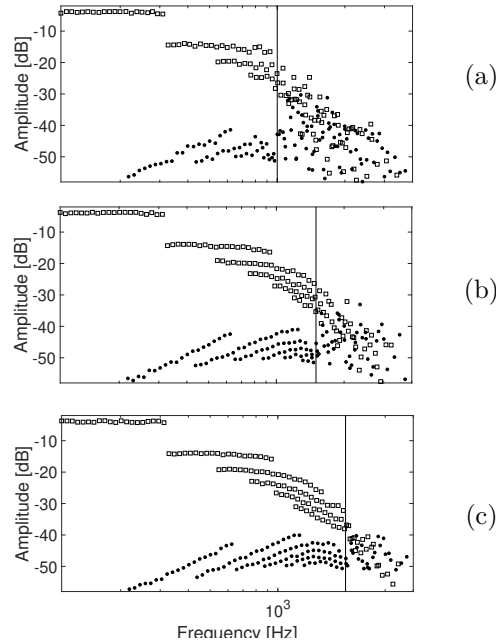


FIGURE 1.17: Internal pressure spectrum of the steady state periodic regime produced in time-domain synthesis for resonators with tonehole lattices designed for cutoff frequencies of (a) 1.0 kHz, (b) 1.5 kHz, (c) 2.0 kHz (denoted by the vertical lines). The main bore length is varied to obtain fundamental frequencies in a chromatic scale from A2 (110 Hz) to E3 (330 Hz). Squares mark odd harmonics and dots mark even harmonics.

1.2.2 The Harmonic Balance Method associated with the Asymptotic Numerical Method of continuation: MANLAB

The Harmonic Balance Method (HBM) finds its place in a larger class of methods of discrete representations of functions of a continuous variable. The typical purpose of such representations is to treat an infinite dimensional problem with numerical tools, by describing it in a simplified, discrete way. This is especially well-suited to treating nonlinear differential equations, for which the unknown is a function that cannot be found with the usual analytical tools. Another common discrete representation technique is orthogonal collocation, which we mention here because it has been used before the HBM to represent periodic solutions in a continuation context in the AUTO software [Doe81; KOGV07]. This technique relies on projecting the solution on Lagrange polynomials. The representation of the function is limited to a finite interval, which in the case of a periodic function can correspond to its period.

The HBM was pioneered by [KB49]. A formulation closer to the modern implementation is found in [NV76]. It relies on the assumption that the solution of the differential system is periodic. Although first applied to industrial systems, both mechanical and electrical, the HBM is well-suited to the study of musical instruments, as periodic solutions are particularly interesting from a musical standpoint – they correspond to self-sustained notes. Self-oscillating instruments classify as autonomous dynamical systems, for which the theoretical framework of the HBM is set since [Sto72]. Therefore, the method was applied to musical instrument models, first in [GKN89], notably single-reed instruments [FFK04; Far+06; KVC10]. Other instruments were also studied using this technique, among which bowed strings [Vig+17] and brass [Fré+19].

As for the Asymptotic Numerical Method (ANM) [CDPF07], it is a continuation method. Continuation methods were developed to search for solutions of equations with no analytical solutions [AG79; Kel86; Bey+02]. They generally apply to an algebraic system, possibly nonlinear, such that

$$R([U^t, \lambda]^t) = 0, \quad (1.71)$$

where λ is a parameter of the system, hereafter called the *continuation parameter*. Continuation

methods have been applied to self-oscillating musical instruments, as ways to investigate the oscillating behavior of the system depending (typically) on a musician control parameter. On matters intimately related to the present work, continuation with respect to the blowing pressure has been used to investigate the effect of inharmonicity on oscillations [GMV19a], with the AUTO software. Among the other numerical continuation tools, one can cite DDE Biftools [ELS00] as particularly suited to delayed systems such as some flute models [TVF13].

Several of the concepts developed in this section are illustrated a simple dynamic system, the Van der Pol oscillator, in the formulation proposed in [Man10]. The governing differential equation of the system is

$$\ddot{y}(t) - (r - y^2)\dot{y}(t) + y(t) = 0, \quad (1.72)$$

where r is parameter of the system. This is an autonomous system, whose trivial solution is $y = 0$. This equilibrium is stable if $r < 0$. When r crosses 0, the equilibrium becomes unstable and oscillations appear. As r increases, the oscillations progressively deform. Figure 1.18 shows these oscillations for $r = 0.434$, where they are very close to sinusoidal, and $r = 1.91$, where they are deformed. In the next paragraphs explain how the HBM can describe these oscillations, and how continuation using the ANM reconstitutes their evolution when varying a parameter such as r .

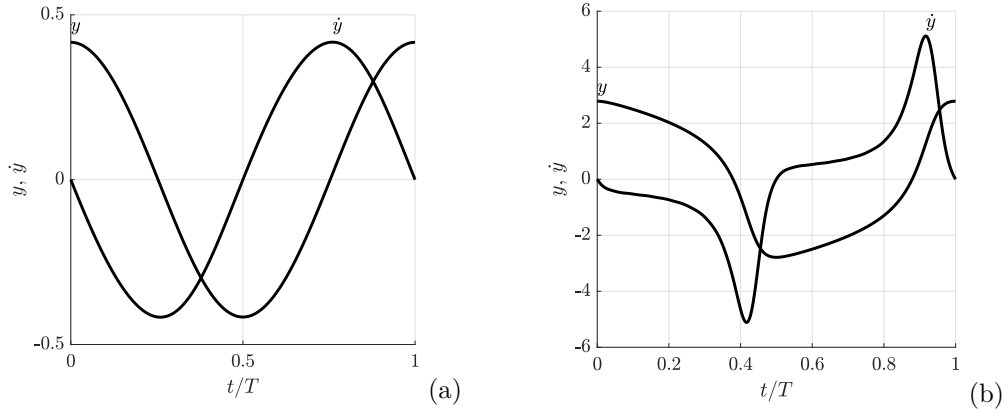


FIGURE 1.18: Oscillations of the Van der Pol oscillator of Eq. 1.72. Two values of r are used: $r = 0.0434$ (a) and $r = 1.91$ (b).

1.2.2.1 Harmonic Balance Method

The hypothesis of periodicity entails that all the variables at play can be decomposed into Fourier series, which for some variable X_i is written

$$X_i(t) = \sum_{h=-\infty}^{\infty} X_{i,h} \exp(jh\omega_0 t), \quad (1.73)$$

where the complex numbers $X_{i,h}$ hold the information of amplitude and phase of harmonic component number h of the i^{th} variable, and ω_0 is the fundamental angular frequency of the solution. To solve the problem numerically, it is necessary to truncate the infinite series and ignore the harmonics higher than a certain rank H . Each real variable is then expressed

$$X_i(t) \simeq \sum_{h=-H}^H X_{i,h} \exp(jh\omega_0 t) \quad , \quad \text{with} \quad X_{i,h} = X_{i,-h}^*. \quad (1.74)$$

Recall that the Fourier series is guaranteed to converge in L^2 -norm if the solution is square-integrable.

Figure 1.19 shows the phase diagrams and the amplitudes of the harmonics of two oscillating solutions of the Van der Pol equation Eq. (1.72), obtained by the HBM. The phase diagram represents a solution in the so-called *phase space*, whose coordinates are the variables of the

system: here, y and its derivative \dot{y} . The small red limit cycle $r = 0.0434$ on the phase diagram is very close to a circle, which signals quasi-sinusoidal oscillations. This is coherent with the amplitudes of its harmonic, with only the first and third harmonic holding some energy. However, when r increases and the oscillations deform, the harmonic coefficients increase. The convergence of the Fourier series in this case can be induced from the rapid exponential decrease of the Fourier coefficients: the last harmonics hold very little energy. Here, the description is truncated to 20 harmonics, i.e. $H = 20$ in Eq. (1.74). One can see the coefficient of the highest harmonic is still relatively small, at less than 0.001. However, if r kept increasing and the solution kept deforming, adding harmonics (increasing H) would be necessary to represent the solution accurately.

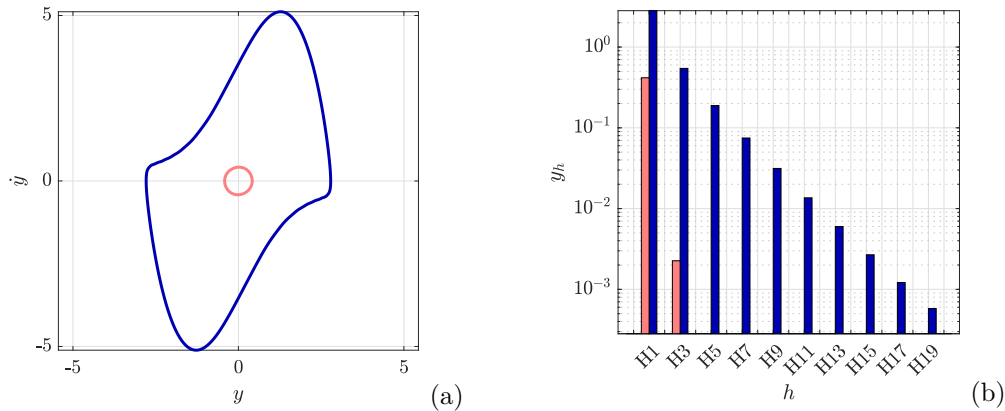


FIGURE 1.19: Phase diagram (a) of the oscillations of the Van der Pol oscillator of Eq. 1.72 and associated Fourier coefficients. Two values of r are used: $r = 0.0434$ in red and $r = 1.91$ in blue, same as in figure 1.18. Even harmonic coefficient are extremely small due to the imparity of the solution.

To find the periodic solution of an autonomous differential system such as

$$\dot{\mathbf{X}} = f(\mathbf{X}), \quad (1.75)$$

where $\mathbf{X} = [X_1, X_2, \dots, X_{N_v}]^t$ contains all the N_v variables of the system, all the variables are expanded into Fourier series truncated at order H . Using the orthogonality of complex exponential functions, the differential system is transformed into an algebraic system

$$R(U) = 0, \quad (1.76)$$

where the unknowns vector is $U = [\{X_{i,k}, k \in \llbracket 0, H \rrbracket, i \in \llbracket 1, N_v \rrbracket\}, \omega_0]$, where N_v stands for the number of variables in the differential system: the unknowns are the $2H + 1$ Fourier coefficients $X_{i,k}$ for each variable X_i , and the fundamental angular frequency ω_0 . A measure of the error committed with an approximate solution \tilde{U} is then simply given by $R(\tilde{U})$.

1.2.2.2 Asymptotic Numerical Method

In the framework of the ANM, the continuation parameter λ is considered as an unknown of the system, so we set $\mathbf{U} = [U^t, \lambda]^t$ the complete vector of unknowns for system (1.71). This system can be, for example, the system obtained by applying the HBM to a woodwind model, with the dimensionless pressure γ as the continuation parameter. Knowing a solution U_0 of the system for some value λ_0 of the continuation parameter, the goal of continuation methods in general is to find solutions U for neighboring values of $\lambda = \lambda_0 + \delta\lambda$. These neighboring solutions constitute a *branch* of solutions, on which we find the point (U_0, λ_0) .

The formulation of the ANM used in the MANLAB software requires the equation system to be quadratic, meaning that it can be reformulated as

$$R(\mathbf{U}) = C + L(\mathbf{U}) + Q(\mathbf{U}, \mathbf{U}) = 0, \quad (1.77)$$

where C is a constant, L is a linear operator and Q is a quadratic operator. Although this condition may seem restrictive, a large class of nonlinear systems can be recast under this form, eventually by introducing auxiliary variables. These systems may include nonsmooth Coulomb friction [Vig+17] and fractional derivatives [Vig+19], delayed terms or neutral delayed terms [GVC19]. An example of quadratic recast is given for the regularization of the absolute value and sign functions in Eq. (1.17): the regularized absolute value of variable x using the auxiliary variable A_x is

$$0 = A_x^2 - x^2 - \eta, \quad (1.78)$$

and the regularized sign of x with the auxiliary variable S_x is

$$0 = S_x \times A_x - x. \quad (1.79)$$

All rational nonlinearities can be treated similarly. The complete saxophone model presented in section 1.1 is presented in quadratic form in appendix A. Note that transcendental nonlinearities can also be reformulated quadratically using their derivatives (see [GCV19] for details). In these conditions, knowing a regular solution \mathbf{U}_0 of the system, the ANM specifies that the branch of solutions around it can be approximated by a power series expansion truncated to order n_{ANM} , namely

$$\mathbf{U}(a) = \mathbf{U}_0 + a\mathbf{U}_1 + \dots + a^{n_{ANM}}\mathbf{U}_{n_{ANM}}, \quad (1.80)$$

where a is the pseudo-arc length separating \mathbf{U} from \mathbf{U}_0 , defined as $a = (\mathbf{U} - \mathbf{U}_0)^t \mathbf{U}_1$, and the vectors U_p , $p = 1, \dots, n_{ANM}$ must be determined. Note that most continuation methods – so-called *predictor-corrector* approaches – only use the two first terms in this expansion [AG79]. The vector U_1 is the tangent vector of the branch at U_0 , defined by

$$J_{\mathbf{U}_0} \mathbf{U}_1 = 0, \quad (1.81)$$

where $J_{\mathbf{U}_0}$ is the jacobian matrix of the system at \mathbf{U}_0 , i.e. the matrix of partial derivatives evaluated at $\mathbf{U} = \mathbf{U}_0$. Replacing Eq. (1.80) into Eq. (1.77), the subsequent vectors U_p , $p = 2, \dots, n_{ANM}$ are also found using the jacobian

$$J_{\mathbf{U}_0} \mathbf{U}_p + \sum_{i=1}^{n_{ANM}} Q(\mathbf{U}_i, \mathbf{U}_{p-i}) = 0, \quad (1.82)$$

to which conditions of norm and orthogonality imposed by replacing \mathbf{U} by Eq. (1.80) in the definition of a are added

$$\mathbf{U}_1^t \mathbf{U}_1 = 1, \quad \mathbf{U}_p^t \mathbf{U}_1 = 0. \quad (1.83)$$

All of the systems in Eqs. (1.81), (1.82) and (1.83) are linear. Although the number of equations was multiplied by n_{ANM} compared to (1.71), all systems are now linear and therefore much easier to solve. Note that the only matrix to invert is $J_{\mathbf{U}_0}$, which is the same for all p in Eq. (1.82). Once the vectors \mathbf{U}_p , $p = 1, \dots, n_{ANM}$ are determined, the last step is to find the maximum pseudo-arclength a_{max} such that

$$\forall a \leq a_{max}, \quad \|R(\mathbf{U}(a))\| \leq \epsilon_r, \quad (1.84)$$

with ϵ_r is an arbitrary, user-defined threshold. Note that the adaptation of the step length is automatic as a function of the series expansion of Eq. (1.80). The step length is auto-adaptive and is related to the convergence radius of the series expansion Eq. (1.80). The next continuation step can then be performed in the same fashion by setting $\mathbf{U}_0 := \mathbf{U}(a_{max})$. Note that all the solutions $\mathbf{U}(a)$ for $a < a_{max}$ are valid solutions of the system: this is how a continuous branch of solutions can be constructed.

As a first illustration of the continuation process, Figure 1.20 shows a branch obtained by the ANM. Starting from the quasi-sinusoidal solution of Figure 1.18 (a), the ANM shows the evolution of the solution along a branch as continuation parameter r increases, until solution 1.18 (b). The branch itself, in green, represents the evolution of a single Fourier coefficient as

a function of the continuation parameter r . This representation, called *bifurcation diagram*, plots a single descriptor of the solutions with respect to the continuation parameter to give an idea of the solution's evolution. Although it only displays one characteristic of the solution, the bifurcation diagram is very useful to show the points where solutions change stability or disappear. These points, called bifurcations, are detailed in next section.

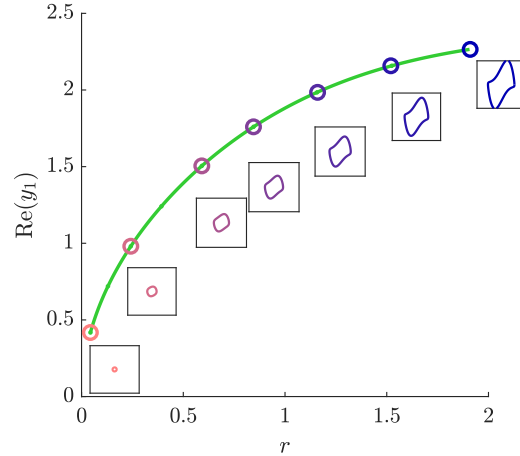


FIGURE 1.20: Bifurcation diagram of the branch of periodic solutions obtained by continuation (ANM) of the Van der Pol oscillator, Eq. (1.72), treated with HBM. In addition to the branch in green, phase diagrams corresponding to select points of the branches are drawn to illustrate the morphing of the solution between the two phase diagrams of Figure 1.19 (a) as r increases.

1.2.2.3 Some bifurcation theory

Bifurcations of dynamical systems describe particular points where a change in parameters leads to a qualitative change in behavior of the system, typically by the change of stability, appearance or disappearance of one or several solutions. These particular points have been extensively studied and categorized [DKK91; Kuz95; Sey10; Ras89]

For instance, in woodwind models, a bifurcation can be associated with the lowest blowing pressure value necessary for a sound to be produced. One can argue that this minimal pressure is an indicator of the ease of playing of the instrument (for instance, if it is too high, the player will have to blow very hard in order to trigger a sound) [GMV19a]. In this work, bifurcations are studied as a convenient and elegant way to describe a model's behavior globally, because they outline the zones where desired or undesired regimes can be produced. Here, we succinctly present the bifurcations encountered throughout this dissertation. Two types of bifurcations, the Hopf and fold bifurcations, are devoted more attention, and we also describe the point where they collide.

1.2.2.3.a Preliminary: stability, eigenvalues of the Jacobian and Floquet exponents

The stability of a solution of the system can be characterized using the corresponding Jacobian matrix, specifically its eigenvalues (see [Sey10] for a complete discussion or [Bac19] for a more pedagogical approach, applied to linear systems). As an illustrative example, let's linearize the differential system of Eq. (1.75) around a constant solution \mathbf{X}_0 (also called equilibrium) with an additive perturbation $\mathbf{y}(t)$, such that $\mathbf{X}(t) = \mathbf{X}_0 + \mathbf{y}(t)$. We get the linear system with constant coefficients

$$\dot{\mathbf{y}}(t) = \mathbf{J}_{\mathbf{X}_0} \mathbf{y}(t), \quad (1.85)$$

where $J_{\mathbf{X}_0}$ is the Jacobian matrix computed at \mathbf{X}_0 . Because the matrix $J_{\mathbf{X}_0}$ has constant coefficients, the solution of this system is

$$\mathbf{y}(t) = \exp(\mathbf{J}_{\mathbf{X}_0} t) \mathbf{y}(0), \quad (1.86)$$

which can be reformulated by decomposing \mathbf{y}_0 over the eigenvectors \mathbf{p}_i of the Jacobian

$$\mathbf{y}(t) = \sum_{i=1}^{N_v} \exp(\beta_i t) (\mathbf{p}_i \cdot \mathbf{y}(0)) \mathbf{p}_i, \quad (1.87)$$

where the β_i are the eigenvalues of $\mathbf{J}_{\mathbf{X}_0}$. Therefore, if all β_i have a negative real part, $\mathbf{y}(t)$ converges to 0 as time tends to infinity. Hence, $\mathbf{X}(t)$ converges back to \mathbf{X}_0 , which is therefore considered *stable*. If there is at least one β_i with a positive real part, $\mathbf{X}(t)$ will diverge from \mathbf{X}_0 , which is therefore unstable. Also note that a purely imaginary $\beta_i = j\omega$ leads to permanent oscillations of \mathbf{y} at angular frequency ω .

The determination of the stability of oscillating regimes studied with the HBM is analogous, but instead of the Jacobian matrix the Hill matrix is used [LT10; Gui+20]. The main idea is still to linearize the system around a (periodic) solution and to study how a perturbation evolves along time. A periodic solution is stable if and only if all the Floquets exponents, which are the eigenvalues of the Hill matrix [Flo79], have strictly negative real parts.

1.2.2.3.b The Hopf bifurcation

The Hopf bifurcation for a musical instrument can often be seen as the threshold of apparition (or disparition) of a certain oscillation regime. It is defined by the apparition of a limit cycle from equilibrium \mathbf{X}_0 , and characterized by a pair of complex conjugate eigenvalues of the Jacobian matrix $J_{\mathbf{X}_0}$ crossing the imaginary axis. Consequently, the equilibrium is unstable beyond the Hopf bifurcation.

A Hopf bifurcation can be supercritical, in which case the appearing oscillating regime is stable from its lowest amplitude, or subcritical, if the emerging regime is unstable. The bifurcation diagram's appearance around both types of Hopf bifurcation is depicted in Figure 1.21. The distinction is very important when studying saxophone models, as subcritical Hopf bifurcations in low fingerings are sometimes cited as a characteristic separating conical woodwinds from cylindrical ones (see Section 3.5 for further discussion). This phenomenon has a direct musical consequence on the lowest nuances the instrument can produce. Near a supercritical Hopf bifurcation, the low amplitude (*pianissimo*) regimes are stable, but they are unstable near an inverse Hopf bifurcation.

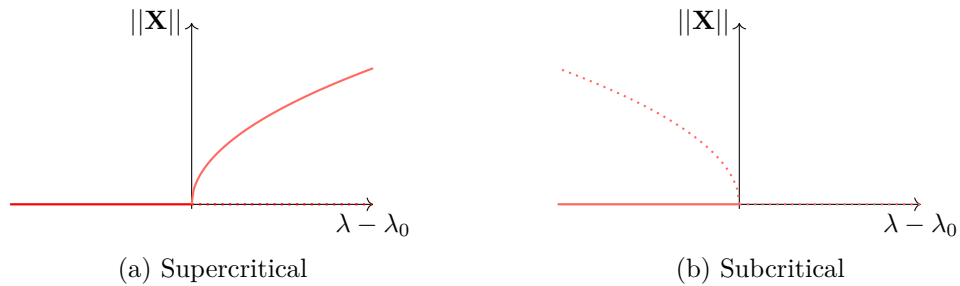


FIGURE 1.21: Hopf bifurcations at $\lambda = \lambda_0$, as they appear on bifurcation diagrams. Solid lines indicate stable regimes and dotted lines indicate unstable regimes. $\|\mathbf{X}\|$ is the amplitude of the emerging periodic solution.

Figure 1.22 shows the Hopf bifurcation of Eq. (1.72), where the equilibrium becomes unstable and oscillations arise. This Hopf bifurcation is direct, and the solutions' amplitude is subject to a classical evolution proportional to the square root of the continuation parameter. For this simple system, a first harmonic approximation (HBM with $H = 1$) around $r = 0$ gives this evolution analytically. Notice how the ANM branch fits the analytical approximation while the solution is still quasi-sinusoidal for small r values, and slowly diverges from it as r increases and upper harmonics gain importance.

1.2.2.3.c The fold bifurcation

The fold bifurcation is defined by a stable and unstable solution collapsing and disappearing. On a bifurcation diagram, it can be seen as a turn-up point where the branch changes stability (see schema in Figure 1.23). On saxophone models, two subsequent fold bifurcations are

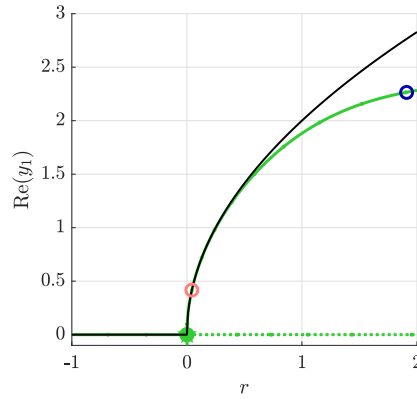


FIGURE 1.22: Bifurcation diagram of the branch of periodic solutions obtained by continuation (ANM) of the Van der Pol oscillator, Eq. (1.72), treated with HBM, near the Hopf bifurcation at $r = 0$. In addition to the ANM branch in **green**, an analytic approximation of the first Fourier coefficient amplitude is displayed as reference in **black**. Circles markers correspond to the solutions of Figure 1.18.

associated with control parameter zones where multiple regimes are stable (see the discussion below about the cusp bifurcation for more details).

The fold bifurcation is characterized by a single eigenvalue crossing the origin point at $\lambda = \lambda_0$. Note that this definition is classically given for fold bifurcation of equilibria (non-oscillating regimes), but also applies to periodic regimes when the system is treated with the HBM. Indeed, once the HBM is applied to a differential system, the solutions are represented by algebraic unknowns (harmonic amplitudes and fundamental frequency). Therefore, there are many cases where parallels can be drawn between properties of the equilibrium of a system and properties derived for periodic solutions of a system solved using the HBM.

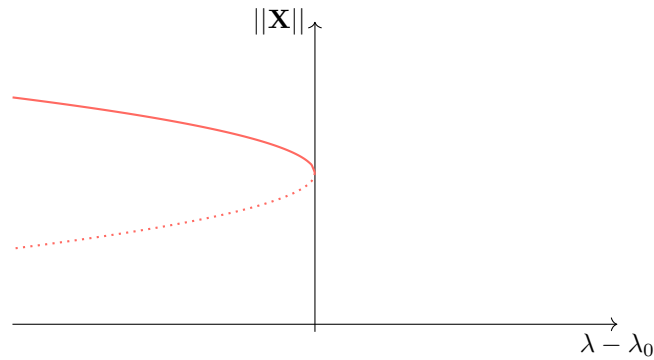


FIGURE 1.23: Fold bifurcation of a periodic solution at $\lambda = \lambda_0$, as it appears on bifurcation diagrams. $\|\mathbf{X}\|$ is the amplitude of a periodic solution.

1.2.2.3.d The pitchfork bifurcation

A pitchfork bifurcation is a degenerate fold bifurcation which marks a single solution dividing into three separate solutions [BD19]. This phenomenon is characterized, like the fold bifurcation, by a null eigenvalue of the Jacobian matrix. The degeneracy consists in from the second derivative of function f from Eq. (1.75) being null at the bifurcation location, as well as its first derivative with respect to the continuation parameter. Figure 1.24 schematizes a pitchfork bifurcation. Notice the similarity with the fold bifurcation (Figure 1.23), as well as the Hopf bifurcation (Figure 1.21). A pitchfork bifurcation can be supercritical or subcritical, just like a Hopf bifurcation. For brevity, Figure 1.24 only displays the supercritical case.

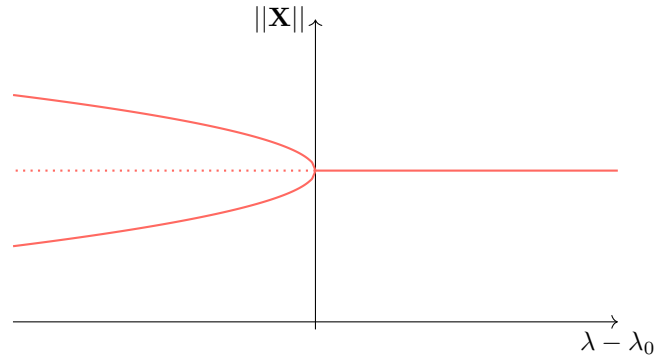


FIGURE 1.24: Supercritical pitchfork bifurcation of a periodic solution at $\lambda = \lambda_0$, as it appears on bifurcation diagrams. $\|\mathbf{X}\|$ is the amplitude of a periodic solution.

1.2.2.3.e The Neimark-Sacker bifurcation and quasi-periodic regimes

Neimark-Sacker bifurcations are analogous to Hopf bifurcation in the case of established periodic oscillations. Instead of a periodic solution emerging from an equilibrium, a quasi-periodic solution emerges from a periodic solution. The Neimark-Sacker bifurcation is characterized, much like the Hopf bifurcation, by a pair of complex conjugate Floquet exponents crossing the imaginary axis. At the Neimark-Sacker bifurcation, the periodic solution changes stability. Figure 1.25 schematizes the bifurcation diagram around a Neimark-Sacker. It also shows typical phase diagrams before and after the bifurcation. Phase diagrams are a very popular representation of a dynamic systems trajectory (see the first chapter of [Kuz95]). They represent the conjoint evolution of the state variables – the components of \mathbf{X} according to Eq. (1.75) – in the so-called *phase space*. A periodic solution describes a 1D closed cycle in the phase space, for $\lambda > \lambda_0$ here. On the other side of the bifurcation, for $\lambda < \lambda_0$ here, the quasi-periodic solution describes a torus in the phase space. The phase diagrams, intended here merely as illustration of an invariant torus and a limit cycle, are computed using the saxophone model used in Chapter 5 (modal formalism, D \sharp fingering) around Neimark-Sacker bifurcation NS1 for $\gamma = 0.639$ and $\gamma = 0.64$. The projection of the phase space used here relies on the modal components p_k and their derivatives \dot{p}_k (see Eq. (1.21)).

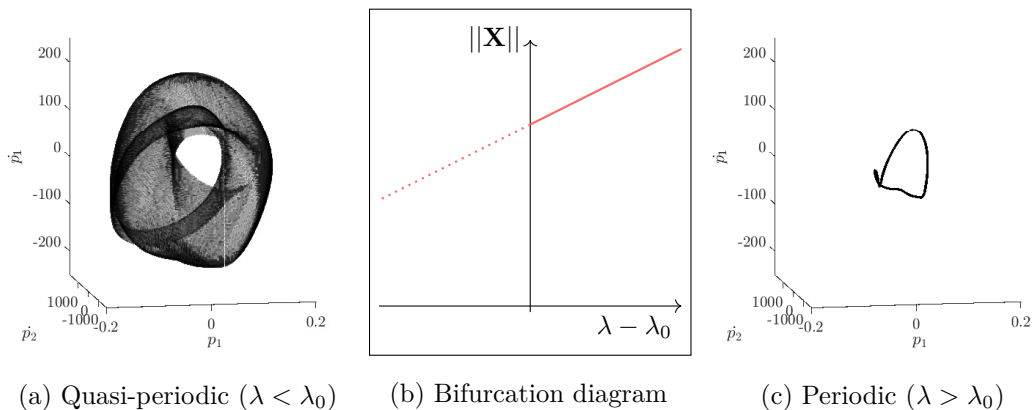


FIGURE 1.25: (a) Neimark-Sacker bifurcation at $\lambda = \lambda_0$, as it appears on bifurcation diagrams, (b) and (c) associated phase diagram examples on both sides of the bifurcation. $\|\mathbf{X}\|$ is the amplitude of a periodic solution.

The Neimark-Sacker bifurcations also relate to specific musical phenomena. Quasi-periodic regimes correspond to *multiphonics*, used musically since the 1950s (see for example John Coltrane's *Harmonique*) [Bac78; RPE14]. Quasi-periodic regimes can also manifest as unwanted disturbances of a periodic regimes. An example is found on the low fingerings of the saxophone, where embouchure defects can entail an amplitude modulation effect known as *pumping* on coupled oscillators [Gen+01; GGL06].

1.2.2.3.f The period-doubling bifurcation

The period-doubling bifurcation marks a periodic solution of half frequency emerging from another periodic solution. The phase diagrams of figure 1.26 are extracted from the case study of chapter 5 on both sides of period-doubling bifurcation PD2, with $\gamma = 0.868$ and $\gamma = 0.87$. They illustrate the period doubling phenomenon: in this case, it transforms a second register regime into a first register regime (an octave down). Notice the projection of the phase space, on the first two modal components of the pressure p_1 and p_2 and the derivative of p_2 . The period doubling bifurcation expands the limit cycle on the coordinate p_1 , signaling the apparition of a frequency component near the first mode.

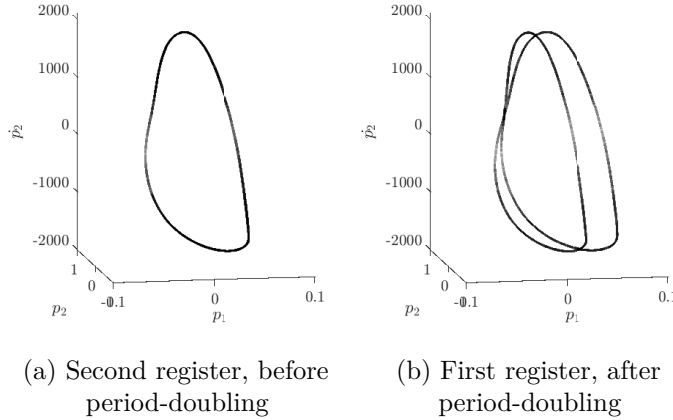


FIGURE 1.26: Phase diagrams obtained in synthesis on both sides of a period-doubling bifurcation, for a saxophone model in the modal formalism. The situation correspond to bifurcation diagram Figure 1.27 (a).

The original periodic solution changes stability at the bifurcation. Figure 1.27 shows bifurcation diagram archetypes near a period-doubling bifurcation. It plays a large part in defining characteristic regime types of the saxophone, because it marks the apparition of the double two-step regime from the second register (see Section 3.3). The period-doubling bifurcation can be seen as a particular case of the Neimark-Sacker bifurcation, as it is characterized by a Floquet exponent crossing the imaginary axis at $\pm i\pi$.

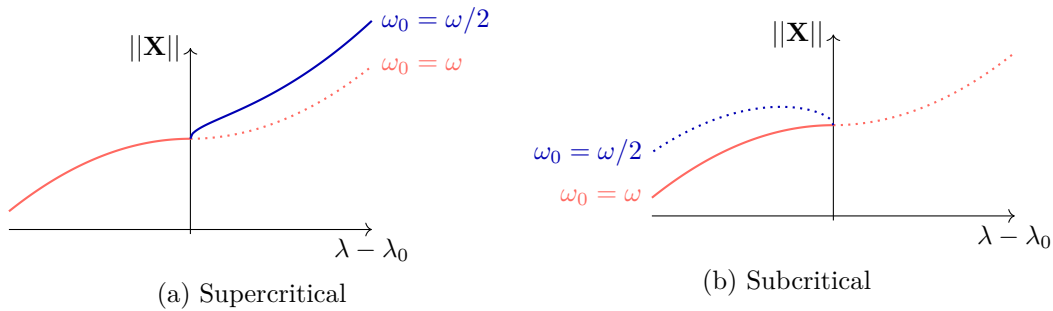


FIGURE 1.27: Period-doubling bifurcation at $\lambda = \lambda_0$, as it appears on bifurcation diagrams. $\|\mathbf{X}\|$ is the amplitude of a periodic solution. The fundamental frequency ω_0 associated with each colored branch is specified on the diagrams.

1.2.2.3.g The cusp and Bautin bifurcations: forming hysteresis cycles

In this work, we study woodwind model dynamics in a two-dimensional space of control parameters (γ, ζ) . One way to introduce this is considering that the bifurcation diagram along γ evolves when increasing the other parameter ζ . In particular, the bifurcations themselves can move, thus drawing *bifurcation curves* in the two-parameter space [Kuz95]. The bifurcations can also appear, collide or disappear, which corresponds to limit points on the bifurcation

curves. These points where bifurcations appear or disappear correspond to major dynamic changes in the system, and they are called two-parameter bifurcations or *codimension two* bifurcations (because they are characterized by two conditions, instead of one).

A very practical consequence of certain codimension two bifurcations is that they mark the apparition of a possible hysteresis cycle, as in the two examples presented in Figure 1.28. The cusp correspond respectively to two folds of periodic solutions colliding and disappearing, while the Bautin bifurcation corresponds a fold of limit cycle and a Hopf merging into one Hopf bifurcation. Both cases show a possible hysteresis cycle due to simultaneously stable regimes disappearing. The vast question of multistability and hysteresis on saxophone models is further detailed in sections 3.2 and 3.3 and chapter 5.

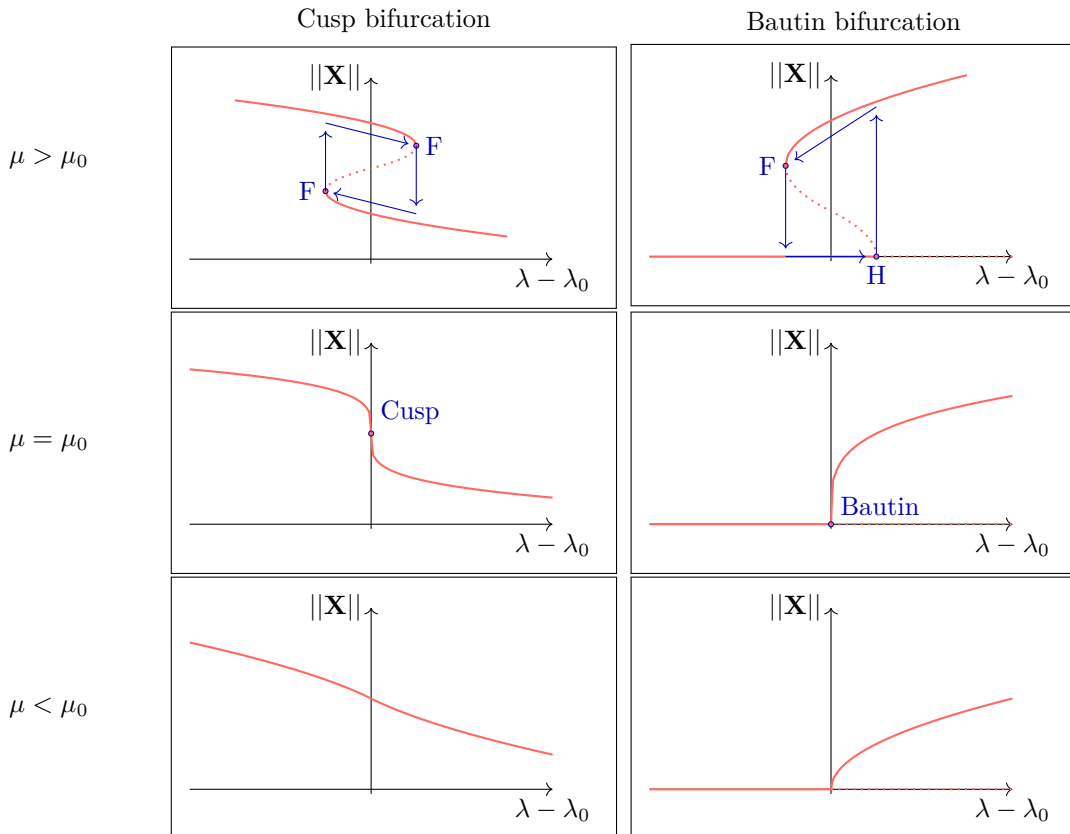


FIGURE 1.28: Evolution of a bifurcation diagram in λ due to another variable μ showing (a) a cusp bifurcation and (b) a Bautin bifurcation. Arrows outline possible hysteresis cycles. Letters mark bifurcations : F for fold, H for Hopf. $\|\mathbf{X}\|$ is the amplitude of periodic solutions.

This section lays the building blocks for the numerical study of a reed instrument model. Recall however that the main purpose of such model in the current framework is to be used as a virtual prototype, for developing new instruments. Through dissecting the model's behavior, there is hope of defining objective design criteria, quick to assess and reproduce numerically. Of course, identifying these criteria is only a partial answer to the problematic of designing a new instrument. It leaves the question of implementing these criteria: adjusting the geometry of the instrument so that it can have the desired dynamical or acoustical characteristics. In the context of a numerically oriented scientific work, the natural answer lies in computerized optimization procedures, that are detailed in next section.

1.3 Numerical optimization

Designing the resonator of a woodwind is, to say the least, a complicated task. Even if we ignore all of the keywork to focus only on the internal geometry, the number of geometrical parameters are easily several tens, including hole placement and size. A hole plays its largest part on

the fingering(s) where it is first to be open, in which case its position roughly determines the effective length of the resonator and thus the playable notes. However, downstream open holes also play a part in this effective length, and in the higher resonances of the bore. Therefore, fixing the acoustical characteristics of a woodwind resonator is an ill-defined problem with a lot of parameters. Furthermore, even if the link between the geometry and the linear acoustics of the bore can be determined – which in itself is not easy – recall that the quality criteria on which an instrument is assessed depend on its dynamical behavior and are not even known explicitly.

1.3.1 Typical optimization problem

Optimization problems are not formulated as equations: the formulated aim is not to attain exactly the desired objective, as in most cases it is impossible, but rather to get *as close as possible*. This idea translates into the standard formulation [NW06; BV04] of an optimization problem

$$\underset{\Theta}{\text{minimize}} \quad \Phi(\Theta), \quad (1.88)$$

read ‘find Θ such that $\Phi(\Theta)$ is minimal’, where Θ is the vector of parameters of the optimized object, and the so-called *cost function* Φ (sometimes *objective function*) measures some kind of distance between the optimized object and the target. In most applications, the optimized object is subject to constraints. In the case of a woodwind resonator, some of these constraints can be of geometrical nature, specifying for instance that a hole cannot be of greater radius than the main bore underneath it. These constraints are then added to the optimization problem which becomes

$$\underset{\Theta}{\text{minimize}} \quad \Phi(\Theta), \quad (1.89)$$

$$\text{subject to} \quad h_i(\Theta) \leq 0, \quad i = 1, \dots, N_c \quad (1.90)$$

where N_c is the number of inequality constraint functions h_i . Figure 1.29 displays a cost function $\Phi(\Theta)$, where the parameter space is bidimensional. In this case, the cost function can be represented as a surface.

In this example, there is one inequality constraint function $h_1(\Theta)$. This function Φ presents one global minimum labelled m_3 and two local minima labeled m_1 and m_2 . Note that the global minimum m_3 does not satisfy the constraint, therefore it is not a valid solution to the optimization problem. In this case, the best solution to the optimization problem would be the local minimum m_1 . Higher local minima that satisfy the constraint, such as m_2 , constitute a difficulty in solving the optimization problem. Indeed, when computing the cost function only in their vicinity, they can be mistaken as valid solutions to the problem, even though better ones exist. Note that other ‘artificial’ local minima can appear on the constraint border: in this case, they is one around the mid-point between m_1 and m_3 , but it is higher than m_1 and does not constitute the best solution. Finding and recognizing local from global minima is a hard task, that often requires extensive computation or careful analysis, especially in high dimensional problems. One of the main issues addressed in Chapter 2 is quantifying the validity of the found minimum in a resonator optimization problem.

In the present context, we use numerical optimization to determine the geometry of a resonator so its acoustical characteristics correspond to a certain objective. Then, the parameters Θ are the geometrical parameters of the resonator, meaning for instance the radius $a(x)$ of the main bore along its length, as well as the position L_h , radius b_h and height h_h of each hole (see Figure 1.30).

Many cost function examples were proposed in the past to be applied to wind instrument design, and they can be separated into three categories. The first type of cost function relies on acoustical descriptors of the resonances of the optimized resonator. A cost function built around modal frequencies f_k associated with target frequencies $f_{tar,k}$, is of the form

$$\Phi(\Theta) = \sum_k w_k (f_{tar,k} - f_k)^2, \quad (1.91)$$

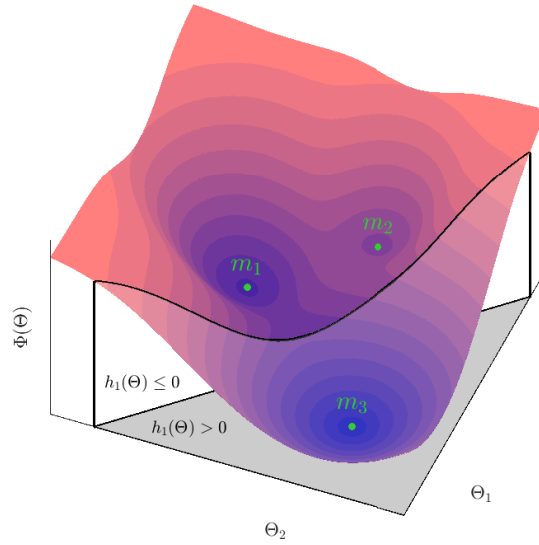


FIGURE 1.29: Schematic example of a cost function $\Phi(\Theta)$ and an inequality constraint $h_1(\Theta)$. The color of the surface corresponds to the value of the cost function Φ , from low: **blue** to high: **red**. A gray shade marks a forbidden region, where the constraint $h_1 \leq 0$ is not satisfied. **Green** dots indicate the minima.

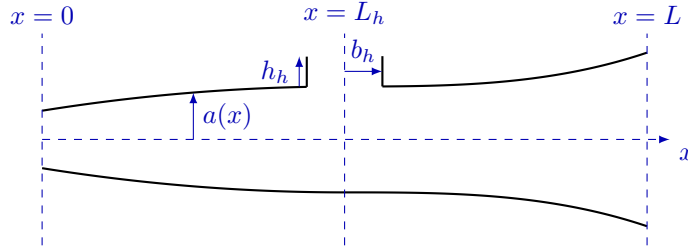


FIGURE 1.30: Schematic profile of a woodwind resonator with one hole, to introduce possible geometrical design parameters.

for each fingering, where the w_k are weighting coefficients. This type of cost function is used for instance in [Nor+13], for the first two resonances of a clarinet-like instrument ($f_{tar,1}$ and $3f_{tar,1}$) or more resonances for the trombone [BNC09]. A certain number of optimization studies applied to wind instruments seek to reduce the inharmonicity of the resonator, defined as the discrepancies between higher resonances and integer multiple of the first. The quena (Andine flute) is treated in [DLC+16], while [MD11] proposes a trumpet design. Other studies [DK94; DV17] propose many designs of resonators with perfect harmonicity (although with analytical tools instead of optimization). Many formulas, all more or less equivalent, exist for inharmonicity. An example of an inharmonicity-based cost function can be

$$\Phi(\Theta) = \sum_k \left(H_{tar,k} - \frac{f_k}{k f_1} \right)^2, \quad (1.92)$$

where $H_{tar,k}$ is the target harmonicity value for resonance labelled k . This definition corresponds well to saxophone-like instruments, where the first few resonances occur around all integer multiples of the fundamental. For clarinet-like instruments that only have resonances around odd multiples of the fundamental, the definition can be adapted easily by replacing k by $2k - 1$ in the denominator. Ernout [Ern+20] proposes several types of impedance descriptor-based cost functions. The fit of the resonance frequency relies on comparing the unwrapped phase of

the reflection coefficient ϕ_R (see Eq. (1.37)) at the fixed target frequencies $f_{tar,k}$ to $2(k-1)\pi$, such that

$$\Phi_k(\Theta) = \left(\frac{\phi_R(f_{tar,k}, \Theta)}{2\pi} - (k-1) \right)^2, \quad (1.93)$$

for the k^{th} resonance of a given fingering. The height ratio between the second and first peaks, which plays a role in second register production, is assigned the cost function

$$\Phi(\Theta) = \left(\frac{A_2(\Theta)/A_1(\Theta) - r_{tar}}{r_{tar}} \right)^2, \quad (1.94)$$

where A_2 and A_1 are indicators of the peaks amplitude, taken here as the modal coefficients of Eq. 1.22, and r_{tar} is the target peak-amplitude ratio.

The second approach is adjusting a full bandwidth acoustical quantity characterizing the resonator, such as the impedance, instead of focusing on the resonances. Studies applied to the design of trumpets [Kau01] and trombones [BNC09], or to bore reconstruction of a woodwind [SCH17a] use cost functions of the form

$$\Phi(\Theta) = \sum_{\omega=\omega_{min}}^{\omega_{max}} |Z_{tar}(\omega) - Z(\omega, \Theta)|^2 \quad (1.95)$$

where Z_{tar} is a target input impedance and Z is the input impedance of the optimized resonator. The slightly different cost function

$$\Phi(\Theta) = \sum_{\omega=\omega_{min}}^{\omega_{max}} \left| |Z_{tar}(\omega)|^3 - |Z(\omega, \Theta)|^3 \right|^{1/3} \quad (1.96)$$

was applied to the saxophone in [GK11] to estimate geometrical parameters of simplified resonator models for numerical synthesis.

The third type of cost function is computed from signals produced using the resonator. For instance, [Tou+17] compares the mean fundamental frequency $\bar{f}_0(\Theta)$ of synthesized sounds produced using several sets of control parameters to a target frequency f_{tar} . The associated cost function writes

$$\Phi(\Theta) = \left| 1200 \log_2 \left(\frac{\bar{f}_0(\Theta)}{f_{tar}} \right) \right|, \quad (1.97)$$

for each note. This kind of cost function is arguably the closest to the evaluation of an instrument by a musician, because it relies on making the instrument play. However, synthesizing sound is very costly compared to computing an input impedance or its descriptors. Additionally, a lot of questions may arise as to the correspondance between the synthesized sounds and the behavior of a real instrument, both pertaining to the model itself and the representation of the musician's action.

1.3.2 Optimization algorithms

There exists a great diversity of methods to solve an optimization problem. In this work, we choose to outline only the two optimization algorithms that will be mentioned in Chapter 2: trust-region algorithms and genetic algorithms.

Note that most optimization algorithms proceed by steps, each of which examines one or several points of the parameter space. From one step to the next, these points are moved around in the space until they provide a good approximation of the solution to the optimization problem: the coordinates of a minimum of cost function Φ that satisfies the constraints.

1.3.2.1 Trust-region algorithm

Trust-region optimization methods rely on a local (often quadratic) approximation $Q_i(\Theta)$ around current point θ_i of the cost function to estimate the next step [NW06; CGT00]. Dating

back to [Lev44] and [GQT66], trust-region algorithms associate the approximation $Q_i(\Theta)$ with a zone of the parameter space around the current point where it is considered reliable. This zone is called the trust-region. Its size is adapted along the steps of the optimization to reflect how well the approximation locally corresponds to the cost function.

Figure 1.31 shows an unidimensional illustration of the trust-region optimization procedure, inspired by the two-dimensional example provided in [CGT00]. For a point θ_i , provided that Φ is twice continuously differentiable, a quadratic local approximation of the cost function Φ is given by the following Taylor expansion

$$Q_i(\Theta) = \Phi(\theta_i) + (\Theta - \theta_i)^t \nabla \Phi(\theta_i) + \frac{1}{2} (\Theta - \theta_i)^t \nabla^2 \Phi(\theta_i) (\Theta - \theta_i), \quad (1.98)$$

using the gradient $\nabla \Phi$ and the Hessian matrix $\nabla^2 \Phi$, both evaluated at point θ_i . Note that approximation Q_i is often inspired by the gradient and Hessian at θ_i , but it doesn't necessarily use them as is. Panel (a) of Figure 1.31 shows the approximation of Φ around an initial point θ_0 , associated with its trust-region (whose width is fixed arbitrarily for the sake of the example). Many solutions exist for the trust-region, the method used in Chapter 2 based on [CL96] uses an ellipsoidal trust-region. Once the approximation Q_i is known, we test a possible next iterate θ_{i+1} , defined as the coordinates of the minimum of Q_i within the trust-region. Note that this minimum can be strictly within the trust-region, as is the case for θ_1 in graph 1.31 (a), or on its boundaries like θ_2 in graph 1.31 (b). The test of next iterate consists in verifying if it effectively improves the cost function: we want $\Phi(\theta_{i+1}) < \Phi(\theta_i)$. If this is the case, the iterate is validated and the optimization procedure continues until a satisfying minimum is reached, for instance at θ_5 in graph 1.31 (b).

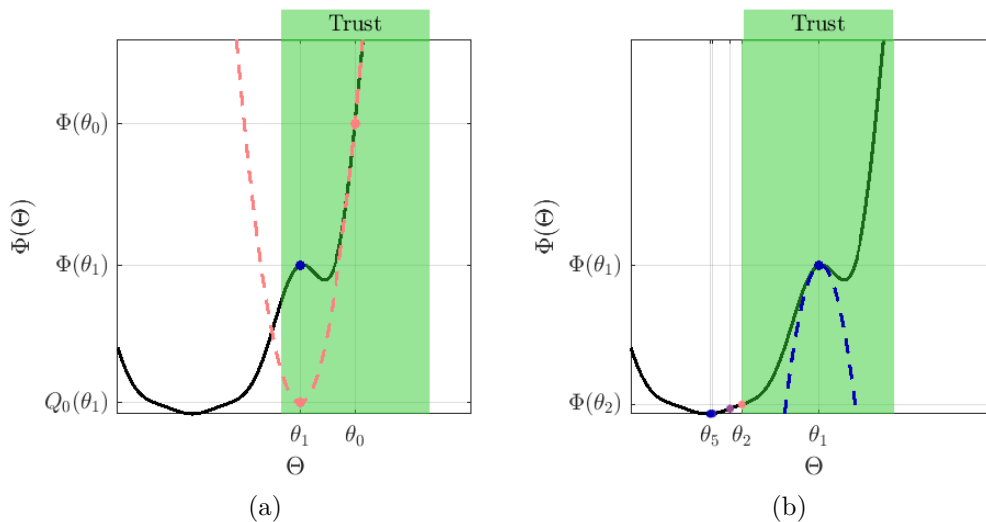


FIGURE 1.31: Trust-region algorithm application example. (a) Initial step (b) next steps. The **black** line is the cost function Φ , dotted lines are the quadratic approximations Q_{θ_i} around point θ_i . The **green** shaded region is the trust region around θ_0 in (a) and θ_1 in (b).

Figure 1.32 details the process of trust-region optimization in a slightly less straightforward case. It starts with the same θ_0 and a slightly smaller trust-region, which occasions iterate θ_1 to land on the bound of the trust region (panel (a)). Next step, represented in panel (b), represents a case of rejection of iterate. Indeed, if condition $\Phi(\theta_{i+1}) < \Phi(\theta_i)$ does not hold, meaning next iterate does not improve the cost function, the iterate is rejected. Furthermore, the trust-region shrinks: the approximation was so bad that it made the next point be worse than current point, so we trust it less.

This is the case in graph 1.32 (b) for rejected iterate θ_2^w . After reducing the size of the cost function, a new iterate is computed and tested. Here, the next tested iterate θ_2 is valid, so the algorithm proceeds. The trust-region can also be expanded, if the approximation Q_i underestimates the cost-function improvement. This is the case for θ_3 in graph 1.32 (b), where $Q_2(\theta_3) > \Phi(\theta_3)$. Trust-region algorithms usually test iterates and update the trust-region size

using a quantity called ρ_i , given by an expression of the form

$$\rho_i = \frac{\Phi(\theta_{i+1}) - \Phi(\theta_i)}{Q_i(\theta_{i+1}) - Q_i(\theta_i)}. \quad (1.99)$$

To evaluate the iterate, the quantity ρ_i is compared to thresholds. If ρ_i is negative, the iterate is undesirable and the trust-region should be reduced. Very often, the iterate is also considered undesirable and the trust-region reduced if ρ_i smaller than a small threshold μ . Whenever $\rho_i > 1$, the iterate is considered so valid that it calls for an expansion of the trust region. More generally, a threshold η is defined so this condition is actually $\rho_i > \eta > \mu$. The last case, where ρ_i lies in between the thresholds μ and η , indicates a valid iterate that does not call for expanding the trust region.

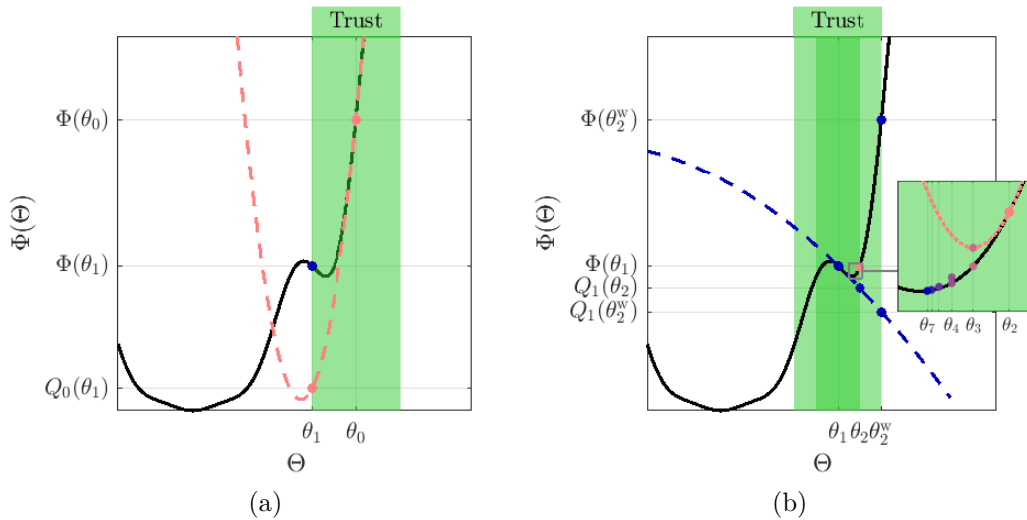


FIGURE 1.32: Trust-region algorithm application example. (a) Initial step (b) next steps. The **black** line is the cost function Φ , dotted lines are the quadratic approximations Q_{θ_i} around point θ_i . The **green** shaded region is the trust region around θ_0 in (a) and θ_1 in (b). In (b), the narrower **green** shade marks the reduced trust region, following the rejection of ‘wrong’ point θ_2^w because $\Phi(\theta_2^w) > \Phi(\theta_1)$.

As Figure 1.32 shows, trust-region algorithms are inherently local, so they may converge to a local minimum depending on the initial conditions. However, the trust-region formulation prevents the algorithm from diverging, and the algorithm is often rather computationally inexpensive. The next subsection presents a different class of optimization methods that are more robust to local minima: genetic algorithms.

1.3.2.2 Genetic algorithms

Genetic algorithms get their name from the inspiration they draw from biological evolution mechanisms [Hol75; GH88]. Figure 1.33 illustrates the steps of a genetic algorithm. In the first panel (Fig. 1.33 (a)), an initial *population* of N_θ points is spread across the parameter space Θ , randomly or using an appropriate sampling. For each point θ , the cost function $\Phi(\theta)$ is evaluated and constraints $h_i(\theta) \leq 0$ are checked. Points that do not respect the constraints are eliminated from the population, and the remaining points are sorted according to their cost function values. A certain fraction of points with the highest cost function values are eliminated from the population. At this stage, the only points in the population are those with the lowest cost function values. For the next generation new points are constructed, until the population is back to N_θ points. This can be done in a number of ways that involve combining the coordinates of existing points and introducing some degree of randomness in new points. The method of construction of new points should implement a compromise between conserving the characteristics of existing ‘good’ points and creating novelty so that the parameter space is thoroughly explored. Once the new population is complete, the cost function values are calculated and the points sorted accordingly, the highest are eliminated, and so on. Panels (b),

(c) and (d) of Figure 1.33 show the evolution of the population during three generations of points. The population progressively concentrates around the lowest minimum that satisfies the constraint.

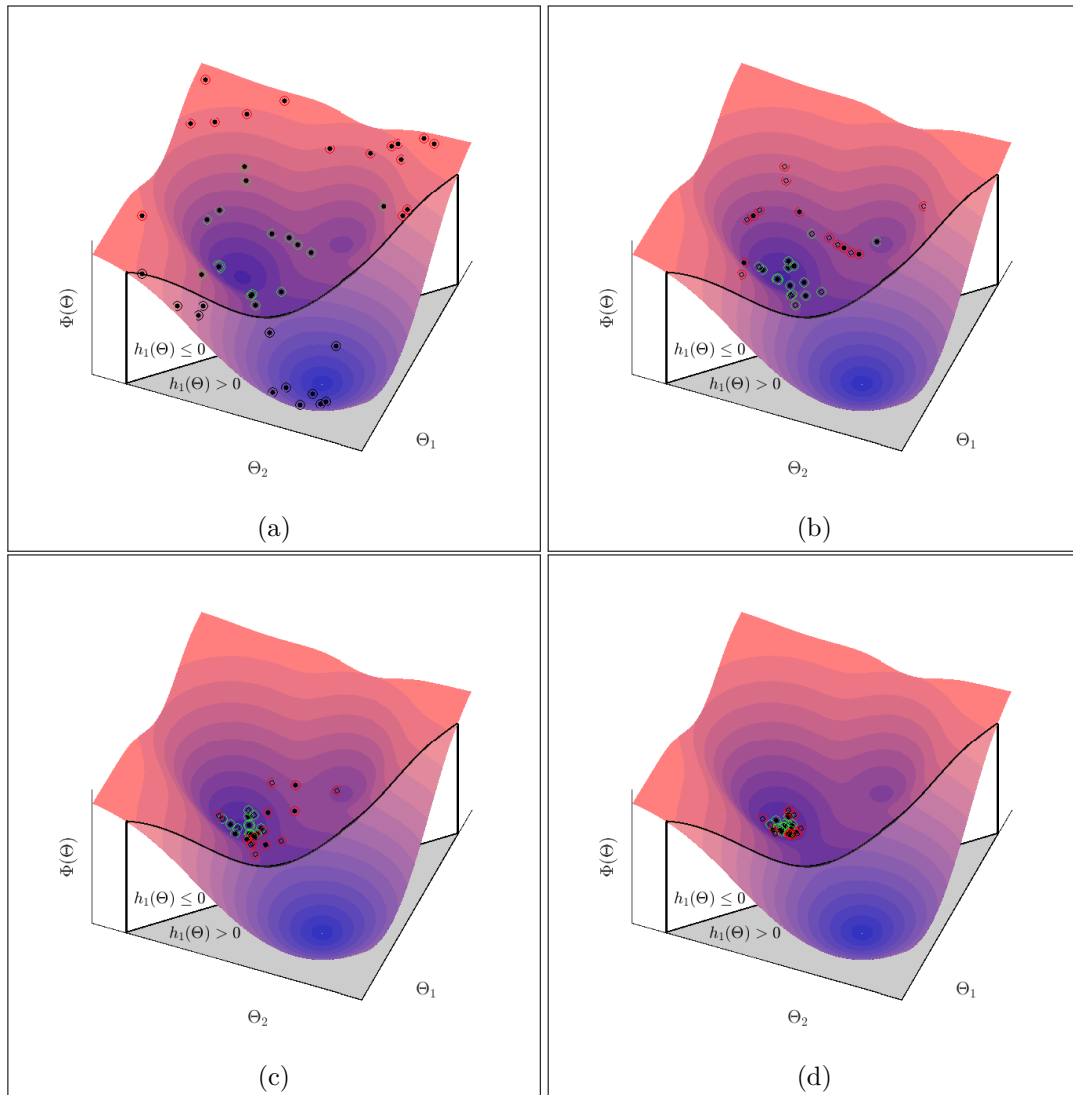


FIGURE 1.33: Principle of a genetic algorithm. (a) Initial population, (b), (c) and (d) next generations. Surface: cost function Φ , from low: **blue** to high: **light red**. Gray shade: constraint $h_1 \leq 0$ not satisfied. Black dots indicate points in the population (empty: old, full: new), circled **black** if eliminated by the constraint, **red** if eliminated for their high cost Φ or **green** if kept for next generation.

This class of algorithms presents the main advantage of being extremely robust to local minima of the cost function. Panel 1.33 (b) shows that one point in the population is kept around the local minimum on the right, but is quickly eliminated in panel (c) when all other points concentrate near the lowest minimum. Genetic algorithms are also insensitive to nonsmooth or noisy cost functions, that can cause fundamental difficulties in the local approximation necessary to methods such as the one presented in 1.3.2.1. They are also easily parallelizable (point generations and cost function evaluations), which means they are able to profit from high computational power when available. However, the robustness of a genetic algorithm highly depends on the number of points in the population. Large and high dimensional parameter spaces quickly leads to high computational cost. Moreover, fine convergence of a genetic algorithm can be slow compared to gradient-based methods.

1.4 Experimental tools

In order to be applied to instrument design, simulations must accurately represent playing a real instrument. This is why experimental work was undertaken during the preparation of this thesis. There are two main aspects to this. First, measurements inform the *a priori* tuning of the simulation parameters. The parameters linked to the exciter (reed, contact force, reed channel dimensions) are taken from previous experimental studies and the parameters representing resonators are due to impedance measurements performed in LMA, in part by the current author. The second way to use measurements in combination with simulations is *a posteriori* comparison of the dynamic behavior of the real and virtual instrument. This work makes use of an instrumented mouthpiece, which allows the *in vivo* characterization of the musician's action and the instrument's response.

1.4.1 The instrumented mouthpiece

Studying the dynamics of a real saxophone in a somewhat controlled fashion requires monitoring of the control parameters imposed on the instrument. To that end, we use an instrumented mouthpiece, which was chosen over an artificial mouth for several reasons listed below.

Many pioneering studies use artificial mouths to monitor the oscillating patterns of the clarinet [MG41; Bac61], the bassoon [Gok79] and later on saxophones [Gaz94; Dal+95] and brass instruments [VR97; GPP98]. An artificial mouth is a device replacing the musician completely to grant the operator precise control over parameters such as blowing pressure or reed opening at rest. This degree of control means for instance being able to vary one parameter at a time, to investigate its effect on the playing frequency for instance [Bac63; GPP98; Fri+05] or to measure oscillation thresholds and compare them to a model [CGC00; Ter+15; CHPV17]. Artificial mouths can also be equipped with sensors much more easily than musicians, which makes them the tool of choice for fundamental experimental exploration into an instrument's physics [Alm+17; Tai18], such as measuring the nonlinear characteristic of the reed channel [Alm+02; DGO03]. They also provide a means to go beyond the endurance of a musician and produce extensive mapping of an instrument's behavior using robotization [Alm+10; Fer+10; HLC12; Gro12; LHC13; Alm+13; DV15; Li+16].

However, artificial mouths must be finely tuned to work properly, and the repeatability of measurements often poses a challenge. Moreover, some phenomena observed with an artificial mouth may be impossible to obtain by a musician, for instance because the control required is beyond the limits of the human body [MAGD18]. This greatly affects the musical relevance of the results and the impact they can have on describing the playability of an instrument.

These reasons have driven us to focus on another type of experimental device: instrumented mouthpieces. Instrumented mouthpieces are modified wind instrument mouthpieces that include sensors monitoring the action of the musician and the internal acoustical and mechanical signals of the instruments. Straightforward examples include brass mouthpieces equipped with an optical devices to observe the lip movement [Mar42; Gok81; NCG08]. Devices monitoring the control parameters of the musician allow quantitative comparisons of their action on different instruments [FS99]. Instrumented mouthpieces have been used recently to study technical gestures: vibrato and glissando on the saxophone [SLS08; Gui+10] and clarinet [CSW09a], attacks with or without the tongue on the saxophone [HG14] and clarinet [PVHC18] and various techniques on the saxophone [CSW08; CSW11] and clarinet [Tai18]. Instrumented mouthpieces also allow investigations into the multiphonics on the trombone [VVG16] and its general technique [FS13; BSW20]. An instrumented mouthpiece is also used in [MA+16; Cha+19a] to estimate reed parameters while the instrument is being played by a musician.

Note that the instrumented mouthpiece presented hereafter was not developed specifically for the needs of this thesis, or by the current author. While some degree of development, calibrating and fine-tuning took place, the instrumented mouthpiece is mostly used as pre-existing tool to complete and bolster the simulation results via experimentation.

1.4.1.1 Structure of the instrumented saxophone mouthpiece

A Buffet-Crampon saxophone mouthpiece has been modified by P. Sanchez to incorporate two pressure probes and an optical displacement sensor (Everlight ITR8307). A legended schematic is represented on Figure 1.34. The apparatus used in this work is based on [Gui+10]

(although the FSR strain sensor on the reed is not connected), with an added photodiode-based displacement sensor inspired by [MA+16]. The first pressure probe sticks out the front of the mouthpiece into the mouth of the musician, and measures the blowing pressure. The second pressure probe goes into the middle of the chamber of the mouthpiece and measures the pressure signal just before the entrance of the main bore. The two pressure probes are plastic capillary tubes of radius 0.55 mm and of lengths 20 mm (mouth pressure) and 62 mm (pressure in the mouthpiece). Both pressure probes are connected to Honeywell TSCDRRN005PDUCV differential pressure sensors. The optical displacement sensor is attached to the roof of the mouthpiece and points near the tip of the reed, to measure the opening of the reed channel. All signals are conditioned by a homemade electronic board and converted to digital by a NI USB-9234 card (National Instruments). The sampling rate used is 51.2 kHz. Unless otherwise specified, Rico Strength 2 Alto saxophone reeds are used.

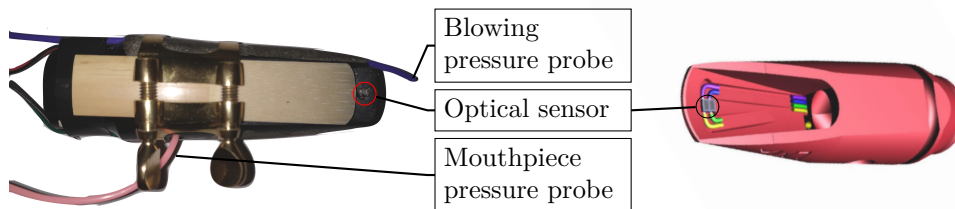


FIGURE 1.34: Instrumented mouthpiece. On the left, the reed was moved so the optical sensor can be seen. The right representation is a 3D rendering, without pressure probes, that shows the optical sensor and the path of the attached wires through the mouthpiece (credit: P. Sanchez).

1.4.1.2 Calibration of the optical displacement sensor (internship A. Goloubkov)

The onboard miniaturized optical sensor for measuring the displacement of the reed is not calibrated. Having a quantitative value of the reed displacement is crucial to estimate, for instance, the control parameter linked to reed opening at rest ζ . Therefore a static calibration procedure was developed and applied, in collaboration with intern Alexandra Goloubkov, that I supervised. This procedure, rather than yielding a precise estimate of the linearity and the sensitivity of the sensor, serves here to explore the limitations of the sensor and take them into account while designing further experiments. The experimental setup is schematized in Figure 1.35. The mouthpiece is clamped into place using the crook of the saxophone, and the reed is moved slowly by hand (by placing a finger on its shoulder) until closure of the reed channel, several times, in measurements runs of 15 s. Two reference laser sensors (Keyence LG-K) are used to measure the displacement of the reed relative to the mouthpiece. These reference sensors are precalibrated. One of the two reference sensor measures the distance to the point of the exterior face of the reed aligned with the embedded sensor inside the reed, while the other measures the displacement of the mouthpiece itself. The difference between the two reference sensors' signals gives the reference signal of displacement of the reed relative to the mouthpiece, to which the output signal of the embedded sensor is compared.

Optical displacement sensors must be calibrated, as their sensitivity depends on the shade of the reed, the sensor's temperature, and the reed dampness, as pointed out in [MA+16]. In our case, the main issue observed on the embedded sensor is due to the dampness of the reed, which affects both its linearity and its coefficient of sensitivity. The sensor relies on reflected infrared light on the target surface to estimate its position, therefore any changes in

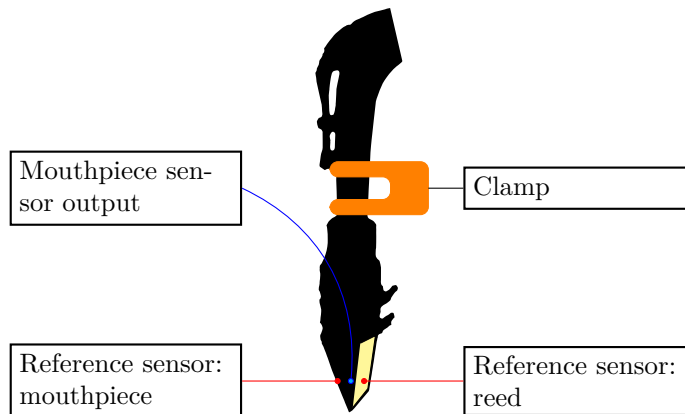


FIGURE 1.35: Schematic of the optical sensor calibration apparatus. Red straight lines indicate the reference sensors' laser beams, and the blue line the output wires of the embedded optical sensor.

the optical properties of the object affects the measurement. Figure 1.36 shows two calibration curves performed one directly after the other, using the exact same conditions except for the dampness of the reed: graph (a) with a very dry reed (new, out of the box), graph (b) with the same reed humidified using the tongue. Each graph shows two repetitions of the experiment with the same reed, which leads to the two different fitted lines. This indicates the degree of variability of the coefficients in the same situation. The sensitivity coefficient of the sensor using a dry reed is 0.5 mm/V, while it is about 0.3 mm/V with the wet reed. There is a notable variability in sensitivity with the wet reed, as the fitted curves in Figure 1.36 (b) show. The linearity of the sensor seems affected, with a saturation phenomenon occurring just above -2 V in the case of the dry reed. The dampness of the reed can vary slowly during the musician's performance due to condensation and saliva, affecting the sensitivity coefficient of the optical sensor. Note that some preliminary tests have also shown that the embedded mouthpiece sensor is sensitive to exterior light, especially neon light that superimposes 100 Hz noise to the measured displacement signal. Calibrations are therefore performed with only continuous light (sunlight in our case), obscured as much as possible by curtains. Note that perturbations due to exterior light are less severe in playing situation, where the mouthpiece is in the musician's mouth. Care is also taken as to possible saturation of the sensor, especially at the beginning of a measurement session before the reed becomes damp.

Due to the instabilities of the instrumented mouthpieces' sensors, for the rest of this work, the reed displacement signals are used only as qualitative indicators of the reed's position and examined over short periods of time. In general, pending more solid validations of the sensors, the instrumented mouthpiece is interpreted qualitatively. However, promising preliminary results were obtained with the objective of estimating the dimensionless musician control parameters in real-time from instrumented mouthpiece signals, as discussed in appendix B. This would open the door to more quantitative comparisons with the models.

1.4.2 Measuring impedances with the CTTM impedance sensor

The applicability to concrete design situations of the mathematical models presented in this work depends in large part on measurements performed on real instruments. Measuring the acoustical characteristics of the resonators is a critical part of the process. Indeed, the modal coefficients or the reflection function that are extracted from such measurements greatly influence the pitch of instruments produced by the model. Consequently, this section details

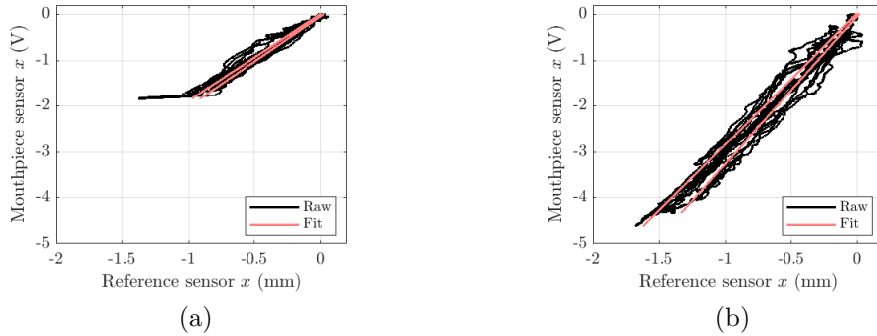


FIGURE 1.36: Static calibration of the displacement optical sensor of the instrument mouthpiece, for (a) a dry reed and (b) a wet reed. Each graph contains two fits (red lines) due to two separate calibration signals (in black).

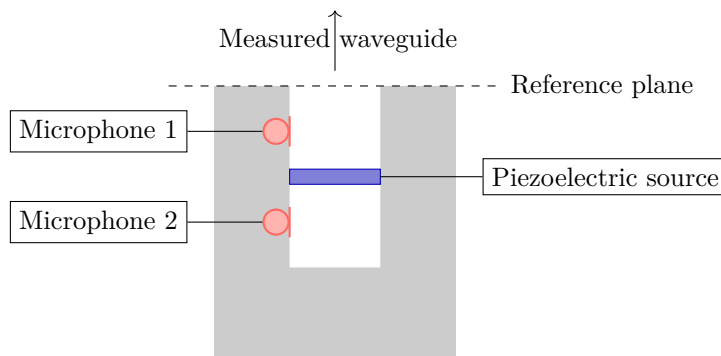


FIGURE 1.37: Schematic of the CTTM impedance sensor cavities, microphones and sources.

the impedance measurement apparatus, as well as its limitations in terms of frequency and uncertainty. Two internships supervised in part by the current author were dedicated to estimating the uncertainty associated to impedance measurement on two kinds of conical woodwinds: the oboe and the saxophone.

1.4.2.1 Presentation of the CTTM impedance sensor

The CTTM impedance sensor [DLR08; DLR13] is used to measure the input impedance of the saxophone resonators used all along this work. The sensor (see schema on Figure 1.37) relies on a cavity containing a piezoelectric buzzer, that sends an excitation signal at the input of the resonator, and two microphones, one on each side of the buzzer. The transfer function between the front microphone (microphone 1) and the back microphone (microphone 2) can be converted into the impedance Z at the reference plane, i.e. at the input of the measured waveguide. The excitation signal is a sine sweep. The measurement procedure allows a decomposition of the measurement frequency range into several portions, each of which is characterized using a separate sine sweep. The transfer function is then reassembled from these separate responses.

1.4.2.2 Repeatability measurements applied to the oboe (internship R. Buttard)

The oboe is a woodwind with a mostly conical resonator, but it differs from the saxophone in many aspects. A oboe is represented in Figure 1.38. The instrument is played with a double reed, which is connected to the main body with a tube of very small diameter (1.9 mm) called the backbone. The body of the oboe is wooden and therefore much thicker than the metal resonator of the saxophone. This entails that some of the oboe's holes, notably those nearest to the reed, have very long chimneys. They are also very narrow, and the oboe's pads are positioned very close above the tonehole. Some of the oboe's pads are pierced with a very

narrow hole, to be used to correct the intonation of some fingerings. All of these geometrical particularities lead to questions pertaining to the impedance measurement procedure's linearity and repeatability. Experimental investigations were carried out by Rémi Buttard during an internship in 2018.



FIGURE 1.38: A oboe (Buffet-Crampon Prestige), with zoom on the reed and backbore.

Side holes with a small radii may cause nonlinear effect, as first measured in [Siv35]. A subsequent experimental study [IL50] shows the role of the hole thickness, in link with the acoustic streams around the hole which highly depend on its shape [THJC57; Bui+11]. These nonlinear losses, in addition to modifying the sound of the instrument [ADG04], can compromise measurements of assumed linear quantities like the input impedance of the resonator. In the case of the oboe, nonlinear phenomena were found to create artifacts in the estimated impedance. Figure 1.39 illustrates this phenomena by superimposing two measurements. On the red curve, the artifact is revealed as an additive oscillatory component, particularly present around the impedance peaks. In order to make these artifacts disappear, it was proposed to limit the frequency range of the sweep used to measure the impedance to less than an octave: the highest frequency of the sweep is smaller than twice the first. This way, the harmonic content generated by the nonlinearity lies beyond the measured frequency range and is not taken into account. Note that this method only corresponds to ignoring the nonlinear phenomena, and does not attenuate or counter it in any way. This method yields the black curve in figure 1.39. In order to validate the procedure, a narrow cylindrical tube is used, whose impedance is easily calculated using the classical (linear) Transfer Matrix Method. This calculation serves as reference to which the result of the measurements are compared. Using sweeps no longer than an octave, the measurements match the model until 2 kHz, and the artifacts due to nonlinearities disappear. This protocol is therefore used to measure the input impedance of a oboe.

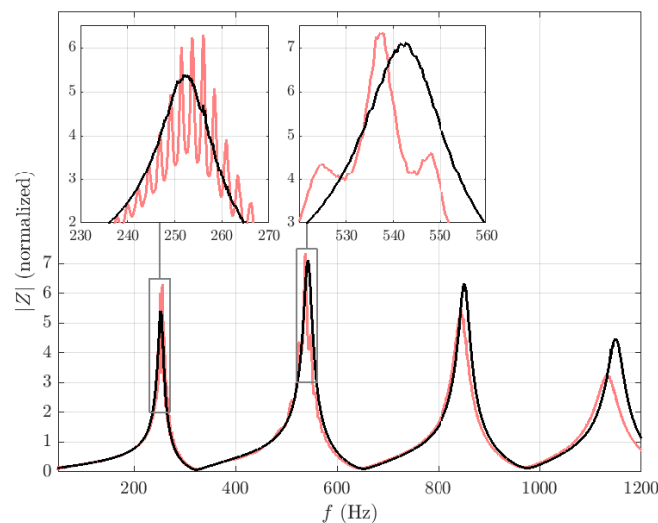


FIGURE 1.39: Measured impedance for the low B fingering of a Buffet-Crampon oboe. In red, the artifact due to nonlinear phenomena is present. In black, as reference, a subsequent measurement without the artifact.

The uncertainty of oboe impedance measurements (as with most instruments) can be due to the assembling of the resonator and its mounting on the sensor, as well as actions of the operator during the measurement (pressing the keys when measuring a given fingering and possible extraneous noise). Measurements performed in repeatability conditions, decomposing the experimental protocol, have shown that the assembly of the resonator and manual application of the fingering does not increase the uncertainty. Nominal uncertainties, defined as

$$U = \frac{\sigma}{\sqrt{N_{meas}}} \quad (1.100)$$

where σ is the standard deviation and N_{meas} is the number of measurements are typically less than 2 Hz for the resonance frequencies and less than 0.3 dB for the peak amplitudes. These values are considered satisfactory to be used for instrument making, as they allow two different oboes to be clearly separated.

1.4.2.3 Measuring the impedance of the saxophone family (internship C. Marmion)

Measured saxophone impedances constitute the basis for the modal and reflection function representation of the resonator in almost all the simulations presented in this work. Therefore, some time was spent improving the impedance measurement procedure applied to saxophone resonators, in association with intern Clément Marmion. First, adaptation pieces to mount the instrument on the sensor in a repeatable manner were designed and 3D printed. Each adaptation piece adapts to the shape of the cork cone at the beginning of the neck (see Figure 1.40) so that the input of the neck reaches the output plane of the sensor's cavity. Figure 1.41 provides a schematic of the assembly. The contact area between the adaptation piece and the air in the sensor's cavity is very small, which makes the leak-tightness of the adaptation piece easier to secure (the LMA uses fused filament fabrication 3D-printing, which tends to produce porous objects). This principle supposes that the instrument is carefully pushed into the adaptation piece. If the instrument is pushed in too much or not enough, the measured impedance can be affected. Using the adaptation piece and a careful positioning of the instrument, the uncertainty on the peaks is about 5 cents for the frequency and 0.5 dB for the amplitude.

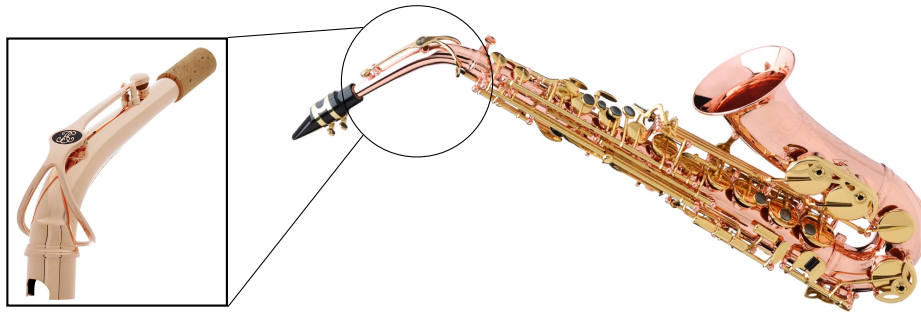


FIGURE 1.40: An alto saxophone (Buffet-Crampon Senzo), with zoom on the neck and cork.

The input impedance was measured on several instruments of the saxophone family: the Buffet-Crampon Senzo alto saxophone represented in Figure 1.40 and three Yamaha saxophones, a soprano, an alto (YAS-280) and a tenor (YSS-280). One may wonder how acoustical characteristics set the saxophones aside from each other, whether between two altos for instance or between an alto and a tenor or a soprano. As a first look into the question of the homogeneity of the saxophone family, Figure 1.42 presents superimposed impedance moduli for three fingerings of the four measured resonators, where the frequency axis is contracted to compensate for the soprano and the tenor's transposing with respect to the alto. The approach is simplistic: the frequency axis of the tenor's measurements is dilated by multiplying by 4/3 (up a perfect fourth between B \flat and E \flat), while the frequency axis for the soprano is contracted by multiplying it by 2/3 (down a perfect fifth from B \flat and E \flat). The frequency axes corresponding to the two altos (Yamaha and Buffet-Crampon) are unchanged. Figure 1.42

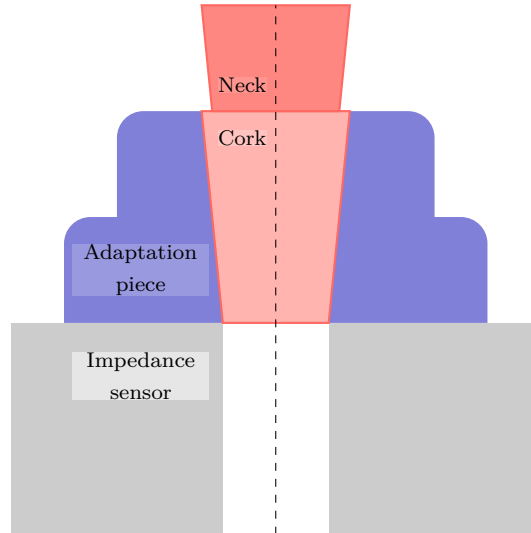


FIGURE 1.41: Schematic of the adaptation piece connecting the saxophones neck to the impedance sensor.

shows that the peak structure remarkably lines up in some frequency regions (above 700 Hz for the C \sharp fingering for instance). This prompts the use of quantitative metric to precise the similarities in the family.

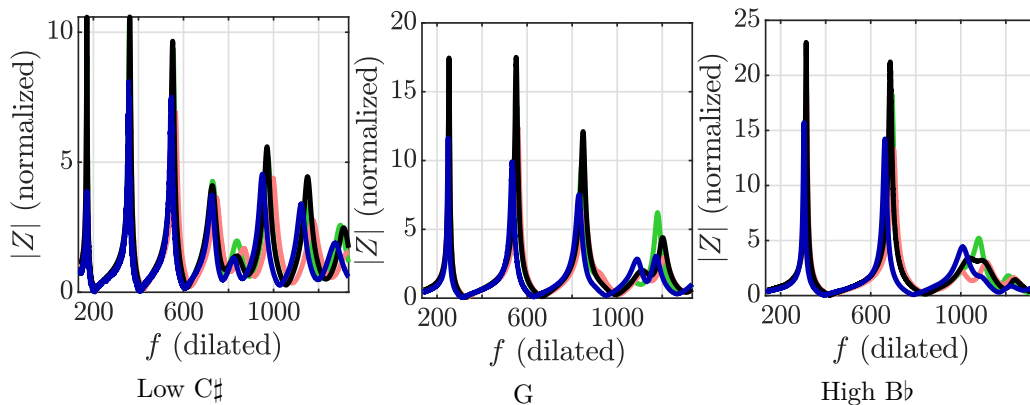


FIGURE 1.42: Measured impedance modulus for 3 first register fingerings (low C \sharp , G and high B \flat) of the four measured saxophones: **green** Buffet-Crampon alto, and Yamaha **black** alto, **red** soprano and **blue** tenor. Frequency axis is unchanged for the altos, contracted ($\times 2/3$) for the soprano and dilated ($\times 4/3$) for the tenor.

Two metrics are used to compare saxophone impedances across the fingerings of the first register, represented in Figure 1.43. The first metric is the L 2 -norm of the difference between impedance moduli, which is the distance used in the optimization of Chapter 2, written here

$$N_2 = \sum_{\omega=\omega_{min}}^{\omega_{max}} \left| |Z_{test}(\omega)|^2 - |Z_{ref}(\omega)|^2 \right|^{1/2}, \quad (1.101)$$

where $Z_{ref}(\omega)$ is the dimensionless input impedance of the Senzo alto saxophone and $Z_{test}(\omega)$ is the dimensionless input impedance of one of the three other saxophones (Yamaha alto, tenor and soprano). This way, the differences between two alto saxophones can be put into perspective with the differences between an alto and a tenor, or an alto and a soprano. Note that this comparison has no ambition of being general. Any kind of general result in this area would require a complete specific study with (if nothing else) a much greater number of saxophones. However, it is interesting that, as Figure 1.43 (a) shows, although the norm

between the reference alto and the tenor is always greater than that between two altos, it is not the case for the soprano sax. The latter is actually even closer to the reference alto saxophone in the upper fingerings of the first register than the second alto is. The other metric applied to compare the saxophone family relates to the cutoff frequency of the tonehole lattice. The cutoff of a woodwind resonator pertains to the global structure of its acoustical response, and shapes the spectrum of the sounds it produces [BL88; BK88; Pet+19b]. We use the transition band metric presented in [Pet+20] to provide an approximation of the cutoff. This frequency band f_t^R describes the roll-off of the reflection coefficient as defined between two frequency $f_{t,min}^R$ and $f_{t,max}^R$ which are the lowest frequencies such that

$$|R(f_{t,min}^R)| = \frac{1}{\sqrt{2}} \quad |R(f_{t,max}^R)| = \frac{1}{2}. \quad (1.102)$$

The idea is that below the transition band, most of the energy is reflected back to the instrument's input, while within and above it there are frequencies where most of the energy propagates and radiates. This metric has the particularity to necessitate no knowledge of the geometry of the instrument, but it was shown to follow more sophisticated geometry-based cutoff indicators on the saxophone. Figure 1.43 (b) represents the transition band f_t^R , scaled to compensate for each instrument's tonality ($\times 2/3$ for the soprano, $\times 4/3$ for the tenor). Note that the lowest fingering represented is the low C because lower fingerings have too few open holes to constitute a tonehole lattice and thus to define a cutoff. The transition bands of the four instruments follow the same trend: they increase with higher fingerings. While the width of the transition band however does not seem to fit a particular pattern, the frequency values themselves line up remarkably once scaled, with a transition band around 500 to 700 Hz for fingerings below E, shifting up to around 900 to 1200 Hz upwards of fingering G. As the cutoff shapes the external tone of the instrument, this begs the question of whether this scaling in the family relates to some qualities of the 'saxophone sound' common to the alto, soprano and tenor.

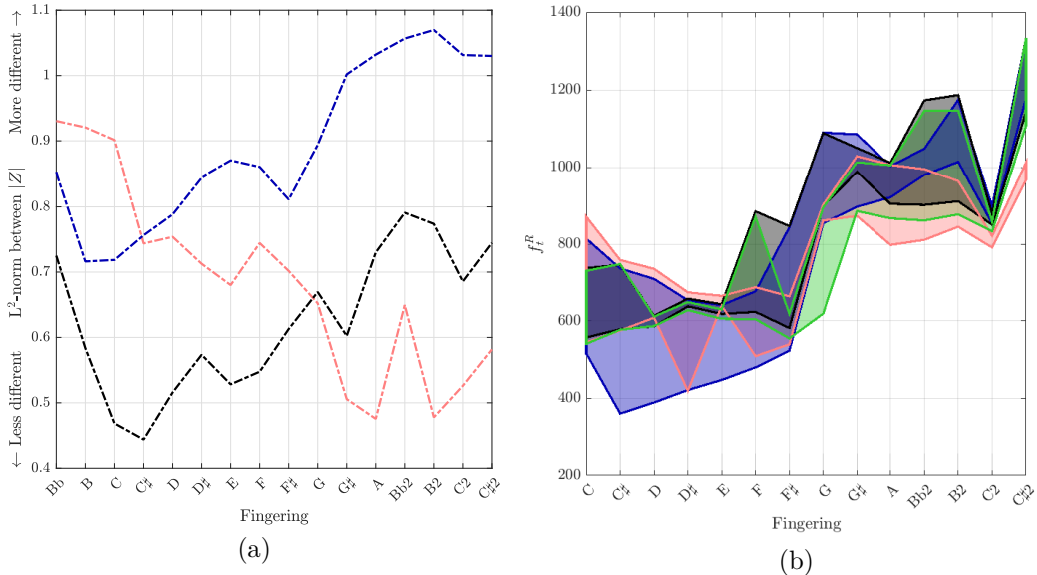


FIGURE 1.43: Two comparisons in the saxophone family. (a) L^2 -norm between the impedance moduli of the reference Buffet-Crampon alto and the Yamaha **black** alto, **red** soprano and **blue** tenor. (b) Approximation of the cutoff by the transition frequency band f_t^R . Same color code for the addition of the **green** Buffet-Crampon alto. Frequency axis is unchanged for the altos, contracted ($\times 2/3$) for the soprano and dilated ($\times 4/3$) for the tenor.

Chapter 2

Optimizing the geometry of a bicylindrical resonator based on the acoustical characteristics of a saxophone

2.1 Motivation and summary

This chapter treats the problem of optimizing the geometry of a resonator in order to achieve certain acoustical characteristics. Note that the focus is on the process of computerized search of the *optimal* geometry, rather than the geometry itself. Indeed, several questions arise whenever designing such computerized methods, notably about the existence and unicity of the optimum, as well as the certainty of convergence towards it. This chapter, rather than a drastically incomplete answer to these questions, should be understood as the token of our attention to them. Hereafter, a simple case study is presented, with a limited number of geometrical variables, and arguably naive target acoustical characteristics: the optimized instrument's input impedance is hoped to match that of a real saxophone. These restrictions may reduce the direct impact of the work on instrument design *per se*, but they are crucial to efficiently convey reflections on the optimization process. Indeed, they facilitate relevant visual representations, and allow the introduction of a cost function family that possesses the smoothness properties necessary to prove that the chosen algorithm converges everytime to an optimum.

The placement of this discussion at the start of the dissertation, rather than at its end, should seem surprising. Is the question of the optimal acoustical characteristics of a saxophone-like instrument so trivial that they are treated entirely in this chapter, as a mere preamble to a work focusing on the optimization process itself? It is rather the contrary. Once the optimization process is well understood, we dispose of powerful numerical tools to adjust the geometry of a resonator to choose its acoustical characteristics. But in this chapter this choice, as mentioned, is rather naive. Thus remains to be addressed the major issue of a well-informed choice. This optimization chapter begs for results linking these acoustical characteristics to the sounds the instrument actually produces. The rest of this work is then aimed at offering elements to guide this choice, and get closer to applying optimization with well-informed targets.

The resonator to optimize is comprised of two cylinders, placed in parallel after the mouthpiece. It is inspired by the so-called *transverse saxophone* approximation, where a conical resonator such as that of a saxophone is replaced by two or more cylinders. This approximation of cones allows the derivation of analytical results and simplifies the real-time implementation of real-time numerical synthesis. But more so, the cylindrical saxophone is an instrument design challenge. It inspired prototypes in LMA, such as the coaxial saxophone [Doc+16] represented in figure 2.1. In 2016, the Yamaha Venova (figure 2.2) was commercialized, with a soprano saxophone mouthpiece adapted to a branched cylindrical resonator.

This paper explores the analogy between a saxophone resonator and a bicylindrical resonator, sometimes called transverse saxophone or cylindrical saxophone. The dimensions of

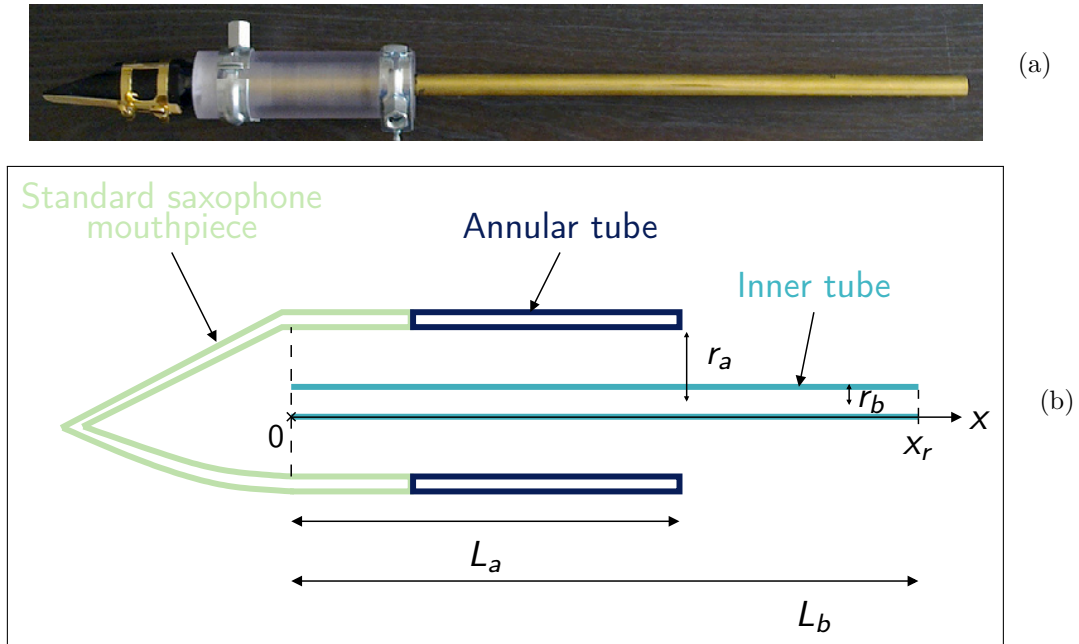


FIGURE 2.1: Profile view of coaxial saxophone (a) and schematic representation (b) (reproduced from [Doc+16], with the authorization of the author).



FIGURE 2.2: The Yamaha Venova.

a bicylindrical resonator are optimized numerically to approximate a saxophone impedance. The target is the impedance measured on a usual saxophone (Buffet-Crampon Senzo). A classical gradient-based non-linear least-square fit function is used. Several cost functions corresponding to distances to the target impedance are assessed, according to their influence on the optimal geometry. These cost functions correspond to the p -norm of the difference between the impedance moduli. Compromises appear between the frequency regions depending on the cost function. It is shown that the chosen cost functions are differentiable and locally convex, which ensures convergence of the selected algorithm. The convexity region contains the initial geometrical dimensions obtained by crude approximation of the first resonance frequency of the target. The convexity region is estimated by computing the cost function on projections of the parameter space around the optimum, and by checking the convergence of the algorithm with randomly generated initial conditions. Another 'undesirable' local optimum is located, but it can be eliminated because it corresponds to poorly fitted impedance peaks, as can be seen on figure 2.14. The best optimal geometry is submitted to further analysis using descriptors of the impedance. Its deviations from the target saxophone are put into perspective with the discrepancies between the target saxophone and a saxophone from a different manufacture (Yamaha YAS-280). Descriptors such as harmonicity or impedance peak ratio set the bicylindrical resonator apart from saxophone resonators, despite a good agreement of the resonance frequencies. Therefore, a reed instrument with a bicylindrical resonator could be tuned to produce the same notes as a saxophone, but due to differences in the intrinsic characteristics of the resonator, it should be considered not as a saxophone but as a distinct instrument.

Reading guidelines

The following sections (from 2.2 to 2.7 included) constitute an *in extenso* reproduction of the work published as:

Colinot, Tom et al. (2019). "Numerical optimization of a bicylindrical resonator impedance: differences and common features between a saxophone resonator and a bicylindrical resonator". In: *Acta Acustica united with Acustica* 105(6), pp. 1217-1227.

The title and abstract of the article were removed, as they are functionally replaced by the present chapter's title and introductory section (2.1).

2.2 Introduction

This work deals with the bicylindrical approximation of a conical geometry, where two cylinders are put in parallel. As a purely academic approximation of a conical instrument such as the saxophone, a "cylindrical saxophone" model permits to obtain analytical results on the produced sound [Ben88; ODK04] and dynamic behavior [ODK04; DGK00]. A patent describing bicylindrical resonators to be used for saxophone-like instruments [MS11] shows that industrial interest exists for such innovative resonator shapes. This paper presents a bicylindrical resonator numerically optimized to replicate the acoustical impedance of an existing saxophone, and compares it to the target saxophone and another "control" saxophone. The goal is to judge whether bicylindrical resonators may be considered as saxophones or not.

Traditionally, instrument makers design new products by trial and error, drawing on empirical knowledge acquired over years of practice. They adjust the manufacturing parameters to maximize the "quality" of successive prototypes in terms of complex criteria involving not only sound characteristics such as intonation and timbre features, but also ergonomics, playability, and feeling of the musician. Given the complexity of this task, as well as the large number of parameters involved, the process is long and requires building several prototypes, amounting to a significant overall cost before the production begins. Numerical optimization may take simple criteria into account to offer geometrical dimensions for new resonators in a quick, repeatable and cheap manner. The optimized resonators would probably have to be fine-tuned to satisfy the more complex criteria, but there is hope that overall, the prototyping stage would be accelerated.

From the point of view of an acoustician, the optimization of a musical instrument could, at first, use some criteria pertaining directly to the characteristics of the produced sound, such as the playing frequency. Predicting the sound produced by the instrument for various excitation conditions is possible by numerical synthesis, and has been applied to optimization problems with up to five optimization variables [Tou+17]. However, this method is time consuming, hence incompatible with the optimization of dozens of parameters. Consequently, many wind instrument optimization methods adjust the resonance frequencies of the resonator, for instance using an analytic model accounting for small modifications of the bore of a trumpet [MD11]. Similarly, acoustical considerations were used to adjust iteratively the positions and dimensions of the holes in a quena to obtain a desired tuning profile [VFC13]. Recent works also propose a method to compute the eigenfrequencies of a variety of multi-cylindrical resonators [LV15; DV17; LV17], with instrument design in mind. For problems with many parameters, computerized optimization strategies are the preferred choice. For example, the complete tone hole geometry of a clarinet was optimized by a gradient descent based on the first and second impedance peaks [Nor+13], and the geometry and control of a clarinet model was optimized to reproduce signals obtained with an artificial blowing machine [Cha+19b]. It is also possible to use the input impedance deduced from a time-domain discretization of the Euler equations in the optimization of a saxophone bore [SCH17b]. Some authors take into account the complete input impedance in the cost function, rather than the resonance frequencies alone. This type of objective was applied to trumpets [Kau01] and trombones [BNC09], with Rosenbrock's numerical optimization method [Ros60], and saxophones [GK11] using the CMA-ES (Evolution Strategy with Covariance Matrix Adaptation) optimization method [Han06]. In previous work, numerical optimization has mostly served as a tool to adjust or redesign existing instruments, but it can also be seen as a means to explore innovative geometries.

This article presents the optimization of the geometry of a bicylindrical resonator to match the impedance measured on a saxophone, which has a predominantly conical resonator. These geometries being fundamentally different, the fit cannot be perfect. The acoustical differences between the optimum and the target are analyzed. The optimization is performed numerically, relying on an impedance model of the designed instrument. Objective criteria depending only on linear acoustics considerations are used. This allows to maintain a moderate computational cost. Since our purpose is to compare the bicylindrical resonator with existing saxophones, the target of the optimization relies on impedances measured on a professional alto saxophone (see 2.3.1). The impedance is measured for several fingerings of the first register, the optimization is performed for these fingerings. By choice, the optimization is limited to a given frequency range: the impedance of the bicylindrical resonator is fitted to the target impedance between 70 and 1200 Hz, which contains the main impedance peaks. The fit is done according to a given norm (see 2.4.2). The effect of the choice of this norm on the result of the optimization is studied. Moreover, since the optimization algorithm is local, the initial condition is modified to check if the procedure still converges to the same optimum (see 2.4.3). The influence of each design parameter on the cost function is revealed around the optimum. Finally, the optimized geometry for the example studied here is presented in section 2.5. The numerical optimization procedure yields the bicylindrical resonator that is as close as possible to a saxophone – considering our criterion and our degrees of freedom. The purpose of this process is to better define the limit of the approximation of a saxophone resonator by a bicylindrical resonator, when it is conducted on several fingerings of the saxophone. The deviations between the impedances of the optimized geometry and the target saxophone are computed, and they are compared with the discrepancies between the target saxophone and a saxophone of another brand.

2.3 Input impedance of the saxophone and the bicylindrical resonator

In order to optimize the dimensions of the bicylindrical resonator (see figure 2.3), it is necessary to use a model giving the impedance of such resonator based on its geometrical dimensions. The computed impedance is then fitted to the target impedance : the impedance measured on a saxophone, for 16 fingerings of the first register.

2.3.1 Saxophone impedance measurement: target and control

Impedance measurements were performed on two saxophones. The first produces the target impedance. The second saxophone, of a different model and different brand, is called the “control saxophone”. It serves as reference in the analysis of the difference of characteristics between the bicylindrical resonator resulting from the optimization and the target instrument. This way, we aim to check whether the optimized resonator is as close to the target saxophone as another saxophone. If the differences between two saxophones are of the same order than the differences between the bicylindrical resonator and a saxophone, then the bicylindrical resonator may be considered as a saxophone, at least from the input impedance point of view. The details of this comparison are presented in section 2.5. The target instrument and the control instrument are commercial models of alto saxophones.

Impedance measurements are carried out using the impedance sensor apparatus developed in [DLR08] on the first register (closed register hole) of the target and control saxophones. All the measurements are carried out in a semi-anechoic room. In total, 16 fingerings of the first register are measured. In written pitch for the alto saxophone, the fingerings range from the low B \flat to the C \sharp 2 of the first register – which correspond to the notes D \flat 3 (138.59 Hz) to E4 (329.63 Hz) in concert pitch. The written pitch notation is kept throughout the rest of this paper.

Since the apparatus does not allow impedance measurements of the instrument with its mouthpiece, a cylindrical mouthpiece chamber of typical dimensions (radius 12 mm and length

$L_m = 60$ mm) is added in post-treatment, such that the dimensionless target impedance writes

$$Z_{tar} = \frac{Z_{c,m}j \tan(k_m L_m) + Z_{mes}}{Z_{c,m} + Z_{mes}j \tan(k_m L_m)}, \quad (2.1)$$

where Z_{mes} is the input impedance measured without the mouthpiece. In order to eliminate the noisy parts of the measurement, the target impedance is truncated at low frequencies, below 70 Hz. To decrease the computation time of the optimization, the target impedance is also truncated above 1200 Hz. For the fingerings considered, the main impedance peaks fall between 70 and 1200 Hz. Beyond 1200 Hz the combined effect of the conicity of the resonator and the tone hole network contribute to lowering the impedance peaks. The actual target impedance is discrete vector with 1413 samples, the frequency step between two samples being 0.8 Hz.

2.3.2 Impedance of a bicylindrical resonator

The bicylindrical resonator, as defined in [Doc+16], is composed of a cylindrical mouthpiece (i.e. a mouthpiece with cylindrical chamber) followed by the parallel association of two cylinders (see figure 2.3). Therefore, the entire instrument's dimensionless input impedance writes

$$Z_{des} = \frac{Z_{c,m}j \tan(k_m L_m) + Z_{ts}}{Z_{c,m} + Z_{ts}j \tan(k_m L_m)}, \quad (2.2)$$

where L_m is the length of the cylindrical mouthpiece, $Z_{c,m} = \rho c / S_m$ is its characteristic impedance depending on its cross section S_m , the ambient air density ρ , the sound velocity c . It is worth noting that the parameter L_m should be understood as the equivalent length of the chamber of the mouthpiece, not including the length of the reed. Z_{ts} is the input impedance of the parallel association of two cylinders. The wave number k_i [PS81] depends on the equivalent radius r_i of each section such that

$$k_i(\omega) = \frac{\omega}{c} - (1 + j)3.10^{-5} \frac{\sqrt{\omega/2\pi}}{r_i}, \quad (2.3)$$

where ($i = \{b, m\}$) associates with the long cylinder b or the mouthpiece m . The short pipe a is defined by its equivalent radius

$$r_{eq,a} = \sqrt{S_a/\pi}, \quad (2.4)$$

where S_a is the annular cross-section between the inner wall of cylinder a and the outer wall of cylinder b (see figure 2.3). Since this pipe is ring-shaped, losses are adjusted by a factor μ' corresponding to the ratio of the internal wall surface of the ring a to the internal wall surface of a cylinder of radius $r_{eq,a}$

$$k_a(\omega) = \frac{\omega}{c} - \mu'(1 + j)3.10^{-5} \frac{\sqrt{\omega/2\pi}}{r_{eq,a}}, \quad (2.5)$$

$$\mu' = \frac{\sqrt{r_{eq,a}^2 + (r_b + e)^2} + r_b + e}{r_{eq,a}}, \quad (2.6)$$

e being the thickness of the wall of cylinder b , fixed at 1 mm for the rest of the article.

The impedance Z_{ts} of the parallel association of cylinders seen from the end of the mouthpiece L_m is written as

$$Z_{ts} = Z_{c,m} \left(\frac{Z_{c,a} + Z_{r,a}j \tan(kL_a)}{Z_{c,a}j \tan(kL_a) + Z_{r,a}} + \frac{Z_{c,b} + Z_{r,b}j \tan(k_b L_b)}{Z_{c,b}j \tan(k_b L_b) + Z_{r,b}} \right)^{-1}, \quad (2.7)$$

where L_i is the length of each cylinder ($i = \{a, b\}$), $Z_{c,i} = \rho c / S_i$ the characteristic impedance of cylinders a and b and $Z_{r,i}$ the radiating impedance (according to [LS48]) on the output of

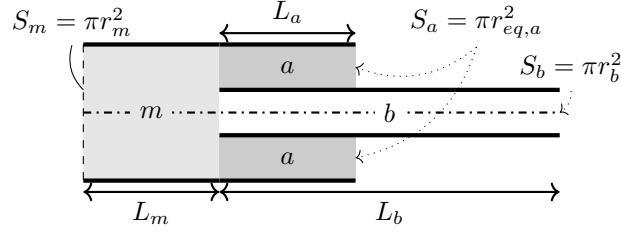


FIGURE 2.3: Schematic layout of the optimized resonator: a bicylindrical resonator. Labels: mouthpiece chamber m , short cylinder a and long cylinder b .

the equivalent unflanged cylinder i such that

$$Z_{r,i} = Z_{c,i} \left(jk_i \Delta \ell_i + \frac{1}{4} (k_i r_i)^2 \right). \quad (2.8)$$

In this expression, the length correction $\Delta \ell_i$ is taken as $0.6133r_i$, because both cylinders are assumed unflanged and the influence of their thickness at output is ignored. The influence of the long cylinder on the radiation of the short one is neglected, which corresponds to a plane-wave approximation. A comparison with a flanged impedance radiation model [Sil+09] for the output of the short cylinder yields almost no difference in the considered frequency range. These impedance models of the bicylindrical resonator are validated by comparison with impedance measurement carried out on a bicylindrical resonator prototype in [Doc+16].

2.3.3 Initial geometrical parameters of the optimization

For the optimization on the 16 notes of the first register of the designed instrument, the 20 varying parameters of the model are

$$X = \{L_{b1}, \dots, L_{b16}, r_b, L_a, r_{eq,a}, L_m\}. \quad (2.9)$$

See figure 2.3 for a schematic representation of the geometry. L_{bn} corresponds to the length of the longest cylinder for the n^{th} fingering. This definition corresponds to a low frequency approximation of the tone holes: each fingering is represented by an effective length, that can be interpreted as the distance from the input of the instrument to the first open tone hole for this fingering. In this approximation, the effect of the other open tone holes and their interactions are ignored. Note that as a refinement, the optimization procedure is conducted taking into account the effect of the tone hole network in appendix 2.7.2. The other parameters $r_b, L_a, r_{eq,a}, L_m$ are geometrical dimensions of the designed instruments that cannot be changed between notes.

At the start of the optimization, the parameters of the bicylindrical resonator are assigned initial values. For a gradient-based optimization procedure like the one used in this work (see section 2.4), the optimized geometry is obtained by adjusting this initial geometry. The initial set of parameters should be chosen in a vicinity of the optimal parameters. Here, based on our knowledge of the characteristics of a bicylindrical resonator, it is possible to suggest an initial geometry that is a coarse approximation of the target, as explained below.

Among the twenty parameters to initialize, two are chosen based on the geometrical dimensions of an alto saxophone: the initial length of the short cylinder L_a^0 is set at 200 mm, which corresponds to the missing length of the top of the conical resonator, and the initial mouthpiece length L_m^0 is set at 10 mm. The length of the long cylinder is based on the first-order approximation of the first resonance frequency for the bicylindrical resonator, taking into account the length corrections due to the radiation impedance. $L_{b,n}^0$ (for all fingerings $n \in \{1, 16\}$) is set so that

$$\frac{c}{2(L_{b,n}^0 + L_a^0 + 2L_m^0 + 0.6133r_{eq,a}^0 + 0.6133r_b^0)} = f_n, \quad (2.10)$$

where f_n is the frequency of the n^{th} note based on the tempered scale. The initial cross sections of the tubes are taken equal, such that their initial equivalent radii are $r_{eq,a}^0 = r_b^0 = 4.3$ mm (see figure 2.3). The total input section of the initial geometry is the same as the one of the measured instrument (see 2.3.1). The choice of this initial geometry is not critical to the convergence of the optimization algorithm, as the robustness test of subsection 2.4.3 shows.

2.4 Optimization procedure

In this section, a set of geometrical parameters for the designed instrument is provided by a numerical fit of its input impedance to a target impedance, using a gradient-based, nonlinear least squares optimization procedure.

2.4.1 Optimization method

The optimization is performed through a gradient-based approach (trust-region reflective algorithm), using the `lsqnonlin` function from the Matlab Optimization toolbox. This function implements non-linear least-square curve fitting with a convenient interface. The algorithm used is trust-region-reflective [BSS87]. This algorithm is chosen because it allows bounds on the parameters: in our case, all parameters must remain positive. It is inherently local, which means it may converge to different local minima depending on initial conditions. Due to the size of the problem, the maximal number of evaluations of the cost function is set at 20000 and the maximal number of iterations at 1000. Stopping criteria are based on thresholds: the algorithm stops under a chosen variation of cost function per step, a chosen step length, a chosen optimality descriptor value or a chosen cost function value. In all the optimization procedures presented here, the algorithm stops because the variation of the cost function value at a given step is too low. This threshold may be lowered (from the default 10^{-6} to 10^{-12}) to give very precise value of the optimal parameters. Section 2.4.3 shows that the choice of initial conditions is not critical for the case at hand, and the optimum found is valid over a large region of the parameter space. The convergence properties of this algorithm also depend on the derivability properties of the cost function [CL96]: the convergence of the algorithm is proven (with some assumptions on the problem) for a twice continuously differentiable cost function. This property is verified by the cost functions used in this work (see 2.4.2 and appendix 2.7.1). In addition, the solver is rather fast: one optimization procedure lasts about 10 seconds on a laptop computer.

2.4.2 Choice of the cost function

In this work, it is decided to use a cost function taking into account the complete input impedance, over a given frequency range. This choice is motivated by the lack of a priori knowledge on the relative importance of specific impedance descriptors, such as resonance frequency and peak height, for an unusual type of resonator. Still, an assumption is made that high-amplitude impedance peaks play a crucial role in the sound production (see for instance [Dal+95]). Therefore, we investigate norms under the form

$$J_p(\omega, X) = \left| |\mathcal{Z}_{des}(\omega, X)| - |\mathcal{Z}_{tar}(\omega)| \right|^p \quad (2.11)$$

where p is an integer, and \mathcal{Z}_{tar} and \mathcal{Z}_{des} are respectively the impedance of the target and designed instruments. The notation X stands for the vector of optimization variables. Another motivation for choosing this type of function is that a straightforward mathematical expression allows for easy demonstration of properties of the cost function, like derivability. For $\mathcal{Z}_{des} \neq 0$ (which is the case for $\omega \neq 0$), these cost functions are at least twice continuously differentiable with respect to the optimization variables (see appendix 2.7.1), which is beneficial to the convergence properties of the optimization algorithm [CL96]. Figure 2.4 displays two cost functions (defined by eq. (2.11)) for $p = 2$ and $p = 5$. It can be seen on this figure that, as expected, the highest exponent gives more importance to the impedance peaks relative to the troughs. Indeed, a high exponent makes the cost function tend towards a infinite norm.

The optimization algorithm minimizes the sum of the cost function values over the whole frequency range for every considered fingerings: the cost function that is effectively minimized

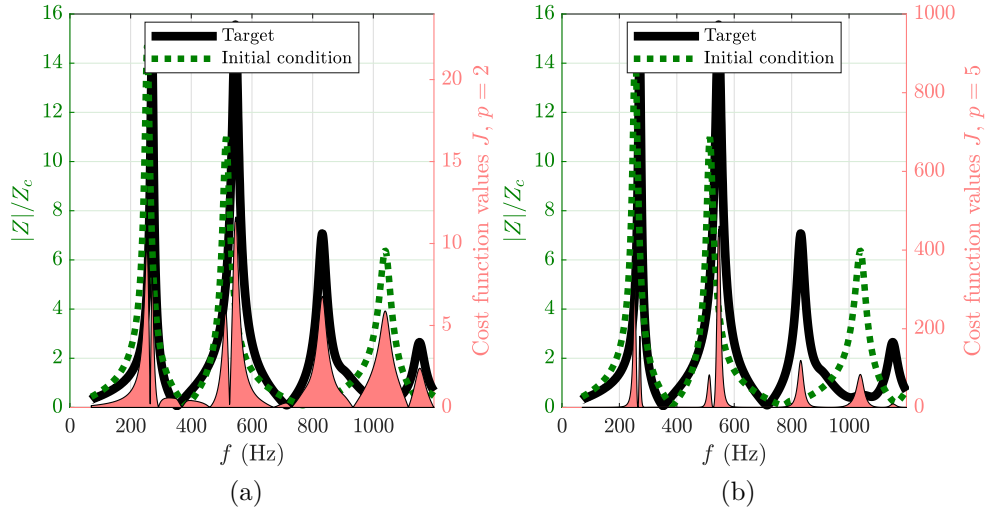


FIGURE 2.4: Comparison before optimization, between the target impedance (solid line) and initial impedance for the bicylindrical resonator (dashed line) for the A fingering. The area is cost function eq. 2.11 between the two impedances: (a) with $p = 2$; (b) with $p = 5$. Note that the magnitude of the cost functions values (right axes) is very different between (a) and (b).

is

$$J_p^{full}(X) = \sum_{n=1}^{16} \sum_{\omega=\omega_{min}}^{\omega_{max}} \left| |Z_{des,n}(\omega, X)| - |Z_{tar,n}(\omega)| \right|^p, \quad (2.12)$$

where $Z_{des,n}$ and $Z_{tar,n}$ are the impedances of the n^{th} fingering, respectively for the bicylindrical resonator and the target instrument, and $\omega_{min} = 2\pi \times 70 \text{ rad.s}^{-1}$ and $\omega_{max} = 2\pi \times 1200 \text{ rad.s}^{-1}$ are the angular frequencies at which the impedances are truncated.

In order to explore the influence of the exponent p on the optimal geometry, several optimization procedures are launched using the `lsqnonlin` function, the only difference being the exponent p of the cost function. Five values of p are tested: 1, 2, 3, 5 and 10. The optimal sets of geometrical parameters are slightly different. As expected, the highest p exponents give a more accurate fit of the impedance peaks with the greatest modulus, at the expense of the lowest. The ratios between the frequency of the impedance peaks are conserved, which could be expected since the bicylindrical resonator has few geometrical degrees of freedom. For the target instrument, the first impedance peak, which corresponds to the first register, is lower than the next for the 12 first fingerings (from low Bb to high Bb). The value $p = 1$ is set aside because of the differentiability issue it entails and because the impedance minima are of lesser importance than the maxima. Therefore, the exponent $p = 2$ is chosen for the cost function so as not to reduce the importance of the first peak in the optimization too much.

2.4.3 Robustness of the optimization procedure

The chosen method is a local optimization procedure. As such, its result depends on the initial conditions, so we seek to further qualify the validity of the optimum, particularly its robustness to a change of initial geometry. As announced in subsection 2.4.2, the exponent in the cost function (eq. 2.11) is $p = 2$ from now on.

As a preliminary study, the optimization procedure is tested using a temporary target: a simulated impedance for a bicylindrical resonator with known geometry (the geometry of the optimum presented in section 2.5). The result of this optimization can then be assessed, by comparing it to the known geometry of the temporary target. A test is performed in which the optimization procedure starts with 50 different initial geometries placed around the geometry of the temporary target. Each parameter is placed at a certain initial distance from its value for the temporary target, yielding a set of extreme initial geometries. The possible distances are $\pm 80 \text{ mm}$ for each length $L_{b,n}$, $\pm 30 \text{ mm}$ for the length of the short cylinder

L_a , $[-2, +5]$ mm for the radius r_b and the equivalent radius $r_{eq,a}$, and $[-10, +30]$ mm for the mouthpiece chamber length L_m . With these extreme initial conditions, the algorithm converges to optimal dimensions within 10^{-3} mm of the dimensions of the temporary target. For this controlled problem, this procedure gives the order of magnitude of the size of basin where the optimized geometry converges to the correct optimum.

We now apply a similar method to studying the main optimization problem: optimizing the bicylindrical resonator to fit a target impedance measured on a saxophone. In this case, 50 initial geometries are generated, each parameter within a certain range of the value assigned to it in section 2.3.3. This range is set as $\pm 10\%$ for each $L_{b,n}$, $\pm 30\%$ for L_a and L_m , $\pm 50\%$ for r_b and $r_{eq,a}$. The size of the range is inspired by the preliminary test with the temporary bicylindrical target and adapted to fill the convergence basin.

With 50 different initial geometries, the optimization converges every time to similar optimal geometries: less than 0.002% of variation for each optimal parameter, except for the optimal mouthpiece lengths L_m which has a 0.01% spread (less than $2 \mu\text{m}$). This larger spread on the parameter L_m can be explained by looking at its influence on the cost function (figure 2.8, detailed below). The dispersion on optimal value is due to the stopping criterion of the optimization procedure and can be reduced by restricting the conditions under which the algorithm stops. One of the conclusion that can be drawn from this result is that even though the optimization procedure is local, the initial geometry is not critical: when it is changed the resulting optimal geometry remains the same.

In order to appreciate the evolution of the cost function, the history plot of its value during the optimization is plotted in figure 2.5. In this figure, the different fingerings are separated (inner sum in equation (2.12)). Most of the improvement is accomplished during the first five iterations. During the rest of the optimization, compromises between fingerings appear. It can be seen that for some fingerings, one of the earlier iterations has a better cost function value than the final iteration. The fit of those fingerings is then degraded to improve the global value of the cost function.

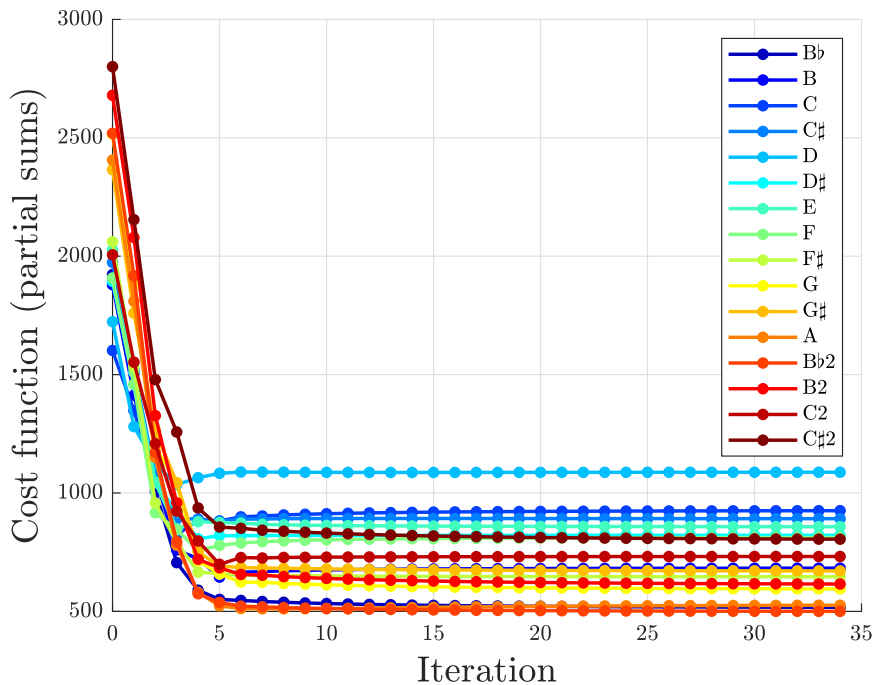


FIGURE 2.5: Evolution of the cost function values during the optimization: partial sums over each fingering (inner sum in Eq. 2.12).

To gain information on the convergence behavior that can be expected from the algorithm, it is useful to study the projection of the cost function around the optimal set of parameters. Here, it is chosen to compute the cost function over the complete frequency range and the

16 fingerings by varying one or two of the parameters around the optimum (all the other parameters are left at their optimal values).

Figure 2.6 shows the variation of the cost function depending on each length of the long cylinder L_b , within 100 mm of the initial lengths. All the other parameters are fixed at their optimal values. The cost function appears locally convex, and the optimum corresponds to the minimum of the cost function in the plotted range for each lengths: choosing any set of initial lengths L_b in a 100 mm range from the optimum appears viable to obtain convergence. Initial points used in the robustness test are between brackets on figure 2.6. They are all in the convexity region according to the represented projections. This is coherent with the algorithm converging every time.

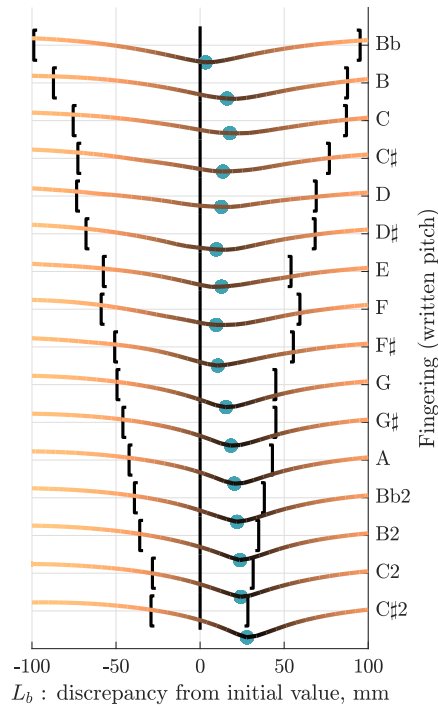


FIGURE 2.6: Variation of the cost function of Eq. (2.12) (solid lines) depending on each parameter L_b , around the optimum obtained for $p = 2$ in Eq. 2.11 (light dot). The displayed cost function values are normalized. All lengths are displayed with respect to the initial values (vertical black line). The brackets stand for the minimal and maximal initial lengths used in the robustness test.

The projection of the cost function space on the parameters r_b and $r_{eq,a}$ is displayed on figure 2.7. It may be noted, on figures 2.7 and 2.8, the initial conditions are not on the surface representing the projection of the cost function around the optimum. This is because all the parameters of the initial conditions differ from their optimal value, whereas the surface is constructed by varying only two parameters. Once again, the cost function appears convex, although there is a slope inversion for very small values of the radius r_b . It can be noted that the configuration where the two radii are equal seems privileged (a local minimum follows the main diagonal on the figure). This is the configuration of the usual cylindrical saxophone approximation [Ben88].

Figure 2.8 displays the projection along the length of the short cylinder L_a and the length of the mouthpiece L_m . There, two features may be noted: there is a slope inversion for lengths of the short cylinder above $L_a = 230$ mm and below $L_a = 50$ mm, and the length of the mouthpiece L_m appears to have small influence on the cost function value. This explains the larger dispersion in optimal mouthpiece lengths: a change in the parameter L_m amounts to a very small modification of the cost function value.

It can be seen on the figures 2.6, 2.7 and 2.8 that the cost function appears continuously differentiable, as announced in subsection 2.4.2. This is one of the necessary hypotheses in the proof of the convergence of the trust-region reflective algorithm of the `lsqnonlin`

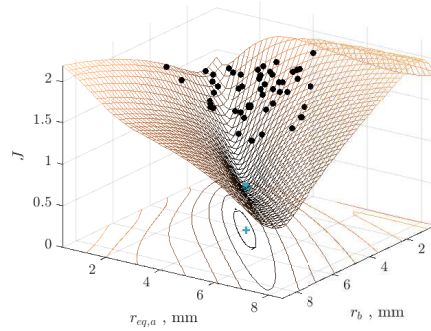


FIGURE 2.7: Variation of the cost function of Eq. (2.12) (mesh) depending on the radii of the two cylinders r_b and $r_{eq,a}$ around the optimum obtained for $p = 2$ in Eq. 2.11 (clear dot). Black dots: initial conditions in the robustness test.

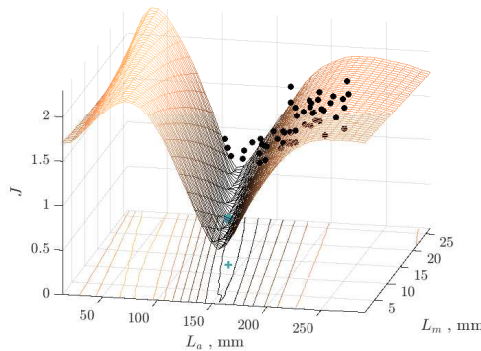


FIGURE 2.8: Variation of the cost function of Eq. (2.12) (mesh) depending on the lengths of the short cylinder L_a and the mouthpiece L_m around the optimum obtained for $p = 2$ in Eq. (2.12) (clear dots). Black dots: initial conditions in the robustness test.

function. Overall, this study on the profile of the cost function near the optimum contributes to justifying the use of a local, gradient-based optimization method.

2.5 Differences between the bicylindrical resonator and the saxophone resonators

The geometrical and acoustical characteristics of the optimized bicylindrical resonator are discussed, in relation with the target instrument. The target saxophone is also compared to the control saxophone, in order to observe the differences that can exist between two saxophones on various impedance descriptors. The differences between the bicylindrical resonator and the target saxophone are then compared with the differences between the two saxophones.

2.5.1 Optimization results

The optimization procedure yields geometrical dimensions for the designed instrument, summarized in table 2.1. Several comments can be made on the proposed values of the geometrical parameters, notably in relation to the dimensions of the target instrument. The length of the instrument L_b corresponds to the approximate length of the bore of an alto saxophone, ranging from 1000 mm to under 300 mm. In the coaxial configuration of the bicylindrical resonator (see figure 2.3) where the short cylinder is around the long cylinder, the total input

radius of the optimized resonator is

$$r_m = \sqrt{S_m/\pi} = \sqrt{\frac{\pi r_{eq,a}^2 + \pi(r_b + e)^2}{\pi}} = 6.6 \text{ mm.} \quad (2.13)$$

It is very close to the input radius of the target instrument, 6.0 mm. However, the optimal mouthpiece is shorter than the mouthpiece added to the impedance measurements of the target instrument (12.5 mm versus 60 mm). This is consistent with the usual formulation of the cylindrical saxophone approximation, where a complete conical instrument including its mouthpiece is replaced by two parallel cylinders without any mouthpiece [DGK00]. This suggests that the mouthpiece chamber should be as short as possible, which is possible in the coaxial configuration (see figure 2.3).

Long cylinder	radius lengths	r_b L_b	4.2 mm [323.6; 1016.9] mm
Short cylinder	Eq. radius length	$r_{eq,a}$ L_a	4.1 mm 138.2 mm
Mouthpiece	length	L_m	12.5 mm

TABLE 2.1: Optimized geometrical parameters of the designed bicylindrical resonator.

For further analysis of the optimum geometry, it is necessary to consider the input impedance of the designed instrument, computed from (2.2). For the sake of clarity, among the total of 16 fingerings in the optimization procedure, 2 fingerings are displayed in figure 2.9. They correspond to the low B and the A in written pitch, or $D_3 = 146.83$ Hz and $C_4 = 261.63$ Hz in concert pitch. Even though the complete display of the impedance holds a quantity of information too large to be interpreted clearly, it is natural to look at it first in this context: the optimization procedure aims to match the impedance curves themselves (see Eq. (2.12)) and does not rely on impedance descriptors. In the frequency range where the optimization is performed, from $\omega_{min}/(2\pi) = 70$ Hz to $\omega_{max}/(2\pi) = 1200$ Hz, the impedance corresponding to the optimum shows good qualitative agreement with the target. The impedance peaks are slightly higher for the target. This phenomenon can be related to the difference in the geometry of the two instruments: the optimized geometry being composed only of cylinders, the losses and radiation mechanisms differ from those encountered in the mainly conical resonator of the target instrument. In terms of phase, the impedance of the designed instrument fits that of the target more accurately at the resonances (i.e. when the phase goes from positive to negative) than at the anti-resonances. The chosen cost function (see 2.4.2) appears to have emphasized the importance of these peaks in the optimization strategy. However, the bicylindrical resonator shows additional resonances in high frequency – between 1200 Hz and 2200 Hz – above the optimized region. This second group of peaks is inherent to the bicylindrical geometry, but it is worth noting that an adequate tone hole network could attenuate these peaks, by introducing a cutoff frequency [MK11]. In terms of global impedance shape, this phenomenon is the major difference with real saxophones. It is possible that these resonances would affect the production of sound.

2.5.2 Comparison between characteristics of the impedances

In order to quantify the difference between the impedance curves, we use a descriptor: the frequency of the first resonance, represented by the first impedance peak, that plays a large role in determining the playing frequency for the first register. In practice, these resonance frequencies are detected as the points where the phase passes from positive to negative. Figure 2.10 compares the frequency of the first impedance peak for every note of the first register of the target instrument and the optimized geometry. The same descriptor is computed for the control saxophone: the differences between the two saxophones serve as references when comparing the optimized geometry to the target. A common reference is taken as the 12-tone tempered scale based on $A_4 = 440$ Hz. There is a shared global tendency along the first register: the discrepancy between the resonance frequencies and the reference frequencies becomes larger towards the top of the register. It appears on the figure that the two saxophones

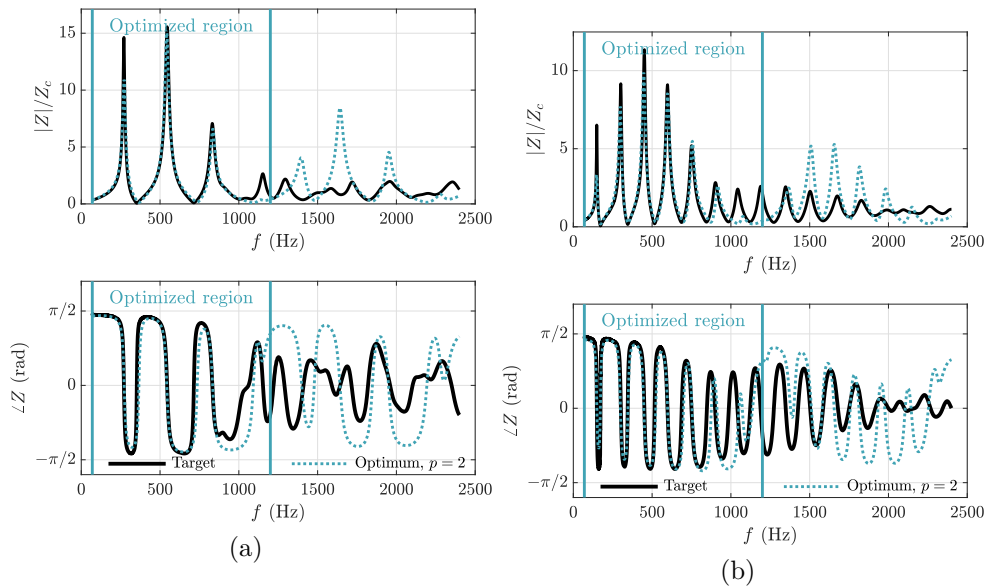


FIGURE 2.9: Comparison between target impedance (solid line) and impedance for the designed bicylindrical geometry (dotted line) for (a) the A fingering and (b) the low B fingering.

(target and control) are closer together than the target and the optimum. There is a good agreement between the optimized resonator and the target for the highest fingerings of the register (high B2, C2 and C \sharp 2). This is possibly due to the smaller number of impedance peaks in the frequency range taken into account for the optimization (70 Hz to 1200 Hz) for the highest fingerings. Indeed, when there is no third or fourth impedance peak in the frequency range, the geometrical degrees of freedom are entirely devoted to fitting the first and second peak. Otherwise, for the rest of the fingerings, a compromise must be made, that leads to a slightly poorer fit of the first peak.

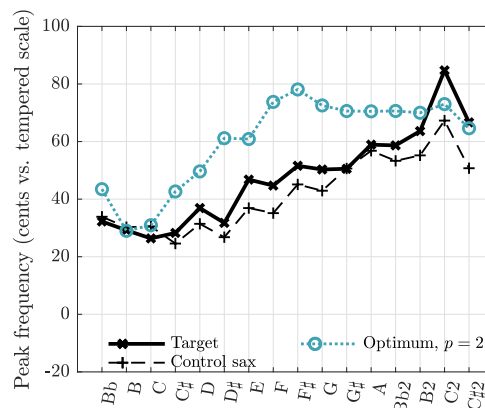


FIGURE 2.10: First impedance peak frequency: target (cross, solid), the control saxophone (plus, dashed) and the optimum for the cost function Eq. (2.12) with $p = 2$ (circle, dotted). Discrepancy in cents versus the corresponding notes in the tempered scale.

Table 2.2 summarizes the difference for the first four peaks by averaging the difference over the studied fingerings. Although it is difficult to draw final conclusions from the mean value of an indicator over several fingerings, it is a simple quantitative way to qualify the global difference between target and optimum, and compare it with the difference between the two saxophones. There, we can see that except for the first peak, the average difference between the target and the optimized resonator is similar to the difference between the two real saxophones (target and control). Looking at this average descriptor only, the bicylindrical

Instrument	Optimum, $p = 2$ vs. Target	Control saxophone vs. Target
Peak 1	+12.5	-5.61
Peak 2	-7.47	-7.96
Peak 3	+5.77	+6.18
Peak 4	+16.5	+12.1

TABLE 2.2: Mean discrepancy to the resonance frequencies of the target, for the optimum ($p = 2$) and the control sax, in cents.

resonator could be assimilated to a saxophone resonator. However, other descriptors point out the limits of the cylindrical saxophone analogy in terms of impedance characteristics.

Another way to study the resonance frequencies of an instrument is to compare them with its first resonance frequency. The ratio between the second and the first resonance frequencies has been shown to influence the tone color and tuning of the instrument [Dal+95]. A descriptor called harmonicity can be defined

$$\text{Harmonicity} = 100 \times \frac{f_2}{2f_1}, \quad (2.14)$$

expressed in percents, where f_1 and f_2 are the first and second resonance frequencies. A global reference when looking at this descriptor is the integer multiples of the first resonance frequency. For instance, if the second resonance corresponds to the octave of the first, the harmonicity for the second peak is worth exactly 100%. Figure 2.11 shows the harmonicity for the second resonance. The trend along the register clearly differs between the optimum and the two saxophones. It can be noted that the bicylindrical resonator has harmonicity closer to 100% for the second peak. This is one of the possible characteristics of a bicylindrical resonator compared to a conical one. Doc [DV15] shows that a few percents of difference on the harmonicity conditions the production of certain regimes, quasi-periodic for example, on a saxophone. The high-frequency resonances that appear with the bicylindrical resonator (see figure 2.9) may also change the sound production behavior. Therefore, the bicylindrical resonator can be expected to play quite differently from a usual saxophone.

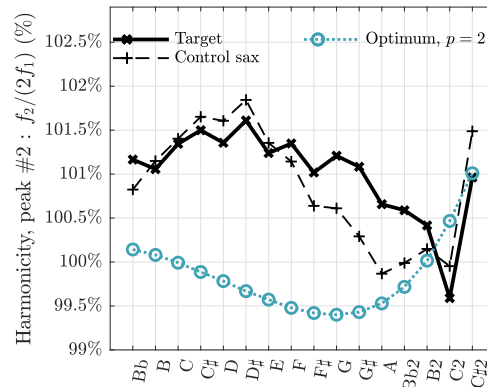


FIGURE 2.11: Harmonicity between the second and first impedance peaks for the target (cross, solid), the control saxophone (plus, dashed) and the optimum for the cost function eq (2.12) with $p = 2$ (circle, dotted).

Another indicator of fundamental difference between a usual saxophone and the bicylindrical resonator studied here is the height of the impedance peaks, defined as the impedance modulus at the resonance frequency. As with the harmonicity, the first resonance for each fingering can be taken as reference to study the other, leading to a height ratio of the form

$$\text{Peak height ratio} = \frac{|Z(f_2)|}{|Z(f_1)|}. \quad (2.15)$$

The value of the ratio is very different for the bicylindrical resonator, as shown in figure 2.12. An analytical and numerical study [Ric+09] shows that this may also lead to differences in the

sound production characteristics, in particular the ease of playing in the first register. The harmonicity and relative amplitude of the first two peaks may also change the timbre of the instrument, notably by affecting the harmonics of the produced sound.

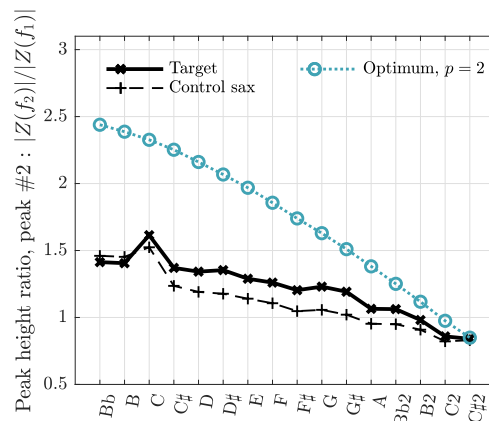


FIGURE 2.12: Ratio between the height (modulus of the impedance) of the second and first impedance peak height for the target (cross, solid), the control saxophone (plus, dashed) and the optimum for the cost function Eq. (2.11) with $p = 2$ (circle, dotted).

2.6 Conclusion

The optimization of the bicylindrical resonator to fit impedance measurements performed on an usual saxophone shows that compromises on the optimum are inevitable, to fit certain impedance peaks or others. We have shown that choosing between cost functions allows to emphasize certain parts of the target impedance and control this compromise. Some practical properties of the type of cost functions chosen in this work, such as derivability and local convexity, have been exhibited. In the present case of optimization on a complete instrument with a rather simple geometrical model, a local, least-square method has proven sufficiently robust to initial conditions. The development of original resonators may particularly benefit from optimization procedures, to yield sensible geometrical parameters as a starting point in the design of completely new instruments. In this context, adding geometrical degrees of freedom – for instance the parameters of a tone hole network – would be a way to provide a more precise fit of the target impedance.

Here, the optimized resonator has characteristic trends along the register that are inherent to its cylindrical nature and differ from those of the (conical) target. On the second, third and fourth resonance frequencies alone, the bicylindrical resonator does not differ from the target more than another saxophone does. However, descriptors like harmonicity and peak height ratio show notable differences. The interpretation that can be made from such results is that the bicylindrical resonator can be tuned to produce the same notes as a saxophone, like an oboe may produce the same notes as a saxophone, but intrinsic characteristics of the resonator differ. This means that, even in low frequency, a reed instrument with bicylindrical resonator should probably be envisioned as a new instrument rather than a pure copy of the existing saxophones, although they share some global acoustic features. The bicylindrical geometry requires further study in terms of sound production, to conclude on its similarity with existing saxophones and its viability as a musical instrument.

Acknowledgements

The authors would like to thank Buffet-Crampon for the loan of the target instrument, and Erik Petersen for his helpful comments. This work has been carried out in the framework of the Labex MEC (ANR-10-LABX-0092) and of the A*MIDEX project (ANR-11-IDEX-0001-02), funded by the Investissements d’Avenir French Government program managed by the French

National Research Agency (ANR). This study has been supported by the French ANR LabCom LIAMFI (ANR-16-LCV2-007-01).

2.7 Appendices

2.7.1 Derivability and derivatives of the cost function

The cost function defined by Eq. (2.11) with $p = 2$ is twice continuously differentiable, as long as $|Z_{des}(\omega, X)| \neq 0$, which is true for strictly positive frequencies. The first order derivative with respect to a given parameter X_i writes

$$\begin{aligned} \frac{\partial J_2(\omega, X)}{\partial X_i} &= 2Z_{des}(\omega, X) \frac{\partial Z_{des}(\omega, X)}{\partial X_i} \\ &\times \frac{|Z_{des}(\omega, X)| - |Z_{tar}(\omega)|}{|Z_{des}(\omega, X)|}, \end{aligned} \quad (2.16)$$

where the derivative of the impedance Z_{des} with respect to each parameter can be computed from Eq. (2.2) and exists for nonzero values of the geometrical parameters. The expression in Eq. (2.16) may be differentiated a second time with respect to a geometrical parameter, leading to a continuous function, still under the assumption $|Z_{des}(\omega, X)| \neq 0$.

2.7.2 Optimization of a bicylindrical resonator with tone holes

As a refinement, the impedance model may be modified to include tone holes. An optimization is performed using this model, with tone holes whose radii are identical and fixed at half the radius of the long cylinder. The number of optimization parameters is the same as in the case without tone holes : 1 total length of the main cylinder, corresponding to the lowest note, 15 positions of tone holes (one for each of the other fingerings), the radius of the longest cylinder r_b , the equivalent radius $r_{eq,a}$ and length L_a of the short cylinder and the mouthpiece length L_m . The optimization is significantly longer (by a factor of 10) due to the added complexity of the impedance model, but the optimum is very close in terms of impedance. Figure 2.13 shows the comparison between the target and the two optimums. The closeness of the impedances may be explained by the fact that the tone-hole network has a high frequency effect. On figure 2.13 the impedances start to differ at about 2000 Hz, which is beyond the frequency range taken into account in the optimization. A calculation of the associated cutoff frequency, as the Helmholtz frequency of the resonators formed by each association of a tone hole and the pipe section underneath, yields results between 3.4 kHz and 5 kHz, well above the frequency of the main impedance peaks.

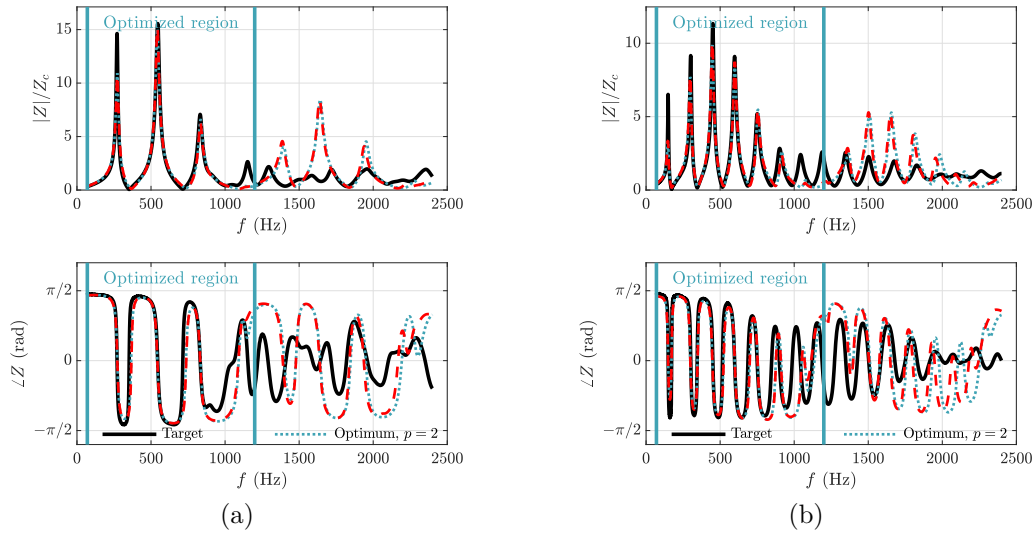


FIGURE 2.13: Comparison between target impedance (solid line), impedance for the optimized bicylindrical resonator without tone holes (blue dotted line) and with toneholes (red dashed line), for (a) the A fingering and (b) the low B fingering.

2.8 Supplementary results

2.8.1 Another optimum

Another 'undesirable' local optimum is located, but it can be eliminated because it corresponds to poorly fitted impedance peaks, as can be seen on figure 2.14.

2.8.2 Another cost function, based on $\log(|Z|)$

An optimization was performed with a cost function based on $\log(|Z|)$, defined as

$$J_{\log} = \sum_{\text{fingerings}} \int_{\omega=\omega_{\min}}^{\omega_{\max}} \log |Z_{\text{tar}}(\omega)| - \log |Z_{\text{des}}(\omega)| d\omega. \quad (2.17)$$

This cost function treats the impedance minima as accurately as the maxima. Consequently, it can be seen on figure 2.15 that the impedance of the optimum has a very satisfactory phase shape : it crosses 0 upwards and downwards at the same frequencies as the target impedance, signaling a good positioning of the minima and the maxima. However, the modulus of the impedance peaks is off, due to the necessary compromise made to improve the fit at the minima. In the case of the saxophone, the first impedance minima have limited importance, since the harmonics of the produced sound are placed around the impedance peaks. Hence, the use of $\log(|Z|)$ in the cost function is not retained in the paper.

2.8.3 Details on comparing the cost functions

Figures 2.16 present a comparison. Since the differences between the optimal parameters are small, the initial value of each parameters is used as a reference. The figures exhibit the diversity of geometrical compromises possible to approximate the target impedance. The geometrical compromise appears clearly when looking at the lengths of the short and long cylinder L_a and L_b (see figure 2.16): when L_a is small (for $p = 1$ for instance), all the L_b are larger, whereas a large L_a (for $p = 10$) corresponds to smaller L_b – a shorter long cylinder. The optimal lengths of the cylinders vary monotonously with p . The tendency is less clear for the other parameters, but their variations are small: both optimal radii stay within 0.3 mm of each other, and the mouthpiece length remains between 0.1 and 14 mm.

Different geometrical compromises appear depending on the choice of the cost function: how do they translate to acoustic characteristics of the instrument? Given the properties of the

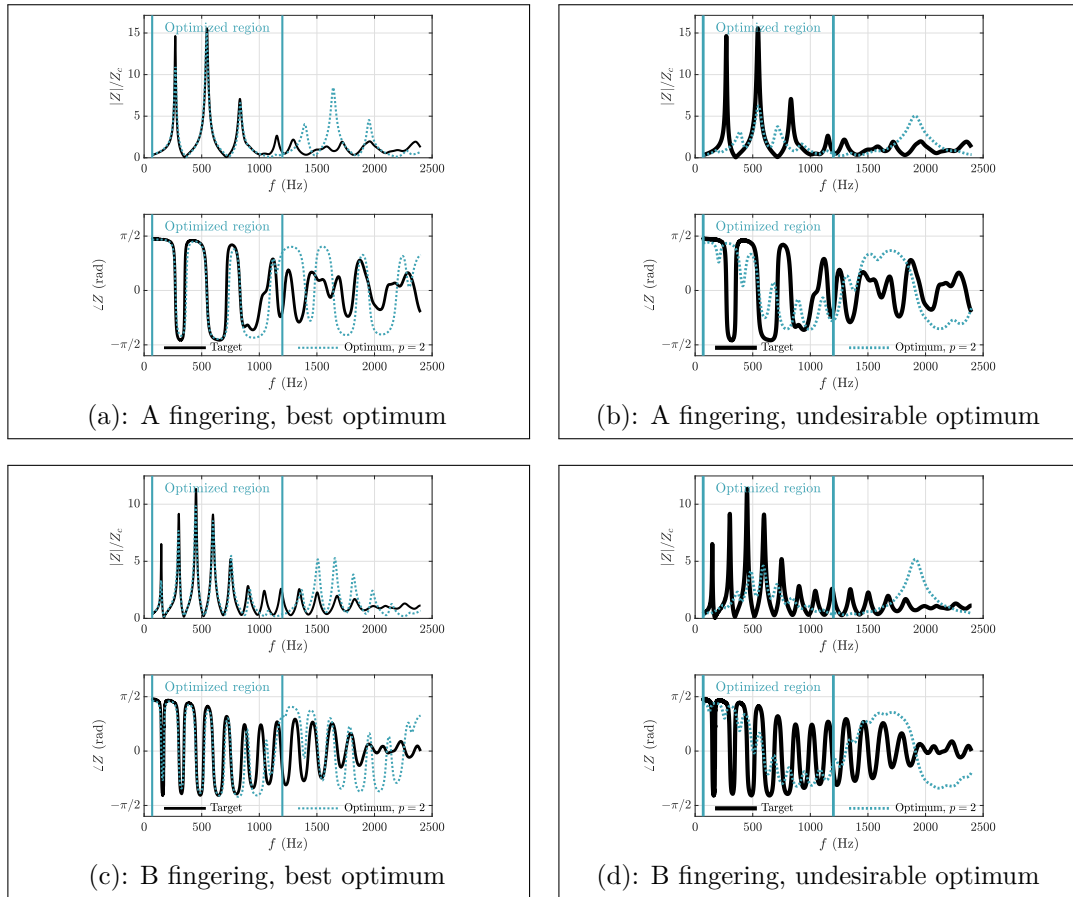


FIGURE 2.14: Comparison of the best optimum with the undesirable optimum: target (solid black) and optimized (dotted blue) input impedance for two fingerings (A and low B).

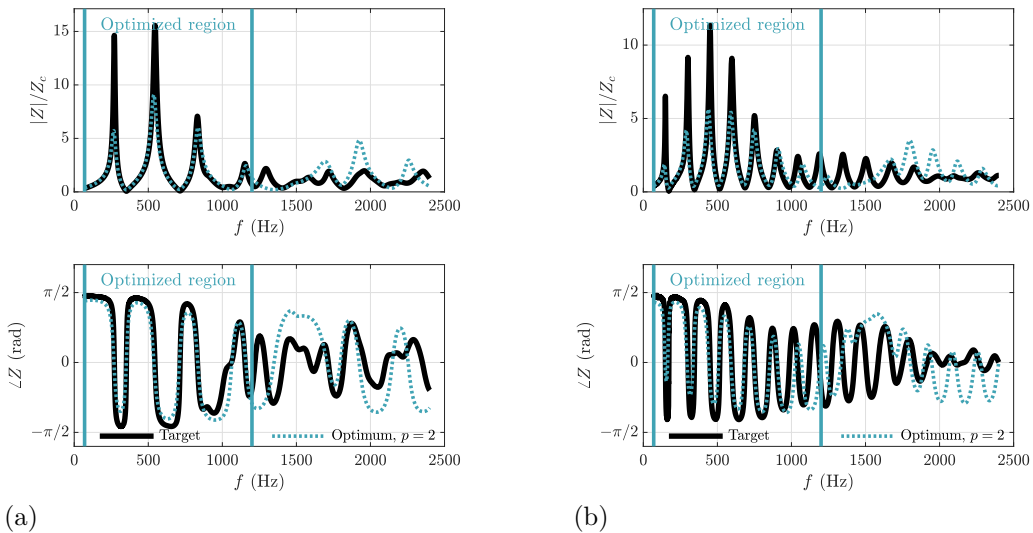


FIGURE 2.15: Comparison between target impedance (solid line), impedance for the optimized bicylindrical resonator with cost function based on $\log(|Z|)$ (blue dotted line), for (a) the A fingering and (b) the low B fingering.

norms, one would expect that a higher p exponent lead to a better fit of the highest impedance peaks. Here, rather than representing the complete impedance in modulus and phase, we use two linear acoustic descriptors: the height of the peaks, and the first resonance frequency. The goal of these descriptors is to assess and compare the optima for each cost function in a

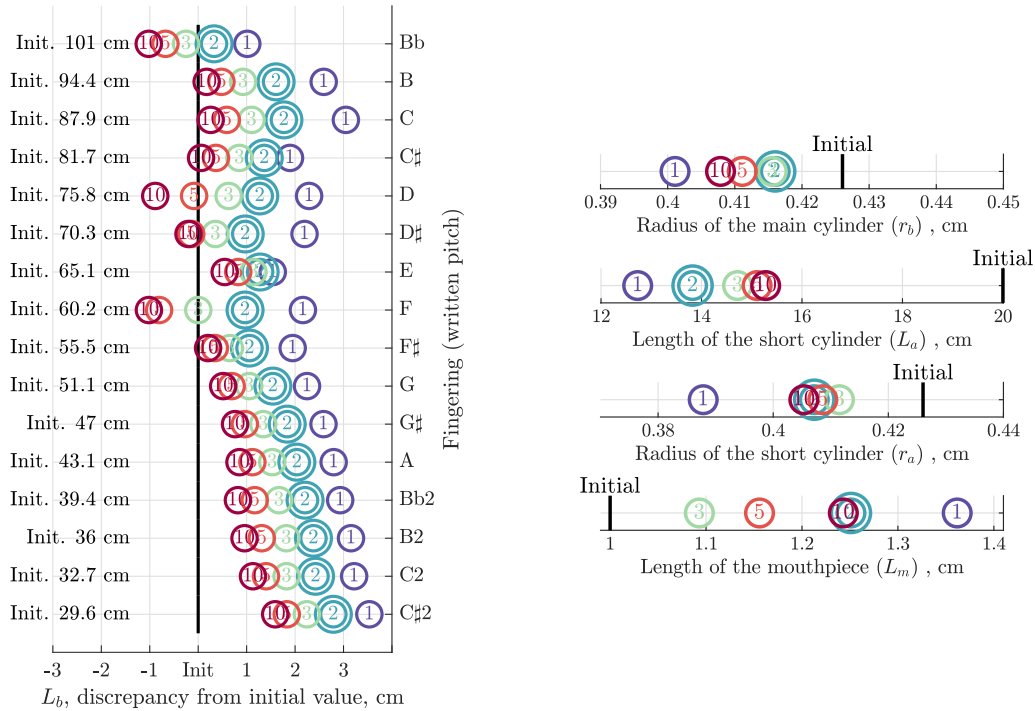


FIGURE 2.16: Optimal parameters: (a) long cylinder length L_b for each fingerings, shown in distance from its initial value in the optimization, (b) radii r_b , $r_{eq,a}$, length of the short cylinder L_a , and length of the mouthpiece L_m , for several values of the exponent p in the cost function: 1, 2, 3, 5 and 10.

quantifiable manner, with a reduced amount of data. Table 2.3 displays the difference between the frequency of the first peak of the target instrument and the optimums for the different values of the exponents. The difference is an average over the 16 studied fingerings, expressed in cents. Here, another compromise appears: the first resonance frequency is better fitted by the highest exponents, and the second is not. For the first resonance frequency, the mean discrepancy varies from -13.6 to -10.8 cents, whereas for the second resonance frequency it rises from 7.14 to 10.2 cents. The magnitude of the variation is approximately the same (3 cents). Even if quantitative interpretation is hard, due to the indicator being an average over several fingerings, the variation can be considered small from a musical perspective (the differentiation threshold of a human ear is around 10 cents [SB31]). Additionally, 10 cents are within the range of adjustment of the frequency that can be made when playing the instrument [Coy+15].

Cost function exponent	Discrepancies in cents	
	Peak 1 (target vs. optimum)	Peak 2 (target vs. optimum)
$p = 1$	-13.6	7.14
$p = 2$	-12.5	7.47
$p = 3$	-10.9	8.27
$p = 5$	-11.4	9.09
$p = 10$	-10.8	10.2

TABLE 2.3: Discrepancy between the resonance frequencies of the target and the optimums, averaged over all the studied fingerings, for various exponents p .

Since the previous indicator dealt with only with the frequencies of the resonances, we now focus on the height of the impedance peaks, which is the magnitude of the impedance at

the resonances. Figure 2.18 shows the amplitude of the first impedance peak for the target impedance and the optimums. A similar compromise can be observed for the height of the impedance peaks. Here, a tendency can be identified: the highest exponents p correspond to optimums for which the first peak is higher and closer to the target impedance. However, it can be seen on figure 2.18 that the height of the second peak in the higher note of the register is poorly fitted by higher exponents.

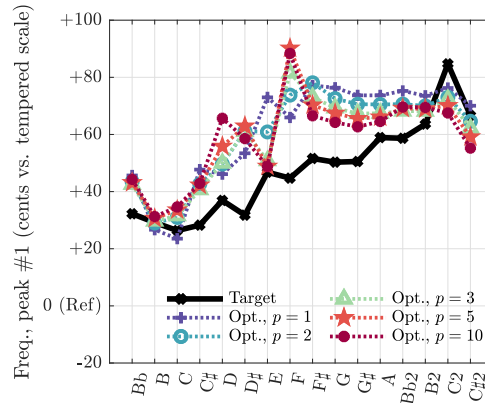


FIGURE 2.17: First impedance peak frequency: discrepancy in cents versus the corresponding notes in the tempered scale.

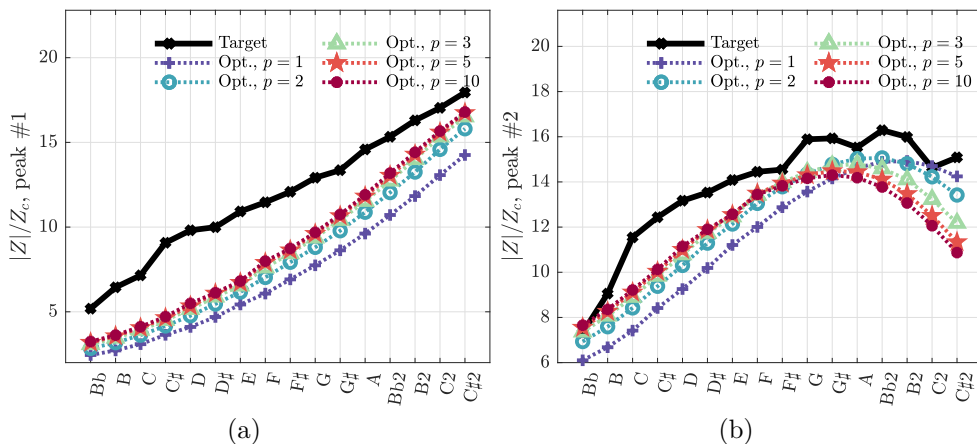


FIGURE 2.18: Height of the impedance peaks: comparison between the target (solid line) and the optimums (dotted lines) for different exponents p of the cost function eq. 2.11. (a) first peak, (b) second peak.

A compromise appears between the fitting of the first and second impedance peaks, depending on the exponent of the cost function. Without further hypotheses on the relative importance of these two impedance peaks in terms of sound production, it is hard to justify privileging one or the other. This is why we chose to study the result of the optimization procedure with the exponent $p = 2$ (euclidean norm).

2.8.4 Preliminary optimization tests: using a noisy bicylindrical impedance as target

As a preliminary verification, the optimization algorithm was launched with a simulated target: the normalized impedance of a bicylindrical resonator of known dimensions, with added gaussian noise of standard deviation $1/2$. Figure 2.20 shows the result of this optimization. The optimized dimensions are within ± 0.3 of the target geometry. When the standard deviation of the added noise increases to 1, the optimized dimensions are within $\pm 2\%$, except for the length of the mouthpiece which is 6% more than the target (less than 1 mm). Even a high

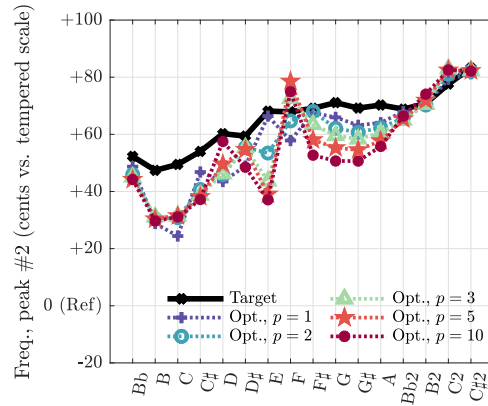


FIGURE 2.19:]

Second impedance peak frequency: discrepancy in cents versus the corresponding notes in the tempered scale.

level of noise added to a simulated impedance has limited impact on the optimized geometry. This result contributes to validating the use of a possibly noisy measured impedance as target.

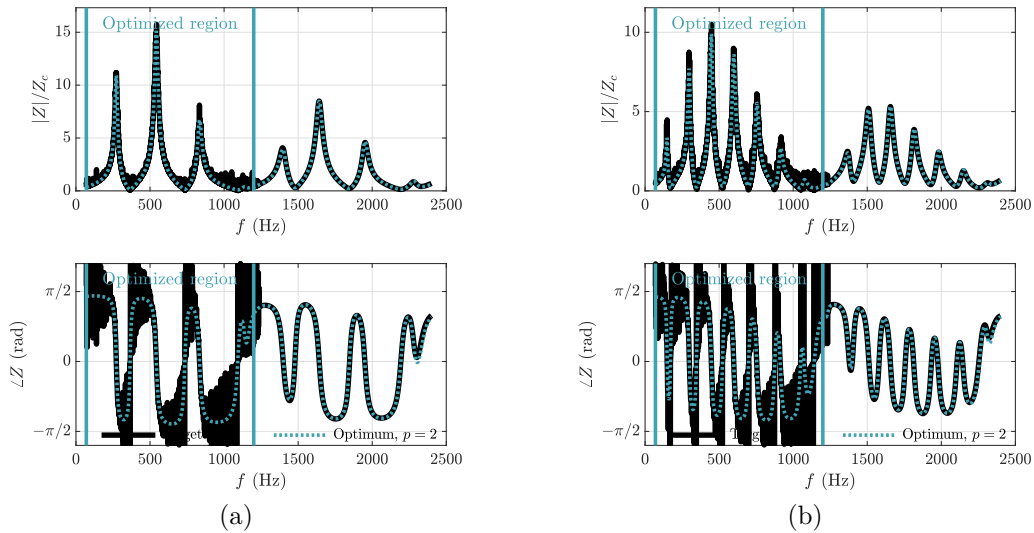


FIGURE 2.20: Comparison between target impedance (solid line) and impedance for the optimized bicylindrical resonator (blue dotted line) when the target is a simulated bicylindrical resonator impedance with added gaussian noise, for (a) the A fingering and (b) the low B fingering.

2.8.5 Global inharmonicity descriptor

A global inharmonicity descriptor such as

$$\text{Global Harmonicity} = \sum_{k=1}^{N_m} |f_k/k - f_1| \quad (2.18)$$

can be studied to check the correspondance between the frequency of all the peaks and a harmonic series. The analysis of such a descriptor like seems hard because it takes into account all the peaks of the impedance, even the smallest. However, when plotted (figure 2.21), this descriptors signals that the bicylindrical resonator has resonances closer to a harmonic series than saxophones, which is coherent with usual assumptions on cylindrical versus conical resonators [DK94].

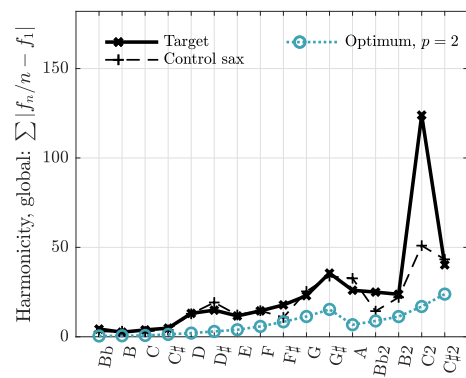


FIGURE 2.21: Global inharmonicity descriptor

Chapter 3

Oscillation regimes and bifurcation diagrams

3.1 Foreword

What sounds can a saxophone make? From an experienced musician's point of view, this question seems to be already answered, and quite thoroughly. The craft of playing the saxophone, or any instrument for that matter, requires the knowledge its sounds, among which the musician picks the desired one. However, the exercise of linking a certain sound to a certain action, as central as it is to the musical craft, is largely undescribed from a scientific perspective.

First, without touching on the musician's action, the mere description of the self-oscillations themselves is incomplete. What are their possible frequencies? During each of them, does the reed channel close completely, or only partially? Such apparently simple questions actually require solid scientific responses based on the observation of the internal variables of an instrument. The subsequent question of linking each of these regimes to the musician requires monitoring the control they apply.

The first route that comes to mind is to use sensors and observe these variables while a musician plays, which we have done using an instrumented mouthpiece. However, obtaining conclusive scientific results from this kind of device is hindered by the lack of repeatability of the experiments, as well as the difficulty of accurately measuring and quantifying their complex actions on the instrument. For these reasons, the role of experimental results due to the instrumented mouthpiece is limited in this work to qualitative proofs of concept. The quantitative bulk of the work is performed using a physical model, where the parameters representing the musician's control are unambiguously defined and each simulation can be finely controlled and reproduced as many times as necessary. The simulations must include the strong nonlinearities necessary to produce self-oscillating regimes, ruling out most analytical methods. This is why we favor numerical tools, where the complete control parameter space can be explored with no restrictions due to the model's nonlinear nature. In that context, the regimes that occur over the virtual control parameter space can be studied and categorized. We apply the procedure to several saxophone fingerings, in order to give a notion of the evolution of the dynamical response of the instrument along its range.

This chapter is organized by the underlying concept of studying the evolution of the oscillating regimes of a saxophone model when varying only one control parameter. Simplifying the question of control to only one parameter allows a much clearer view of the phenomena involved. It is also a natural approach when using continuation tools like MANLAB. Note that the explicit formulation of the model, as implemented into MANLAB, is laid out in appendix A. In most examples, the blowing pressure parameter γ is primarily varied. All wind instruments involve the player acting on the blowing pressure while playing¹. Bifurcation diagrams of wind instruments are classically represented as a function of this parameter in the literature. The first three sections of this chapter concern different portions of the first register, where different types of dynamics have been found to appear, while the fourth proposes a global study on a different, simplified model.

¹This is not the case for the parameter representing the action on the reed, ζ , or the reed parameters q_r and ω_r : in some instruments like bagpipes or crumhorns the player does not touch the reed in playing situation.

Section 3.2 treats the highest fingerings of the first register (typically above A), where only two types of regimes appear: the standard and inverted two-step motions. These regimes are described in [ODK04] involve the reed channel closing once in each period. In the classical approximation, the closure duration depends only on the geometry of the resonator, and thus is fixed for a given fingering, regardless of the control parameters. Section 3.2 refines this result on a numerical model, by showing how the closure duration depends on the blowing pressure. Further more, depending on the control parameter ζ , it shows a continuum of stable regimes with all closure durations exist between the standard and the inverted regime. It is found that for other values of control parameter ζ , both regimes are clearly separated, and hysteresis appears between them. The apparition of hysteresis is marked by a cusp bifurcation, which we find by developing a fold bifurcation tracking on MANLAB.

Section 3.3 presents behaviors specific to the lowest fingerings of the instrument. It uses a combined numerical and experimental approach. First, an instrumented saxophone mouthpiece is used to identify qualitatively different oscillating regimes. Notably, the experimental results show regimes featuring not one but two closures of the reed channel per cycle. These are called double two-step regimes. They are well documented on bowed string instruments and some were already described on the Uilleann pipes, but never on the saxophone. The emergence of these regimes is linked with the value of the blowing pressure parameter, both in experiment and in a complementary simulation using the HBM and ANM on a model. The two methods qualitatively agree: the various regime types appear in the same order as the blowing pressure is increased.

Section 3.4 tackles a rather academic question, in the light of previously evoked studies, by exploring the impact of a common simplification on the bifurcation diagram. This simplification, often applied to woodwind models, consists in leaving the reed move through the mouthpiece lay unimpeded by any contact force. Bifurcation diagrams in both cases are compared and it is found that the ghost reed simplification has limited influence. In particular, at low values of the blowing pressure parameter, the diagrams are very similar. Unsurprisingly, the most noticeable discrepancies occur near the extinction of the oscillations at high blowing pressure, where the reed closure episode is longest.

The last section 3.5 is a simplified extensive parametric study of a model's behavior. The usual model having too many parameters, we use a so-called idealized model, with a single geometrical parameter: the length of the conical resonator. Depending on this length, we describe the emergence of oscillations at the Hopf bifurcation. For the usual saxophone model, this bifurcation is inverse on the lowest fingerings and becomes direct on the highest fingerings of the first register. Time-domain integration shows that longest lengths (i.e. the 'lowest fingerings') exhibit a brutal amplitude jump characteristic of inverse Hopf bifurcations, while short lengths lead to progressive augmentation of the amplitude indicating a direct Hopf bifurcation. Further analysis using the HBM and ANM demonstrates that the Hopf bifurcation is actually always direct, and the amplitude jump is due to two subsequent fold bifurcations. In that, the behavior of the idealized model qualitatively differ from that of the usual model.

3.2 High fingering: continuous variation between standard and inverted two-step regime

Reading guidelines

The following subsections (3.2.1 and 3.2.2) are a reproduction of the extended abstract accepted by the 2020 European Nonlinear Dynamics Conference (ENOC), which was postponed to 2021:

Tom Colinot, Philippe Guillemain, Christophe Vergez and Jean-Baptiste Doc. (2020) "Continuous transition between standard and inverted two-step motion in the saxophone". In: *Proceedings of the 10th European Nonlinear Dynamics Conference*.

For brevity, the summary of the extended abstract is omitted, as well as a very succinct presentation of the saxophone model which is explained in further detail in chapter 1.

3.2.1 Standard and inverted two-step motion

Conical reed instruments produce signals that are classically described as *two-step* motions [ODK04], in analogous manner with stick-slip motions on bowed string instruments: one step has the reed channel closed, null acoustic flow, and a low acoustic pressure in the mouthpiece, and the second step corresponds to an open reed channel, nonzero acoustic flow and high acoustic pressure in the mouthpiece. If the reed closure episode is shorter than half the period, the regime is called standard. If it is longer the regime is called inverted. Figure 3.1 shows periodic pressure signals obtained by the harmonic balance method, corresponding to standard and inverted regime. Figure 3.1 (middle) represents the evolution of the duration ratio of the closure episode over the oscillation period, depending on the blowing pressure parameter γ , for a small reed opening parameter $\zeta = 0.4$. Two regions appear : low γ leads to standard motion while high γ leads to inverted motion. The closure duration is not constant inside either region, although in the standard region it is around the value $x_1/(\ell + x_1)$, where x_1 is the length of the missing apex of the conical resonator and ℓ is the length of the resonator until the first open tonehole, that is the first approximation deduced from the conical geometry [CK08].

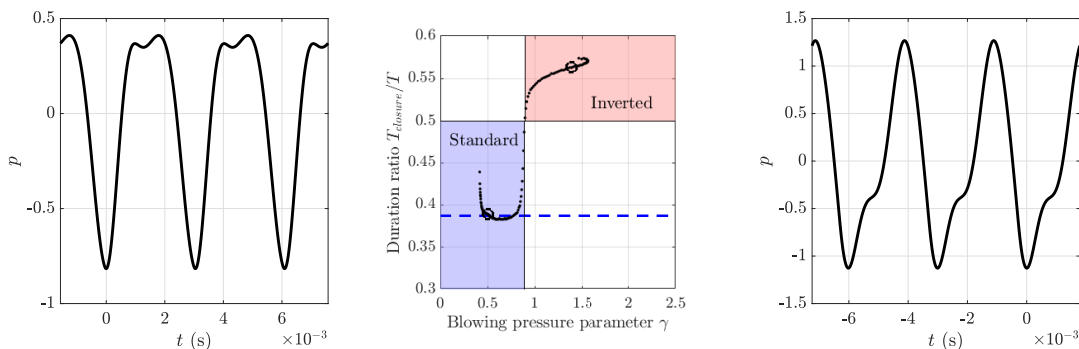


FIGURE 3.1: Left and right : pressure signals corresponding to standard and inverted two-step motions. Center : ratio of the closure episode duration over the period depending on the blowing pressure parameter γ . Circle markers correspond to the waveforms plotted to the sides. The dashed blue line marks the analytical Helmholtz ratio $x_1/(\ell + x_1)$. Here, the reed opening parameter is $\zeta = 0.4$.

3.2.2 Continuous transition between standard and inverted motion in a saxophone model

Using continuation (Asymptotic Numerical Method) in addition to harmonic balance [CV09], it is possible to find branches of periodic solutions of the model, depending on a parameter such as the blowing pressure parameter γ . Figure 3.2 presents the L^2 -norm of the acoustic pressure p inside the mouthpiece depending on the blowing pressure parameter γ for two

values of the reed opening parameter: $\zeta = 0.4$ and $\zeta = 0.7$. For the low ζ value it can be seen that standard and inverted two-step motions are continuously connected by stable regimes, indicated by solid lines. However, for the high ζ value, an unstable portion of the branch separates standard and inverted motion. This unstable portion appears between two Fold bifurcations. A cusp bifurcation of periodic orbits is anticipated where the two Fold bifurcations appear, at the threshold between the behaviors of continuous and discontinuous transition. In the discontinuous transition case (large ζ), standard and inverted regimes can coexist: they are both stable for certain given control parameter couples (γ, ζ) .

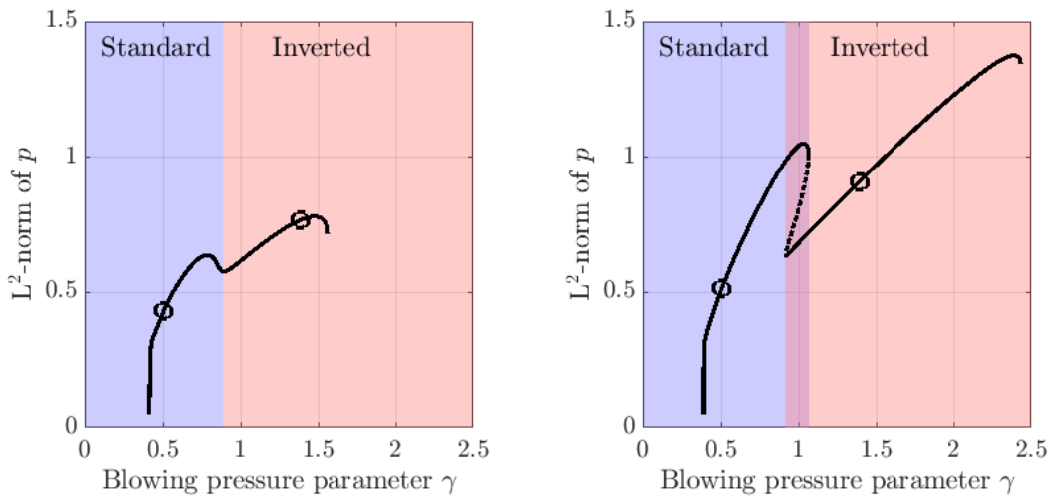


FIGURE 3.2: Bifurcation diagrams of the L^2 -norm of the acoustic pressure p depending on the blowing pressure parameter γ for reed opening parameters $\zeta = 0.4$ (left) and $\zeta = 0.7$ (right). Solid lines indicate stable regimes, dotted lines indicate unstable regimes. Circle markers correspond to the waveforms plotted in Fig 3.1. The purple patch on the right figure signals a region where both regimes are stable.

Saxophone signals archetypes like standard and inverted two-step motion appear valid near the low and high oscillation threshold. In the branch of periodic solutions between these thresholds, all duration ratios between closure and opening episodes can be found, at sufficiently small values of the reed opening parameter ζ . The analysis of the bifurcation diagram, obtained by Asymptotic-Numerical Method and Harmonic Balance Method allows to understand the seemingly contradictory observations of continuous or discontinuous transitions between direct and inverse Helmholtz regimes when the pressure in the mouth is modified.

3.2.3 Fold continuation

The two types of behaviors exhibited in figure 3.2 can be characterized by the presence or absence of the two fold bifurcations. Finding the limit value of control parameter ζ above which standard and inverted two-step regimes can coexist amounts to finding the point where both fold bifurcations disappear. This point is called a cusp bifurcation (see subsection 1.2.2.3). Rather than computing bifurcation diagrams for multiple values of ζ , which can be long and imprecise, an elegant way to find the cusp is to describe the location of the fold bifurcations directly. To this end, we use MANLAB to implement fold bifurcation continuation.

3.2.3.1 Tracking folds: the augmented system

Bifurcation continuation requires characterizing the desired bifurcation point, and imposing these characteristics as supplementary equations. Associated with the original equations of the model, which still need to be verified, they form the so-called *augmented system*. Here, we know that a fold bifurcation is characterized by a null eigenvalue of the Jacobian matrix, as mentioned in subsection 1.2.2.3. Thus, at the coordinates \mathbf{X}_F of the fold, there exists an eigenvector \mathbf{p}_F of the linearized system such that

$$J_{\mathbf{X}_F} \mathbf{p}_F = \mathbf{0}, \quad (3.1)$$

where $J_{\mathbf{X}_F}$ is the Jacobian matrix of the system computed at point \mathbf{X}_F . There is as many unknowns (components of \mathbf{p}_F) as there are equations in 3.1. Now recall that, since the bifurcation continuation applies to the two-dimensional plane (γ, ζ) , the parameter ζ must be allowed to vary. This parameter then constitutes a supplementary unknown, which did not exist in the original system. Therefore, an equation must be added so that the problem is not underdetermined. This supplementary equation, as proposed in [MS80; Bey+02], is a scaling of the eigenvector \mathbf{p}_F , for instance

$$\mathbf{p}_F^t \mathbf{p}_F = 1. \quad (3.2)$$

The standard augmented system comprises the original system Eq. (1.75) as well as Eqs. (3.1) and (3.2), ensuring that the system encounters a fold bifurcation.

In the numerical implementation of the fold continuation, the minimally augmented system does not suffice. During the trial stages of the methods, it was found that the ANM did not function correctly on the minimally augmented system, failing to follow the bifurcation. To make the system less stiff, an unknown is added to the system, and a corresponding equation. Following the idea of [Bey+02] concerning fold bifurcations of periodic orbits, we introduce a second supplementary unknown κ , which represents the critical eigenvalue of the system. This eigenvalue κ is supposed to stay at 0, so we introduce the equation

$$\kappa^2 = 0. \quad (3.3)$$

Then κ is introduced as an eigenvalue in equation (3.1)

$$J_{\mathbf{X}_F} \mathbf{p}_F = \kappa \mathbf{p}_F. \quad (3.4)$$

Since κ must be very close to 0, as ensured by Eq. (3.3), the new equation (3.4) is functionnally equivalent to Eq. (3.1).

Additionally, Eq. (3.2) is modified, by adding κ^2 as a desingularization term. In addition, for merely practical implementation reasons, the norm of \mathbf{p}_F is fixed to that of the initial critical eigenvector in the continuation \mathbf{p}_{F0} (rather than 1). The modified scaling equation is

$$\mathbf{p}_F^t \mathbf{p}_F = \mathbf{p}_{F0}^t \mathbf{p}_{F0} - \kappa^2. \quad (3.5)$$

Again, recall that κ is kept very small by Eq. (3.3), so the last equation ensures that norm of \mathbf{p}_F is almost equal to that of \mathbf{p}_{F0} .

The differential version of the augmented system is then Eqs. (1.75), (3.4), (3.5), (3.3). The unknowns of this augmented system are the variables of the original system \mathbf{X}_F , the critical eigenvector \mathbf{p}_F associated to the critical eigen value κ and the two control parameters

(γ, ζ) . Note that this increase in dimension of the system increases the computation time. However, as the following examples demonstrate, bifurcation continuation condenses a lot of relevant information that are scattered across a very large number of standard bifurcation diagrams.

3.2.3.2 Toy problem: Dessi's 5th order Van der Pol oscillator

As a benchmark test for the fold continuation tool, we use a minimal system for which the location of fold bifurcations can be computed analytically: the single degree of freedom Van der Pol oscillator described in [DMM04]. The governing equation of this system is

$$\ddot{x} + (\mu + \sigma(x^2 + x^2) + \nu(\dot{x}^2 + x^2)^2) \dot{x} + x = 0, \quad (3.6)$$

where μ , σ and ν are parameters. The amplitude of the oscillating solution for this system is obtained by replacing x by $X \cos(t + \phi)$ in Eq. (3.6), which corresponds to applying the HBM with only one harmonic. The obtained amplitude is

$$X = \sqrt{\frac{-\sigma \pm \sqrt{\sigma^2 - 4\mu\nu}}{2\nu}}. \quad (3.7)$$

Only the real amplitudes are conserved. Note that this is possibly multivalued (due to the \pm sign), which is expected in the case of a fold bifurcation (see Figure 3.3).

First, MANLAB is used to do standard continuation along parameter μ of the system, with $\sigma = -0.5$ and $\nu = 0.5$. After quadratic recast, the bifurcation diagram of figure 3.3 is computed with $H = 20$ harmonics. Figure 3.3 superimposes the analytical L^2 norm deduced from 3.7. The agreement between analytical and numerical results is due to the amplitude of the harmonics of the solution being very small: the oscillations are very close to a sinus. The coordinates of the fold bifurcation (highlighted on the figure) and the corresponding critical eigenvector are extracted from the original system. They serve as a starting point in the fold continuation procedure.

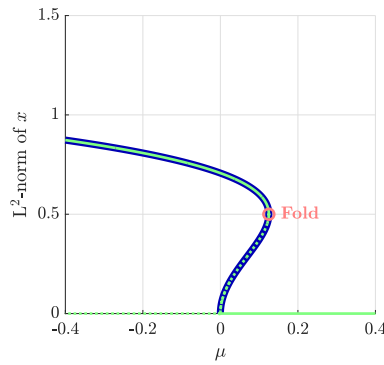


FIGURE 3.3: Amplitude of the solution of Eq. (3.6) depending on parameters μ , for $\nu = 0.5$ and $\sigma = -0.5$, in blue (analytical, Eq. (3.7)). In green, bifurcation diagram obtained using MANLAB with $H = 20$. The fold bifurcation given by Eq. (3.8) is highlighted in red.

In order to assess the performance of the fold continuation tool, the analytical location of the folds is computed. The value of the parameter μ corresponding to the fold bifurcations is

$$\mu_F = \frac{\sigma^2}{4\nu}. \quad (3.8)$$

Figure 3.4 shows the amplitude of solutions as a surface over the plane (μ, σ) for a fixed $\nu = 0.5$. The fold bifurcations given by Eq. (3.8) are highlighted as a black line, projected on the plane to give the location of the fold in (μ, σ) . This location is the parabola

$$\mu_F = \frac{\sigma^2}{2}, \quad (3.9)$$

using the numerical value $\nu = 0.5$ in Eq (3.8). The result of the fold continuation using MANLAB, with $H = 20$ harmonics, is also displayed, and corresponds to the analytically predicted location of the folds. The equations of the extended system are composed of the quadratic recast of Eq. (3.6), and the extensions (3.4), (3.3) and (3.5). There is a Hopf bifurcation at $\mu = 0$ for all the values of σ . At $\sigma = 0$, the Fold bifurcation collides with the Hopf bifurcation and disappears. This phenomenon is called the Bautin bifurcation [Kuz95]. Unpredictably, the fold continuation procedure goes beyond the Bautin bifurcation and follows the Hopf bifurcation. This phenomenon is due to the fact that equilibria can be seen as degenerate periodic solutions and thus computed with HBM (with all harmonics at amplitude 0). Therefore, in this context, the Hopf bifurcation which connects periodic orbits to an equilibrium resembles a pitchfork bifurcation. As stated in section 1.2.2.3, the pitchfork bifurcation has a null eigenvalue, like a fold, and therefore can be followed in the same fashion. This flexible behavior is not judged undesirable, as we explain in subsection 3.2.3.3. Consequently, no attempt is made to prevent it.

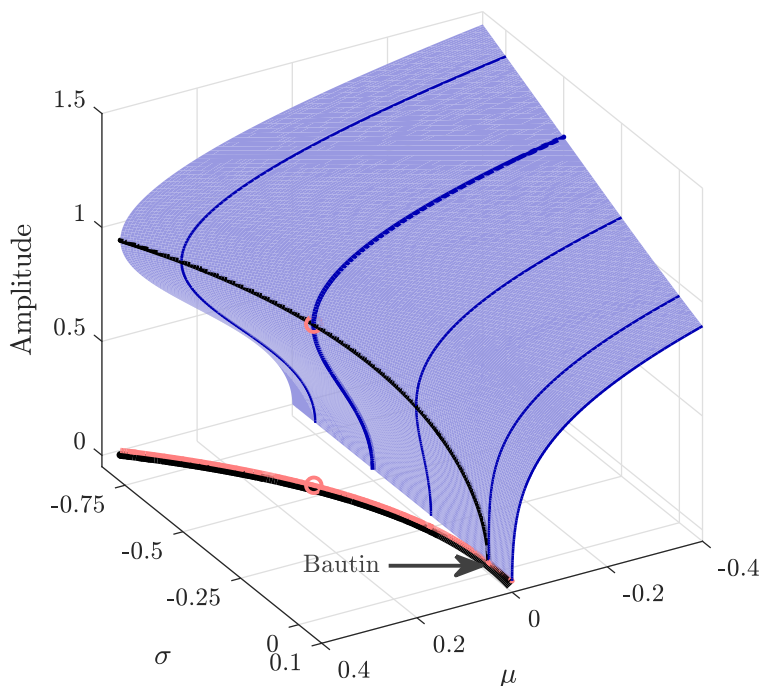


FIGURE 3.4: Amplitude of the solution of Eq. (3.6) depending on parameters μ and σ , for $\nu = 0.5$, in blue (analytical). The thickest blue line corresponds to figure 3.3. In black is the analytical location of the fold bifurcations and its projection on the parameter plane (μ, σ) , from Eq. (3.9), and in red is the location of the fold bifurcations obtained by fold continuation, using MANLAB. The starting fold bifurcation is denoted by a red circle. The point marked Bautin corresponds to the Bautin bifurcation where the branch of folds collides with the Hopf bifurcation.

3.2.3.3 Application to the saxophone

3.2.3.3.a Cusp: the limit of hysteretic behavior

According to the results of section 3.2.2, the saxophone model presents two distinct fold bifurcations in its bifurcation diagram with respect to γ . These bifurcations are not always present, as there is a value of ζ where they collide and disappear in a cusp bifurcation (see section 1.2.2.3). In order to find this limit value of ζ , separating the two behaviors of figure 3.2, the fold continuation procedure is applied to the saxophone model with phantom reed on the high C fingering. First, using standard continuation along the blowing pressure parameter γ for a fixed value of ζ , a fold is found and set as the starting point for fold continuation. The result of the fold continuation is displayed in figure 3.5, verified by the folds extracted from standard bifurcation diagrams in γ . On this diagram, the fold curves collide, making the

cusplike bifurcation appears at $\zeta = 0.48$ and $\gamma = 1.05$, at the tip of the typically expected caustic curve. The fold continuation, shown by the red line in the plane (γ, ζ) , provides a direct and precise location of the cusp, while multiple diagrams with a single continuation parameter are required to estimate it. The value $\zeta = 0.48$ separates, for this fingering of the studied saxophone, the continuous and hysteretic transition between standard and inverted two-step regimes. The size of the hysteresis zone increases with ζ as the branches of the caustic part, as can be observed in figure 3.5. Note that Figure 3.5 shows all the blue curves due to standard continuation, as a pedagogical illustration and a visual verification tool, but only one of them is necessary to find a fold and compute directly the location of all fold bifurcations.

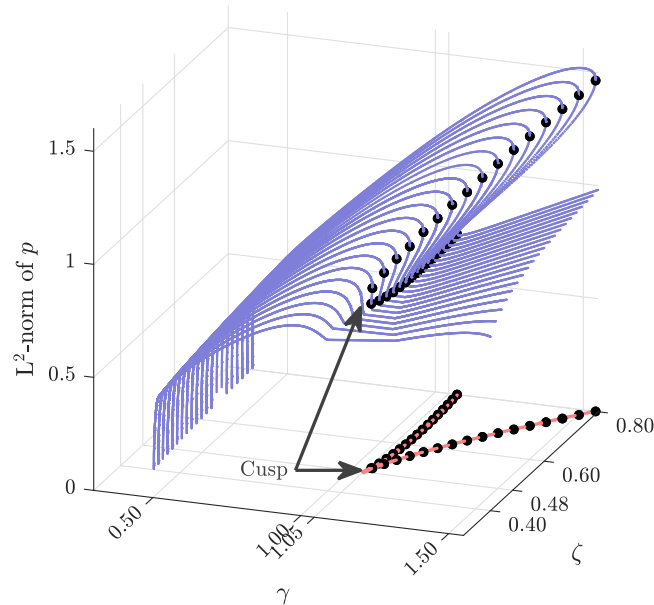


FIGURE 3.5: L^2 -norm of the solution the saxophone model depending on parameters γ and ζ in blue (standard continuation). The location of the fold bifurcations and its projection on the parameter plane (γ, ζ) is in black dots, to be compared to the location of the fold bifurcation obtained by fold continuation in red.

3.2.3.3.b Outer folds: the limits of existence of oscillations

The next example concerns the same fingering, but the fold continuation starts from the fold bifurcation with the highest γ . This fold bifurcation is found using standard one-parameter continuation with respect to γ , as shown in Figure 3.6. This bifurcation is important because beyond it, only the equilibrium is stable, while before there is still a possibility for an oscillating regime to exist.

Figure 3.7 shows the result of the fold continuation, overlaid with standard bifurcation diagrams. Some bifurcation diagrams were computed using ζ as a continuation parameter for a finer view of the oscillation thresholds at low ζ .

Figure 3.7 can be read starting from the highest γ values. The fold continuation – red branch in plane (γ, ζ) – follows the location of folds, until $\gamma \simeq 1$ and $\zeta \simeq 0.12$. At this point, the fold collides with the Hopf bifurcation and disappears, forming a Bautin bifurcation that can be seen in the zoomed figure 3.7 (d). This Bautin bifurcation is the point at which the Hopf bifurcation changes from direct to inverse, as discussed in [GGL97; Dal+05; Sil+08; TK15] for clarinet-like instruments and [DGK00; Ric+09] for saxophone-like instruments. As seen previously with figure 3.4, the fold continuation then follows the Hopf bifurcations of the system, until another Bautin bifurcation, depicted in figure 3.7 (c). This second Bautin bifurcation appears at $\gamma \simeq 0.38$ and $\zeta \simeq 1$, and separates two very characteristic behaviors. Below the Bautin bifurcation, oscillations emerge through a direct Hopf bifurcation, which means stable oscillations can exist around the threshold with arbitrary low amplitude. This is

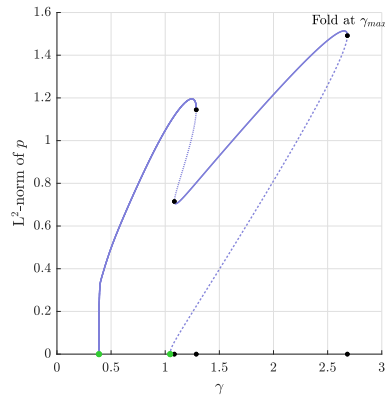


FIGURE 3.6: L^2 -norm of the solution the saxophone model depending on parameters γ in blue (standard continuation). The location of the fold bifurcations and its projection on the γ axis is in black dots, with the fold at the highest γ marked "Fold at γ_{max} ".

often interpreted in musical terms as the possibility to play as *pianissimo* as desired. On the contrary, above this Bautin bifurcation, the Hopf bifurcation is inverse, which means there is a strictly positive lower bound on the amplitude of the stable oscillations around the apparition

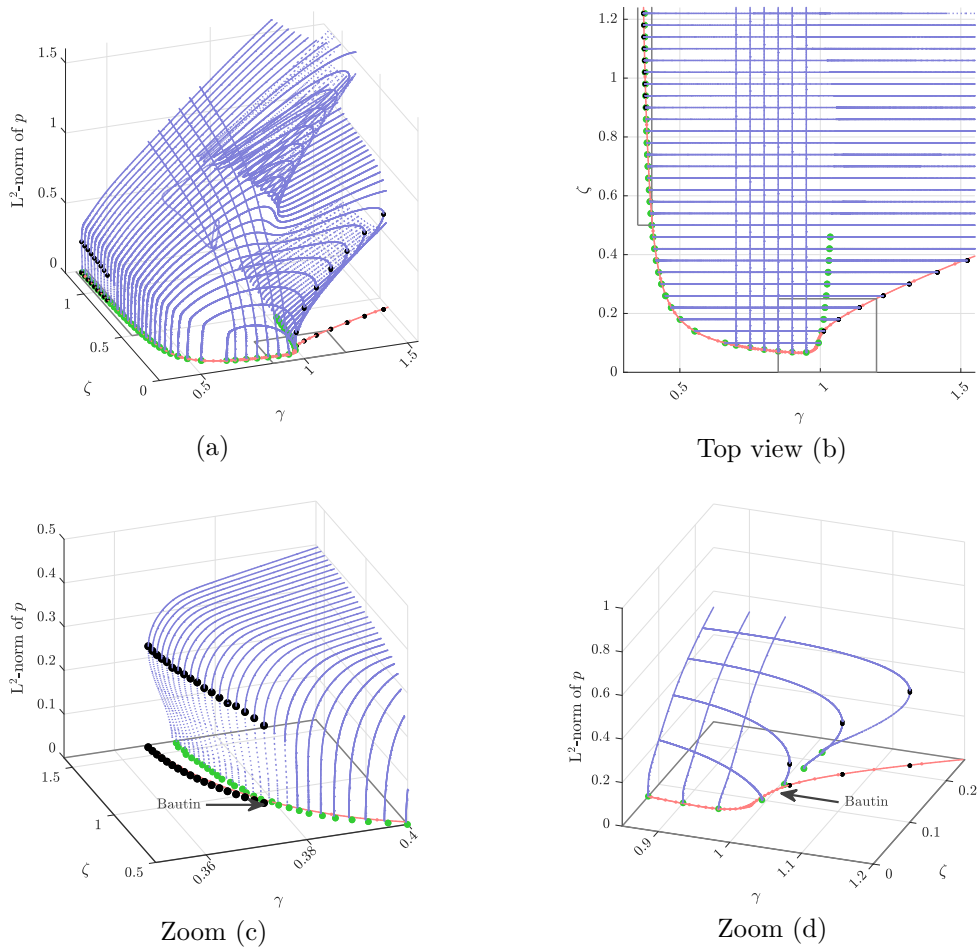


FIGURE 3.7: Bifurcation diagrams. Standard continuation with respect to γ or ζ in blue, with fold bifurcations and their projection on the plane (γ, ζ) in black dots, and Hopf bifurcations in green dots. Fold continuation in red. Gray rectangles in (a) and (b) correspond to zooms (c) and (d).

threshold: some *pianissimo* sounds may be impossible to obtain using these values of ζ . In the case of an inverse Hopf bifurcation near the apparition of the oscillation, the lowest value of γ leading to oscillations, associated with the lowest possible amplitude of these oscillations, is given by the fold bifurcation [GMV19b].

More generally, this whole application of the fold continuation procedure actually outlines the limit values of γ and ζ that can lead to oscillations, as the top view in figure 3.7 (b) shows: all the oscillating solutions in blue are contained in the zone delimited by the fold continuation. It is in this regard that being able to pass Bautin bifurcations to follow Hopf bifurcations instead of folds is not deemed undesirable: the obtained region has a clear meaning. Note that describing such region, outside of which oscillations cannot appear, could have direct applications in describing the ease of production of regimes on the instrument.

Reading guidelines

The following section (3.3) is an *in extenso* reproduction of the article (except title and abstract) published as:

Colinot, Tom, Philippe Guillemain, Christophe Vergez, Jean-Baptiste Doc, and Patrick Sanchez (2020). "Multiple two-step oscillation regimes produced by the alto saxophone".

In: *The Journal of the Acoustical Society of America*, 147(4), pp. 2406-2413.

Note that some paragraphs in this article are explained in further detail in chapter 1, namely those presenting the instrumented mouthpiece 3.3.2.1, the Harmonic Balance Method 3.3.3.2 and the physical model of saxophone 3.3.3.1.

3.3 Low fingering: double and inverted double two-step regimes. Illustration with HBM and instrumented mouthpiece

3.3.1 Introduction

Various oscillating regimes, defined as the pattern of oscillations both mechanical and acoustical that correspond to the production of a periodic sound, have been observed and classified on bowed string instruments [Sch73]. The strongly non-linear friction law between bow and string leads to an oscillation pattern known as stick-slip motion, where the string sticks to the bow for a part of the period and then slips for another part of the period. The stick-slip phases may occur twice per period, leading to the so-called "double stick-slip" motion.

Reed conical instruments have often been compared to bowed strings, by virtue of the cylindrical saxophone approximation, which replaces the conical resonator with two parallel cylinders [ODK04] because their impedance is similar in low frequency. In reed instruments, the analogous motion to stick-slip is called two-step motion [OKD05]. It consists in a beating reed regime, where the reed channel is closed for part of the period, and open for the rest of the period. The most common case, where the reed closure episode is shorter than half the period, is called standard two-step motion. Otherwise, the regime is called inverted. Standard and inverted two-step motions have been observed experimentally on a saxophone and predicted analytically on a cylindrical equivalent [DGK00]. Oscillating regimes showing more than one closure of the reed per period were never studied on the saxophone to our knowledge. They have been observed on a double reed instrument, the Irish Uilleann pipes [DLV14]. To observe the signals produced by a wind instrument in playing situation, with a musician, an instrumented mouthpiece fitted with a reed displacement and pressure sensors can be used. Instrumented mouthpieces can help explain features of the produced sound, for instance spectral content on a saxophone [Gui+10] or transient descriptors on a clarinet [PVHC18]. They also provide a means to estimate some of the parameters of a physical model based on the dynamical behavior of the system [MA+16].

This paper reports experiments in playing conditions exhibiting classic standard and inverted regimes, as well as double two-step motions, where the reed channel closes twice per period. To complete the study, we show that a simple saxophone model based on the input impedance of the saxophone used for the experiment is able to reproduce these double two-step regimes. The Harmonic Balance Method associated with continuation (Asymptotic Numerical Method) is used to obtain periodic signals corresponding to several control parameter combinations. The numerical simulations, in addition to experimental data, provide insights about the possible ways of transition between single and double two-step regimes, as well as the second register of the instrument. We also show that similar behavior occurs for neighboring fingerings and control parameter values. Describing and categorizing the oscillation regimes of the saxophone, as well as the musician's actions needed to obtain them, is among the first steps towards objective characterization of the ease of playing of an instrument.

3.3.2 Experimental observation of double two-step motions on a saxophone

3.3.2.1 Experimental apparatus

An instrumented mouthpiece is used to monitor the blowing pressure, the pressure inside the mouthpiece, and the position of the reed. It is shown in figure 3.8. It consists in a modified saxophone mouthpiece (Buffet-Crampon) incorporating two pressure probes: one going into the mouth of the musician and one into the mouthpiece, as well as an optical sensor (Everlight ITR8307) measuring the displacement of the reed. The pressure probe tubes are connected to a Honeywell TSCDRRN005PDUCV pressure sensor. The tubes have a radius of 0.55 mm and a length of 20 mm (mouth pressure) and 62 mm (pressure in the mouthpiece). According to [Gui+10], the transfer function of these capillary tubes is well represented by a model with non-isothermal boundary conditions [Kee84]. An inverse filtering was performed on the pressure signals to compensate the effect of the probe tubes. Signals are then acquired using an NI USB-9234 card by National Instruments at a 51.2 kHz sampling rate. Experimental signals displayed hereafter are not scaled or converted as this work focuses on qualitative study of the regime types. The instrumented mouthpiece is equipped with a saxophone reed (Rico Royal strength 2) and mounted on a commercial alto saxophone (Buffet-Crampon Senzo).

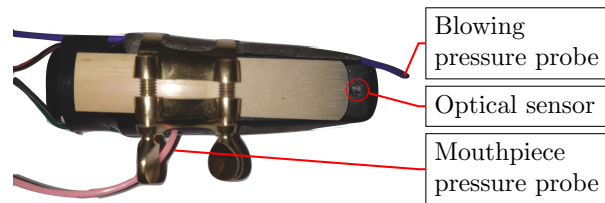


FIGURE 3.8: Instrumented alto saxophone mouthpiece including pressure probes for the pressure in the mouth of the musician and in the mouthpiece, and an optical sensor measuring the displacement of the reed. The reed is pulled back so that the optical sensor is uncovered.

Throughout the remainder of the paper, a low B fingering (written pitch) is studied. In concert pitch, the fundamental note expected with this fingering is a $D3$ at the frequency 146.83 Hz. The input impedance of the saxophone for this fingering has been measured using the CTTM impedance sensor [DLR08]. Its modulus is displayed in figure 3.9. The B fingering, which produces the second lowest note on the instrument, is chosen because the double two-step regimes studied in this work tend to appear more easily on the lowest notes of the saxophone. Note that for this fingering, the note most commonly expected by musicians is the first register, whose frequency is around the first impedance peak. On this fingering, the first register is often hard to produce, especially for beginner musicians. This can be understood when looking at the impedance modulus curve on figure 3.9, where the first peak is lower than the next three peaks: the upper resonances of the bore play a large part in the sound production, leading to a complicated sound production behavior. This profile of amplitude of the first few impedance peaks is also found in soprano and tenor saxophone [CSW09b]. The lowest fingering ($B\flat$) was not chosen, although it was tested, because it is more subject to producing undesired multiphonics and quasi-periodic regimes.

3.3.2.2 Observation of single and double two-step oscillating regimes

The main oscillating regimes of a saxophone are beating, which means that the reed channel closes completely during part of the cycle. They can be thought of as two-step motions [ODK04] and classified as standard or inverted, depending on the relative duration of the open and closed episode. Different regimes can be obtained for the same fingering, just by varying the control parameters such as the blowing pressure. Figure 3.10 shows measured examples of these two-step regimes. The reed displacement signal was post-processed by subtracting its moving average over a period, to be centered around 0. The standard regime is characterized by an open episode and a short closed episode. As can be seen on figure 3.10 (a), the reed is opened – and displays small amplitude oscillations around the highest values of x – for about 6 ms. Its closure corresponds to the main dip in the waveform and it lasts for about 1 ms

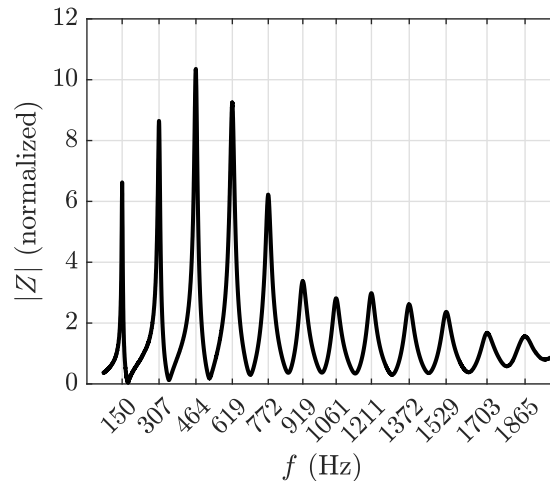


FIGURE 3.9: Input impedance modulus measured for the studied fingering of the alto saxophone: low B in written pitch. The modulus of the impedance is normalized by the characteristic impedance at the input of the instrument.

per period. For the inverted motion on figure 3.10 (b), the duration ratio is reversed: the reed channel is almost at its narrowest about 6 ms and opens wide briefly for about 1 ms. Note that the standard regime is obtained for lower values of the blowing pressure than the inverted regime.

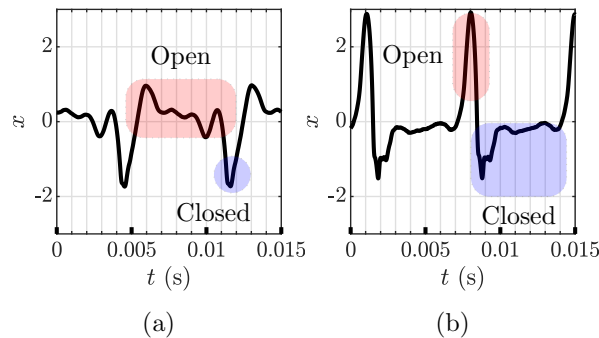


FIGURE 3.10: Measured reed position for simple two-step motions: standard (a) and inverted (b). The reed channel is closed when x is low. These waveforms correspond to different blowing pressures (see circle markers on figure 3.16).

The analogy with bowed string instruments suggests the apparition of other types of regimes. For example, under given excitation condition, bowed strings are subject to the double stick-slip phenomenon [Woo14], an oscillation regime where the string slips under the bow twice per period (instead of once for the standard Helmholtz motion). When transposed to conical reed instruments, this phenomenon corresponds to two closures of the reed channel per period. These regimes are observed experimentally on the low fingerings of the saxophone and they can be standard or inverted, as shown in figure 3.11. This oscillating regime can be called “double two-step”. Note that the double two-step regime is distinct from second register regimes: it is a first register regime, as it produces the same note as the standard two-step regime. For the standard version of the double two-step regime, the closure episodes are about 1 ms, almost the same duration as in the single standard two-step motion (figure 3.10, (a)). For the inverted double two-step regime, the short openings of the reed channel also last for about 1 ms.

For illustration purposes, the audible sound outside the instrument was recorded and short clips are provided as multimedia files 3.3.2.2, 3.3.2.2, 3.12 and 3.3.2.2. Note that the audible

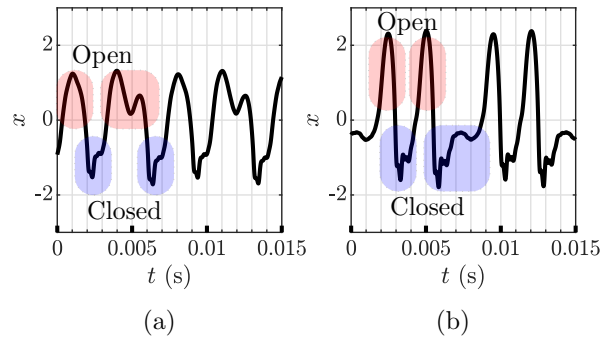


FIGURE 3.11: Measured reed position for double two-step motions: standard (a) and inverted (b). These waveforms correspond to different blowing pressures (see circle markers on figure 3.16).

Multimedia/ch3-Low/MM1.wav

FIGURE 3.12: Multimedia file: Sound recorded outside the resonator for the standard two-step motion, corresponding to the measured displacement shown in figure 3.10, (a).

sound corresponding to these double two-step regimes (Mm. 3.3.2.2 and 3.3.2.2) is clearly different from single regimes (Mm. 3.12 and 3.3.2.2). The difference in audible sound is less clear between a standard regime and its inverted counterpart.

In order to estimate the relative regions of production of each kind of regime in the control parameter space, a blowing pressure ramp is performed by a musician and recorded using an instrumented mouthpiece for the B fingering of the test saxophone. The musician sees the evolution of the blowing pressure parameter in real-time on a screen. The player makes as little embouchure adjustments as possible and focuses on increasing the blowing pressure progressively. Results are shown in figure 3.16. This ramp was obtained in a single breath after several tries. For clarity, the blowing pressure signal is smoothed by a moving average with a rectangular window, adjusted to reject the fundamental frequency of the oscillations and keep only the slowly varying value of the signal. Regimes are classified automatically based on the ratio of duration of the open and closed reed episodes. The reed displacement signal is high-pass filtered in order to remove the DC component. The reed is then considered “open” when the displacement signal is above 0 and “closed” when it is below 0. The ratio between closed duration and oscillation period is then computed and averaged over 4 periods. Thresholds are defined arbitrarily to separate between the different types of regimes, at 0.1, 0.25, 0.5, 0.6 and 0.8 (see dotted lines on figure 3.16). Looking at the pressure ramp in its entirety shows a possible order of the regimes when increasing the blowing pressure: standard and double two-step motions, second register, and inverted double then inverted two-step motions. Note that in this ramp, the episode between 1 and 2 seconds with a closure ratio of little above 0.25 is actually a quasi-periodic oscillation, with the actual double two-step oscillation starting at around 2.3 seconds.

3.3.3 Numerical study of the regimes using a physical model

3.3.3.1 Saxophone model

A simplified saxophone model consists of three main elements: the resonator, the reed channel and reed dynamics. Here all variables are dimensionless and obtained from their physical

Multimedia/ch3-Low/MM2.wav

FIGURE 3.13: Multimedia file: Sound recorded outside the resonator for the inverted two-step motion, corresponding to the measured displacement shown in figure 3.10, (b).

Multimedia/ch3-Low/MM3.wav

FIGURE 3.14: Multimedia file: Sound recorded outside the resonator for the double two-step motion, corresponding to the measured displacement shown in figure 3.11, (a).

Multimedia/ch3-Low/MM4.wav

FIGURE 3.15: Multimedia file: Sound recorded outside the resonator for the inverted double two-step motion, corresponding to the measured displacement shown in figure 3.11, (b).

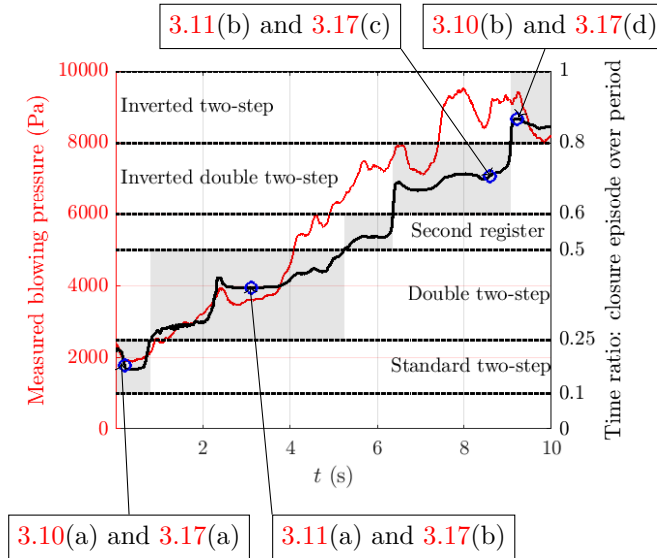


FIGURE 3.16: Result of a blowing pressure increase (low B fingering, alto saxophone) recorded with the instrumented mouthpiece. Left y-axis (red online): measured smoothed blowing pressure in Pa. Right y-axis: ratio between closure episode duration and oscillation period (solid line), and regime separation thresholds (dotted lines). Greyed areas emphasize the duration of each type of regime. Circles correspond to reed displacement signals in figures 3.10, 3.11 and pressure signals in figure 3.17.

counterparts (denoted with a hat) as

$$p = \frac{\hat{p}}{p_M} \quad , \quad u = Z_c \frac{\hat{u}}{p_M} \quad , \quad x = \frac{\hat{x}}{H}, \quad (3.10)$$

where p_M is the static pressure necessary to close the reed completely, Z_c is the characteristic impedance at the input of the resonator, and H is the distance separating the reed from the mouthpiece lay at rest. Note that $x = 0$ denotes the reed at equilibrium, and $x = -1$ corresponds to a closed reed channel.

The resonator is represented by its dimensionless input impedance, decomposed as a sum of modes

$$Z(\omega) = \frac{P(\omega)}{U(\omega)} = \sum_{n=0}^{N_m} \frac{C_n}{i\omega - s_n} + \frac{\bar{C}_n}{i\omega - \bar{s}_n}, \quad (3.11)$$

where C_n are the complex residues and s_n the complex poles. These modal parameters are estimated from a measured saxophone input impedance [Tai+18]. Eq. (3.18) can be transformed into the temporal evolution of the modal components p_n , since $j\omega$ translates into a time-domain derivative by inverse Fourier transform

$$\dot{p}_n(t) = s_n p_n(t) + C_n u(t). \quad (3.12)$$

The acoustic pressure p at the input of the tube is expressed as a sum including the modal components

$$p(t) = 2 \sum_{n=1}^{N_m} \operatorname{Re}(p_n(t)). \quad (3.13)$$

The number of modes N_m is chosen as $N_m = 12$, sufficiently large to represent the main resonances of the resonator. Results obtained using $N_m = 6$ lead to similar conclusions. The flow u at the input of the resonator is governed by the nonlinear characteristic [WB74]

$$u = \zeta [x + 1]^+ \operatorname{sign}(\gamma - p) \sqrt{|\gamma - p|}, \quad (3.14)$$

where $[x + 1]^+ = \max(x + 1, 0)$. This nonlinear characteristic uses the dimensionless control parameters of reed opening at rest ζ and blowing pressure γ . The expression of these parameters are

$$\zeta = wHZ_c \sqrt{\frac{2}{\rho p_M}}, \quad \gamma = \frac{\hat{\gamma}}{p_M}, \quad (3.15)$$

where w is the effective width of the reed channel, ρ the density of air and $\hat{\gamma}$ is the physical value of the blowing pressure. For this study the parameter ζ is fixed at $\zeta = 0.6$, unless otherwise specified. Following the values of reed channel height at rest $H = 17 \times 10^{-5}$ m and reed stiffness $K = 6.4 \times 10^6$ Pa.m provided in [MA+16], with an approximate effective width of $w = 1.10^{-2}$ m and characteristic impedance $Z_c = 3.10^6$ Pa.s/m³, one finds $\zeta = Z_c w \sqrt{2H/\rho K} = 0.58$ which justifies studying $\zeta \simeq 0.6$ in this work. To use Harmonic Balance Method and Asymptotic Numerical Method, described in subsection 3.3.3.2, it is convenient to regularize the characteristic of Eq. (3.20) using $|\cdot| \simeq \sqrt{\cdot^2 + \eta}$, where the parameter η is fixed at 10^{-3} [Ker+16].

The reed is modeled as a single degree of freedom oscillator driven by the pressure difference between the input of the resonator and the mouth of the resonator

$$\frac{\ddot{x}}{\omega_r^2} + q_r \frac{\dot{x}}{\omega_r} + x = -(\gamma - p), \quad (3.16)$$

where ω_r and q_r are the angular frequency and damping coefficient of the reed, chosen at $\omega_r = 4224$ rad/s based on [MA+16] and $q_r = 1$. In this model, the impact of the reed on the mouthpiece lay is ignored [DVM14; DGK00]. For further details on the effect of ignoring reed impact in a saxophone model, see [Col+19].

3.3.3.2 Numerical resolution with harmonic balance method

Periodic solutions to the system of equations (3.18), (3.20) and (3.21) are found using the harmonic balance method (HBM), under the formalism proposed in [CV09]. The HBM was pioneered by [KB49; NV76], and was applied to musical instrument models first in [GKN89]. Each variable X (where X can stand for p_n , u , x ...) is assumed to be periodic and thus decomposed into its Fourier series truncated at order H

$$X(t) = \sum_{k=-\infty}^{\infty} X_k \exp(ik\omega_0 t) \simeq \sum_{k=-H}^H X_k \exp(ik\omega_0 t), \quad (3.17)$$

where ω_0 is the angular frequency. This yield an algebraic system where the unknowns are the Fourier coefficients and the angular frequency. Hereafter, $H = 20$ is chosen, because it appears sufficient for a good representation of the studied regimes. The emergence of these different regimes depends on the value of the blowing pressure parameter γ . To compare the value of γ leading to each regime to the experimental results of figure 3.16, a Taylor-series based continuation method (Asymptotic Numerical Method) is applied to the algebraic system obtained by harmonic balance [GCV19]. The source code for this method may be found online at <http://manlab.lma.cnrs-mrs.fr/>. The continuation yields possible periodic solutions, as well as their stability [LT10; BL18]. This may be displayed as a bifurcation diagram representing

the evolution of one descriptor of the periodic solutions as a function of the blowing pressure. The bifurcation diagrams displayed here do not change when adding more harmonics, but their computation is more time consuming.

3.3.3.3 Results

Depending on the value of the blowing pressure parameter γ , all types of two-step regimes observed experimentally are found to be stable periodic solutions of the model. Figure 3.17 compares the regime types found in measurement and simulation from their pressure waveforms. No a posteriori adjustment of the model is performed, and therefore no precise agreement of the waveforms is expected. Many differences between synthesized and measured signals could be explained by the reed opening parameter ζ being constant and not adjusted in the model, and the response of the pressure probe tube affecting the measured pressure signal. Some high frequency components of synthesized signal can also be misrepresented due to the modal truncation of the impedance. However, several main features of the measured signals can be identified on the synthesized signals, such as the duration of the short low-pressure episodes on the standard and double two-step regimes, and the short high-pressure episodes on the inverted double and inverted two-step regimes. It can also be noted that both synthesized and measured signals exhibit secondary fast oscillations of small amplitude during the long episodes (open or closed). A similar “minor oscillations” phenomenon is known to appear on bowed strings [KM71]. The opening duration of the synthesized inverted two-step regime presented in figure 3.17 (g) is longer than the closure duration of the synthesized standard two-step of figure 3.17 (a), which is contrary to the usual Helmholtz motion formulation in which both durations are determined only by the geometry of the resonator. This is always the case with the model of this paper, with both time-domain synthesis and the harmonic balance: the synthesized and standard and inverted two-step display a whole range of opening or closure durations depending on the value of the blowing pressure. This phenomenon is further detailed below, in multimedia file 3.3.3.3, figure 3.19 and the corresponding commentary.

The bifurcation diagram summarizing the evolution of the different oscillating regimes depending on the blowing pressure parameter γ is presented in figure 3.19. A parameter of the oscillating regimes, the amplitude of the first cosine – i.e., the real part of the first Fourier coefficient of Eq. (3.17) – of the first modal pressure p_1 is displayed. This parameter was chosen because it allows for clear separation of the branches corresponding to each regime. Note that the sign of this coefficient can be either positive or negative depending solely on a choice of phase of the oscillation. On the diagrams displayed hereafter, the sign of p_1 is chosen so that the different solution branches are as easy to distinguish as possible. The most important part of the branches are stable regimes (thick lines in the figure). Each branch is labeled with the type of regime it corresponds to. The regime type is determined manually by observing the waveform, which can be done exhaustively using animations such as multimedia file 5. Note that the animation shows the standard two-step regime morphing gradually into the inverted two-step regime, on the same branch. The closure duration of the reed increases progressively with the blowing pressure parameter γ , in clear contradiction with the Helmholtz motion approximation. The topic of continuous transition between standard and inverted regimes for a conical woodwind remains to be fully understood, although experimental explorations point to similar results [Dal07]. All the other branches correspond to only one type of regime each.

Figure 3.19 is qualitatively coherent with the experimental findings in figure 3.16, in terms of order of emergence of the stable regimes when varying the blowing pressure. Starting with a low blowing pressure, the first stable regime is the standard two-step. When the blowing pressure increases, the stable branch is followed until its end, and then the system jumps on another stable branch. At the end of the standard two-step branch, around $\gamma = 0.69$, there are two coexisting branches: the inverted two-step and the double two-step. Note that for the parameter values where two stable regimes coexist, different initial conditions may lead to one or the other. Describing the conditions leading to one or the other regime (called their “attraction basin”) exhaustively is almost impossible. Consequently, when using the bifurcation diagram to predict which regimes can be produced when increasing the blowing pressure, several scenarios can be devised, and it is extremely difficult to decide which one is the most probable without checking it experimentally. For instance, according to this bifurcation diagram, it would be possible for the system to start from the standard two-step,

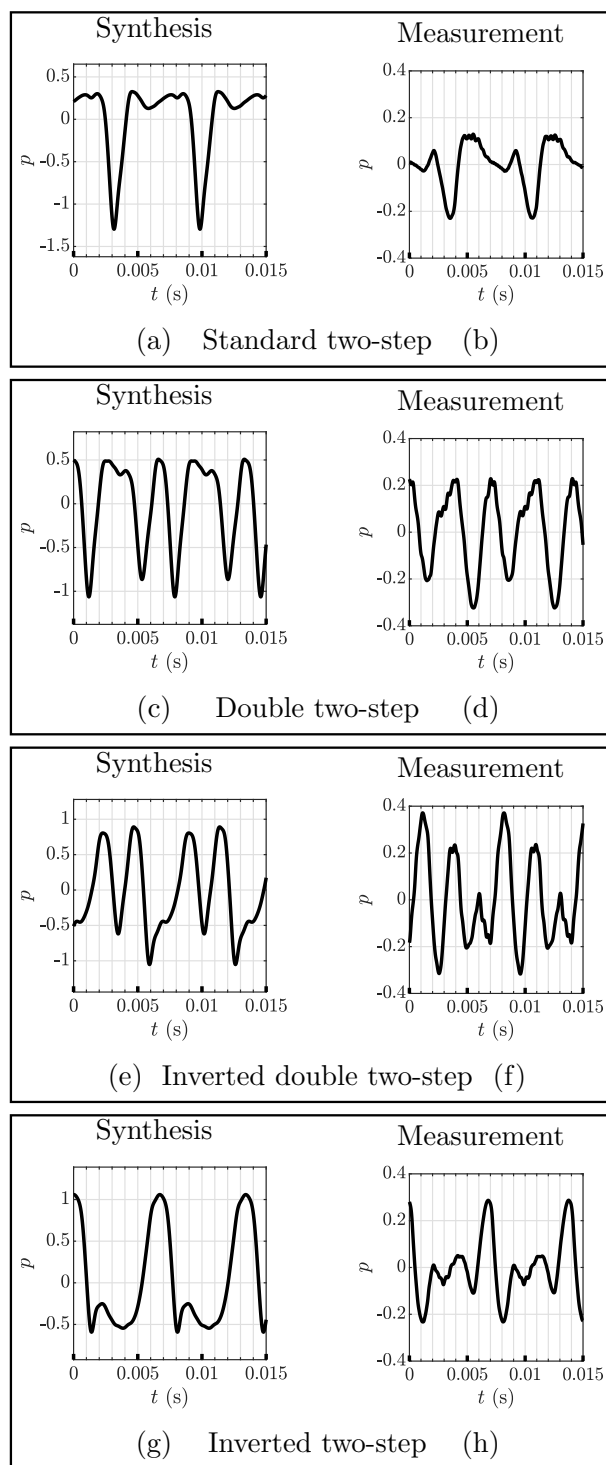


FIGURE 3.17: Synthesized and measured pressure signals in the mouthpiece for two-step regimes. Arbitrary units.

[Multimedia/ch3-Low/MM5.mp4](#)

FIGURE 3.18: Multimedia file: Animation: evolution of the acoustic pressure waveform and spectrum following the stable branches of the bifurcation diagram in figure 3.19.

jump to an inverted two-step regime and follow this branch until extinction at high blowing pressure ($\gamma \simeq 1.5$), with no production of double two-step regimes. However, we could not obtain this scenario experimentally. Another possible order suggested by the bifurcation diagram, after the standard two-step, is jumping to double two-step, second register, inverted double two-step, and then inverted two-step, when it is the only stable branch (for $\gamma > 1.5$). The experiment shows that it is possible to obtain all these regimes in this order of emergence when increasing the blowing pressure.

Figure 3.19 shows that the double two-step branches are linked to the second register branch: a continuum of solutions exist between second register and double two-step motion – even though some of the solutions on the path are unstable. The junction between these branches can be seen as a period-doubling of the second register. Inverted regimes appear at high blowing pressure, which is coherent with the static behavior as the reed tends to close more and more when the blowing pressure is higher. During the oscillation, the reed closes for a longer and longer portion of the period, thus transitioning from standard to inverted motion. A high blowing pressure leads to extinction of the oscillation: the reed channel stays closed. Figure 3.19 (b) shows the same metric as figure 3.16, the duration ratio between closure episode and period. It can be noted that the thresholds between the different regimes are not the same as those fixed empirically. Additionally, the model predicts that inverted two-step can appear at relatively low closure ratios, but these were never found experimentally. This may be due to the inverted double two-step being very stable in this blowing pressure regions, thus making it hard to find other solutions.

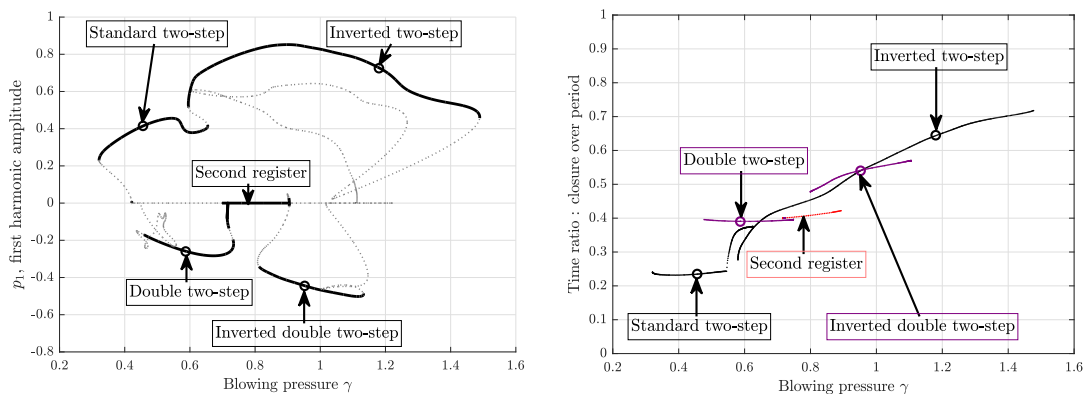


FIGURE 3.19: Bifurcation diagram: (a) amplitude of the first cosine of the first modal pressure p_1 and (b) ratio between closure episode duration and oscillation period ; with respect to the blowing pressure parameter γ , for the low B fingering of an alto saxophone. In (a), the line aspect denotes stability of the regimes: thick black is stable, dotted gray is unstable. Circle markers correspond to the plots in figure 3.17. $\zeta = 0.6$.

It is worth noting that the same oscillating regimes appear in the same order for other values of the reed opening parameter ζ , around the one used in figure 3.19 ($\zeta = 0.6$). Figure 3.20 shows two bifurcation diagrams, obtained for $\zeta = 0.5$ and $\zeta = 0.75$ respectively. The stability region of the regimes are affected by the value of ζ . In particular, a lower ζ enlarges the zone of stability of the second register while a greater ζ reduces it. It can also be noted that in this particular case, a higher ζ value leads to an uninterrupted single two-step branch, where standard and inverted two-step are connected by stable regimes. Another comment can be made on the bifurcation diagram obtained for $\zeta = 0.5$ (Figure 3.20 (a)), on the inverted double two-step branch. In this case, the inverted double-two-step branch that is connected to the second register branch only contains unstable regimes – on figure 3.20 (a) it is the small branch of negative p_1 , between $\gamma = 0.86$ and $\gamma = 1.04$. This branch corresponds to the branch in figure 3.19 where the inverted double two-step becomes stable. However, on figure 3.20 (a), another inverted double two-step branch shows stable regimes, that are indicated by the inverted double two-step arrow. This other branch is not connected to the second register, but to the inverted single two-step branch, by a long unstable portion of branch. Therefore it appears that double two-step regimes can be considered as degenerate from the single two-step or the second register, depending on the value of the control parameters.

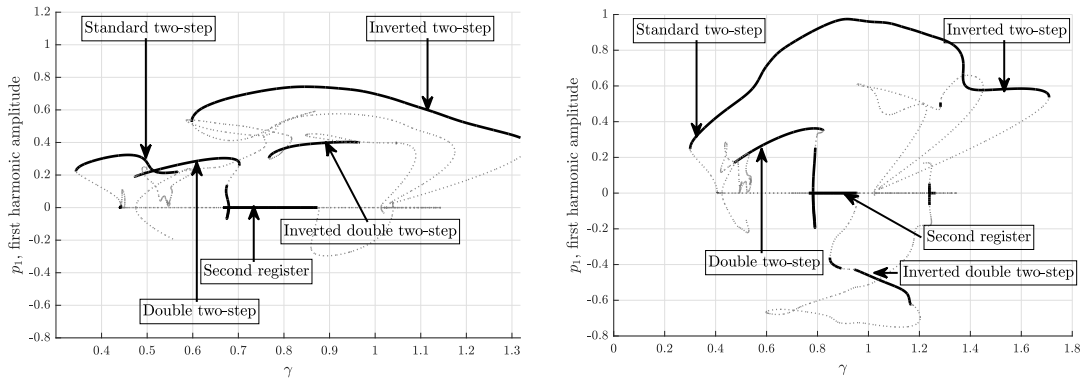


FIGURE 3.20: Bifurcation diagram: amplitude of the first cosine of the first modal pressure p_1 with respect to the blowing pressure parameter γ , for the low B fingering of an alto saxophone. (a) $\zeta = 0.5$, (b) $\zeta = 0.75$. The line aspect denotes stability of the regimes: thick black is stable, dotted gray is unstable

[Multimedia/ch3-Low/MM6.mp4](#)

FIGURE 3.21: Multimedia file: Animation: evolution of the acoustic pressure waveform and spectrum during a continuous transition between double two-step regime and second register for the low C fingering of an alto saxophone, following branches of the bifurcation diagram in figure 3.22.

A similar behavior is also observed for neighboring fingerings. Figure 3.22 shows the bifurcation diagram for the fingering just above the one used for figures 3.19 and 3.20: the low C fingering. The bifurcation diagram in figure 3.22 has the same structure as the others, although the inverted double two-step regime is unstable. In particular, the transition between standard two-step and inverted two-step regimes is an unstable portion of branch featuring two fold bifurcations (two points where two solutions collide and disappear, which can be seen as turning-up points on the bifurcation diagram), similar to that of figure 3.20, up, and figure 3.19. It is also worth noting that on this fingering, the double two-step branch and second register branch are connected by stable regimes only: the thick lines connect at $\gamma = 0.8$. This indicates that for this fingering, it is possible to have continuous transition between double two-step and second register using only stable regimes. A synthesized example of this transition is shown in multimedia file 3.3.3.3.

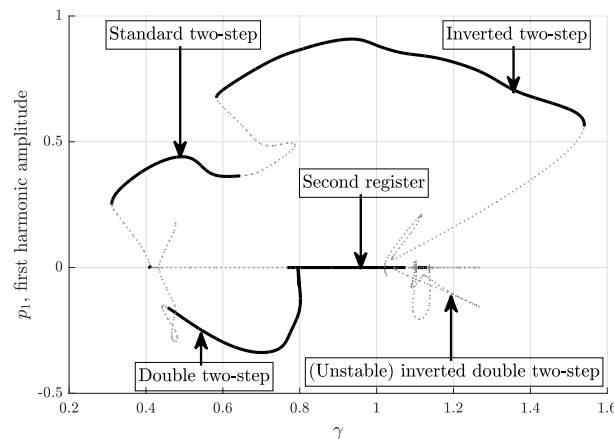


FIGURE 3.22: Bifurcation diagram: amplitude of the first cosine of the first modal pressure p_1 with respect to the blowing pressure parameter γ , for the low C fingering of an alto saxophone. $\zeta = 0.6$, same as in figure 3.19.

The double two-step regime becomes unstable on fingerings D and higher for the main value of $\zeta = 0.6$ studied here. This may be a sign that its production is linked to the high

amplitude of the second and third resonances of the resonator, which is a characteristic of the low fingerings of the saxophone.

3.3.4 Conclusion

Alto saxophones are able to produce double two-steps motions, that seem analogous to double stick-slip motions in bowed strings [Woo14]. The production region of these regimes appears linked to the second register of the resonator. The appearance of the many oscillating regimes on the studied fingerings may be due to the strong role of the second and third mode of the resonator. The simple saxophone model used in this paper is capable of reproducing these regimes, even though it ignores the impact between the reed and the mouthpiece lay. The model also corroborates the order of appearance of these regimes when increasing the blowing pressure on a real saxophone. Complementary numerical studies show that the double two-step phenomenon is not restricted to a particular set of parameters, but appears for several combinations of control parameters and several fingerings. The description of the playability of a saxophone in the low fingerings may take these regimes into account, whether they are undesirable, as is the case for the double fly-back motion in violins, or a useful tool of expressivity for the musician. Acoustical or geometrical characteristics of the resonator remain to be linked to the ease of production of double two-step regimes.

Acknowledgments

The authors would like to thank Louis Guillot for advice and guidance in the construction of the bifurcation diagram. This work has been carried out in the framework of the Labex MEC (ANR-10-LABX-0092) and of the A*MIDEX project (ANR-11-IDEX-0001-02), funded by the Investissements d'Avenir French Government program managed by the French National Research Agency (ANR). This study has been supported by the French ANR 659 LabCom LIAMFI (ANR-16-LCV2-007-01).

Reading guidelines

The following section (3.3) is an *in extenso* reproduction of the short article (except title and abstract) published as:

Colinot, Tom, Louis Guillot, Christophe Vergez, Philippe Guillemain, Jean-Baptiste Doc and Bruno Cochelin (2019). "Influence of the "ghost reed" simplification on the bifurcation diagram fo a saxophone model". In: *Acta Acustica united with Acustica*, 105(6), pp. 1291-1294.

Note that this article's presentation of the physical model of saxophone 3.4.2 is explained in further detail in chapter 1.

3.4 Medium fingering : study of the influence of the reed impact

3.4.1 Introduction

Reed instrument models are strongly nonlinear, which explains how different oscillating regimes can be produced for the same fingering. The produced regimes depend on the control parameters imposed by the musician, such as the blowing pressure or the opening at rest between the reed and the mouthpiece lay. This work assesses a choice done in many analytical studies of reed instrument models: the impact between the reed and the mouthpiece lay is ignored. In this simplification, called "ghost reed" hereafter, the reed penetrates the mouthpiece wall freely. This free interpenetration is nonphysical but it allows analytical developments [DGK00; Ned98] and numerical studies of minimal models [DVM14; Ker+16]. To lesser extent, it may also lessen the computational cost. It is interesting to note that the "ghost reed" simplification is carried out *de facto* in models ignoring reed dynamics, such as in [Gui+15; Ker+16; ODK04]. Lumped models of the contact between reed and lay have been developed using variable stiffness for the reed [VWA07], or a separate contact force with stiffness and damping [BTC15; CW12]. The last cited contact model was used in comparison with experimental data to estimate reed parameters [MA+16]. In this paper, we investigate how the reed impact affects the overall behavior of the instrument model and which phenomena are reproduced similarly with and without the ghost reed simplification. This paper compares a recent lumped impact model [BTC15] with the ghost reed model, in the case of a saxophone, using continuation associated with the harmonic balance method to describe the oscillatory regimes corresponding to the first two registers for the whole playing range with respect to the blowing pressure.

3.4.2 Mathematical model of reed instrument

The model studied here is similar to the one presented in [Coy+15] in the case of the clarinet. It is assumed that the acoustics of the resonator is linear. The relationship between the air flow U and the acoustic pressure P at the input of the resonator is classically written in the frequency domain thanks to the input impedance $Z(\omega)$, defined by:

$$Z(\omega) = Z_c \frac{P(\omega)}{U(\omega)} = Z_c \sum_{n=0}^{+N_m} \frac{C_n}{i\omega - s_n} + \frac{\tilde{C}_n}{i\omega - \bar{s}_n} \quad (3.18)$$

where Z_c is a characteristic impedance, s_n are the (complex) poles of the impedance and C_n the associated dimensionless residues. N_m is taken equal to 8 in our case, in order to limit the complexity of the problem while representing all the main modes of the resonator. In the time domain, this relation gives the complex linear equations of the resonator model:

$$\dot{p}_n(t) - s_n p_n(t) = Z_c C_n u(t), \quad (3.19)$$

where p_n are the modal pressures such that the total acoustic pressure is: $p(t) = 2 \sum_{n=1}^{N_m} \Re(p_n(t))$.

Following the work of [WB74], the input flow u writes

$$u = \zeta \text{sign}(\gamma - p) \sqrt{|\gamma - p|} \max(x + 1, 0), \quad (3.20)$$

where ζ is a dimensionless parameter characterizing the embouchure [Coy+15], $\gamma = p_m/p_M$ is the dimensionless version of the blowing pressure p_m , normalized by the static pressure p_M necessary to displace the reed until the mouthpiece lay, and p is the dimensionless acoustic pressure in the mouthpiece. x is the dimensionless reed displacement, and the factor $\max(x + 1, 0) = \frac{1}{2}((x + 1) + |x + 1|)$ is equal to $x + 1$ if the reed channel is open ($x + 1 > 0$) and 0 if it is closed ($x + 1 < 0$). Note that equation (3.20) is used for both cases studied: with and without the ghost reed simplification.

In order to facilitate numerical application of the harmonic balance and continuation methods, the absolute values in Eq. (3.20) are regularized with $|z| \simeq \sqrt{z^2 + \eta}$. One has $\text{sign}(\gamma - p) = \frac{\gamma - p}{|\gamma - p|}$. The raw and regularized nonlinear characteristic are displayed in figure 3.23. The regularization parameter η is taken equal to 10^{-3} so that the regularized nonlinear characteristic stays close to its raw version.

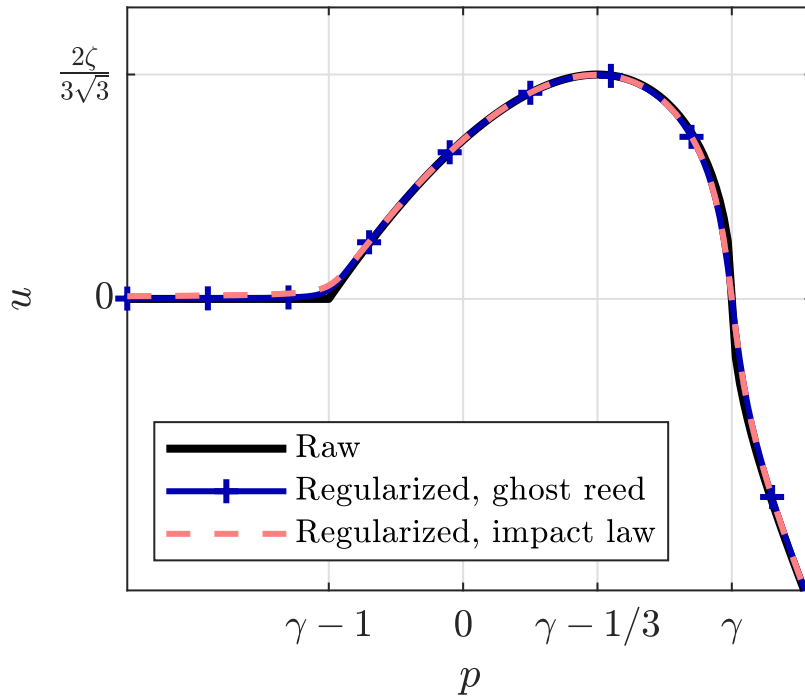


FIGURE 3.23: Nonlinear characteristics in static regimes: raw (Eq. (3.20)) and regularized versions, using $|z| \simeq \sqrt{z^2 + \eta}$ with $\eta = 10^{-3}$.

The motion of the reed is modeled by a one degree of freedom oscillator subject to a force coming from a pressure difference across the reed and an impact force. The dimensionless equation describing the motion is:

$$\frac{\ddot{x}}{\omega_r^2} + q_r \frac{\dot{x}}{\omega_r} + x = -(\gamma - p) + F_c(x) - \beta \dot{x} F_c(x) \quad (3.21)$$

where ω_r is the natural angular frequency of the reed and q_r is a damping constant (inverse of a quality factor). F_c follows the law suggested by [BTC15] which is

$$F_c(x) = K_c \min(x + 1, 0)^\alpha \quad (3.22)$$

where K_c is the impact stiffness and α is an exponent which characterizes the impact. The term $\beta \dot{x} F_c$ can be thought of as a nonlinear damping term, *i.e.* the impact induces some loss of energy. It is regularized by writing $\min(x + 1, 0) = -\frac{1}{2}(|x + 1| - (x + 1))$ with the absolute value approximated as: $|x + 1| \simeq \sqrt{(x + 1)^2 + \eta}$. Considerations on the reed material and

the mouthpiece material suggest an impact stiffness value of $K_c = 100$, although there is no obvious experimental evidence. This means that the mouthpiece is one hundred times stiffer than the reed. The studies [DGO03; AVW04] treat this question in more details. The ghost reed simplification is implemented by $K_c = 0$: the reed moves freely through the mouthpiece lay. All the values of the parameters are summarized in table 3.1.

Parameter	Notation	Value
Impact stiffness	K_c	100 or 0
Impact exponent	α	2
Impact damping	β	0.01
Reed angular frequency	ω_r	4224 rad.s ⁻¹
Reed damping	q_r	1
Blowing pressure	γ	[variable]
Embouchure	ζ	0.6
Regularization	η	0.001

TABLE 3.1: Parameters of the model. Parameters with no units are dimensionless.

3.4.3 Comparison between the ghost reed simplification and the impact model

Now the comparison is made between the ghost reed simplification, without impact force to limit the reed displacement ($K_c = 0$), and the model with impact ($K_c > 0$, here $K_c = 100$). The modal parameters of the resonator are deduced from the impedance measured on an alto saxophone. The fingering of a low D \sharp is used. This fingering is the sixth lowest of the saxophone, and it exhibits both first and second register regimes. Higher fingerings produce less or none of the second register, and lower fingerings produce a great variety of regimes that make the analysis of the bifurcation diagram tedious.

Periodic solutions of the models are found using the harmonic balance method, where all the variables are decomposed into a Fourier series up to harmonics H (see for example [GKN89]). Asymptotic numerical method (ANM) is used to produce the bifurcation diagram corresponding to each model [CV09; GCV19]. In this work, $H = 50$ for first register regimes and $H = 80$ for second register regimes. Only periodic regimes can be computed by the harmonic balance method, so the waveform comparison excludes transients. Stability of the regimes is determined using the method presented in [LT10] and [BL18].

3.4.3.1 Waveforms

As a first comparison step, temporal waveforms of the reed displacement x as well as the acoustic pressure p and flow u , are displayed in figures 3.24 and 3.25. These regimes correspond to the first register of the instrument: their frequency is close to the first resonance frequency of the resonator. Figure 3.24 shows the established periodic regime obtained for $\gamma = 0.5$: it corresponds to the standard Helmholtz motion, typical of conical instruments [ODK04]. As expected, the reed displacement waveforms are quite different: the impact force penalizes the displacement of the reed below $x = -1$, whereas the ghost reed simplification lets it move freely below $x = -1$. Note that this formulation of impact force lets the reed squash against the lay and go slightly below -1 , though far less than the ghost reed model. This is the main difference between the reed displacements generated by the two models. Over the period, the displacement signals are most similar right before the contact occurs. As for the acoustic pressure p , the two waveforms are nearly superimposed, except for some higher frequency components. This is confirmed by a good match in the amplitude of the harmonics, especially the first nine. Similar comments can be made on the flow u . For this particular value of the blowing pressure γ , the reed impact model has no major influence on the pressure and flow waveform.

Figure 3.25 presents the waveforms obtained for a higher value of the blowing pressure $\gamma = 1.5$. Eventhough $\gamma > 1$ corresponds to sufficient pressure to close the reed channel

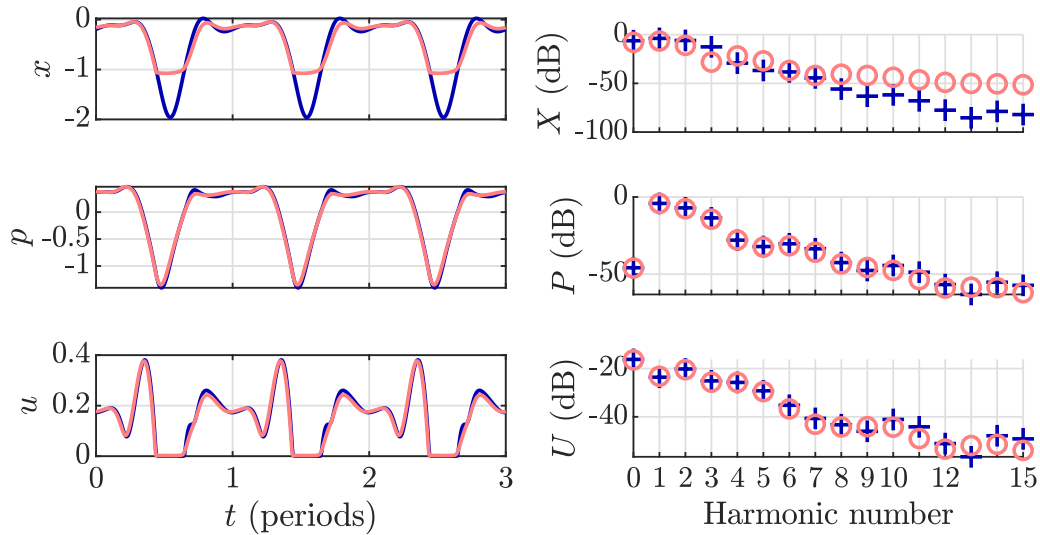


FIGURE 3.24: Steady periodic regime for the reed displacement x , and the acoustic pressure p and flow u . Waveforms (left) and amplitude of harmonics (right). Model with impact force (light red) and ghost reed simplification (dark blue). Blowing pressure $\gamma = 0.5$.

completely in a static configuration, oscillations may still be sustained for $\gamma > 1$. The obtained oscillating regime correspond to the inverted Helmholtz motion [ODK04], where the reed stays in contact with the lay for more than half the period. In this case, the reed displacement waveform presents even more differences than on figure 3.24. However, the acoustic pressure and flow waveforms stay very similar, as they are on figure 3.24, and their first seven harmonics are very close. In order to qualify the effect of the reed impact model on a variety of regimes, the associated bifurcation diagrams are now studied.

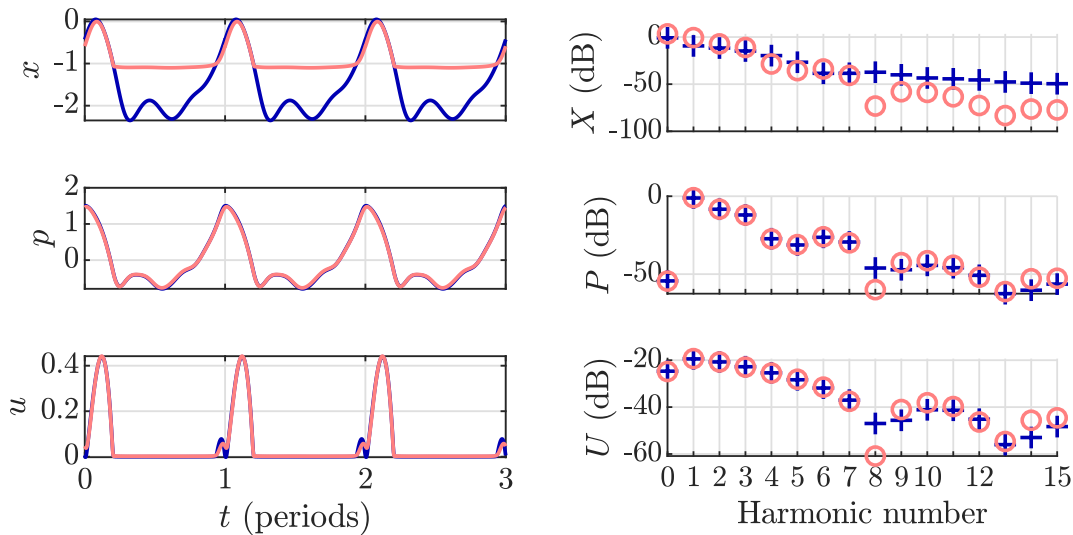


FIGURE 3.25: Steady periodic regime for acoustic pressure p and flow u , and reed displacement x . Waveforms (left) and amplitude of harmonics (right). Model with impact force (light red) and ghost reed simplification (dark blue). Blowing pressure $\gamma = 1.5$.

3.4.3.2 Bifurcation diagrams

The bifurcation diagram in figure 3.26 shows the L^2 norm of the acoustic pressure p , with respect to the blowing pressure γ . The L^2 norm is defined by

$$\|p\|_{L^2} = \frac{1}{T} \int_0^T p(t)^2 dt, \quad (3.23)$$

where T is the period of p . The first register is computed with Fourier series truncated at $H = 50$ harmonics, the second one with $H = 80$ harmonics. These truncation orders have been chosen to ensure a good convergence of the solution and of the stability information of the periodic solution branches. Several common features appear between the structure of the overlaid diagrams, corresponding to the ghost reed and to the impact model. In terms of oscillation threshold, both cases exhibit two Hopf bifurcations on the equilibrium branch (not shown here, corresponds to $\|p\|_{L^2} = 0$). They are marked H in figure 3.26. The first one, a sub-critical Hopf bifurcation around $\gamma = 0.4$ for both models, is associated with the first register of the saxophone. The second one, a super-critical Hopf bifurcation around $\gamma = 0.43$ for both models as well, is associated with the second register. Branches of the two models share common characteristics, but are not superimposed. For instance, the range of γ where stable periodic oscillations exist is reduced when taking into account the impact force. The right Neimark-Sacker bifurcation on the second register solution branch appears very sensible to the impact model in this case. Without impact force, it is located around $\gamma = 1.25$, below the fold bifurcation point. However, with impact force, the right Neimark-Sacker bifurcation is located around $\gamma = 1.8$, above the fold bifurcation. The highest values of the blowing pressure present the most discrepancies between the two models. This can be explained by the fact the duration of the contact between the reed and the lay is longer for higher blowing pressure values, and thus it is the region where the impact model has the most influence.

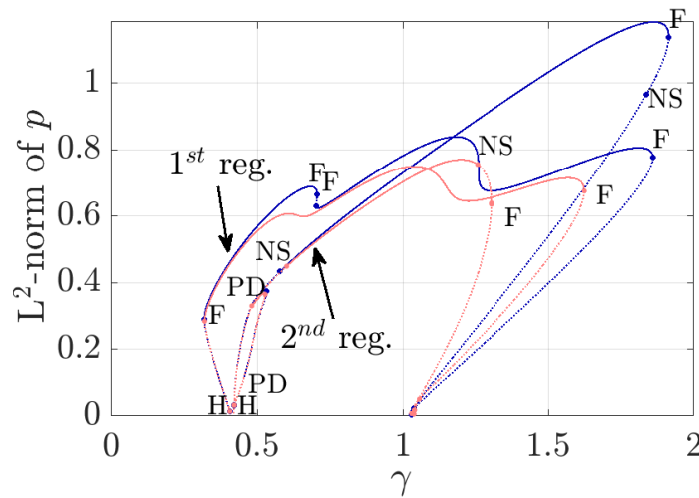


FIGURE 3.26: Bifurcation diagram: L^2 norm of the acoustic pressure p with respect to blowing pressure γ . Stable solutions are in solid lines, unstable solutions are in dotted lines. Dark blue: ghost reed simplification; light red: impact force model. Bifurcation labels are H: Hopf; PD: period doubling; F: fold; NS: Neimark-Sacker.

Figure 3.27 is a close-up of figure 3.26 for values of γ smaller than 1. In this area, which is expected to be more commonly reached than the area $\gamma > 1$ by the instrument players (it corresponds to moderate playing levels), the differences between the two models exist but are mostly negligible. The periodic solutions arising from the two Hopf bifurcations encounter generic bifurcations of periodic solutions, namely fold bifurcation, period doubling bifurcation and Neimark-Sacker bifurcation. The bifurcations are almost superimposed for both models. The branch of unstable periodic solutions arising from the period doubling bifurcations are exactly superimposed. Despite a very good agreement over the range of the figure 3.27 there

is a non-negligible difference on the first register for $0.5 < \gamma < 0.7$, with two fold bifurcations for the ghost reed simplification that are not found with the impact model.

The same study has been performed for other values of ζ , which confirms the results presented here. With the formulation of the impact chosen in this paper, it is possible to vary continuously between impact model and ghost reed simplifications: for values of K_c in between 0 and 100, the solution branches are in between the two branches displayed in figure 3.26.

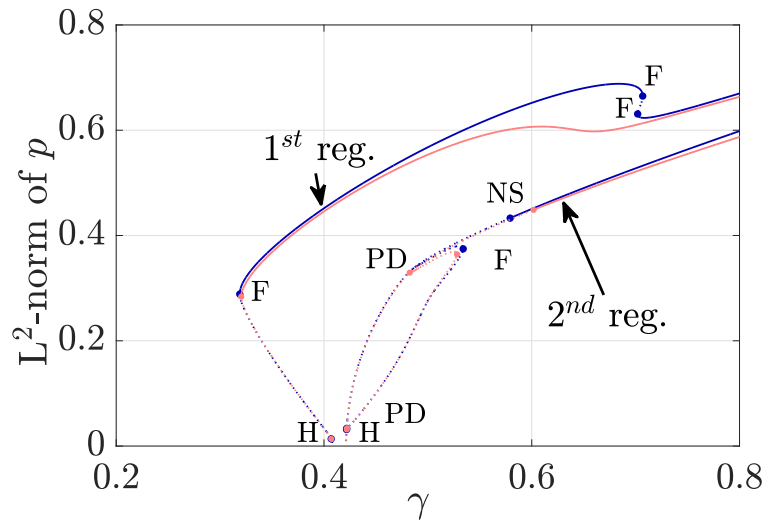


FIGURE 3.27: Zoom of figure 3.26.

3.4.4 Conclusion

Taking into account reed impact in a saxophone model has definite influence on regimes obtained with high values of the blowing pressure parameter, for which the reed is in contact with the mouthpiece lay for a large part of the oscillation period. However, if the study is limited at low blowing pressures, around the low oscillation threshold for instance, the ghost reed simplification delivers results very close to elaborate impact models at a much lower computational cost. The effect of the nature of the reed impact on the transients and other non-stationary phenomena remains to be studied, as part of a much wider field of investigation.

Reading guidelines

The following section (3.5) is an *in extenso* reproduction of the conference article (except title and abstract) published as:

Colinot, Tom, Louis Guillot, and Jean Kergomard (2019). "Direct and inverse Hopf bifurcation in a neutral delay differential equation model of reed conical instrument". In: *Proceedings of the 23rd International Congress on Acoustics*, pp. 6446-6451.

3.5 Exhaustive geometrical study of the bifurcation of an idealized model

3.6 Introduction

The study of periodic solutions of physical models has shown to be an efficient tool to understand the behavior of the systems considered. A first common application is to predict and avoid undesired instabilities. In musical acoustics, the periodic solutions are sought for as they correspond to the regimes where an instrument produces a note. A lot of methods are available in the literature to study these regimes. Among those, two essentially different approaches will be considered. The first one is time-integration method. From the knowledge of the system before the starting time of integration, it reconstructs the behavior of the system for all greater times. Without *a priori* knowledge on the solution type, it is then possible to reconstruct the whole signal or waveform. For all the values of the parameters, a new time-integration is performed and thus the behavior of the system is known on a range of the parameters. However, this can be more complex in the case of several co-existing solutions and these methods are often unable to obtain unstable regimes. If the aim is the study of periodic solutions, the transient regime before the steady state can be very long and difficult to characterize. The second type of approach is continuation methods. These methods allow to keep track of the waveform as one parameter of the system is varied. Only steady-state solutions are considered. Thus, from one starting periodic solution a whole branch of periodic solution is determined. From the solution branch, it is possible to determine the critical value of the parameter above which a sound arise (the Hopf bifurcation point). A study of the oscillation thresholds of the clarinet by continuation is proposed in [KVC12a].

In this short article, the two complementary approaches are applied to a simplified model of saxophone. Previous work treat the bifurcation of saxophone-like instruments using multi-cylindrical approximations of the resonator [ODK04; DGK00] or approaches based on the input impedance [Ric+09]. The model we use here has a conical resonator modelled by a delayed system. It is taken from [Ker+16]. Although losses and reed dynamics are ignored, this model has been shown to reproduce internal pressure waveform for the saxophone. A reformulation of the model leads to a strongly nonlinear neutral delay differential equation, for which no analytical solution exists. However, the equation can be solved numerically using sound synthesis (time-integration) or harmonic balance. From sound synthesis, the general features of the produced sound are determined in a two-dimensional space of parameters value. This study helps to give a hint of the behavior of the system but fails to state clearly whether the Hopf bifurcation is super-critical or sub-critical. In practice, this information is interesting from the musician point of view. The super-critical case features a soft appearance of the sound in the instrument while the sub-critical case is often linked with a sudden appearance of the sound and a hysteresis loop. The continuation study of the same model is performed with a Taylor series based method coupled with the harmonic balance method [GVC19]. It allows to have a continuous representation of the solution-branch. From the continuation diagram, the nature (super- or sub-critical) of the Hopf bifurcation and the hysteresis loops can be determined. The results obtained with the two methods are compared to validate the approaches.

3.7 Model and numerical methods

3.7.1 Model

The acoustical variables at the input of the resonator p and u are in dimensionless form, obtained from the the physical values \hat{p} and \hat{u} as

$$p = \frac{\hat{p}}{p_M} \quad , \quad u = Z_c \frac{\hat{u}}{p_M}, \quad (3.24)$$

where p_M is the static pressure necessary to close the reed channel completely, and $Z_c = \frac{\rho c}{S}$ is the characteristic impedance. The control parameters of the model are

$$\gamma = \frac{p_m}{p_M} \quad , \quad \zeta = Z_c w H \sqrt{\frac{2}{\rho p_M}}, \quad (3.25)$$

where p_m is the pressure in the mouth of the musician, w is the width of the reed channel and H is the height of the reed channel at rest. The control parameter ζ represents dimensionless reed opening at rest.

The reed is considered as a spring without mass: its position is proportional to the pressure difference between the input of the instrument and the mouth of the musician. The nonlinear characteristic giving the flow u depending on the pressure p and the control parameters is deduced from the Bernoulli law [WB74] and writes

$$u = F(p) = \begin{cases} \zeta(1 - \gamma + p)\text{sign}(\gamma - p)\sqrt{|\gamma - p|} & \text{if } p \geq \gamma - 1 \\ 0 & \text{if } p < \gamma - 1 \end{cases}. \quad (3.26)$$

The resonator of the saxophone is considered as a lossless conical waveguide with a lumped mouthpiece, whose volume equals the volume of the missing apex of the cone [Ker+16]. The pressure p at the input obeys the equation

$$\frac{dp}{dt}(t) = \frac{dp}{dt}(t - \hat{\tau}) - \frac{6c}{x_1} \left[p^-(t) + p^+(t - \hat{\tau}) + \frac{c}{2x_1} \int_{t-\hat{\tau}}^t p(t') dt' \right], \quad (3.27)$$

where $p^+ = (p + u)/2$ and $p^- = (p - u)/2$ and the parameters are x_1 the length of the missing apex of the cone, $\hat{\tau} = 2\ell/c$ is the duration of a round trip in the resonator of length ℓ .

Deriving equation (3.27) leads to an equation in p only, that can be used for harmonic balance:

$$\ddot{p} + \sqrt{3}(1 - F'(p))\dot{p} + p = \ddot{p}_\tau - \sqrt{3}(1 + F'(p_\tau))\dot{p}_\tau + p_\tau, \quad (3.28)$$

where p_τ is the delayed pressure and the time and delay are dimensionless:

$$\tilde{t} = \frac{c}{x_1} \sqrt{3} t \quad , \quad \tau = \frac{2\ell}{x_1} \sqrt{3}. \quad (3.29)$$

The dot notation signals derivation with respect to the dimensionless time. With the dimensionless time, there are only 3 parameters : the control parameters ζ and γ , and the delay τ which is proportional to the ratio ℓ/x_1 . In this paper, ζ is fixed at 1 and x_1 at 0.4 m, which is a typical value for alto saxophones, as we concentrate on the effects of parameters γ and ℓ .

3.7.2 Sound synthesis

Equation (3.27) may be discretized to serve for sound synthesis synthesis with time step t_s :

$$I_n = I_{n-1} + \frac{ct_s}{4x_1} (p_n + p_{n-1} - p_{n-2M} - p_{n-2M-1}) \quad (3.30)$$

$$p_{n+1} = p_n + p_{n-2M+1} - p_{n-2M} - \frac{6ct_s}{x_1} \left(\frac{1}{2}(p_n - u_n) + \frac{1}{2}(p_{n-2M} + u_{n-2M}) + I_n \right) \quad (3.31)$$

$$u_{n+1} = F(p_{n+1}), \quad (3.32)$$

where $M = \ell/(ct_s)$ and I_n is the discretized version of the integral of p .

In order to explore the oscillating regimes of the model, a cartography is calculated by time-integration, describing the peak-to-peak amplitude of the last 0.1 s of the pressure signal p in simulations of 1 second of sound each, with different values of γ and ℓ . Figure 3.28 presents this cartography. The mouth pressure parameter γ varies from 0.25 to 0.5, around the threshold where oscillations appear, at about $1/3$. The lengths ℓ range from 0.3 m, below x_1 , to 1.1 m which is approximately the total length of an alto saxophone resonator. A change in behavior appears at the apparition of the oscillation ($\gamma \simeq 0.35$), depending on the value of the length ℓ : for $\ell < x_1$ the amplitude of the oscillations increases smoothly with γ , and for $\ell > 2x_1$ the change in amplitude is brutal. There is an intermediary region with a smooth increase of the amplitude followed by a brutal jump. This could indicate a change in the nature of the Hopf bifurcation, from super-critical to sub-critical. To verify this idea, we use harmonic balance, and continuation in function of γ for 3 particular values of ℓ : $\ell = x_1 = 0.4$, $\ell = 0.6$ m and $\ell = 1$ m.

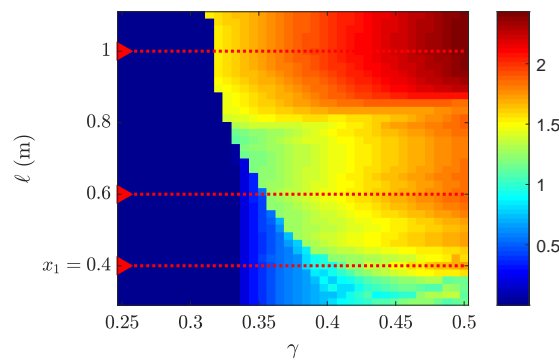


FIGURE 3.28: Cartography of the final peak-to-peak amplitude of the internal pressure signal p . Red dotted lines: particular values of ℓ where the bifurcation is studied by continuation (figures 3.30 and 3.29).

3.7.3 Continuation with harmonic balance method

A Taylor-series based continuation method, called asymptotic numerical method (ANM), is used. It is based on the numerical continuation of a system of equations

$$R(X, \lambda) = 0 \quad \text{where } X, R(X, \lambda) \in \mathbb{R}^n \text{ and } \lambda \in \mathbb{R}. \quad (3.33)$$

The parameter λ is the continuation parameter and the vector of unknowns is X . The solution-set of equations (3.33) can be represented as a collection of (one-dimensional) curves in the total space (X, λ) . The ANM has the specificity to require a specific treatment of the equations to obtain an equivalent system of equation with at most quadratic nonlinearities [GCV19]. This allows to compute an approximation of the solution branches $(X(a), \lambda(a))$ on the form of Taylor series

$$X(a) = X_0 + X_1 a + X_2 a^2 + \dots \quad \text{and} \quad \lambda(a) = \lambda_0 + \lambda_1 a + \lambda_2 a^2 + \dots \quad (3.34)$$

where a is a parametrization of the solution-branch which verifies here $a = X_1(X - X_0) + \lambda_1(\lambda - \lambda_0)$. In the present work, the equation of the model is discretized in the frequency domain using harmonic balance method (HBM), that is a truncated Fourier expansion of the unknown

$$p(t) = p_0 + \sum_{k=1}^H p_{c,k} \cos(k\omega t) + p_{s,k} \sin(k\omega t) \quad (3.35)$$

This ansatz is put in the quadratic recast of the model equation in order to obtain a system of the form (3.33) where X is a vector containing the all Fourier coefficients and the unknown angular frequency ω . The parameter λ is γ or ℓ in the following study. The truncated Fourier expansion (at order $H = 50$ in the applications) of p and the angular frequency ω are then

known along the solution branch. The generalization of the coupling between HBM and ANM in the case of systems with time-delay has been done in [GVC19].

3.8 Results

The results in this section are presented on the form of several figures. On these figures, the amplitude and the angular frequency of the acoustic pressure p computed with the continuation method are represented in blue solid lines. The truncation order for the Fourier series is $H = 50$. The red crosses are the point-wise periodic solutions given by the sound synthesis algorithm. The red circles are quasi-periodic steady state solutions. The comparison is made for values of the parameters along the red dotted lines of the figure 3.28. The agreement of both methods is very good on most of the results. A surprising feature of the system at ℓ fixed is that even if the Hopf bifurcation seems super-critical in all cases, the larger ℓ is, the sooner the Hopf bifurcation is followed by a first fold bifurcation (or limit point), before the second one where the periodic solution retrieves its stability. For ℓ sufficiently small (see right figure 3.30) the two fold bifurcations are getting closer and with less effect on the dynamics of the system. However, in this case the periodic solution seems to become unstable quickly to the benefit of a quasi-periodic solution obtained with sound synthesis. In terms of frequency, a pitch-flattening effect is observed for high γ values, but before the first fold bifurcation, the pitch rises when γ augments.

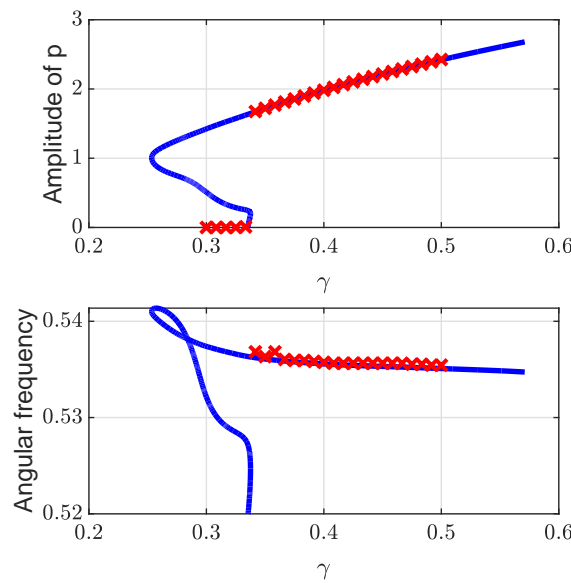


FIGURE 3.29: Bifurcation diagram representing the final peak-to-peak amplitude and the frequency of the internal pressure signal p , for $\ell = 1$. Blue line: continuation and harmonic balance. Red crosses: sound synthesis.

3.9 Conclusions

For this simple saxophone model, the Hopf bifurcation is never found to be sub-critical, but hysteretic behavior can appear due to the presence of two fold bifurcations, which are increasingly far apart as the length of the resonator augments. Further work may include a study of the dependence of these phenomena on the volume of the mouthpiece or the reed opening control parameter ζ , as well as a study on the stability of the equilibrium and the oscillating solution in the region where they coexist.

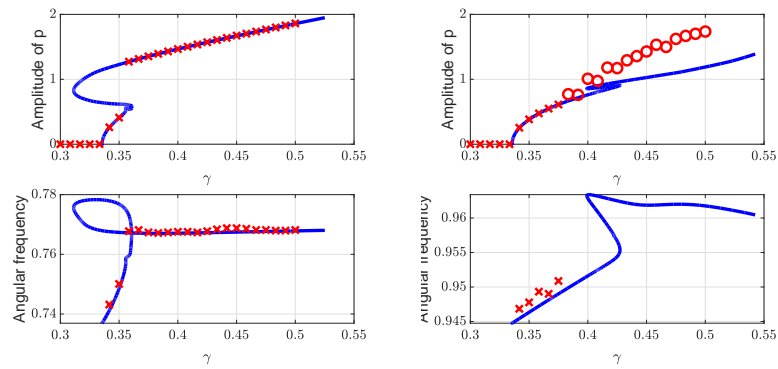


FIGURE 3.30: Bifurcation diagram representing the final peak-to-peak amplitude and the frequency of the internal pressure signal p . Blue line: continuation and harmonic balance. Red crosses: sound synthesis. Left : $\ell = 0.6$. Right : $\ell = 0.4$.

Chapter 4

Sound production cartography in the space of musician control parameters

4.1 Introduction

The present chapter discusses the representations of the nonlinear dynamics of a saxophone model in the control parameter space. This space represents the range of actions of the virtual musician. Representing the dynamics of the model in this control space amounts to linking point or regions of this space to a corresponding produced sound. Ideally, the maps obtained through this process of *sound production cartography* hold information that is preliminary to the notion of "ease of playing". On such maps, a tiny control parameter region leading to a given regime means that very few control situations lead to this regime being produced. One could state that having very few control options to produce this regime indicates that it is 'hard' to obtain using the model – which, hopefully, points to it being hard to play by the musician on the real instrument. Reciprocally, a large control parameter region leading to a given regime potentially indicates that it is 'easy' to play, provided the region is in a humanly attainable range of the control parameters. Thus, sound production cartography is a way to characterize the broad dynamic features of an instrument, in a way that is directly linked to the estimation of the "ease of playing".

The approach presented in this chapter differs from that of Chapter 3 both in its methods and its goals. Here, the dynamics of the instrument are explored through through the whole control parameter space, and not just limited to a single continuation parameter. Furthermore, the objective shifts from merely describing the dynamics of the model to interpreting them and linking them to designing or playing the instrument. Note, however, that sound production cartography does not immediately indicate the "ease of playing" of the corresponding instrument – notably for lack of controlled experiments quantifying the ease of playing. Actually, multiple biases (detailed in the chapter) entail that cartography is only an incomplete representation of the model's behavior. Taking into account these fundamental issues, sound production cartography is used as a method of comparison: between two instruments, fingerings, models... Fortunately, this framework leaves many possible applications for the cartography, and careful choice of the compared maps reveal a lot about the nonlinear dynamics of the saxophone.

In our case, the control parameter space includes coordinates γ (blowing pressure) and ζ (action on the reed), but also the reed eigenfrequency ω_r and damping q_r , that the player can modify with their lip. Even with our relatively simple model, the control parameter space is at least 4-dimensional, which hinders clear and complete visualization of the data. Therefore, for this study pertaining specifically to the representation of dynamics, a two-dimensional projection is used. Using two dimensions to represent the behavior of a woodwind model can be seen in founding work [WB74], followed by [Sil+08; KVC12b], to represent instability thresholds in a plane corresponding to (ω_r, γ) . In the present work, the variable parameters are always the blowing pressure γ and the reed opening parameter ζ . However, all the methods and representation presented hereafter can be generalized directly to include a reed parameter instead of γ or ζ .

As for all the numerical results presented in this work, two approaches are distinguished and used to complement each other's results. First, section 4.2 uses time-domain synthesis

to map out the behavior of the model. In strict application of the idea of sound production cartography, signals are synthesized over a grid of control parameters, and descriptors (such as fundamental frequency) are extracted from these signals and represented on the grid so as to constitute a *map*. Note that this representation is incomplete because it only uses a discrete set of points in the control parameter space. There is no strict way, in the case of a strongly nonlinear model, to predict what occurs between the points. Furthermore, the representations only allow one type of regime to be associated with a given control parameter set. This amounts to ignoring some effects of the strong nonlinearity, notably the fact that several regimes can coexist for a given set of control parameters, and one or the other can be produced depending on the system's history. This multistability phenomenon and the possible bias it entails are discussed at length in Chapter 5. Here, it is all the more reason to use sound production cartography as a comparative tool. We present a convenient representation for the comparison, obtained by overlaying two regime maps. Several illustrative example give perspective on how regime maps relate to a real instrument's behavior. Namely, we show how opening the register hole affects the type of the produced regimes – in particular, how much it favors the second register regimes. Then, two alto saxophones from different brands (the ‘target’ and ‘control’ from chapter 2) are also compared, to get an idea of how close the maps appear if the instruments are both accepted playable saxophones. To end section 4.2, the behavior of the bicylindrical resonator optimized in chapter 2 is mapped out against its optimization target, the Buffet-Crampon Senzo.

The second approach, in section 4.3, is a less direct application of the cartography method. It uses numerical continuation of Hopf points to provide a view of the instability thresholds of a given model. This outlines the regions of the control parameter space where the equilibrium (silent regime) is unstable. This method is presented here as the basic idea for a possible alternative to time-domain synthesized regime maps which, instead of describing the produced sound on a set of control points, would use bifurcation continuation to outline the stability domains of interesting regimes. The Hopf continuation procedure is only the first step in such endeavor, the next posing many practical and theoretical difficulties. However, the Hopf continuation by itself has the advantage of being very fast (a few seconds computation time, against a few hours for a compelling regime map). Although the instability thresholds have an unambiguous mathematical definition, they only provide limited information as to the regimes that are effectively produced by the model. Nevertheless, they can be used as an indicator of the dynamic behavior, more informative than the mere modal parameters, but quicker than a complete bifurcation diagram or regime map. This method is used to outline the similarities and differences that exist in the dynamics of the saxophone family, by representing the threshold for soprano, alto and tenor saxophones.

4.2 Cartography

In this document, the word *cartography* refers to a representation of the behavior of an instrument in a multi-dimensional control parameter space. The Figure 4.1 constitutes a *regime map* in two dimensions γ and ζ , where the color coding represents the type of the signal produced for each point: first, second or third register, quasi-periodic regime, or equilibrium. This map corresponds to a grid of control parameter couples (γ, ζ) , with 50 distinct values of γ between 0.2 and 1, and 50 distinct values of ζ between 0 and 1. This amounts to a total of 2500 parameter couples, each of which is used in sound synthesis to produce a signal of 3 seconds. The total computation time of 16 of these maps (the number of studied fingerings in a register) is about five hours on a laptop computer. The synthesis was performed with the reflection function formalism (see section 1.2.1) and trigonometric function regularizations (section 1.1.3.2), with the parameter values given here in table 4.1.

The produced signal is then subjected to descriptor extraction presented in subsection 4.2.1. At this point, it should be noted that the control parameter transient is a step (from 0 to the final value in one sample). This unphysical control transient gives a view of the system's behavior biased in favor of oscillating and quasi-periodic regimes (for more details on the influence on control parameter transients, see chapter 5). It is because of this known bias that the regime maps in this chapter are only presented in overlaid pairs, so that they are used as a comparative tool between two instruments.

Parameter	Notation	Value
Reflection function truncation index	D	1500
Reed angular frequency	ω_r	4224 rad.s ⁻¹
Reed damping	q_r	0.44
Pressure equilibrium regularization	V_a	0.05
Reed opening regularization	O_a	0.05
Sampling rate	F_s	44100 Hz

TABLE 4.1: Parameters of the model. Parameters with no units are dimensionless.

Figure 4.1 decomposes the last map of Figure 4.3 in order to make the process clearer. The color on the regime maps indicates the type of regime, with the white region of the map corresponding to the equilibrium (silent regime). The two regime maps are then overlaid, with the one at the foreground displayed as contours outlining the region of production of each regime. In that example, the separate regime maps clearly show which regime appear in either configuration, but overlaying them opens the door to more comments. In particular, it is easy on overlaid maps to notice the change in the oscillation threshold (the boundary between equilibrium and oscillating regimes), although it demands a close look at the separate maps. Superimposing maps also exhibits the absolute location of the regions immediately, in addition to facilitating the comparison of their sizes. In the present examples, the relative size of the second register region appears clearly different on the separate maps. The overlaid version clearly shows that the second register region of the background is included in that of the foreground.

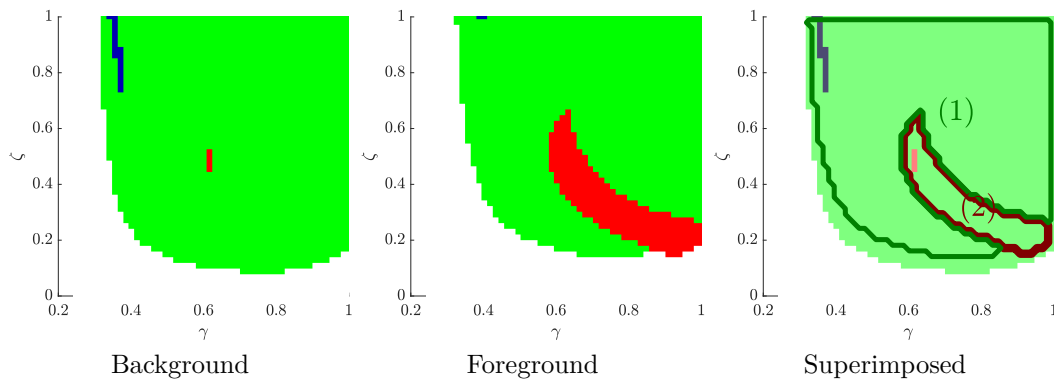


FIGURE 4.1: Cartography (regime map) example: register produced by the synthesis model. The left and middle map are superimposed in the right frame to facilitate their comparison. 1st register: ■ ; 2nd register: ■ ; quasi-periodic: ■.

This section, rather than proving fundamental points on the behavior of the instrument like the chapter 3, is aimed at presenting the interest and the promise in the cartography representation and engage a reflection as to its use. Therefore, we present three illustrative examples. The first two examples give a notion of the sensitivity of the regime maps. They are not meant to provide conclusive statements about the instruments themselves, but rather as reference points according to which further comparisons can be realized. These two examples compare physical objects. First, subsection 4.2.2 studies the effect of the register hole on sound production, by comparing fingerings with the register hole is closed or open. The effect of opening the register hole on a real saxophone can be formulated as "strongly favoring second register production". The associated cartography gives a sense of how such effect translates on regime maps. The second example in subsection 4.2.3 compares the same fingerings between a saxophone and another saxophone. Although the two saxophones are of different make and different quality, comparing these regimes maps give a notion of how similar two maps can be between two commonly played saxophones. The third example (4.2.4) compares the designed bicylindrical resonator from chapter 2 with its target saxophone. This example demonstrates

one foreseen usage of cartography, as an extension for numerical optimization to provide further virtual assessment of a designed instrument.

4.2.1 Computing descriptors

For a given synthesized signal, we use the following procedure to estimate the playing register. First, a rough estimate of the playing frequency $f_{p,0}$ is obtained by detecting the maximum of the auto-correlation function of the signal. The ratio between $f_{p,0}$ and the frequency of the first impedance peak is rounded to give the estimated playing register. To detect quasi-periodic regimes, we use a criterion inspired by [DVM14]. We apply a filterbank centered on the first 4 multiples of $f_{p,0}$, corresponding to the harmonics of the signal. To eliminate the effects of the transient, the first 0.5 s of the signal is ignored. For each output of the filterbank, the variance of the instantaneous frequency is much larger for quasi-periodic regimes than for well-established periodic regimes. Comparing the variance with a variance threshold allows to classify quasi-periodic regimes robustly. It must be pointed out that, according to this method, signals whose transient duration is more than 0.5 s qualify as "quasi-periodic". Finally, the fundamental frequency is precisely estimated by averaging the instantaneous frequency of the output of the filterbank corresponding to the fundamental.

4.2.2 Effect of the register key on regime production

This first example of application of the regime maps presents the effect of opening the register key. This is chosen in order to give perspective on how regimes map relate to a well-known musical action, opening the register hole. Figure 4.2 displays the impedance of three fingerings, when the register hole is closed (black) or open (red). As expected, for the three fingerings, the first impedance peak is affected by opening the register hole, which reduces its height and pushes it towards higher frequencies. The other resonances are only lightly altered. This effect on the impedance is expected to greatly decrease the production of the first register, to the profit of the second and the third register. Indeed, the musical role of the register key is to favor the production of the second register.

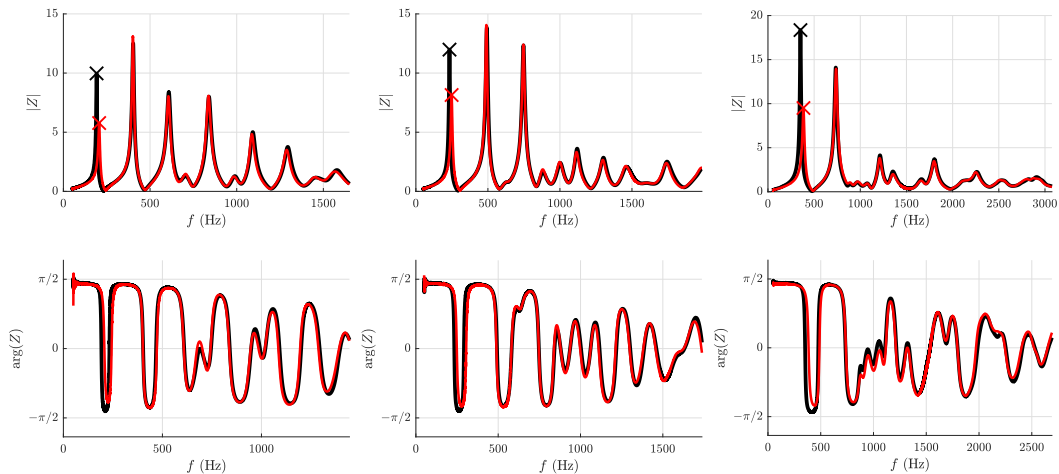


FIGURE 4.2: Impedance modulus and phase for fingerings $D\sharp$, $F\sharp$ and middle C (first register) of the Buffet-Crampon Senzo alto saxophone. **Black**: first register (register hole closed), **red** second register (register key open).

Figure 4.3 overlays the regime maps of fingerings with the register hole closed to those of the same fingerings with the register hole open. When looking at figure 4.3's backgrounds only, which correspond to a closed register hole, it is important to see that the second register is still prone to appear in a large region of the control parameter space. This is especially true for the lowest fingerings $D\sharp$ and $F\sharp$. First register sounds mostly appear for high ζ values (most open reed channel at rest) and low blowing pressure γ . The middle C fingering shows second register for only a few control parameters couple when the register hole is closed. This

is imposed by the first impedance peak being significantly higher than the second one (see figure 4.2).

The foreground contours on figure 4.3 outline the region of production of the different regimes with an open register hole. The $D\sharp$ and $F\sharp$ fingerings produce second register almost everywhere in the parameter space when the register key is open. Nevertheless, first register still appears on both these fingerings for the highest ζ and lowest γ . For the middle C fingering, opening the register hole makes more second register appear, but it does not fill the parameter space as well as for lower fingerings. This is coherent with the musician's experience, according to which the second register becomes harder to produce on higher fingerings, even when opening the register hole. However, the small size of the second register region for the middle C fingering, even when register hole open, incites to caution as to direct interpretation of a regime map in terms of "ease of playing". The second register is in fact considered relatively easy to produce by musicians on these fingerings, and this map makes it appear difficult. This may be explained by the fact that the reed parameter are considered constant (and fixed arbitrarily) in this case. Regardless of the explanation, keeping to strictly comparative comments once again appears more satisfying. On the middle C map, the oscillating zone of the foreground is shrunk compared to the background, with the γ and ζ oscillation thresholds occurring slightly higher. This is linked to the first impedance peak being lower, as discussed in section 4.3.

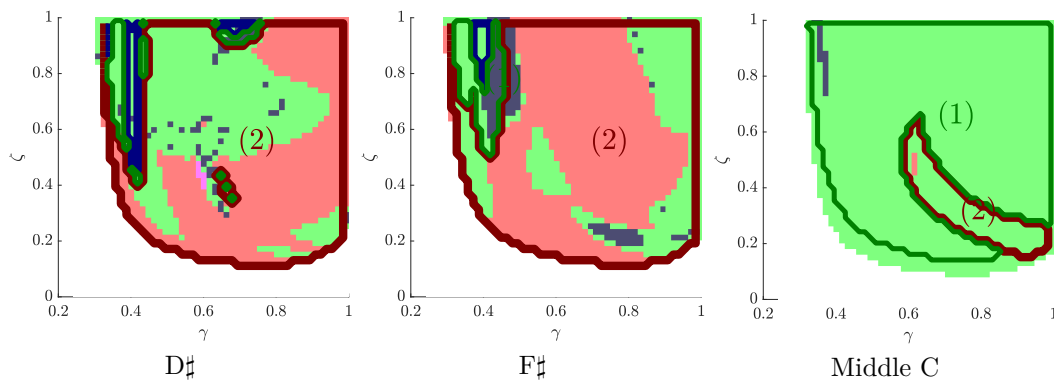


FIGURE 4.3: Register produced by the synthesis model with the input impedances of figure 4.2. Background, faded: register hole closed ; contour, dark: register hole open. 1st register: green ; 2nd register: red ; quasi-periodic: dark blue.

This introducing example prompts care in the examination of the regime maps. In particular, the meaning of small isolated control parameter regions leading to a certain regime (such as the few first register points appearing around $\zeta = 0.4$ and $\gamma = 0.6$ for the $D\sharp$ fingering in figure 4.3) should be taken lightly. Interpretations of regime maps should stay comparative and based on their large-scale features rather than details.

4.2.3 Comparison between two alto saxophones

As a second example of application of the regime maps, two alto saxophones are compared together in figure 4.5: the Buffet-Crampon Senzo (in the background) and the Yamaha Alto Saxophone (YAS-280) in the foreground. Figure 4.4 shows that the impedances of both resonators are very close together. The main difference is that the first peak is always slightly higher for the YAS. A frequency discrepancy can also be observed on the second and third impedance peaks. Therefore, the regime maps computed from these impedances illustrate the difference they can exhibit between extremely similar instruments.

Figure 4.5 overlays the regimes produced in synthesis by the Senzo (background) and the Yamaha Alto Saxophone (foreground, contour). All three regime maps correspond rather well to each other, especially for the lowest fingering $C\sharp$, where the complicated imbrications of the regime production regions globally fit. It can be noted that on this regime map, the region of production of the first register is larger for the YAS. This may be related to its higher first impedance peak. This is also true on the highest fingering here, $G\sharp$, where both second

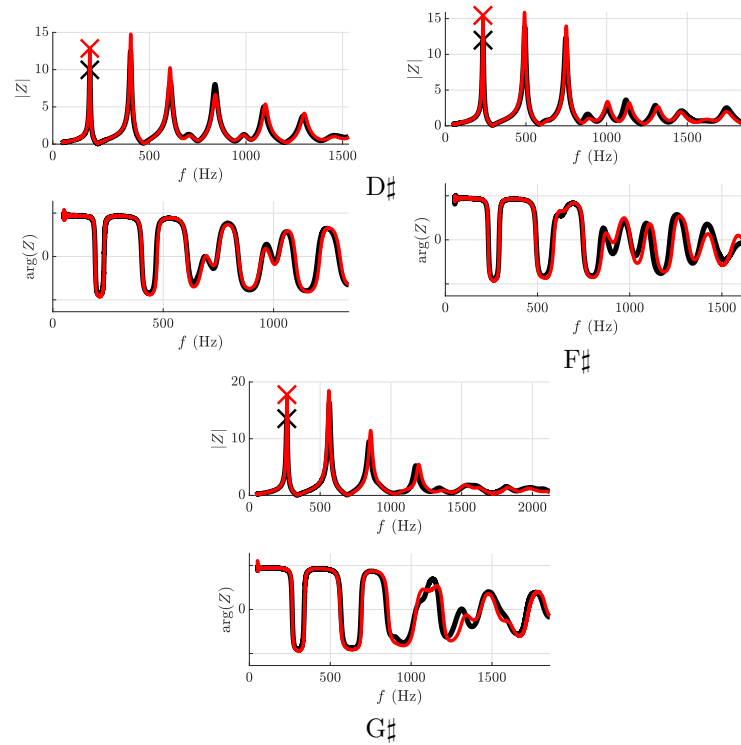


FIGURE 4.4: Impedance modulus and phase for fingerings $D\sharp$, $F\sharp$ and middle C (first register) of the Buffet-Crampon Senzo alto saxophone (**black**) and the Yamaha Alto Saxophone (YAS-280) (**red**).

register zones shrink when passing from Senzo (background) to YAS (foreground). The same phenomenon appears in a more drastic manner for the middle fingering, $D\sharp$, where a large portion of the central second register production zone for the Senzo is replaced by first register for the YAS.

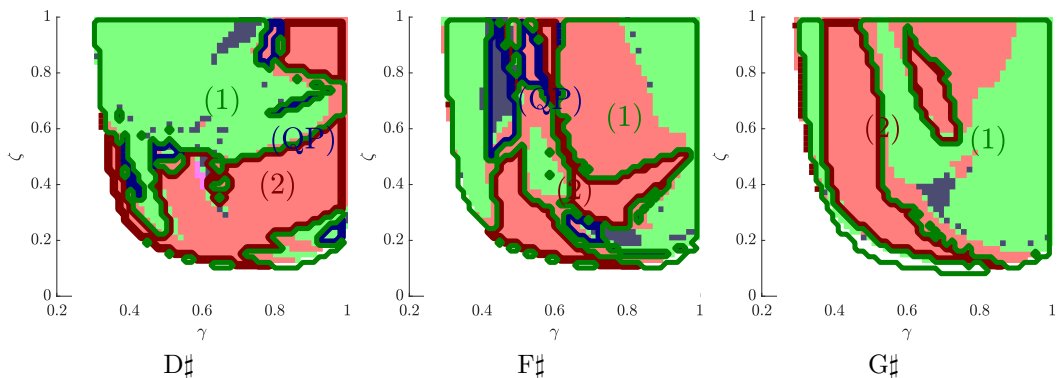


FIGURE 4.5: Register produced by the synthesis model for two alto saxophones. Background, faded: Buffet-Crampon Senzo; contour, dark: Yamaha alto saxophone. 1st register: green ; 2nd register: red ; quasi-periodic: dark blue.

Figure 4.6 displays the playing frequency (fundamental frequency of the synthesized signals) for the same fingering of both models. The middle C fingering, which produces first register almost everywhere, is chosen so that global pitch variation trends appear clearly. The pitch is displayed as a discrepancy in cents when compared to the pitch that is traditionally expected for this fingering according to equal temperament. This gives a certain view off the intonation of the produced signals. Both pitch maps share the same overall profile, with two pitch-flattening regions: one towards for the highest ζ and lowest γ values, and the other for the highest γ values, near $\zeta = 0.5$. Note that the maximum pitch of both models differs

by about 20 cents, which is perfectly audible for a human listener. The amplitude between lowest and highest pitch on the map is comparable in this case, about 100 cents. This value is much lower than the pitch bends an experienced musician can produce with their vocal tract: [Gui+10] shows a downward pitch bend of 190 cents. However, the range of the cartography is comparable with the value obtained when the musician doesn't use their vocal tract: [Gui+10] observes a downward pitch bend of 70 cents in that case. The pitch range is an interesting quantity to look at, because it could be linked to how the instrument is receptive to pitch adjustments applied by the musician. In that regard, it introduces another dimension to the study of a pitch map: in addition to the mere intonation, the map shows how flexible the instrument is. It remains to be determined if musicians favor an instrument which precisely imposes the playing frequency, or an instrument that is easy to adjust around each note.

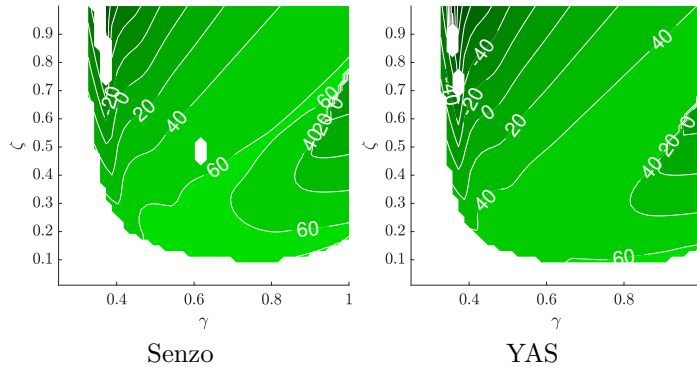


FIGURE 4.6: Fundamental frequency (discrepancy in cents from the expected equal temperament pitch) for fingering middle C of the Buffet-Crampon Senzo and Yamaha Alto Saxophone.

This illustrates how regime maps, although biased, are interesting comparative tools, capable of highlighting the effect of small impedance differences between two instruments. They synthesize the complex acoustical properties of a resonator and tend towards direct musical interpretations.

4.2.4 Comparison between the alto saxophone and bicylindrical resonator

As a supplement to the optimization procedure undertaken in chapter 2, regime maps are produced using the optimized bicylindrical resonator and the target alto saxophone. This is intended as a way to virtually test the designed instrument before building a prototype.

Figure 4.7 represents these regime maps for three fingerings: the low B and the A of the first register, whose input impedance is shown in figure 2.9, and the middle B. These fingerings were chosen because they span most of the first register, and they are representative of the trends that can be observed on the other fingerings (that are not displayed here for brevity). It can be seen that sound synthesis applied to the optimized bicylindrical resonator produces less first register regimes than for the Senzo. For the low B on the bicylindrical resonator, almost all the parameter space leads to third register regimes. For the A fingering, the second register region is larger for the bicylindrical resonator than for the Senzo, in proportions comparable to the effect of opening a register hole (see figure 4.3). Only for the highest fingering presented here does the bicylindrical resonator map contain as much first register as the Senzo. These problematic behaviors can be due to the second peak being comparatively much higher on the bicylindrical resonator for all the lowest fingerings, as exhibited in figure 2.12. The lack of first register production is also possibly aggravated by the inharmonicity of the first two peaks being less positive than for the Senzo as shown in figure 2.11 (for a more in depth discussion, see section 5.6).

Low fingering issues notwithstanding, the study of the synthesis model applied to the bicylindrical resonator can be completed by a pitch map, applied to the middle C fingering. Figure 4.8 compares pitch maps for the Senzo and the bicylindrical resonator. Here, the pitch spread is larger for the bicylindrical resonator (120 cents vs. about 80 cents), and more

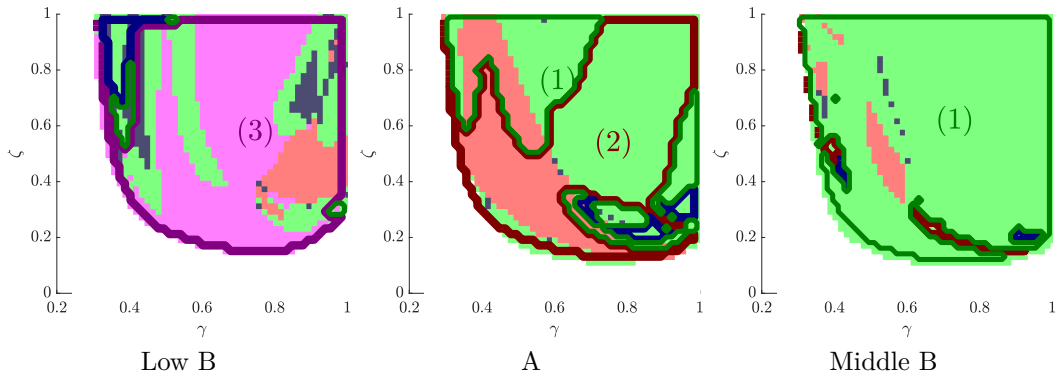


FIGURE 4.7: Register produced by the synthesis model. Background, faded: target (Senzo); contour, dark: designed bicylindrical instrument. 1st register: green; 2nd register: red; 3rd register: purple; quasi-periodic: dark blue.

importantly the overall pitch is about a quarter-tone lower for the bicylindrical instrument. This could be indicative of an intonation issue. It remain to be seen if this intonation issue is one that can be corrected by usual tuning methods, such as pushing the crook further into the mouthpiece. If not, the geometry of the body itself should be adjusted to make the instrument more in tune.

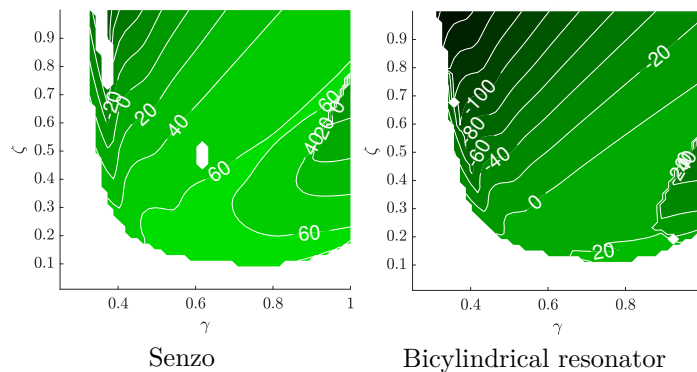


FIGURE 4.8: Fundamental frequency (discrepancy in cents from the expected equal temperament pitch) for fingering middle C of the Buffet-Crampon Senzo and the optimized bicylindrical resonator from chapter 2.

The regime maps applied to the bicylindrical resonator seem to indicate that the instrument would be extremely hard to play on the first register, and possibly out of tune. As pointed out in the conclusions of chapter 2, the bicylindrical resonator behaves differently than a saxophone, and it is likely that attempts at conceiving a bicylindrical woodwind cannot be based only on a saxophone's acoustical characteristics. Improving the acoustical characteristics based on considerations on the dynamic behavior can orient the development of a bicylindrical instrument. This final application shows the potential of sound production cartography as a powerful tool of evaluation of a virtual prototype. However, the quantity of information in a cartography and the relatively high computational cost push to explore other lighter cartography methods such as Hopf bifurcation continuation.

4.3 Emergence of regimes: Hopf bifurcation continuation

As a simple indicator of the nonlinear dynamics of the model, this section focuses on instability thresholds. The instability threshold marks a control parameter values where an oscillating regime emerges from the equilibrium, which becomes unstable. This point is characterized in standard unidimensional continuation by a Hopf bifurcation (see subsection 1.2.2.3). To

generalize the search of the instability threshold to a multidimensional control parameter space as per the idea of sound production cartography, we use the method of Hopf bifurcation continuation. This method yields the continuous line formed by a Hopf bifurcation in a two dimensional space. Beyond this line, the equilibrium is unstable and the model oscillates: a sound is produced. Therefore, this threshold is a global characteristic of the model's dynamics, that constitutes a simpler alternative to the regime and pitch maps presented in the previous section.

This section studies the threshold associated with the first, second and third register. The first two hold clear musical interest, as they are commonly required in musical pieces. The third register is less used, especially with the standard first register fingerings dealt with here. However, it remains included in our results for several reasons. First, including the more undesirable regimes into dynamic studies nuances the results, by introducing negative effects to be put up against the positive ones. Then, the third register instability threshold exhibit a clear discrepancy with the analytical formulas, while the two others registers follow them well. Lastly, it presents interesting variations due to other modes, which shed light on the modal interaction phenomena.

4.3.1 Preliminary: simple analytical formulas for instability thresholds

The problem of locating the control parameter value above for which the equilibrium loses stability lends itself well to analytical formulations, because it can be expressed using a linearization of the model around the equilibrium. A first formula was proposed in [WB74] for a cylindrical tube, which was refined in [Sil+08]. The formulae we use in this work are based on [GGL97] because they are easily applicable to any impedance. The first analytical approximation of the reed resonance, ignoring reed dynamics, is given by

$$F'_r(\gamma, \zeta, p)|_{p=0} = \frac{1}{Z(\omega_0)}, \quad (4.1)$$

where F'_r is the derivative with respect to p of the regularized nonlinear characteristic F_r deduced from the nonlinear characteristic F of Eq. (1.14), and ω_0 is the angular frequency of the oscillation. The angular frequency ω_0 is such that $Z(\omega_0)$ is purely real, because $F'_r(p=0)$ is real. Note that the raw nonlinear characteristic of Eq. (1.14) could lead to problems when used directly into Eq. (4.1), because it is not differentiable everywhere. Therefore, [GGL97] uses a third order polynomial expansion of the characteristic, which ignores the annulation of the flow at $\gamma \geq 1$. Therefore, this formalism does not describe the equilibrium with a closed reed channel. In this work, we use the derivative of the regularized version of the characteristic using the square-root-based regularization of Eq. (1.17). In order to be as explicit as possible, we write the regularized characteristic

$$F_r(\gamma, \zeta, p) = \zeta \frac{1+p-\gamma + \sqrt{(1+p-\gamma)^2 + \eta}}{2} \frac{\gamma-p}{\sqrt{(\gamma-p)^2 + \eta}} \sqrt{\sqrt{(\gamma-p)^2 + \eta}}, \quad (4.2)$$

and its derivative at $p=0$ (equilibrium)

$$F'_r(\gamma, \zeta, p)|_{p=0} = \frac{\zeta}{2} \frac{\sqrt{(1-\gamma)^2 + \eta} - \gamma + 1}{\sqrt[4]{\gamma^2 + \eta}} \left(\frac{\gamma^2}{2(\gamma^2 + \eta)} + \frac{\gamma}{\sqrt{(1-\gamma)^2 + \eta}} - 1 \right). \quad (4.3)$$

Note that this expression only depends on control parameters γ and ζ , and the regularization parameter η . Taking into account reed dynamics leads to modifying Eq. (4.1) by introducing the transfer function due to the reed dynamics, which is obtained by Fourier transform of Eq. (1.5). Following the classic *ghost reed* approximation, we ignore the contact force F_c . This might have influence for values of γ superior to 1, but as illustrated in section 3.4, the ghost reed approximation has little influence on small oscillations. The equation giving the

instability threshold with ghost reed dynamics is

$$F'_r(\gamma, \zeta, p)|_{p=0} = \frac{-\omega_0.^2/\omega_r^2 + j\omega q_r/\omega_r + 1}{Z(\omega_0)}, \quad (4.4)$$

where ω_r and q_r are the reed parameters defined in Eq. (1.5). Note that the whole right-hand side must be real in this case, which entails that ω_0 changes because of the reed dynamics, and therefore $Z(\omega_0)$, with marked impact on the instability thresholds.

4.3.2 Principle of the Hopf continuation

The Hopf bifurcation continuation is implemented using an extended system. Much like the fold continuation of subsection 3.2.3, the augmented system is obtained by introducing equations concerning the eigenvectors and eigenvalues to the original physical system, to ensure that it verifies the conditions for a Hopf bifurcation. The Hopf continuation bears a considerable difference with the fold continuation of subsection 3.2.3: it concerns non-oscillating regimes, so using the HBM is rendered unnecessary. This entails a smaller number of equations of unknowns, and therefore a very reasonable computational cost.

The extended system follows [Kuz95], with the model's equations at Hopf point \mathbf{X}_H assorted with an eigenvalue equation

$$J_{\mathbf{X}_H} \mathbf{p}_H = j\omega_0 \mathbf{p}_H, \quad (4.5)$$

whose unknowns are the critical eigenvector \mathbf{p}_H and the purely imaginary eigenvalue $j\omega_0$. This represents as many equations as there are unknowns in vector \mathbf{p}_H . The eigenvector \mathbf{p}_H is also assigned normalization and orthogonality conditions

$$\mathbf{p}_H^t \mathbf{p}_H = 1, \quad Re(\mathbf{p}_H^t) Im(\mathbf{p}_H) = 0. \quad (4.6)$$

These two additional equations make up for two additional unknowns: ω_0 and μ . The unknown ω_0 is the angular frequency of the oscillating regime emerging for the Hopf bifurcation, and μ is the generic notation the second continuation parameter (when the first is λ). Recall that in the context of this chapter, the first continuation parameter is γ , and the second is ζ . The cartography is realized by applying continuation with the ANM to the extended system, which yields the location of the Hopf bifurcations in a plane comprised of the two continuation parameters γ and ζ .

Figure 4.9 overlays the results of numerical Hopf continuation on the analytical results with reed dynamics (Eq. 4.4) and without (Eq. 4.1), for a medium fingering (D) of the first register of the Buffet-Crampon Senzo alto saxophone. All three first registers of the instrument are associated with a Hopf bifurcation for this fingering. The inside of these curves correspond to the control parameter region where the corresponding oscillating regimes exist. It can be seen that the numerical results match the analytical formulas for the first register, less so for the second register and even less so for the third. Unsurprisingly, the analytical formula that does not account for reed dynamics is farthest for the highest registers. Taking into account reed dynamics makes the analytical approximation closer to the numerical results, but it does not accurately follows the low γ part of the third register instability threshold. This difference may be due to degenerate resonances, or more generally the interactions between the modes.

Comparing usual simple analytical approximations for instability thresholds with the results of the Hopf continuation procedure shows that some nuances are missed by the analytical results, especially on higher registers. Therefore, the rest of this section presents the instability thresholds obtained by Hopf point continuation, but it would be interesting to test further into analytical methods to approach the numerical results even closer.

4.3.3 Effect of varying modal parameters on Hopf bifurcations

This paragraph studies how the acoustical parameters of the resonator affect the position of the instability thresholds of the instrument. It can be seen as a study of sensitivity of this indicator to modification of a resonator. The results are used afterwards in this document to shed light on the comparison between the instability thresholds of different saxophones.

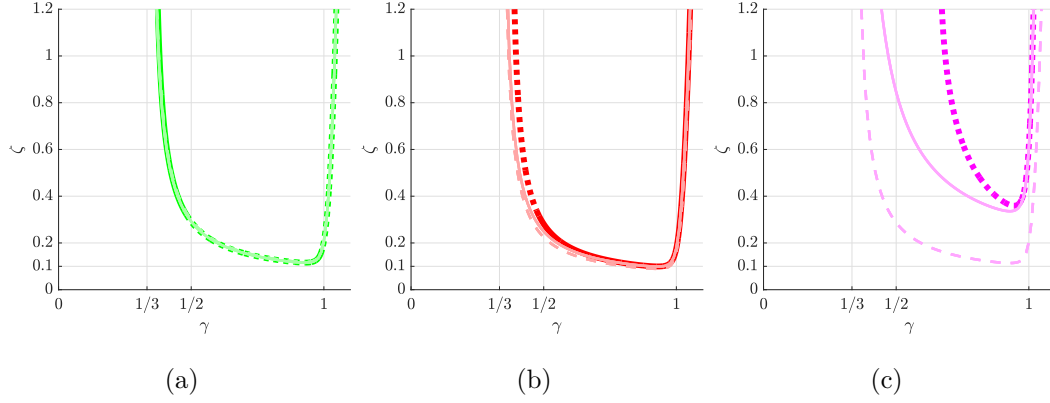


FIGURE 4.9: Hopf bifurcations for the D fingering with $N_m = 3$ modes. Thick line: Hopf bifurcation continuation – solid: stable equilibrium at Hopf bifurcation, dotted: unstable equilibrium at Hopf bifurcation. Thin clear lines: analytical approximations – dashed: no reed dynamics Eq.(4.1), solid: reed dynamics (4.4). (a) first register (b) second register (c) third register.

However, by themselves, they can also hold information relevant to instrument making, by giving a notion of how a fabrication error leading to the modification of a modal coefficient can impact sound production.

4.3.3.1 Modal residue and damping

Two of the modal parameter that affect the instability threshold most are the modal damping coefficient α and residues A (see Eq. (1.22)), because they directly affect the height of the impedance peaks located at the resonances. It is clear that the modal residue and damping coefficient of mode k will affect the Hopf bifurcation of register k , but one can ask whether it can impact the higher or lower register as well. For this parametric study to stay somewhat grounded in the study of real resonators, we choose to vary the modal parameters around their value estimated from the measured input impedance. When varying α_k , we set

$$\alpha_k = M \times \alpha_k^m, \quad (4.7)$$

where α_k^m is the k^{th} modal damping coefficient extracted from the measurement and the multiplier M varies between 0.25 and 2.5. Similarly, the modal residue A_k is varied according to

$$A_k = M \times A_k^m, \quad (4.8)$$

where A_k^m is the modal residue extracted from the measured impedance and M also varies between 0.25 and 2.5.

Figure 4.10 represents the evolution of the Hopf bifurcations associated with the first three registers of the lowest D fingering, when varying the modal damping coefficients of the first three modes. The graphs situated on the diagonal depict the evolution of the register associated with the varying modal damping: they are the one that vary most, as expected – for instance based on the analytic approximations in Eqs. (4.1) and (4.4). Varying a given modal damping coefficient does not seem to affect the instability threshold of lower registers, but it can have an impact on the higher register, as the right graph in the second row shows: when varying α_2 the location of the Hopf bifurcation associated with the third register is impacted.

Similar effects appear on figure 4.11, when varying the modal residues. Unsurprisingly, the instability region of register k grows when the height of peak k , which is controlled by A_k , increases. The Hopf bifurcation of the third register is again affected by a variation of the characteristics of the first or second mode. However, contrary to the previous case where α_k is varied, the effect of A_1 and A_2 on the third register is antagonistic with that on the first and

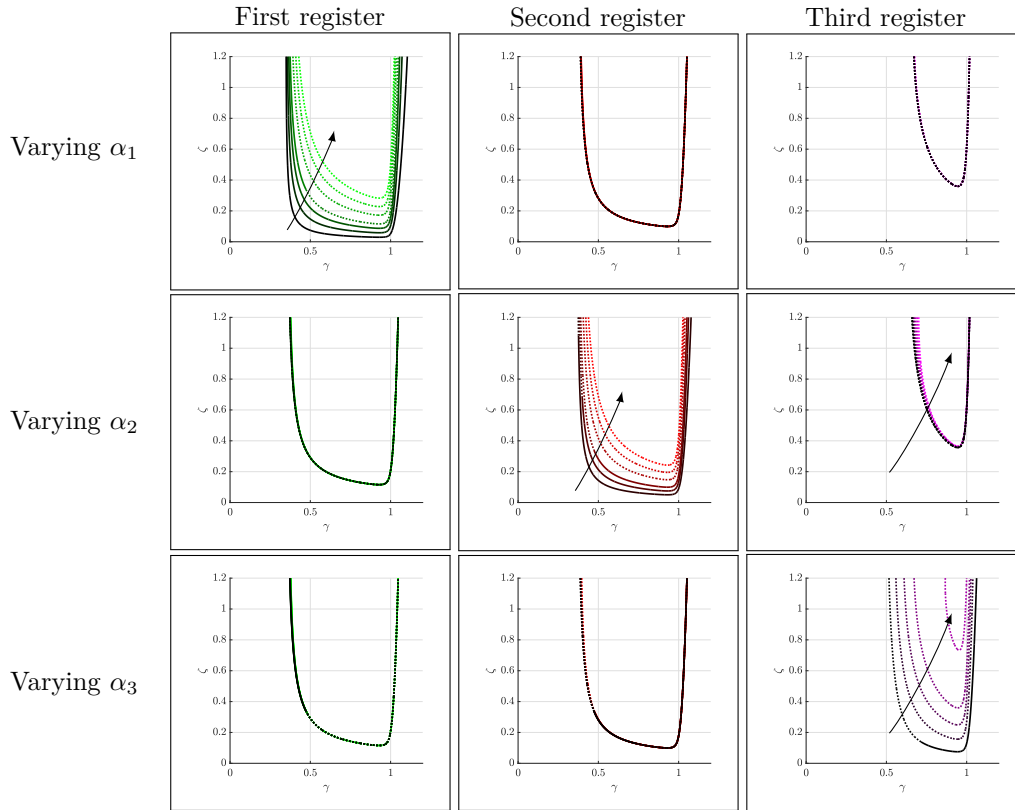


FIGURE 4.10: Effect of varying the k^{th} modal damping coefficient α_k (rows) on the Hopf bifurcation of the k^{th} register (columns) obtained by Hopf continuation. Curve shade indicates the variation of α_k (darkest being the lowest α_k), completed by arrows when the threshold varies sensibly.

second. In this case, when increasing A_1 (or A_2), the third register threshold shrinks while that of the first (or second) expands.

4.3.3.2 Inharmonicity

The influence of another acoustical characteristic on the location of the Hopf bifurcations is tested: the inharmonicity between the first two resonances. This parameter is somewhat variable for the saxophone, being influenced for instance by the size and shape of the chosen mouthpiece. This characteristic is often cited as conditioning regime production in wind instruments [BG68], including brass instrument [GMV19a] and saxophones [DV15]. Examining its effect on the instability threshold is a first way to quantify its influence on global regime production. Figure 4.12 displays the variation of the Hopf bifurcation locations for the three first register of the instrument for fingering D, when varying the second modal frequency f_2 from $1.8f_1$ to $2.2f_1$, while keeping all the other modal parameter constant. Recall that typical saxophone second peak inharmonicity is typically a few percents ($f_2 \sim 2.05f_1$): the variation interval was designed to go well beyond this value. Figure 4.12 shows very little variation of the first and second instability threshold, notably compared to the effects of modal residues and coefficients. The most affected Hopf bifurcation is, rather unexpectedly, that of the third register. We show here that the inharmonicity between the first two resonances has almost no influence on the oscillation thresholds (compared to other modal parameters). However, this parameter still influences sound production, as is discussed in chapter 5.

4.3.4 Comparing oscillation thresholds in the saxophone family

An instrument family is comprised of several instrument with different ranges with a certain homogeneity in geometry, sound quality and playing techniques. As such, instrument families are highly interesting objects, since they represent the options that were derived from a single

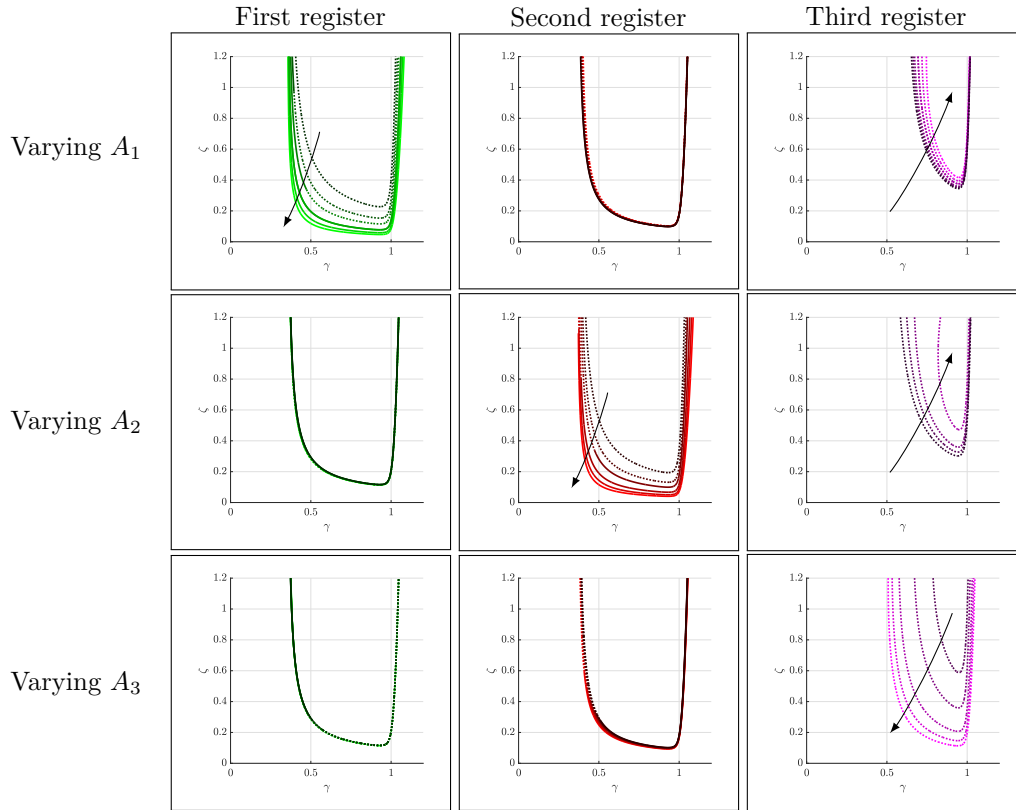


FIGURE 4.11: Effect of varying the k^{th} modal residue A_k (rows) on the Hopf bifurcation of the k^{th} register (columns) obtained by Hopf continuation. Curve shade indicates the variation of A_k (darkest being the lowest A_k), completed by arrows when the threshold varies sensibly.

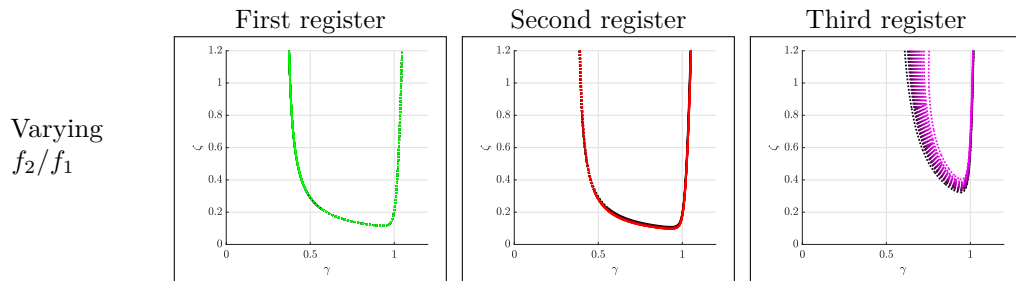


FIGURE 4.12: Effect of varying the inharmonicity f_2/f_1 . Curve shade indicates the variation of A_k (darkest being the lowest f_2/f_1).

geometrical idea and adapted to correspond to the needs and constraints of the musician. Focusing on the common features between the instruments in the same family gives indications as to characteristics that are possibly essential to the homogeneity of the family. These characteristics can be understood as what makes a saxophone be recognized as such. Similarly, any variation that exists in the family signals an effective range of freedom, features that one can adjust or modify to further the evolution of the instrument. From a very practical scientific perspective, looking at a family of instruments is a very oriented parametric study of small dimensions, with only ‘sensible’ parameter values.

4.3.4.1 Preliminary: modal parameters in the saxophone family

As an essential preliminary to the study of the oscillation thresholds *via* a modal formalism, we present the value of the modal parameters of the 4 instruments. The 4 saxophones are the Buffet-Crampon Senzo alto saxophone and 3 Yamaha instruments: the YSS-475 soprano, YAS-280 alto and YTS-280 tenor. The modal parameters are extracted from the measured

input impedance, as presented in subsection 1.1.4.1. The input impedance were measured by the author for the two alto saxophones and by intern C. Marmion for the YTS and the YSS, using the CTTM impedance sensor. In total, 32 fingerings along the first two registers were measured for both instruments. Most of the following studies concentrate on the 16 first register fingerings, from low B \flat to middle C \sharp . Figure 4.13 displays the compared value of the modal parameters. Note that the modal frequency and damping of the tenor and alto saxophones are multiplied by constants corresponding to the transposition of these instruments, to be adequately compared with the altos. For the tenor, the frequencies and damping are multiplied by 4/3 (up a perfect fourth) and for the soprano they are multiplied by 2/3 (down a perfect fifth). This dilatation and contraction can seem extremely naive and artificial, but it actually has scientific meaning: the time in the equations of the model can be made dimensionless by multiplying by the first modal frequency, with no change in the model's dynamics (except for the time dilatation). In this context, all frequency values influence the model's dynamics based on their ratio with this first modal frequency. Therefore, multiplying the parameters to account for the transposition actually accounts for this dimensionless time formulation, and is linked with the model's dynamics more directly than the raw undilated modal parameter values.

Figure 4.13 shows that the modal frequencies of the two alto saxophones are close together, along with the tenor, while the soprano's are comparatively lower. As for the modal damping, all the dampings are in the same region, with the soprano's being slightly higher. Note that this is compensated by the soprano's modal amplitudes being higher. Overall, there are rather important modal parameter variations between instruments, especially for the modal damping coefficients and the modal amplitudes.

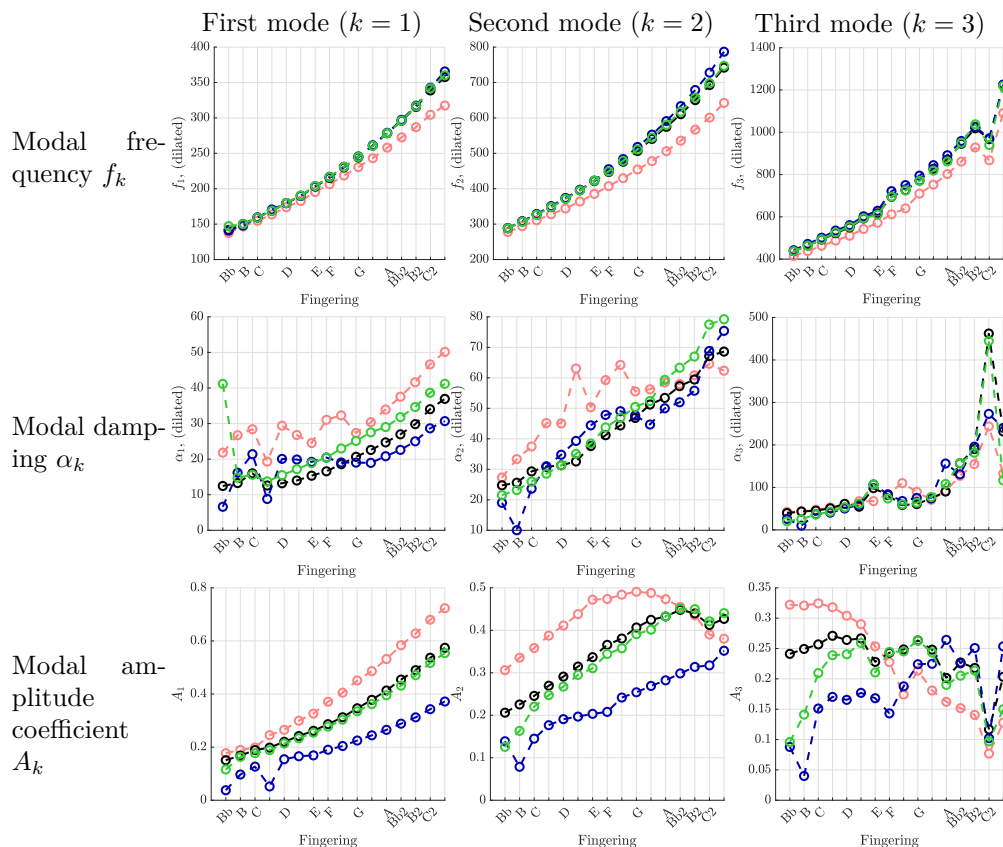


FIGURE 4.13: First three modal parameter for: **green** Buffet-Crampon alto, and Yamaha **black** alto, **red** soprano and **blue** tenor. Frequency and modal damping axis is unchanged for the altos, contracted ($\times 2/3$) for the soprano and dilated ($\times 4/3$) for the tenor.

Overall, this short look at the modal parameters of the saxophone family does not really call for precise conclusion, other than a relative homogeneity between the four instruments, with the two alto saxophones being slightly closer together than to the other members. Even

based on the preceding study of the influence of the modal parameters on the instability thresholds (subsection 4.3.3, very little can be said as to the predicted relative position of said thresholds among the family.

4.3.4.2 Location of the first, second and third Hopf bifurcation for the saxophones

Hopf point continuation was performed on the four saxophones, with a necessary adjustment of the reed eigenfrequency. In order to stay in the same proportions with the first resonance frequencies of each saxophone, the reed angular frequency ω_r was multiplied by 3/4 for the tenor and 3/2 for the soprano. A cylindrical mouthpiece is added, whose length is treated in the same way as the reed eigenfrequency, being multiplied by 4/3 for the tenor and 2/3 for the soprano. These naive adjustments are made to compensate for the instruments' respective range, while keeping a very straightforward relation between them and avoiding any risk of fine-tuning of the parameters by hand to make the results artificially closer.

As a first global look at the instability thresholds along the saxophone family, figure 4.14 shows the results of the Hopf point continuation for the first three registers, for all four instruments. This figure already shows notable similarity between the general shapes of the instability thresholds within each register. The first register threshold is always smaller for the lowest fingerings, which can be associated with the first register being harder to produce for the lowest fingerings than for the higher fingerings. Then, the first register thresholds with an irregular growth until it stabilizes between the low C and F fingering, and stays the widest curve until the highest fingering. The second register instability threshold follows the same very clear trend for the four instruments, by starting as the widest curves for the lowest fingerings, and then progressively shrinking until it almost disappears at the highest fingering. The third register instability threshold is only present in the lowest fingerings (below D) and although its size is comparable with the two other for one or two lowest fingering, it rapidly shrinks and disappears. This homogeneity in the oscillation threshold may relate to practical playing techniques similarities, common to the whole saxophone family, notably as concerns the production of higher registers.

To complete the comparison between the instability thresholds of the four instruments, figures 4.15, 4.16 and 4.17 superimpose the instability thresholds between the Buffet-Crampon Senzo alto saxophone and the three Yamaha. These figures confirm that the instability thresholds are quantitatively very close together, except for certain notable differences that are detailed hereafter.

Figure 4.15 superimposes the Hopf bifurcations obtained for the two alto saxophones. There are two main differences. The first one concern the lowest fingering $B\flat$, for which the first register instability threshold is narrower for the Senzo than for the YAS. This is clearly linked to the first damping coefficient being higher for this fingering of the Senzo (see figure 4.13). The second difference concerns the second register instability threshold for the highest fingering of the register $C\sharp 2$. The Senzo's second register instability threshold disappears for this fingering, whereas it still exists for the YAS. Contrary to the previous comment, this feature was hard to predict looking at the modal parameters only, which are very similar between the two instruments for this fingering. Note that the similarity between the two instrument's instability thresholds should be put in regards with the differences between the regime maps presented in figure 4.5. The instability thresholds are clearly a more tolerant comparative tool than the regime maps, but it can be convenient when comparing instruments that are further away from each other, such as members of the different branches of the saxophone family.

Figure 4.16 compares the Hopf bifurcations of the Buffet-Crampon alto and the Yamaha tenor saxophone (YTS). The main differences here concern the first and third register bifurcation for the lowest fingerings. The YTS's instability region for these fingerings is narrower than the alto's, especially for the first register. This can be attributed to the modal amplitude coefficient A_1 and A_3 being smaller for the YTS than for the Buffet-Crampon alto (see figure 4.13). It can also be noticed that there is a third register instability region for one more fingering on the YTS than the alto. Again, this is not obvious based only on the modal parameters.

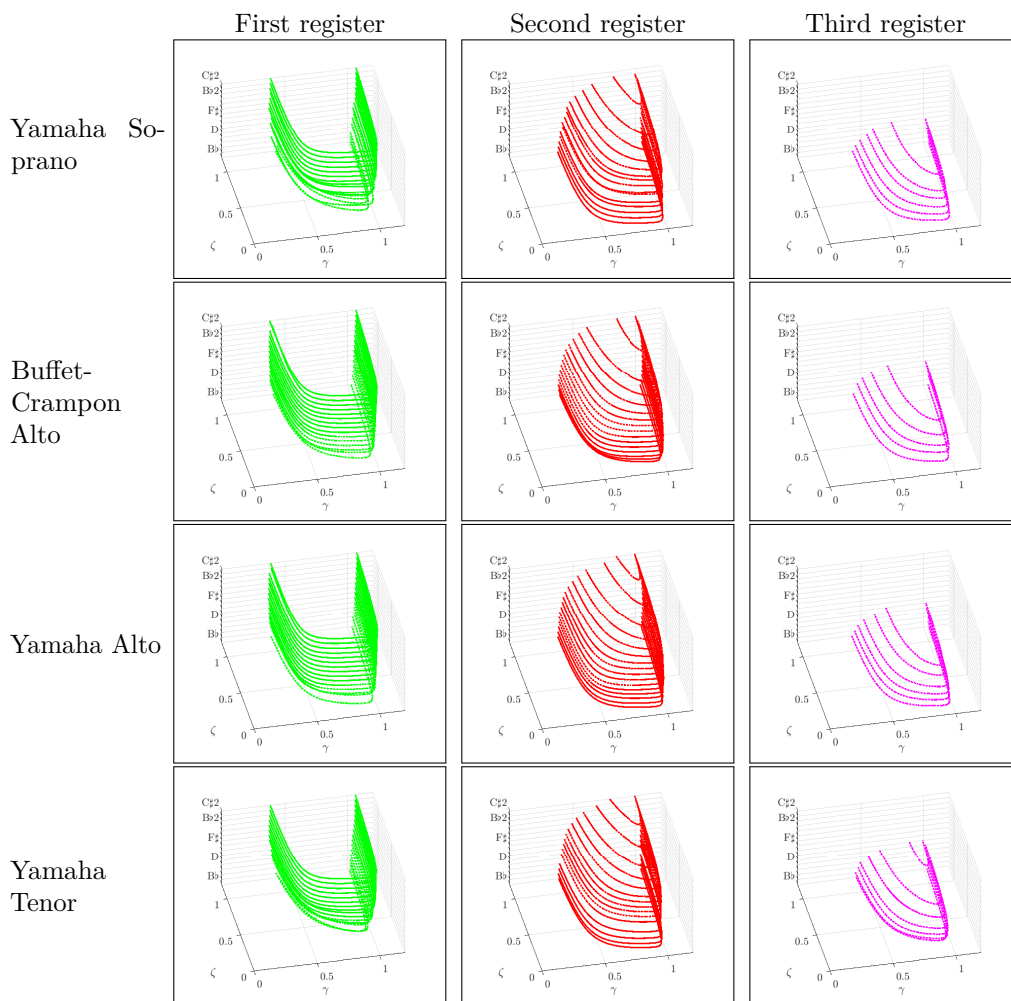


FIGURE 4.14: Continuation of the Hopf bifurcations associated with the three first register of the instruments for four saxophones.

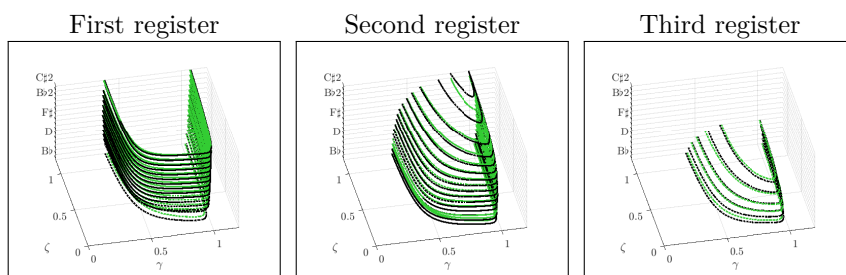


FIGURE 4.15: Comparison of the Hopf bifurcations of the first three registers between **green** Buffet-Crampon alto and **black** Yamaha alto.

Figure 4.17 overlays the instability thresholds of the Buffet-Crampon alto with those of the Yamaha soprano saxophone (YSS). A similar comment can be made on this figure than on figure 4.16: the first register threshold of the YSS is narrower than the alto's for the lowest fingering. Note that this phenomenon can be attributed *a posteriori* to the damping coefficients of the soprano being higher than the alto's for these fingerings, but note that the modal amplitude coefficients contradicts this effect. Therefore, *a priori* intuition based on the modal parameters would be hard to develop in this case.

The instability thresholds of the saxophone family correspond remarkably to each other, even when making only very simple adjustments concerning the mouthpiece and the reed characteristics. This is in spite of a relative dispersion of the modal parameters. Eventhough

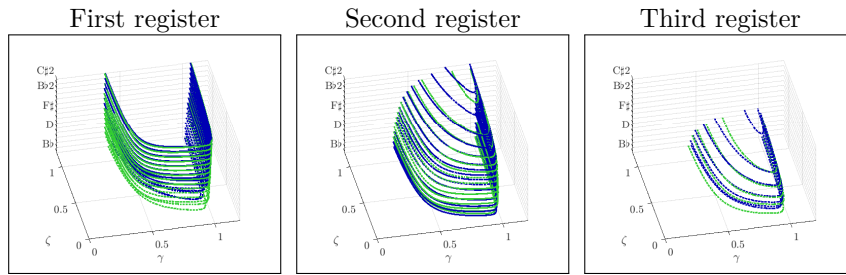


FIGURE 4.16: Comparison of the Hopf bifurcations of the first three registers **green** Buffet-Crampon alto and **blue** Yamaha tenor.

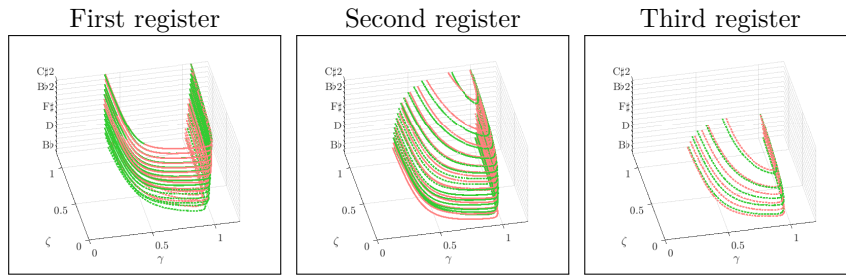


FIGURE 4.17: Comparison of the Hopf bifurcations of the first three registers **green** Buffet-Crampon alto and **red** Yamaha soprano.

they can be linked directly to certain features of the instability thresholds, it has been shown that their global aspect cannot be foreseen with a mere glance at the modal parameters. Instability thresholds are an example of a descriptor that is arguably closer to playability than any characteristic of the impedance itself, while not being as computationally heavy as a complete regime cartography. This kind of analysis has a strong potential to provide optimization criteria that are more relevant than the metrics applied to the impedance, while remaining time-efficient.

This chapter presents and uses the process sound production cartography to highlight certain interesting dynamic features of the saxophone. To this end, certain known biases of the cartography process are bypassed, by using it in a strictly comparative manner. However, in order to understand saxophone dynamics further, these fundamental biases need to be addressed and described. Therefore, next chapter undertakes a more in-depth exploration of the challenge posed by a complete dynamic description, notably through a description of the multistability phenomenon.

Chapter 5

Multistability and attraction basins: effect of the history of the system and of variations of control parameters

5.1 Foreword

So far, this dissertation has presented diverse saxophone regimes and studied their conditions of production in terms of control parameters. Depending on the context, the idea of "conditions leading to the production of a given regime" was found using two different methods. The first, maybe more classic, way to state that a certain oscillating regime can be produced with a given control uses the Harmonic Balance Method to determine whether this regime is stable (see section 1.2.2). The second method relies on time-domain synthesis being launched with constant control parameters until a steady-state regime is established – it is then clear that the obtained regime can be produced using these values of the control parameters. These two characterization of regime production are used almost interchangeably in the previous chapters, but they are fundamentally different. In particular, there is nothing preventing two different solutions to be stable for the same control parameter values, but a single time-domain synthesized signal converges towards a single steady-state regime. This fundamental discrepancy deserves attention, as it exhibits that the binary concept of stability or instability of a regime needs nuance: what makes one stable regime appear in time-domain synthesis rather than another stable regime? The problematic is all the more relevant that, as shown in section 3.3, the saxophone's lower fingerings produce a whole variety of different regimes, with potentially overlapping stability zones.

The first objective of this chapter is gauging the importance of the phenomenon of multistability in a saxophone model, in terms of range of control parameters. To this end, we use continuation to produce the bifurcation diagram of a saxophone model (see section 1.1 and appendix A for detailed descriptions). On this bifurcation diagram, zones where two different regimes are stable at the same time are sought. On the studied example, multistability appears on almost all the range of studied control parameter. Then the attraction basin of each stable regime is explored in the multistability zones using time-domain synthesis. The high dimensionality of the phase space of the model forbids any exhaustive exploration of the attraction basins. Therefore, control scenarios are devised to represent a musically relevant, although very partial, outline of the attraction basins. These control scenarios are directly interpretable in terms of musician actions. The first scenario consists in a slow linear increase of the blowing pressure, followed by a linear decrease. This kind of variation of the control parameters is a classic method of initial exploration of the regimes that can be produced by a nonlinear systems. In the case of multistability, ramps of pression typically exhibit hysteresis, with different regimes being produced in the upwards and downwards parts of the ramp. Overlaid on a bifurcation diagram, the results of these ramps also allow to check the correspondance between time-domain synthesis and the HBM over the complete range of variation of the control parameter. The second control scenario involves the blowing pressure increasing and stabilizing at a final value. It is parametrized by the characteristic time of

increase, allowing to vary between slow and fast attacks. This scenario represents a simple strategy of selection between multistable regimes occurring at the final value of the blowing pressure. Depending on the multistability zones, we show how varying the characteristic time of the attack indeed modifies the steady-state regimes.

In order to improve the vision of the attraction basin that is given by the control scenarios, a more classic approach is undertaken, using time-synthesis launched with various initial conditions in the phase space. This way, a 3D-projection of the attraction basins can be outlined and analyzed with regards to their appearance in the previous scenario. For instance, the second control scenario (with variable attack times) appears unable to lead the system very far from the origin of the phase space, especially for slow attack times. This entails, for instance, that a regime whose attraction basin surrounds the origin is markedly favored by slow attacks. This is always the case when the equilibrium (non-oscillating regime) is stable.

These rather abstract results about coexisting stable regime on a saxophone model and how to choose between them using an arguably oversimplified control scenario are then applied to a succinct sound production study depending on the acoustical features of the resonator. This last part investigates the effect of the inharmonicity between the two first resonance frequencies on sound production, especially first register production on the lowest fingerings. Using the second control scenario with different attack times and final control parameter values, the rate of the each produced regime is computed for several values of the inharmonicity. The first takeaway is that overlooking multistability in a sound production study can alter the results considerably. In particular, if only one sound is synthesized for each final control parameter value – with a fixed attack –, there is a risk of the attack itself favoring one regime over another and leading to fallacious conclusions. The second, more applicative, result is that a second resonance frequency situated at exactly double the first does not facilitate the emission of first register. Instead, a slightly higher second resonance frequency appears to increase the rate of apparition of the first register and decrease the emission of the second register. Incidentally, the second resonance frequency observed on impedance measurements of real saxophone is indeed higher than twice the first, in proportions corresponding with the conditions leading to the most first register in the study. This can come as a surprise knowing the second principle of sound production stated by Benade in [BG68]:

Oscillation is favored at a frequency for which the air column input impedance is large (as in linear systems), and oscillation is also favored if the impedance is large at some or all of the harmonics of this frequency.

However, this work exhibits a case where displacing the second resonance away from the second harmonic of the first register actually favors its production. This last result constitutes an explanation of an instrument making choice based on the objective sound production characteristics of a physical model. Shedding light on the underlying physical reasons that empirically lead instrument makers to certain design choices is a strong first step towards using physical models in the development of new instruments.

Reading guidelines

The rest of this chapter constitutes an *in extenso* reproduction of the work submitted to *Acta Acustica* as:

Colinot, Tom et al. (submitted in 2020). "Multi-stability in a saxophone model: how it manifests when exploring sound production to explain instrument makers' acoustical choices". In: *Acta Acustica*.

The title and abstract of the article were removed, as they are functionally replaced by the present chapter's title and introductory section (5.1).

5.2 Introduction

A classic endeavor in musical acoustics consists in the systematic study of sound production features of a musical instrument. Early studies use an artificial mouth to replace the musician (on the clarinet [MG41; Bac61] or the bassoon [Gok79]) in order to better describe and understand the physical phenomena at play during sound production. Later on, artificial mouths have been robotized to provide a complete mapping of the instrument's behavior, aiming at understanding how the instrument must be acted on to produce such or such sound [HLC12; LHC13] or describing the influence of an acoustical parameter of the resonator on sound production [DV15]. This last study's objective is shared by other works using a rather different approach to systematic description of the instrument's behavior: using a physical model. Based on analytical considerations such as oscillation thresholds [GMV19a], some conclusions can be drawn as to the acoustical characteristics facilitating the production of sound. Numerical resolution of the model's equations also constitute a repeatable way to map the produced sound to the characteristics of the instruments, which has direct applications in instrument making [Tou+17; Fré+19]. However, from a mathematical perspective, as nonlinear dynamical systems, wind instruments models often admit multiple solutions for a given set of parameters. Of course, the question of the stability of each of these solutions holds great importance when aiming to describe or predict the playability of an instrument based on its physical model. But some important questions remain unreachable, even for ideal cases where the stability or instability of each regime would be known. For instance, which regime is produced if two regimes are stable for the same control parameters combination?

In the case of such coexistence of stable solutions, denominated *multistability* hereafter, the convergence towards one or the other solution depends on the initial conditions. Indeed, each solution is associated with a *region of attraction* or *attraction basin*, defined as the region of the phase space where all initial conditions converge towards this solution [Ras89]. For instance, attraction basins are studied in walking models [SW01; Man+11], where the 'walking' (periodic) regime almost always coexists with a stable equilibrium, corresponding to falling. In this case, describing attraction basins informs control strategies in robotics [WSH04; Wis+05]. Attraction basins are also studied for classic dynamical oscillators, such as Chua's circuit [Mat84], with experimental explorations of the attraction basins [Peg+00] as well as numerical investigations [Sta+17]. As strongly nonlinear self-oscillating systems capable of multiple oscillating regimes, wind instrument models are among the systems for which studying attraction basins can shed light on their rich behavior and help understand control strategies used by musicians. However, to our knowledge, no such study has been produced, concerning any self-oscillating musical instruments.

Describing the attraction basins and comparing their sizes is expected to give information on which regime is most likely produced, assuming some probabilistic repartition of the initial conditions in the phase space [BDK15]. However, an exhaustive description is almost impossible for a complete model of instrument, where the phase space is of very large dimension. In such cases, attraction basins may be partially explored, based on a reduction of the phase space to one or two dimensions – see for instance [WLC09] where the infinite-dimensional phase space of a delayed system is described along two dimensions. In the case of musical instruments, a reduction of the phase space is proposed in this paper, based on knowledge of typical musical scenarios. Throughout this work, the case of a model of saxophone is considered, and two scenarios are studied: transition from another established limit-cycle (scenario number 1), and first attack transient of a note, where the blowing pressure parameter goes from 0 to a certain final value (scenario number 2).

Section 5.3 presents the physical saxophone model and the two numerical methods used to solve its equations : the HBM and time-domain synthesis. Next, multistability is introduced by computing the bifurcation diagram with the HBM and continuation (Asymptotic Numerical Method) and exhibiting hysteresis cycles using time-domain synthesis in section 5.4 (scenario number 1). Then, in section 5.5, a simple test-case of scenario number 2 is presented to study sound production, where the blowing pressure increases from 0 to its final value in different durations. We show how that this duration can influence the final regime in multistability regions, and explain these results by presenting the attraction basin of each regime. Section 5.6 demonstrates how knowing about multistability leads to a better description of the behavior of the model. Depending on the inharmonicity of the resonator, the size of the control parameter regions where each regime appears in synthesis is described, taking into account multistability. This provides an interpretation to the inharmonicity value measured on the saxophone by showing it corresponds to an optimum in periodic regime production.

5.3 Numerical simulation framework

5.3.1 Saxophone model

The saxophone model used in this study is comprised of three main elements: a one degree-of-freedom oscillator representing the reed, a regularized nonlinear characteristic giving the flow through the reed channel, and a modal description of the measured impedance of the resonator. Similar models solved by time-domain synthesis (section 5.3.2) are used in conjunction with analytical techniques to study the playing frequency [Coy+15] and spectrum [Pet+19a] of clarinets, as well as their radiated power with a comparison to measurements [Gui+15]. The Harmonic Balance Method (section 5.3.3) can also be applied to this model to study its dynamic behavior, for instance to quantify the effect of neglecting reed contact [Col+19].

Dimensionless [Gok79; Hir95] acoustical Kirchhoff variables (p, u) are used in this work:

$$p = \frac{\hat{p}}{p_M} \quad , \quad u = Z_c \frac{\hat{u}}{p_M}, \quad (5.1)$$

where the hat notation indicates the variable with its physical unit, p_M is the static pressure necessary to close the reed channel completely and Z_c is the characteristic input impedance of the resonator for plane waves. Similarly, the reed displacement from equilibrium is given in dimensionless form

$$x = \frac{\hat{x}}{H} \quad (5.2)$$

where H is the distance between the reed and the mouthpiece lay at rest. With this formalism, the reed channel is closed when $x \leq -1$. In this work, the only time-varying control parameter [WB74] is the dimensionless blowing pressure γ :

$$\gamma(t) = \frac{p_m(t)}{p_M}, \quad (5.3)$$

where p_m is the physical value of the pressure in the mouth of the musician. We leave all other control parameters constant in order to limit the dimensionality of the study. The values and names of the parameters are summarized in table 5.1 and detailed below through the model description. Their values are drawn from [MA+16] for the reed parameters q_r and ω_r , from [CW12] for the order of magnitude of the contact stiffness K_c .

5.3.1.1 The reed model

Following [CW12], the reed is modeled by a single degree of freedom oscillator including a nonlinear contact force accounting for the mouthpiece lay

$$\frac{\ddot{x}}{\omega_r^2} + \frac{q_r}{\omega_r} \dot{x} + x = p - \gamma + F_c(x + 1), \quad (5.4)$$

Name	Notation	Value
Blowing pressure	γ	Variable
Reed opening at rest	ζ	0.6
Reed damping	q_r	1
Reed angular eigenfrequency	ω_r	4224 rad.s ⁻¹
Mouthpiece lay stiffness	K_c	100
Contact regularization	η	10 ⁻³
Number of resonator modes	N_m	8

TABLE 5.1: Parameters of the numerical model: musician control parameters γ and ζ , reed parameters q_r and ω_r , contact parameter K_c and parameters inherent to the numerical implementation η and N_m .

where the two parameters of the reed are its angular eigenfrequency ω_r and its damping coefficient q_r , and the contact force is function of the dimensionless reed opening $x + 1$ and is taken from [BTC15],

$$F_c(x + 1) = K_c \min(x + 1, 0)^2, \quad (5.5)$$

where $K_c = 100$. The ramp function $\min(x + 1, 0)$ is regularized using a parameter $\eta = 10^{-3}$ to avoid non-differentiability at $x = -1$ (reed closure)

$$\min(x + 1, 0) \simeq \frac{x + 1 - \sqrt{(x + 1)^2 + \eta}}{2}. \quad (5.6)$$

Since $x + 1$ is the distance between the reed and the mouthpiece lay, F_c can be interpreted as a quadratic stiffness activated whenever the reed touches the lay.

5.3.1.2 The reed channel

The flow at the input of the resonator is deduced from Bernoulli's law [Bac63; Hir+90] applied to the reed channel and turbulent mixing into the mouthpiece

$$u = \zeta \max(x + 1, 0) \text{sign}(\gamma - p) \sqrt{|\gamma - p|} \quad (5.7)$$

where ζ is the dimensionless control parameter accounting for reed opening at rest

$$\zeta = Z_c w H \sqrt{\frac{2}{\rho}}, \quad (5.8)$$

w being the effective width of the reed channel and ρ the density of the medium. The absolute value and ramp function in (5.7) are regularized with the same parameter η as in Eq. (5.6)

$$|\gamma - p| \simeq \sqrt{(\gamma - p)^2 + \eta} \quad (5.9)$$

$$\max(x + 1, 0) \simeq \frac{x + 1 + \sqrt{(x + 1)^2 + \eta}}{2}. \quad (5.10)$$

5.3.1.3 The resonator

The input impedance is used to represent the resonator's acoustical response. The dimensionless input impedance $Z(\omega)$ of an alto saxophone is measured with the CTTM impedance sensor [DLR08]. In order to use this input impedance for the two numerical synthesis methods presented above, it is decomposed into modes [Coy+15] so that

$$Z(\omega) = \sum_{n=1}^{N_m} \frac{C_n}{j\omega - s_n} + \frac{C_n^*}{j\omega - s_n^*}, \quad (5.11)$$

where C_n and s_n are the estimated complex modal residues and poles [Sil+14] and N_m is the number of modes retained in the simulation. In this paper $N_m = 8$ modes are used.

This translate into the time domain by describing the pressure as a sum of complex modal components p_n , whose evolution depends on the modal coefficients, such that

$$\dot{p}_n(t) - s_k p_n(t) = C_n u(t), \quad \forall n \in [1, N_m], \quad (5.12)$$

$$p(t) = 2 \sum_{n=1}^{N_m} \operatorname{Re}(p_n(t)). \quad (5.13)$$

The flow u in (5.12) is given by (5.7).

5.3.2 Time-domain synthesis

Equations (5.4), (5.7) and (5.12) are discretized using finite-difference approximations for the time-domain derivatives [Coy+15]. The sampling rate used in the simulation is $F_s = 176400$ Hz, higher than the standard audio sampling rate. Such a high sampling rate is required, given the chosen finite difference scheme, to give precise result that match those obtained with the Harmonic Balance Method.

As an illustrative result, figure 5.1 shows an example of synthesized pressure signal and its spectrogram, to illustrate the characteristic of each regime. Note that the signal shown is a portion of the signal used in figure 5.3. It corresponds to the first apparition of the oscillations at a blowing pressure value $\gamma \simeq 0.45$. At this point, the system jumps from equilibrium to the first register and passes through fleeting second register and quasi periodic regimes. The spectrogram (figure 5.1 (b)) shows the second register to be the octave (double the fundamental frequency) of the first register. The quasi-periodic portion of the signal displays amplitude variations, seen in the envelope of the signal (figure 5.1 (a)) and on the odd harmonic components of the spectrogram. Quasi-periodic regimes are well-known on saxophone-like instrument models, documented form instance in [DVM14; DV15].

5.3.3 Harmonic balance and numerical continuation

The harmonic balance method is an analysis method particularly adapted to the study of musical instrument models [GKN89], since it focuses on periodic solutions, which correspond to the produced notes. Assuming periodicity of the solution allows expanding all variables in Fourier series [KB49; NV76]. Applying the method to a differential system transforms it into an algebraic system of which the unknowns are the Fourier coefficients of the variables, as well as the solution's fundamental frequency. A numerical continuation method such as the Asymptotic Numerical Method can then be applied to the resulting algebraic system [CV09; GCV19] to find how the solution changes for other constant values of a chosen control parameter. In this work, simulations were carried out using the MANLAB software (<http://manlab.lma.cnrs-mrs.fr/>). This yields the value of the Fourier coefficients of the oscillating solutions along several values of a control parameter. The Fourier coefficients can then be used to reconstruct the time-domain solutions. This evolution can be summarized as a bifurcation diagram, which represents the variation of some descriptor, say the amplitude, of the solutions of the system with respect to a control parameter, chosen hereafter to be the blowing pressure parameter γ . In addition, the stability of solutions is determined using Floquet theory (for more details refer to [LT10; BL18; Gui+20]).

5.4 Multistability

This section presents the blowing pressure zones where the model can produce each regime, by studying their stability with the HBM. This result is summarized in the bifurcation diagram, on which multistability zones appear as intervals where several regimes are stable. Signals are also synthesized with time-domain synthesis to exhibit how multistability leads to hysteresis. The correspondance between the two methods (the HBM and time-domain synthesis) is also checked.

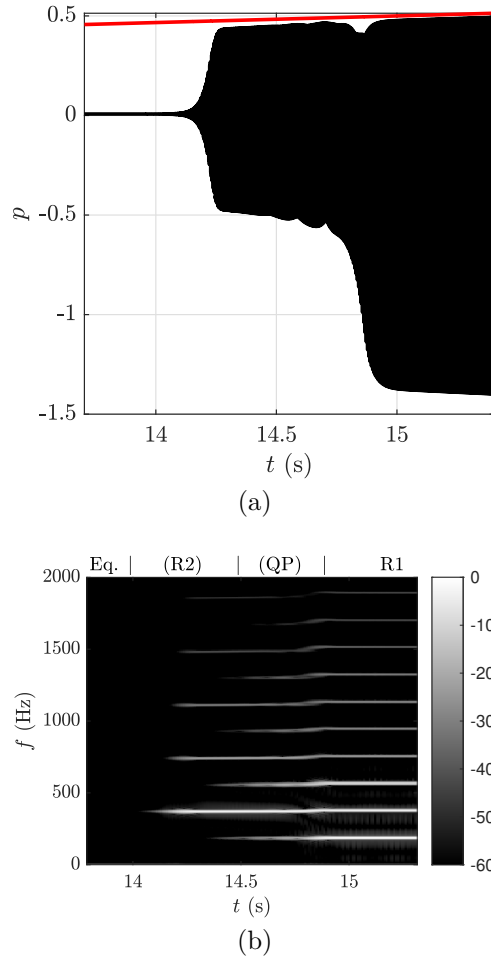


FIGURE 5.1: Time-domain synthesized pressure signal. (a) temporal envelope (black) and blowing pressure parameter γ (red). (b) Spectrogram (dB) with regime names indicated (unstable ones between parentheses): equilibrium, second register, quasi-periodic and first register. The signal is extracted from the same blowing pressure ramp as in figure 5.3, between $\gamma = 0.45$ and $\gamma = 0.51$ (at first apparition of oscillation).

5.4.1 Overlapping stability zones on the bifurcation diagram

The bifurcation diagram is computed for the (written) low $D\sharp$ fingering of an alto saxophone. The written $D\sharp$ produces the heard note $F\sharp 3$, at frequency 185 Hz. This intermediate fingering of the first register is chosen as test case because it exhibits both first and second register regimes, but no stable third register regime and few double two-step phenomena [Col+20]. Figure 5.2 shows the L^2 -norm of the pressure signal

$$\|p\|_2 = \frac{1}{T} \sqrt{\int_0^T p(t)^2 dt}, \quad (5.14)$$

where T is the period of the signal, and identifies which regime each branch corresponds to. The blowing pressure parameter γ spans the interval between 0 and 2. This bifurcation diagram contains branches corresponding to the so-called equilibrium, where no sound is produced, for the lowest and highest γ values. The equilibrium at low γ corresponds to the musician not blowing hard enough into the instrument to obtain a sound, while at high γ equilibrium means the reed channel is clamped shut by a strong pressure in the mouth. For intermediate γ values, the first and second register both appear. The first register is the fundamental pitch obtained with a given fingering, and the second register, sometimes referred to as *overblowing*, is pitched one octave higher than the first register. Eventhough the

saxophone has an octave key facilitating the production of the second register, musicians know how to produce second register regimes without activating it. It is therefore not surprising that both regimes appear on the same fingering. In the present case, this interval contains all the studied limit cycles of the model, and at its bounds, only the equilibrium solution exists and is stable. The diagram in figure 5.2 displays several zones of coexistence between stable regimes (i.e. multistability).

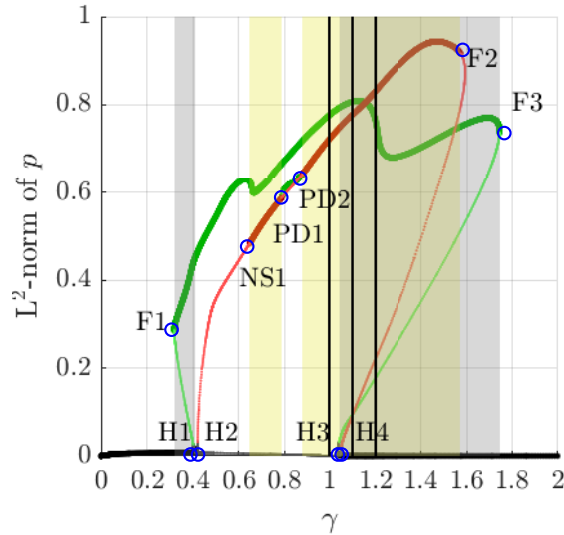


FIGURE 5.2: Bifurcation diagram: L^2 -norm of the acoustical pressure depending on the blowing pressure parameter γ for the low written $D\sharp$ fingering of an alto saxophone. Thick lines: stable solution, thin lines: unstable solutions. Black: equilibrium, green: 1st register regimes, red: 2nd register regimes. Multistability zones are shaded: light yellow where 1st and 2nd register coexist, darker gray for equilibrium and 1st register. Blue circles specify the location of bifurcations. Vertical black lines correspond to those in figure 5.5 (c), and (from left to right) to phase diagrams 5.6 (a), (b) and (c).

Starting from low blowing pressure values, the first coexistence zone appears between the first register and the equilibrium. It is delimited by the Fold bifurcation F1 of the first register around $\gamma = 0.3$ and the inverse Hopf bifurcation H1 at $\gamma = 0.4$ where the equilibrium becomes unstable. The second coexistence zone is between first and second register, in the interval where the second register is stable between the Neimark-Sacker bifurcation NS1 and the period-doubling bifurcation PD1 (respectively at $\gamma = 0.66$ and $\gamma = 0.79$). The Neimark-Sacker bifurcation NS1 mark the destabilization of the second register and the emergence of a quasi-periodic regime (not represented here), sometimes called multiphonics by musicians. The next coexistence zone concerns the interval between the two period-doubling bifurcations PD1 and PD2 on the second register branch, where a stable double two-step solution [Col+20] emerges. This coexistence zone is actually not shaded on the figure, as it could represent less of a musical issue, since double two-step regimes have roughly the same frequency as standard first register regimes. The fourth coexistence zone is more complicated: it starts between first and second register at the period-doubling bifurcation PD2, and then the equilibrium also becomes stable at the Hopf bifurcation H4. The limit of the last coexistence zone is made of the two Fold bifurcations F2 and F3 where the first and second register solutions cease to exist. This diagram shows that coexistence zones between stable regimes span most of the range in γ where oscillating solutions exist, including arguably crucial γ values like the lowest for which an oscillating regime exists. Multistability is not an isolated phenomenon, but rather corresponds to the general situation, at least for this fingering.

5.4.2 Time-domain synthesis with blowing pressure ramps

Once multistability zones are identified, time-domain synthesis can be used to exhibit how they manifest when playing the instrument. One of the main phenomena multistability entails is hysteresis: a different regime is produced depending on whether the blowing pressure is increasing or decreasing. Various multistable regimes are exhibited this way on woodwind models with simplified geometry in [Tak+09]. Figure 5.3 shows the hysteresis cycles obtained by using ramps of γ . The parameter γ is progressively increased from 0 to 2 and then decreased until the end value is reached. Each one of the increasing and decreasing phase of the synthesis has a duration of 60 s. This duration was chosen after several trials, sufficiently long to let stable regimes establish while keeping a γ slope steep enough to limit dynamical bifurcation delays [Ber+13].

Figure 5.3 shows that the synthesized signal starts from $\gamma = 0$ at equilibrium, its L^2 -norm being zero. Then, at Hopf bifurcation H1, the equilibrium becomes unstable, which causes the system to start oscillating. At this point, the synthesis goes through a transient represented in figure 5.1, shortly passing by unstable second register and quasi-periodic regimes before reaching the first register. Once on the first register is established, the branch is followed all the way to extinction, because the first register does not become unstable before Fold bifurcation F3. At this point, the system returns to equilibrium until the highest γ value. The blowing pressure then starts decreasing, and the system stays at equilibrium until Hopf bifurcation H3 is reached, for $\gamma \simeq 1.05$. There, the system jumps to the stable second register regime. The second register branch is followed until the period-doubling bifurcation PD2, where the system briefly follows the double two-step branch. The period doubling appears on the L^2 -norm as small perturbation. The system then rejoins the second register branch at period-doubling PD1. Then, something rather surprising occurs: the system seems to follow the second register branch further than Neimarc-Sacker bifurcation NS1, although it becomes unstable. This is because the quasi-periodic regime emerging at NS1 is actually a stable attractor, and the associated L^2 norm happens to be close to that of the second register. Branches of quasi-periodic regimes have not been computed so as not to clutter figure 5.2, but note that it is possible with HBM and Manlab [GCV19]. Eventually, the system jumps back onto the first register branch, which is followed until Fold bifurcation F1. The path described precedently is highly hysteretic: the sequence of regime produced for increasing and decreasing γ are very different. Actually, the two paths only coincide in three regions: the lowest and highest γ , for which only the equilibrium is stable, and a very small region around $\gamma = 0.5$ where only the first register is stable.

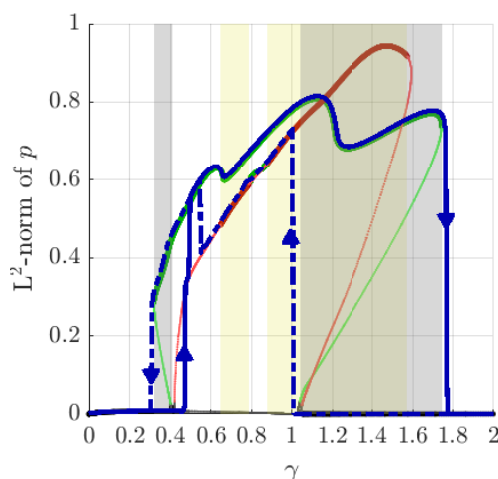


FIGURE 5.3: Amplitude of the time-domain synthesis signal (dark blue line) for a varying blowing pressure parameter γ from 0 to 2 and down, overlaid with the bifurcation diagram of figure 5.2. Solid line indicate the first part of the signal (increasing γ) and dashed line the second (decreasing γ)

The hysteresis phenomenon observed here in time-domain synthesis can be interpreted as the first step in attraction basin description: once a certain stable regime is reached, it is

followed until extinction or loss of stability, even when other regimes are simultaneously stable. This confirms that a stable periodic regime is part of its own attraction basin. Reconstructing stable parts of the bifurcation diagram using time-domain synthesis and comparing them to those obtained using the Harmonic Balance Method also provides validation for the numerical discretization scheme in the context. Here, it shows that time-domain synthesized signals are not perturbed by numerical artifact and can be used as a way to describe properties of the model. Note that even the tiny branch of double two-step solution between period doubling PD1 and PD2 is found by the time-domain synthesis.

This exploration of the blowing pressure space using a long ramp is very useful to exhibit the hysteresis phenomenon, as well as test the coherence between the two synthesis methods. However, this kind of sound is extremely artificial and far from anything a musician would use in everyday practice (provided it is even possible for a musician to produce it). Therefore, we frame the conditions of the rest of the study so that they can rather be interpreted in terms of selection of one regime over another. It is very likely that musicians learn to select between coexisting stable regimes, adjusting their control so that the established regime in a multi-stability region is the one they desire. This idea provides the layout for subsequent control scenarios: we study the effect of a parametrized transient control or initial conditions on the established steady-state regime that follows when the control is constant.

5.5 Effect of the rising time of the blowing pressure

5.5.1 Control scenario: increasing blowing pressure

One way to study the attraction basins more thoroughly is to run many simulations with initial conditions spanning the whole phase space. Since the considered model has a $2N_m + 2$ dimensional phase space, a complete exploration is not possible. Moreover, many of the possible initial conditions are unlikely to be created by the musician. More interesting is the exploration of the regions of the phase space that are crossed by the system when a given control pattern is varied. Here, we focus on a monotonous increase of the blowing pressure γ at the attack: without using the tongue, the player starts blowing progressively into the instrument. Such scenario was proposed in [Sil09]. The blowing pressure starts from 0 and rises up until stabilizing at a certain value γ_f , during a certain time determined by the parameter τ_γ . The temporal variation of γ is given by the

$$\gamma(t) = \frac{\gamma_f}{2} \left(1 + \tanh \left(\frac{t - 5\tau_\gamma}{\tau_\gamma} \right) \right), \quad (5.15)$$

which is differentiable infinitely many times. Figure 5.4 displays four examples of such transient. Notice that the instant $t = 5\tau_\gamma$ where $\gamma = \gamma_f/2$ depends on τ_γ : this is to ensure that the transient starts at γ very close to 0 (here $\gamma(t=0) = 4.5 \times 10^{-5}\gamma_f$).

Other envelopes (sigmoid, sine branch) were tested and they do not affect the results qualitatively. Figures 5.5 show which established regimes appear in time-domain synthesis depending on τ_γ , for final values γ_f belonging to the coexistence zones described in figure 5.2. Each dot on the figure represents the type of established regime after 5 seconds of time-domain synthesis. This synthesis duration was chosen sufficiently long so that the transient is completed and the established regimes can be observed. Regime types are estimated using an energy-based criterion for equilibrium (if the energy of the pressure signals in the last 10 periods is less than that of the first 10, the regime is classified as equilibrium) and a fundamental frequency estimator for first and second register.

Figure 5.5 (a) focuses on the first coexistence region (highlighted in gray in figure 5.2), near the first Hopf bifurcation H1. The two stable regimes in this region are the equilibrium and the first register. For final values γ_f between 0.38 and 0.4, the system can converge to both regime depending on the characteristic rising time τ_γ . It is interesting to note that equilibrium is reached for the longest rising times, i.e. the slowest γ variation, whereas the oscillating regime is reached for the shortest rising times. This is understandable as a quick γ increase tends to drive the system away from equilibrium, and therefore possibly out of its attraction basin.

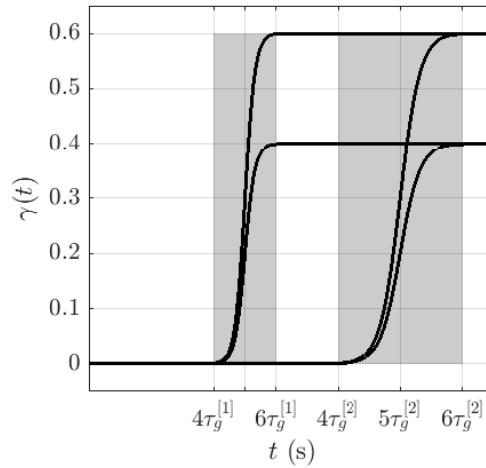


FIGURE 5.4: Four examples of blowing pressure evolutions described by 5.15, for $\gamma_f = 0.4$ and 0.6 and $\tau_g = \tau_g^{[1]} = 10$ ms and $\tau_g^{[2]} = 20$ ms.

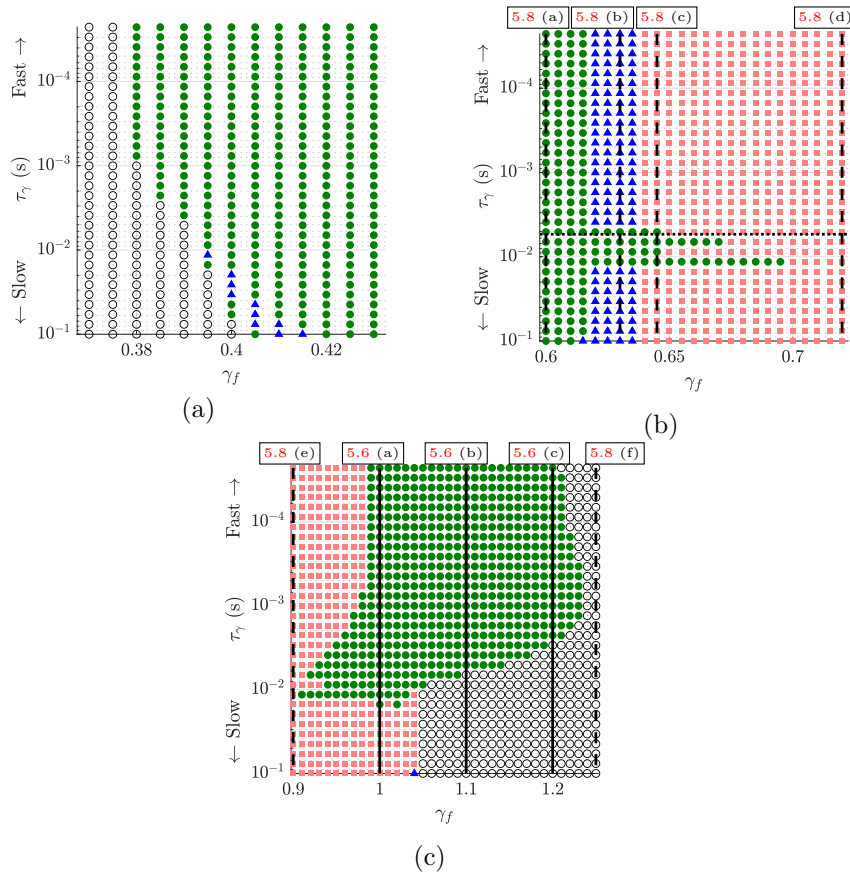


FIGURE 5.5: Classification of the regimes produced depending on the blowing pressure transient parameters: final value γ_f and characteristic time τ_γ . Coexistence zones of stable regimes: (a) equilibrium and first register (b) first and second register (c) all three regime types. Horizontal line on graph (b) shows $\tau = 1/f_1$. The vertical lines highlight the γ values of phase diagrams in figure 5.6 and 5.8.

The second zone of coexistence between stable regimes is explored in figure 5.5 (b). The first and second register are separated by some stable quasi-periodic regimes. This is the same quasi periodic regime that appears in time-domain synthesis in figure 5.1 overlays the unstable

portion of the second register branch. There is a particular range of characteristic time τ_γ that seems to produce more first register. This time range is of the order of magnitude of the period of the first register.

The last zone of coexistence shows that eventhough three regimes are stable at the same time, there is no γ_f region where all three are produced. In this instance, some regime do not appear although they are stable. This can be explained by analyzing the attraction basins (see figure 5.8).

5.5.2 Attraction basins in the phase space

The results concerning the influence of the blowing pressure parameters can be better understood by examining the region of the phase space leading to each regime. A point in the phase space represents the current state of the system, meaning the value of the state variables and their derivatives. Since the system is deterministic, a given point in the phase space will always lead to the same stable established regime. Therefore regions of the phase space can be associated with each regime. These regions are called *attraction basins*.

Because the phase space is has dimension $2N_m + 2$ (all modal components and their derivatives, plus reed position and speed), it is necessary to choose a projection to represent the attraction basins. After some trials, a projection of the phase space on the two first modal components (see Eq. (5.12)) and the derivative of the second, (p_1, p_2, \dot{p}_2) , was chosen as a three-dimensional projection because it allows good separation of the limit cycles and attraction basins. To estimate the attraction basins, time-domain synthesis is launched with initial conditions spanning the projected phase space. 256 initial conditions are scattered in a latin hypercube sampling into a rectangular parallelepiped such that

$$p_1^I \in [-0.2, 0.2], \quad p_2^I \in [-2, 2], \quad \dot{p}_2^I \in [-707, 707]. \quad (5.16)$$

These bounds should be undestood with respect to the amplitude of the limit cycle along each dimension (that can be seen in figures 5.6 and 5.8). They were chosen so that whenever a regime is stable, it is obtained in synthesis at least once. All the other modal pressure components and their derivative are initially zero. The initial values of the variables p , then x and u are computed accordingly through equations (5.7) and (5.4). To reduce the complexity of the problem, the parameter γ does not vary during these simulations. For each initial condition, the initial valueof all the axiliary variables in the synthesis is calculated so that there is no discontinuity when starting the synthesis.

Figure 5.6 shows these initial conditions, associated with the regimes they lead to, for 3 values of the blowing pressure parameter γ . All the phase space points the system passes through during the transient are also part of the attraction basin, so they are represented in the figure as well. Three values of γ are chosen near the last Hopf bifurcation, where the equilibrium becomes stable again. Graph 5.6 (a) is computed at $\gamma = 1$, before the Hopf bifurcations (H3 and H4 in figure 5.2), so only register 1 and 2 are stable. Therefore, none of the initial conditions lead to equilibrium. Each attraction basin is located around the corresponding limit cycle. The attraction basins seem to overlap, but it is merely an effect of the projection of the phase space. For graph 5.6 (b) corresponds to $\gamma = 1.1$, right above the Hopf bifurcations H2 and H3. One can see that some initial conditions located near the origin now lead to equilibrium. This plot can seem surprising when compared to figure 5.5 (c), which only shows equilibrium and register 1 for this value of γ_f using the control scenario, although the attraction basin of the second register seems larger than that of the other regimes. This is both an effect of the projection, which spreads the second register but shrinks the first register, and the fact that the control scenario starts from the origin of the phase space, so attraction basins surrounding the origin (such as that of the first register) are more likely to be crossed. Here we see that the attraction basins need to be assorted with some kind of interpretation in terms of musician action, because their size alone provide little information. Graph 5.6 (c) represents the same results for $\gamma = 1.2$, where figure 5.5 (c) showed more occurences of the equilibrium than for $\gamma = 1.1$. This is explained by the attraction basin of the equilibrium being larger. Notice that the attraction basin of the first register expands, while the attraction basin of the second register shrinks. This process continues until the second register ceases to be stable at fold bifurcation F3 (see figure 5.2).

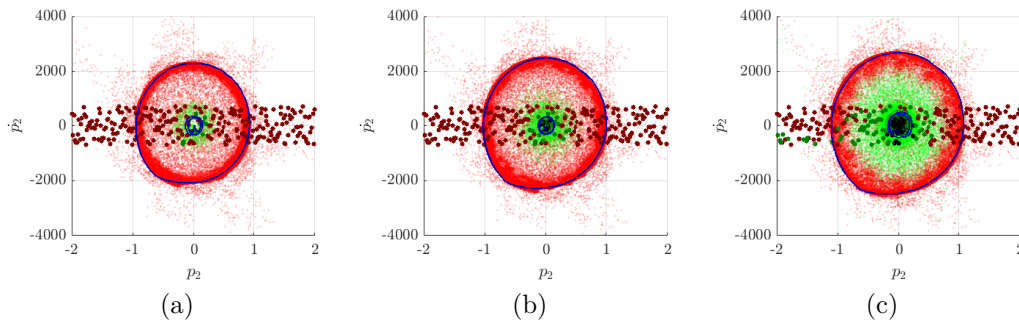


FIGURE 5.6: Projection of the attraction basins. Large dots are initial conditions, small dots are points the synthesis goes through. The dots' colors indicate the final regime they lead to (black: equilibrium, green: first register, red: second register). Dark lines represent the limit cycles. The small inside one is the first register and the outer is the second register. The blowing pressure γ is (a) 1, (b) 1.1, (c) 1.2 (highlighted in figures 5.5 and 5.2).

[Multimedia/ch5/Supp1.mp4](#)

FIGURE 5.7: Multimedia file: Animation: evolution of a 3D projection of the attraction basins along the bifurcation diagram.

Figure 5.8 shows the attraction basins and limit cycles, in a 3-dimensional projection of the phase space (p_1, p_2, \dot{p}_2) , at particular values of γ highlighted in figure 5.5. Graphs 5.8 (a), (b) (c) and (d) should be read as further information on the regime map 5.5 (b), at the beginning of the coexistence zone between stable first and second registers. Graph 5.8 (a) corresponds to $\gamma = 0.6$, and confirms that the first register is the only stable regime: it was the only one to appear in the regime map 5.5 (b). Then, a quasi-periodic attractor appears in graph 5.8 (b), for $\gamma = 0.63$. Although the associated attraction basin seems smaller than that of the first register, it seems to almost surrounds the origin of the phase diagram. Knowing that the control scenario Eq. (5.15) necessarily starts from the origin of the phase space, this explains why regime map 5.5 (b) displays more quasi-periodic regimes than first register. As similar interpretation can be formulated with regards to graphs 5.8 (c) and (d), respectively for $\gamma = 0.645$ and $\gamma = 0.72$, where more second register appears on 5.5 (b). Although the size of the first register's attraction basin seems comparable to that of the second register, the latter clearly holds a central position around the origin of the phase space. When the second register attraction basin grows in graph 5.8 (d), this even translates to the first register disappearing from the regime map 5.5 (b). Note that graph 5.8 (d) confirms that the first register is still stable, as announced by the HBM in fig 5.2. Graphs 5.8 (e) $\gamma = 0.9$ illustrate a slightly different explanation of a similar case of only second register appearing in the regime map 5.5 (c): in this case, the attraction basin of the first register is just too small, it only makes up for a few points in figure 5.8 (e). Graph 5.8 (f) ($\gamma = 1.25$) is comparable to (d) in that many regimes are stable, but only the one with the most central attraction basin appears in the regime map 5.5 (c): the equilibrium, whose attraction basin is smaller than the others but completely surrounds the origin of the phase space. To complete the study, the full evolution sequence of the attraction basins can be found as an animation in multimedia file Supp1.mp4. The authors suggest frequently pausing the animation to observe precisely how the attraction basins develop along multistability zones.

5.6 Effect of the resonator's inharmonicity on regime production

Before using the analysis of woodwind model to developing new instruments, it can be very informative to apply it to existing instruments, in the idea of a reverse engineering procedure. If the analysis method can explain *a posteriori* some design choices made on instruments with known satisfying sound production characteristics, then it might help guide further innovative

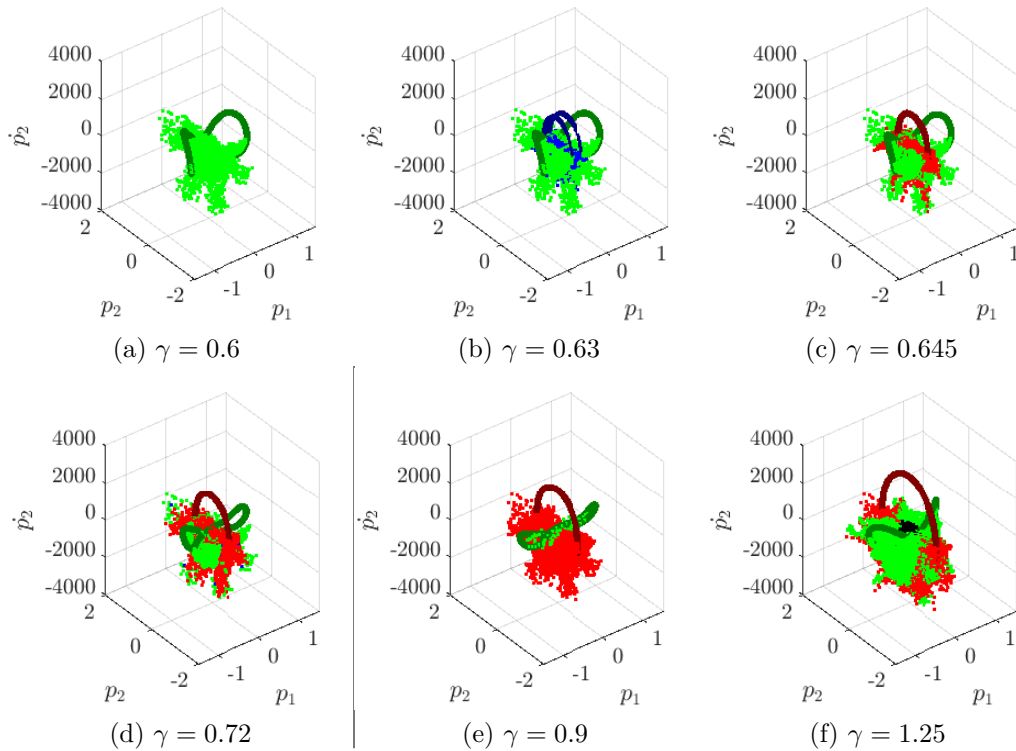


FIGURE 5.8: Attraction basins (dots) and limit cycles (lines) in a 3D projection of the phase space, for different blowing pressures γ . Black: Equilibrium, green: first register, red: second register, blue: quasi-periodic.

design choices in the right direction. In the present case, the produced regimes are studied for the 7 lowest first register fingerings, and one acoustical parameter is varied artificially: the inharmonicity between first and second resonance. According to the so-called *Bouasse-Benade prescription*, near-perfect inharmonicity between the resonances is cited as a condition for good playability of the instrument [GMV19a; BG68; Ben90]. On the saxophone, experimental studies using an artificial mouth has shown that varying inharmonicity greatly affect regime production [DV15; Dal+95]. In this work we define inharmonicity as the ratio between the second and first resonance f_2/f_1 . On a saxophone this ratio is close to 2.

For the purpose of the following study, *optimal* regime production conditions are defined crudely in terms of how much each regime appears in synthesis. Optimizing regime production then simply means maximizing the appearance of the first register while minimizing that of the second register and quasi-periodic regimes. Indeed, one of the challenges many beginner saxophone players face on the lowest fingerings is controlling the instrument so that the first register can be produced rather than the others. Quasi-periodic regimes are largely considered undesirable in common musical practice, however they are a common issue on the lowest fingerings of the saxophone.

5.6.1 Regime production regions

Expanding on the idea of figure 5.5, one can study the produced regime across the two-dimensional parameter space (γ_f, ζ) , while still varying the characteristic time τ_γ . Figure 5.9 shows the classification of obtained regimes, for several combinations γ_f, ζ and several attack times. For readability reasons, the resolution of the cartography presented here is rather coarse, with only 8 values of γ_f and ζ and 3 characteristic times τ_γ , for a total of 192 synthesized signals. As a study case, two maps computed with different inharmonicity values are presented on figure 5.9 (a) and (b), so that they can be compared. In the modal formalism, the inharmonicity is changed very simply by modifying the value of the second modal frequency. Two typical values are chosen: one that could be called null inharmonicity, $f_2/f_1 = 2$; and the value measured on the saxophone which is slightly higher, $f_2/f_1 = 2.065$.

Focusing on figure 5.9 (a), several features can be described, and recognized from the situations explored in section 5.5 with a fixed ζ . Coexistence regions can be noticed on most of the map, with a given (γ_f, ζ) couple leading to different regimes depending on the characteristic time. This further demonstrates that multistability is a very common phenomenon across the control parameter space in woodwind models. A particular case of coexistence occurs near the Hopf bifurcations, where the equilibrium becomes unstable. They can be seen as boundaries between equilibrium and oscillation regimes, near $\gamma = 0.4$, $\zeta = 0.2$ and $\gamma = 1$. These situations entail the same phenomenon as in figure 5.5 (a): long attack times lead to the system staying at equilibrium, while fast attacks can trigger oscillations. Coexistence situations similar to figure 5.5 (b) can also be seen, for example for $\zeta = 1.2$ and $\gamma_f \simeq 0.8$, where the short and long characteristic times lead to the second register, while the medium time leads to a first register. These situations are hard to describe: while it is understandable that the equilibrium tends to appear more for the longest characteristic times, the repartition between two oscillating regime is unpredictable.

Figure 5.9 (a) ($f_2/f_1 = 2$) displays a lot more second register than figure 5.9 (b) ($f_2/f_1 = 2.065$). Contrary to what could be expected, a null inharmonicity, where the second resonance frequency is twice the first, does not lead to more first register production. This might indicate that the first register is harder to produce. Care should be taken with this interpretation, in that the musician probably does not use the control parameter space uniformly when playing the instrument. Since an exact integer ratio between resonances does not facilitate the production of the first register, one can ask if the model shows a particular value of inharmonicity which favors the production of first register.

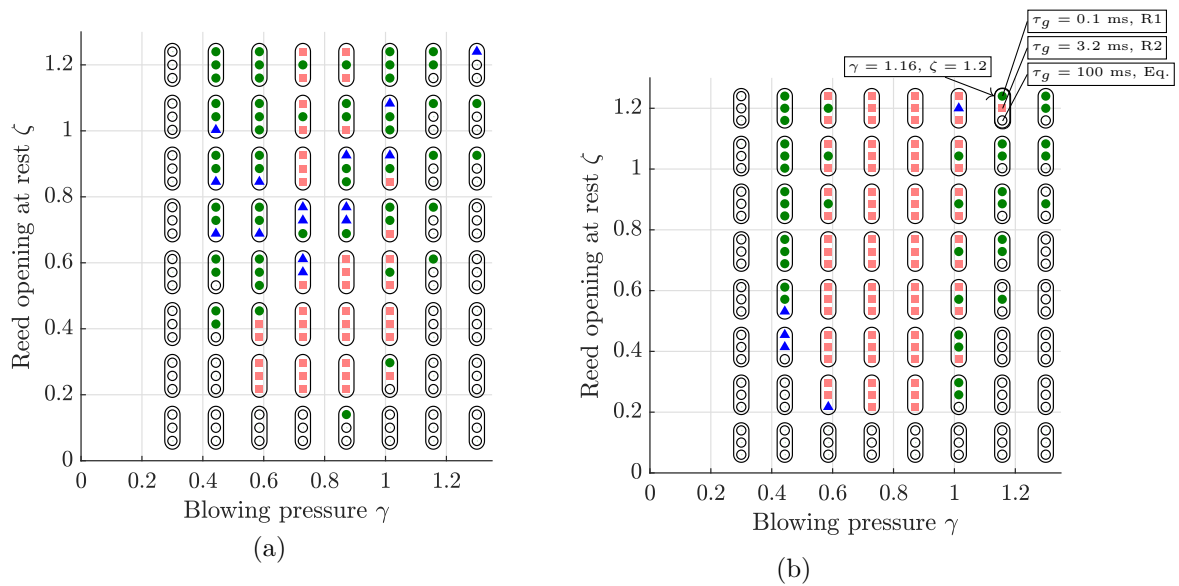


FIGURE 5.9: Classification of the regimes produced (empty circle: equilibrium, green: first register, red: second register, blue: quasi-periodic) depending on control parameters: γ_f and ζ . Each rectangle corresponds to a couple (γ_f, ζ) and the points inside indicate the regime for each characteristic time τ_γ (bottom 0.1 ms, middle 3 ms and top 100 ms). One rectangle on graph (b) is annotated as an example. Graphs correspond to two inharmonicity for low written D \sharp fingering (a) $f_2 = 2.065f_1$, near the measured value. (b) $f_2 = 2f_1$.

5.6.2 Rate of produced regimes: influence of the rise time on global regime production

To study the question of the inharmonicity favoring first register production, several different regime maps are computed for all the first register fingerings of the saxophone, with the second modal frequency f_2 varying from $1.96f_1$ to $2.15f_1$. The total number of computed points is $N_p = 192$ as in figure 5.9. The produced regimes are counted for the whole map, and a rate is

computed for each of them with respect to the total number of oscillating regime as

$$R_i = \frac{N_{p,i}}{N_p}, \quad (5.17)$$

where regime i can either be first register, second register or periodic regimes, $N_{p,i}$ is the number of points corresponding to regime i in the regime map and N_p is the total number of points corresponding to any oscillating regime (i.e. all regimes but equilibrium). Note that this description ignores non-oscillating regimes.

Figure 5.10 depicts the rate of each oscillating regimes produced depending on the inharmonicity descriptor, for the lowest fingering of the first register, Bb . On this figure the regimes were counted separately for each characteristic time τ_g before being summed for the whole map to produce an averaged rate. On the averaged rate, optimal points are highlighted as triangles, they correspond respectively to the maximum of first register and minimum of second register produced. Both appear for values slightly above $f_2/f_1 = 2$. The inharmonicity values maximizing first register production do not correspond to exactly harmonic resonances, but a second resonance slightly sharper than the octave of the first. The proportion of quasi-periodic regimes is also displayed on the figure. Note that inharmonicity values around 2 lead to less quasi-periodic regimes, which is corroborated by existing results [DVM14; DV15]. On figure 5.10, it can be seen that the region of minimal production of the second register coincides with maximal production of quasi-periodic regimes. Thus a compromise must be made, since avoiding the second register seems to favor the production of quasi-periodic regimes. On this figure, it can be seen that using only one value of characteristic time could have led to similar conclusions. However this is not always the case, and figure 5.11 show two examples where studying only one characteristic time can lead to very biased conclusion.

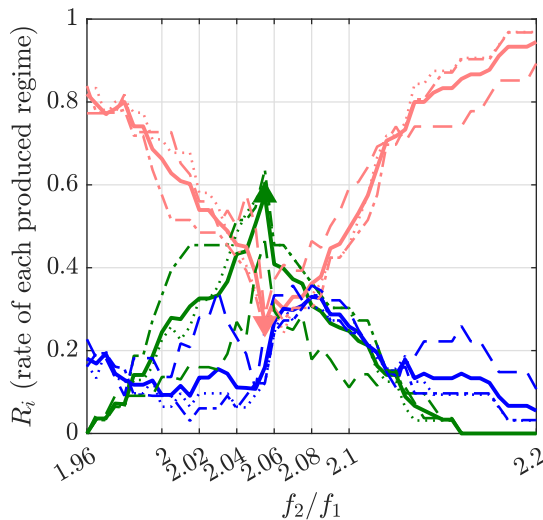


FIGURE 5.10:]

Rate of produced regimes (Eq. (5.17)) for fingering Bb . Green: first register, red: second register, blue: quasi-periodic. Linestyles indicate the characteristic time. Dotted: $\tau_g = 0.1$ ms, dash-dot: $\tau_g = 3.2$ ms, dashed: $\tau_g = 100$ ms, solid: averaged rate. An upward triangle marks the maximum first register averaged rate, a downward triangle marks the minimum second register rate.

For the $D\sharp$ fingering (figure 5.11 (a)), one can see that depending on the chosen increase duration τ_γ the production ratio varies greatly (from 20% to 60%). If any quantitative interpretation is to be expected from these results, it can be changed dramatically depending on the chosen attack time. Figure 5.11 (b) shows the results for the written D fingering. This case exhibits an outlier : the longest attack time yields a optimal inharmonicity value of 2.08, whereas the others point to 2.04. In this case, considering several attack times is a way to smooth out outliers due to a particular value of the attack time. This figure can also lead to a radically different interpretation in terms of musician control strategies. The fact that certain

attack time values seem to markedly decrease the rate of production of a certain regime could be used by the musician to avoid producing it.

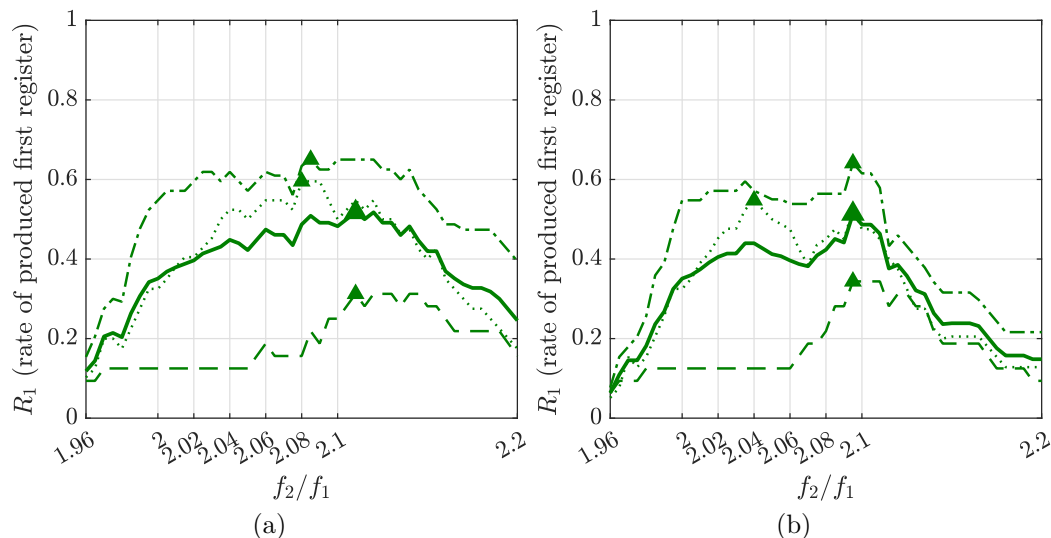


FIGURE 5.11: Rate of first register regime (Eq. (5.17)) produced for (a) written low D# fingering and (b) written low D fingering. Linestyles indicate the characteristic time. Dotted: $\tau_g = 0.1$ ms, dash-dot: $\tau_g = 3.2$ ms, dashed: $\tau_g = 100$ ms, solid: averaged rate. An upward triangle marks the maximums of first register rates.

5.6.3 Inharmonicity of the saxophone

In this section, the optimal inharmonicity in terms of regime production is studied for the 7 lowest first register fingerings of the first register. Higher fingerings are not represented because they add no relevant information: first register regimes production ratios are close to 100% for all the studied inharmonicity. This corresponds to the saxophonists' experience that the high notes of the instrument's first register are often easier to produce than the low notes, and to the fact that the first impedance peak is much higher than the others on the high fingerings [CSW09b]. The optimums are compared with the inharmonicity value measured on the saxophone on which the model is based. Figure 5.12 summarizes the production ratios for all the fingerings. The first comment that can be made on this figure is that the optimal inharmonicity seems to vary across the fingerings. It is always above 2: null inharmonicity does not favor first register production on the low fingerings of the saxophone. The two optimums are close to the measured inharmonicity. Additionally, the trend is respected, with optimal and measured harmonicities increasing for higher fingerings. Note that the optimum for the E fingering is very far from the measured inharmonicity, but the production ratios are almost constant. Overall, the simulation shows that the most first register and least second register is produced by the model for values of inharmonicity near those measured on the saxophone. This result sheds some light on the empirical choice of the acoustical properties on the saxophone. Indeed, if the inharmonicity was far from the values observed on saxophones, the model predicts more second register would be produced. This effect is arguably undesirable. However, this choice goes with a compromise, as it also favors quasi-periodic regime production (see figure 5.10), which are a known issue in low saxophone fingerings.

5.7 Conclusion

In wind instrument models, stable regimes coexist throughout large regions in the space of the musician control parameters. Thus, even an exhaustive description of the stability or instability of each oscillating regime in the control parameter space is only an incomplete answer, as it doesn't suffice to predict which regime emerges in these multistability zones. To quantify multistability, time-domain synthesis can be used in addition to a stability study (done by

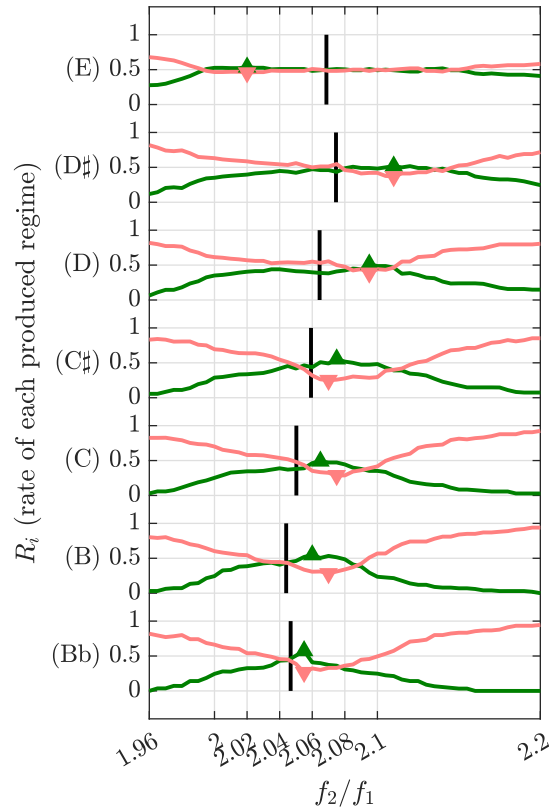


FIGURE 5.12: Rate of produced regimes for the lowest fingerings of the alto saxophone (written pitch). Green: first register, red: second register. An upward triangle marks the maximum first register averaged rate, a downward triangle marks the minimum second register rate. Vertical lines mark the measured inharmonicity values. Curves are vertically offset for clarity.

HBM for instance) to describe the attraction basin of each regime. This paper proposes to explore which regime is produced in multistability zones using a varying control scenario. A description of the attraction basins of each regime in the phase space completes the results of the varying control scenario. Eventhough the proposed control scenario is simplified to the extreme, its results can be tied to real musician actions. Dedicated experimental work, out of the scope of this paper, could help design more realistic control scenarios. Taking into account multistability, a study of synthesized regimes sheds light on an acoustical choice made by instruments makers: the inharmonicity of the saxophone. An integer ratio between the first and second resonance frequencies does not favor the production of first register. Note that this result brings nuance one of Benade's guidelines for favored oscillation frequencies (as stated in the second fundamental principle of [BG68]): subtle competition between register comes into play, depending on more than the mere impedance magnitude at the playing frequency and its harmonics. Instead, it tends to favor the production of second register, which is arguably undesirable for a first register fingering. Carefully tuned inharmonic resonances, where the second is higher than twice the first, can lead to more first register production. The optimal inharmonicity value found on the model corresponds to harmonicity measured on saxophone resonators. This result provides an *a posteriori* interpretation of the acoustical characteristics of the saxophone, as chosen empirically by instrument makers, as the acoustical characteristic leading to easier production of the first register. Such results are among the first steps towards applying numerical simulations as predictive tools to estimate playability in instrument design.

Acknowledgments

This work has been carried out in the framework of the Labex MEC (ANR-10-LABEX-0092) and of the A*MIDEX project (ANR-11-IDEX-0001-02), funded by the Investissements d'Avenir

French Government program managed by the French National Research Agency (ANR). This study has been supported by the French ANR 659 LabCom LIAMFI (ANR-16-LCV2-007-01).

General conclusion

This work contributes to exploring and explaining the dynamic behavior of the saxophone. Oscillating regimes are exhibited and classified, numerically and experimentally, and their arrangement in the control parameter space is characterized and linked to the acoustical parameters of the resonator. Several results are interpreted in terms of their possible use in the development of new instruments.

Concluding remarks

As a summary of the tools explored in the document, Figure 5.13 responds to the block diagram of the general introduction Figure 1 and replaces the schematic descriptions by actual examples of representations drawn from the manuscript, and the broad concepts by the names of the implemented methods. This framework encompasses the results of the whole dissertation, and can be used as basis for further research as an example of exploration method around the acoustical properties of a self-oscillating instrument.

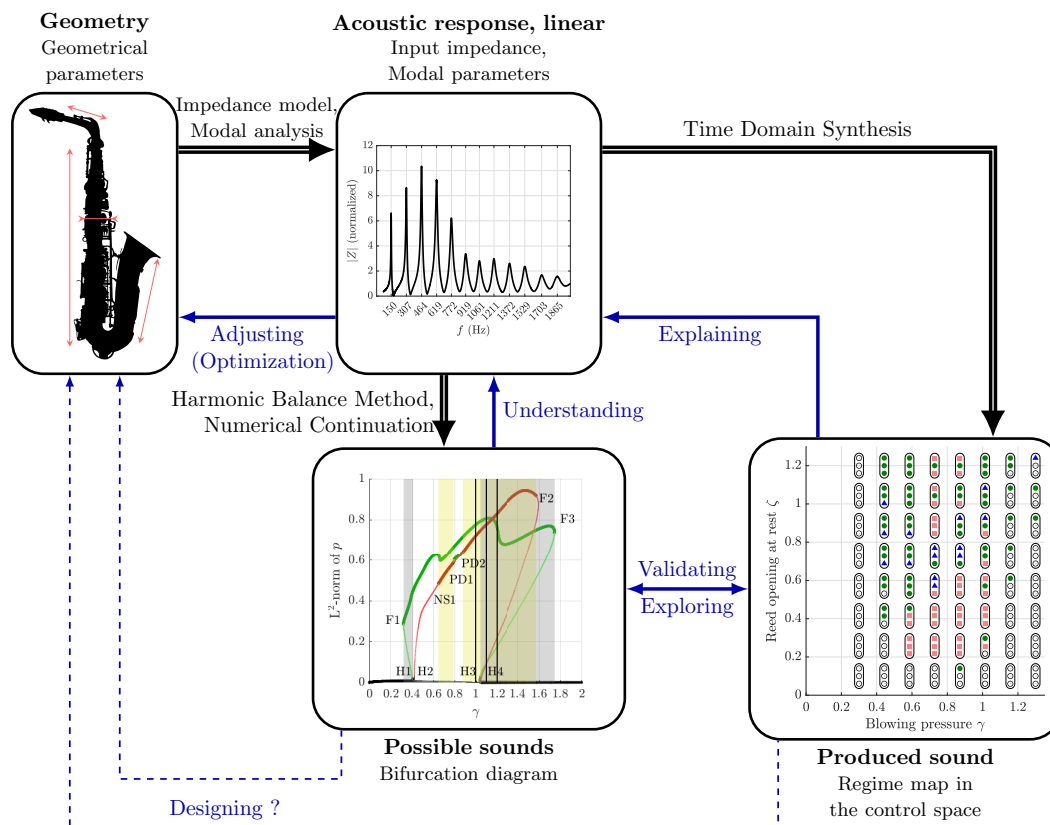


FIGURE 5.13: Graphical layout of the numerical tools and representations explored throughout this dissertation. Compare with the introduction diagram Figure 1.

Chapter 2 deals with the optimization of a bicylindrical resonator based on a saxophone's input impedance. To keep the optimization from diverging, the chosen cost function is a twice differentiable L^2 -norm between input impedance moduli well-suited to gradient-based optimization. To assess the results of numerical optimization in instrument design, introducing

some kind of control group of instruments expands the claims that can be made and greatly solidifies them. Here, based on the use of a *control saxophone*, it was deduced that a bicylindrical (coaxial) resonator is bound to be different from a saxophone, and should be viewed and developed as a separate instrument. This result was demonstrated further in Chapter 4 by the dynamics of the associated time-domain synthesis models. The dynamics are represented as maps of the type of regime produced depending on the control parameters. The maps give a broad view of the dynamics of an instrument. Thus, they lead to direct interpretations very similar to what could be said when trying out a real instrument. For example, the bicylindrical resonator presented here fails to produce first register regimes for its lowest fingerings.

The regime maps of Chapter 4 must be used comparatively, to qualify differences between the behavior of two instrument models. This compensates for multiple biases, such as multistability (Chapter 5). Furthermore, quantitative correspondance lacks between the model's dynamics and the real instrument's behavior – but qualitative validations start to arise, (Chapter 3). Regime maps make the best of qualitative considerations by favoring interpretations in terms of global trends, and the presence or absence of certain regimes. The ability for qualitative observations constitutes a fundamental difference between comparing signals one by one and comparing maps. Comparisons between maps also inform each other: many comments on the bicylindrical resonator's dynamics are only possible in the light of the differences between the target saxophone and a control saxophone, as well as between the target with its register hole closed or open.

Chapter 4 presents a way to outline a model's behavior quicker than regime maps, by finding the instability threshold of the equilibrium through Hopf bifurcation continuation. As one of the simplest possible descriptor of a model's global dynamics, this fits a large-scale dynamic study perfectly. Hopf continuation sheds light on a remarkable homogeneity in the instability thresholds along the saxophone family (soprano, alto and tenor), despite globally different modal parameter values. It remains to be seen how the instability threshold of the model translates in terms of the experience of the musician.

The categorization of the oscillating regimes, as undertaken in chapter 3, is a way to expand the range of qualitative observations that can be made on the global dynamics of a model. In addition to extending the catalog of known signal archetypes produced by the saxophone, this part of the work describes how each one appears depending on the control parameters. This is among the first steps in linking each regime to musical actions and techniques, and assessing how easy they are to produce.

The lowest fingerings exhibit double two-step regimes, where the reed closes two distinct times per period. It is easily found by numerical synthesis and by a musician. This regime is comparable in terms of oscillation mechanism with the well-known double stick-slip observed on violins. Hence, it appears that the analogy between bowed strings and conical woodwinds still holds potential to complete our understanding of the dynamics of both instrument families. An inverted counterpart exists to the double two-step motion, where the reed shortly opens twice per period. Their timbres are similar.

Using continuation on the model shows that the double two-step motions are connected to the second register branch by period-doubling bifurcations. This explicitly links their production to the second mode of the resonator. The complete bifurcation diagram is coherent with the experimental observation of the order in which regimes appear as a function of the blowing pressure (standard two-step, double two-step, second register, inverted double two-step and inverted two-step). The method to obtain this result integrates the qualitative nature of the instrumented mouthpiece by examining the bifurcation diagrams as a whole, where each branch corresponds to the previously classified regime archetypes. In that regard, the bifurcation diagram is a tool well-suited to matching a model to experiments, even when only rough estimates are available for the model's parameters.

On a more fundamental note, Chapter 5 dives into the complexity of the dynamics of the saxophone as a strongly nonlinear physical system. It shows that for low fingerings, several distinct regimes are stable for almost all control parameter combinations. Therefore, a mere stability study, even if it accounts for all the possible regimes of the instrument, is insufficient to predict which regime will be produced. This remark is extremely important as it incites future attempts at predicting the behavior of an instrument from its physical model to go beyond the notion of stability. As a way to go beyond stability, the attraction basins where

initial states lead to each regime are explored. In multistability zones, they mapped out in the phase space, and their arrangement around each other is described. This procedure gives a lot of insight as to how the model can converge to one solution or another. To take into account multistability in a dynamic study, i.e. try to sweep through all the possible stable regimes, we suggest using a parametrized control transient scenario. This method has the advantage of being more musically representative and less time-consuming than an explicit mapping of the phase space. The parameterized control transient is used to refine the cartography of Chapter 4, and it eliminates some bias in the description of the model's dynamic.

Overall, this dissertation advances the understanding of the dynamics of the saxophone, by focusing on the oscillating regimes produced by a numerical model and putting them in relation to one another. It shows what is to be expected in terms of the dynamic behavior of a saxophone model, and to the extent of the experimental capabilities, which behaviors can be directly tied to sound production on a real instrument. Bifurcations are highlighted as crucial points marking great dynamic changes, which makes them strong indicators to summarize sound production characteristics. It is our hope that, in time, all these concepts can be used directly by saxophone makers and musicians, to provide solid scientific footing to certain aspects of their crafts.

Perspectives

In many regards, the results proposed here prompt further studies. The qualitative approach adopted for most dynamical studies naturally begs for quantitative results to bring nuance to the conclusions. Furthermore, larger scale experimental campaigns are required to generalize the observation of certain exhibited phenomena. In general, the results of this dissertation demand to be checked against musical practice, by involving more real instruments and musicians to adjust or rectify the models' architecture and parameters. Only through thorough experimental work, closely tied with musicians, can effective indicators of "ease of playing" be developed, based on the ideas brought forth in the present document.

Notably, a direct improvement of the results presented here would be offered by a survey involving musicians. Even with no further numerical or experimental work, this would greatly refine all the interpretations related to "ease of playing". In particular, questions could concern how often does one play the second register on a low fingering without acting on the register key, or whether inverted or double two-step are known and desirable to musicians – all queries helping to qualify each regime in terms of their musical use. Musicians could also provide general orientation to studies tackling known issues of the instrument, by providing information on the most problematic or hardest fingerings as well as generally undesirable phenomena experienced by beginners or seasoned players. It would be interesting to partially base some of these studies on the understanding of the musical community, and use scientific tools such as those presented in this work to confirm or invalidate the causes musicians tend to attribute to certain phenomena.

Involving instrument manufacturers in the research process is also a way to test and develop the instrument analysis tools presented in this work. Such partnerships already start to exist, such as the ANR Liamfi involving Buffet-Crampon. For instance, collaborating with a manufacturer can be a way to orient the parametric studies concerning the acoustical and geometrical characteristics of the resonator, depending on what is doable. A close collaboration with makers can also lead to the production of instrument prototypes specifically designed to test a scientific hypothesis, for example by systematically modifying only one parameter between several resonators.

A simple way to scale up the results obtained in this study is to extend the set of measured saxophone impedances. Although it could seem repetitive, adding more instruments to the test pool would allow fundamentally different conclusions. With some kind of statistical significance, one could derive some general rules of thumb for the behavior of saxophones in general, and not just one saxophone. It would also give a lot of nuance to the results, by finding out the variability that exists between several copies in the same line of instruments, the same brand, the same branch of the family... Expanding on this idea, it could be very informative to include other reed instruments featuring conical or bicylindrical resonators, such as the oboe, bassoon, *flauta de millo*, or Venova.

Of course, it is possible to envision a complete study of the influence of each control parameter on sound production by a numerical model. Rounding down the control parameters to the 4 main ones discussed in this work (γ , ζ , q_r and ω_r), producing regime maps for all measured fingerings on a 4D-grid of control parameters would represent a high but not absurd computational effort. Although there would be merits to this study, any interpretation would lack some preliminary results consolidating details of the numerical procedure, notably by validating the values of the model's fixed parameters with regards to experimental results. However, once the model's dynamic features (multistability, etc.) are solidly documented, and realistic control scenarios can be drawn from experimental studies, an extensive behavior study could be extremely informative and lay the groundworks to a more detailed understanding of the saxophone.

One of the clearest perspectives of this work lies in the exploitation of an artificial mouth. Based on the present work's identification of certain phenomena (standard and inverted two-step, double two-step), an artificial mouth would be able to provide a more quantitative link between the oscillations obtained numerically and the behavior of a real instrument. The experimental study of certain qualitative phenomena, such as hysteresis or the effect of the characteristic attack time of the blowing pressure, require the precise monitoring of the control parameters that an artificial mouth offers. Following certain experimental studies [DV15; Alm+13; LHC13], it seems that the idea of producing a regime map with an artificial mouth has a lot of potential. The experimental procedures could be inspired by certain principles exposed here through numerical considerations, such as the idea of a strictly comparative use of the maps, or the variable control scenario accounting for multistability. Of course, the reverse may be even more true, with experimental procedures informing the numerical methods, and making them more easily tied with the real instrument's characteristics. An extensive artificial mouth study has the potential to assert the model as a predictive tool. This relies on solid estimation of the model's parameters, notably those related to the reed, based on experimental data. The challenge lies in choosing the adapted hypotheses and parameter values, and in overcoming the satisfaction of having a model that *sounds* like a saxophone to build a model that quantitatively *plays* like one.

Note that all the prospects evoked here, even those whose immediate interest seems mostly academic, can converge to effective assistance to the conception of novel reed instruments. A pathway to this is gearing the interpretation of scientific results towards musical practice or instrument making issues, and providing experimental grounding to all numerical and analytical studies whenever possible.

Appendix A

First-order quadratic saxophone model

This appendix provides an explicit formulation of the quadratic recast of the saxophone model presented in section 1.1, as used in the MANLAB implementation.

A.1 Quadratic recast

The main differential system is

$$\left\{ \begin{array}{l} \dot{R}_k = \text{Re}(C_k)u + \text{Re}(s_k)R_k - \text{Im}(s_k)I_k \\ \dot{I}_k = \text{Im}(C_k)u + \text{Im}(s_k)R_k + \text{Re}(s_k)I_k \\ \dot{y} = \omega_r(-q_r y - x + p - \gamma + F_c - \beta\omega_r\omega_0 F_c y) \\ \dot{x} = \omega_r y, \end{array} \right. , k = 1 \dots N_m \quad (\text{A.1})$$

where R_k and I_k are the real and imaginary part of the modal pressure component p_k , y is the dimensionless speed of the reed \dot{x}/ω_r . There are $2N_m + 2$ main variables. Introducing the reed opening $h = x + 1$ for commodity, the auxiliary variables that allow the system to be quadratic are defined by

$$p = 2 \sum_{k=1}^{N_m} R_k \quad (\text{A.2})$$

$$Abs h^2 = h^2 + \eta \quad (\text{A.3})$$

$$z = \frac{1}{2} \zeta(h + Abs h) \quad (\text{A.4})$$

$$Abs D p^2 = (\gamma - p)^2 + \eta \quad (\text{A.5})$$

$$S_R^2 = Abs D p \quad (\text{A.6})$$

$$s \times Abs D p = \gamma - p \quad (\text{A.7})$$

$$v = s \times S_R \quad (\text{A.8})$$

$$u = z v \quad (\text{A.9})$$

$$F_c = K_c \frac{1}{2} (Abs h - h)^2 \quad (\text{A.10})$$

Note that the auxiliary variable p is not necessary for the system to be quadratic. It is merely defined for convenience, to be readily accessible for plotting. We precise that S_R corresponds to the regularized version of $\sqrt{|\gamma - p|}$ and s is the regularized version of $\text{sign}(\gamma - p)$. There are 9 auxiliary variables. The ghost reed simplification is applied by removing the auxiliary variable F_c and the two associated terms in Eq. (A.1).

A.2 Jacobian matrix

Bifurcation continuation methods of sections 3.2.3 and 4.3 require an explicit Jacobian matrix of the system be provided. The jacobian matrix of the system is

$$\mathbf{J} = \begin{bmatrix}
R_1 & 0 & \dots & 0 & -I_1 & 0 & \dots & 0 & 0 & \dots & \dots & 0 \\
0 & \ddots & \ddots & \ddots & 0 & \ddots & \ddots & \ddots & 0 & \dots & \dots & 0 \\
\vdots & \ddots & \ddots & \ddots & \vdots & \ddots & \ddots & \ddots & \vdots & \dots & \dots & \vdots \\
0 & \dots & 0 & R_{Nm} & 0 & \dots & 0 & -I_{Nm} & 0 & \dots & \dots & 0 \\
I_1 & 0 & \dots & 0 & R_1 & 0 & \dots & 0 & 0 & \dots & \dots & 0 \\
0 & \ddots & \ddots & \ddots & 0 & \ddots & \ddots & \ddots & 0 & \dots & \dots & 0 \\
\vdots & \ddots & \ddots & \ddots & \vdots & \ddots & \ddots & \ddots & \vdots & \dots & \dots & \vdots \\
0 & \dots & 0 & I_{Nm} & 0 & \dots & 0 & R_{Nm} & 0 & \dots & \dots & 0 \\
0 & \dots & \dots & \dots & \dots & 0 & D_{yy} & -\omega_r & \omega_r & 0 & \dots & \dots & 0 & D_{yF_c} \\
0 & \dots & \dots & \dots & \dots & 0 & \omega_r & -1 & \dots & \dots & \dots & \dots & \dots & 0 \\
2 & \dots & \dots & 2 & 0 & \dots & 0 & 0 & 0 & -1 & 0 & \dots & \dots & 0 \\
0 & \dots & \dots & \dots & \dots & 0 & 0 & 2h & 0 & -2Absh & 0 & \dots & \dots & 0 \\
0 & \dots & \dots & \dots & \dots & 0 & 0 & \zeta/2 & 0 & \zeta/2 & -1 & 0 & \dots & 0 \\
0 & \dots & \dots & \dots & \dots & 0 & 0 & -2\Delta p & 0 & 0 & -2AbsDp & 0 & \dots & 0 \\
0 & \dots & \dots & \dots & \dots & 0 & 0 & 0 & 0 & 0 & 1 & -2S_R & 0 & 0 & 0 & 0 \\
0 & \dots & \dots & \dots & \dots & 0 & 0 & -1 & 0 & 0 & -s & 0 & -AbsDp & 0 & 0 & 0 \\
0 & \dots & \dots & \dots & \dots & 0 & 0 & 0 & 0 & 0 & 0 & s & S_R & -1 & 0 & 0 \\
0 & \dots & \dots & \dots & \dots & 0 & 0 & 0 & 0 & 0 & 0 & 0 & 0 & z & -1 & 0 \\
0 & \dots & \dots & \dots & \dots & 0 & D_{Fch} & 0 & -D_{Fch} & 0 & 0 & 0 & 0 & 0 & 0 & -1
\end{bmatrix}, \quad (\text{A.11})$$

where

$$D_{yy} = -q_r \omega_r - \beta \omega_r \omega_0 F_c \quad (\text{A.12})$$

$$D_{yF_c} = \omega_r (1 - \beta \omega_r \omega_0 y) \quad (\text{A.13})$$

$$\Delta p = \gamma - p \quad (\text{A.14})$$

$$D_{Fch} = -K_c (Absh - h)/2. \quad (\text{A.15})$$

Appendix B

Estimation of control parameters (internship A. Pillet, co-supervised)

In order to compare the experimental and numerical results finely, we have attempted to develop a method to estimate the dimensionless control parameters with the instrumented mouthpiece. One of the main challenges is determining the static pressure p_M necessary to close the reed channel entirely. This physical value is necessary to compute the blowing pressure parameter γ and can also help estimate the reed opening parameter ζ . It is subject to variations during playing, due to changes in reed equilibrium position for instance: if the reed is pushed closer to the lay by the lip, the pressure necessary to close it is decreased. Therefore, a dynamic estimate is hard to produce.

2.0.0.0.a Observation of the synthesized signals

First, we look at synthesis, where the reed closure is unambiguously defined by $x \leq -1$ (see (1.5)). In this case, we can construct an estimator to find γ only from the output signals of the synthesis p and x . We chose to base the estimator on the average of the displacement signal x , defined in a periodic state as

$$\langle x \rangle = \frac{1}{T} \int_0^T x(t) dt, \quad (\text{B.1})$$

where T is the oscillation period. Averaging Eq. (1.5), assuming $\langle p \rangle = 0$, gives

$$\langle x \rangle = -\gamma + \frac{1}{T} \int_0^T F_c(x(t)) dt. \quad (\text{B.2})$$

Under nonbeating reed conditions (with a null contact force $F_c = 0$), the static average of $\langle x \rangle$ can be shown to be equal to $-\gamma$, which could make it a good estimator of γ . However, the beating reed phenomenon, where $F_c \neq 0$, compromises this result. The estimator must then be adjusted. A corrective term linked with the beating is introduced, without requiring precise knowledge of $F_c(x)$. We know that $F_c(x)$ is zero for all of the period except for a duration T_c (see Figure B.1). The duration T_c corresponds to when the reed channel is closed ($x \leq -1$ in synthesis). Introducing the average value \bar{F}_c over contact duration T_c , Eq. (B.2) becomes

$$\langle x \rangle = -\gamma + \bar{F}_c \frac{T_c}{T}, \quad (\text{B.3})$$

leading to an estimator of γ of the form

$$\gamma = \langle x \rangle - \bar{F}_c \frac{T_c}{T}, \quad (\text{B.4})$$

the closure duration ratio TR_c is defined as $TR_c = \frac{T_c}{T}$.

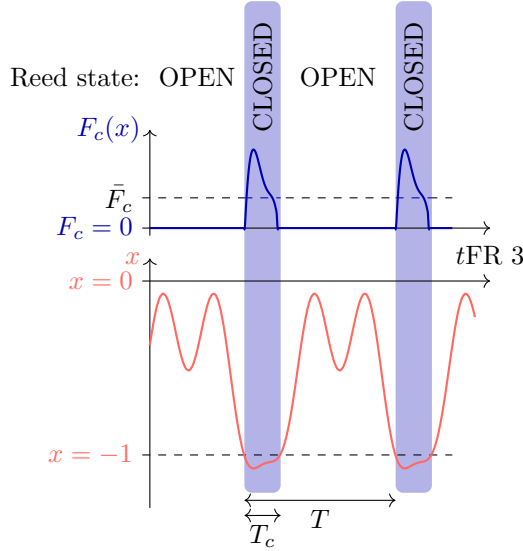


FIGURE B.1: Schematic representation of the reed displacement signal x and contact force $F_c(x)$ in a beating reed regime.

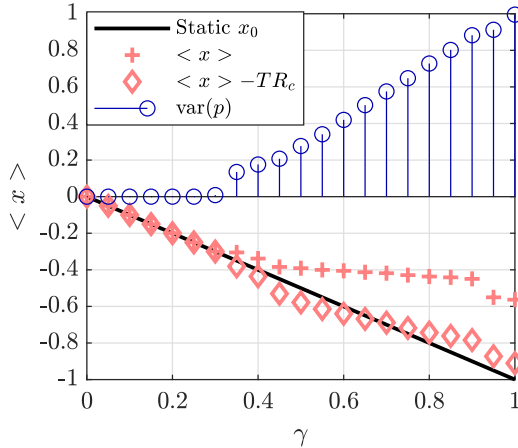


FIGURE B.2: Correspondance between the dimensionless parameter γ and the mean reed position $\langle x \rangle$, in synthesis.

Figure B.2 shows the results obtained from several signals synthesized on the low Bb fingering of the saxophone using the reflection function formalism. These signals are beating reed regimes. In this case, we can see that the average of the position $\langle x \rangle$ diverges from the static value $-\gamma$ whenever there is an oscillation (shown on the graph by $\text{var}(p) > 0$). In this situation, the quantity $\langle x \rangle - TR_c$ is a decent estimation of γ . Unfortunately this method is only applicable to synthesis signals as it supposes a clean, unambiguous definition of the reed closure, as well as the reed equilibrium point, things that are in themselves difficult to estimate on signals measured with the instrumented mouthpiece. Moreover, it does not generalize to other types of regimes such as the second register (at least not without adapting \bar{F}_c). Therefore, we suggest another method based on estimating the static closure pressure p_M .

2.0.0.0.b Estimating p_M and γ on measured signals

The pressure necessary to close the reed channel in the static regime p_M is used in the formal definition of control parameter γ (Eq. (1.3)). The challenge of this subsection is to develop an estimator of p_M that works while the oscillations occur, even though p_M is a quantity defined in the static regime. First, we must locate the instant at which the reed channel closes. This can be done by detecting a peak of acceleration (or rather deceleration) of the reed. For each

period, the greatest acceleration peak corresponds to the reed closure. The pressure difference at this instant can be seen as a dynamic closure pressure, a first estimator of the static closure pressure denoted $p_M^{(1)}$. Note that this estimator is extremely sensitive to any delay between the reed displacement signal and the pressure signals. Here, the reed displacement was delayed to compensate for the propagation of sound waves through the pressure probe. Figure B.3 shows such detection performed on two examples of regime produced on the B fingering of an alto saxophone. Note that this estimator is necessarily biased, as it is intrinsically affected by the reed's dynamic properties (mass and damping). In fact, it always overestimates the static closure pressure. A second estimator is then devised: rather than the reed closure instant, where the reed speed and acceleration are very large, we look at the reed opening instant, which is potentially closer to the static regime with the reed moving slower. The opening instant is defined by the reed speed changing sign (from negative to positive) when the pressure difference is lower than the value at the closure. The pressure difference at this instant is defined as a second estimate $p_M^{(2)}$ of the static closure pressure. Figure B.3 shows the estimated reed opening instants and the associated pressure. Note that these two definitions are compatible with real-time implementation and require minimal computational power.

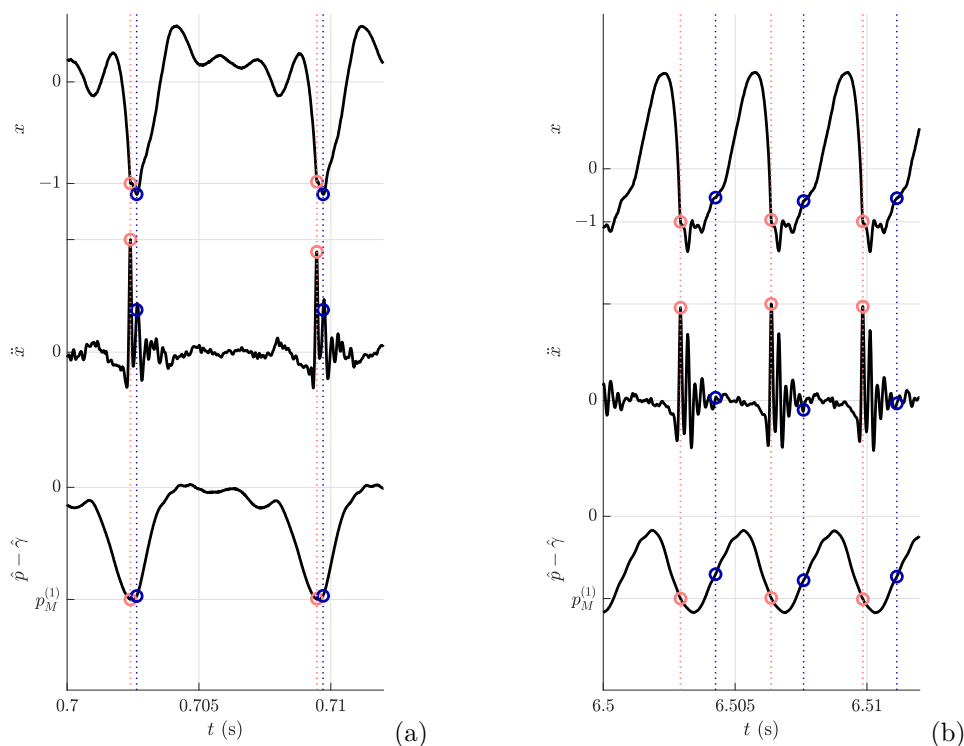


FIGURE B.3: Signals measured with the instrumented mouthpiece while increasing the blowing pressure on fingering B of an alto saxophone, with detection of reed closure instants (red) and opening instants (blue) giving estimates of the static closure pressure p_M as the pressure difference $\hat{\gamma} - \hat{p}$. The y scale is arbitrary. (a) standard two-step motion (first register), (b) second register.

The two estimators can be used conjointly to provide an order of magnitude of the control parameter γ from measured instrumented mouthpiece signals. Figure B.4 shows the estimation performed on a blowing pressure ramp on the B fingering of an alto saxophone (same ramp as in Section 3.3). The order of magnitude of the closure pressure correspond to those that can be found in the literature (between 5 and 10 kPa [DGO03; DV15; Ido+93]). The apparition of the oscillations correspond to an estimated value of γ of about 0.4, which is coherent with usual analytical results ($\gamma > 1/3$) and synthesis. Estimated γ values do not go above 2, which can still possibly lead to oscillations. The used signal includes a whole variety of oscillating regimes (see Section 3.3), and the estimators seem to give mostly coherent values for all of them, especially the first indicator based on reed closure.

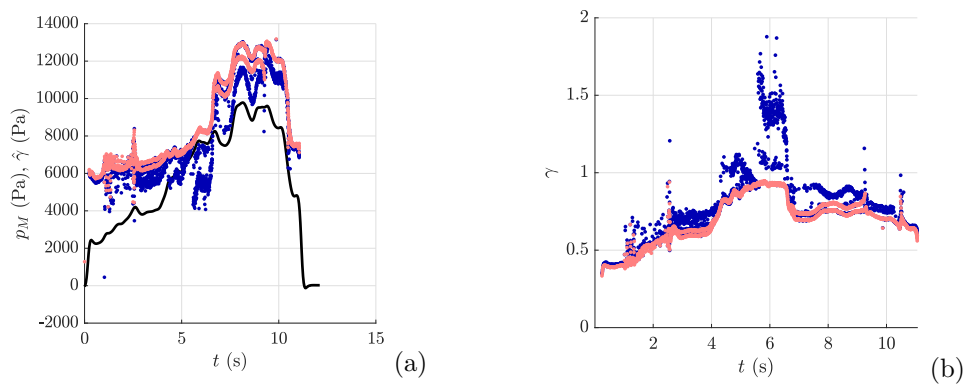


FIGURE B.4: Estimation of blowing pressure γ for an instrumented mouthpiece blowing pressure ramp on fingering B of an alto saxophone. Colors: physical blowing pressure $\hat{\gamma}$ (**black**), and p_M or γ estimations due to reed closure instants (**red**) and opening instants (**blue**).

Bibliography

- [ADG04] Mérouane Atig, Jean-Pierre Dalmont, and Joël Gilbert. “Saturation mechanism in clarinet-like instruments, the effect of the localised non-linear losses”. In: *Applied Acoustics* 65.12 (2004), pp. 1133–1154.
- [AFL12] Roman Auvray, Benoît Fabre, and Pierre-Yves Lagrée. “Regime change and oscillation thresholds in recorder-like instruments”. In: *The Journal of the Acoustical Society of America* 131.2 (2012), pp. 1574–1585.
- [AG79] Eugene L Allgower and Kurt Georg. *Introduction to numerical continuation methods*. SIAM, 1979.
- [Alm+02] André Almeida et al. “Physical study of double-reed instruments for application to sound-synthesis”. In: *Proceedings of the 2017 International Symposium on Musical Acoustics*. 2002.
- [Alm+10] André Almeida et al. “Clarinet parameter cartography: automatic mapping of the sound produced as a function of blowing pressure and reed force”. In: *Proceedings of International Symposium on Music Acoustics*. 2010.
- [Alm+13] Andre Almeida et al. “The clarinet: How blowing pressure, lip force, lip position and reed “hardness” affect pitch, sound level, and spectrum”. In: *The Journal of the Acoustical Society of America* 134.3 (2013), pp. 2247–2255.
- [Alm+17] A Almeida et al. “The mechanism producing initial transients on the clarinet”. In: *The Journal of the Acoustical Society of America* 142.6 (2017), pp. 3376–3386.
- [AR85] Jean-Marie Adrien and Xavier Rodet. “Physical models of instruments: A modular approach, application to strings”. In: *ICMC*. 1985.
- [AS95] Seiji Adachi and Masa-aki Sato. “Time-domain simulation of sound production in the brass instrument”. In: *The Journal of the Acoustical Society of America* 97.6 (1995), pp. 3850–3861.
- [AVW04] Federico Avanzini and Maarten Van Walstijn. “Modelling the mechanical response of the reed-mouthpiece-lip system of a clarinet. Part I. A one-dimensional distributed model”. In: *Acta Acustica united with Acustica* 90.3 (2004), pp. 537–547.
- [Bac19] Andrea Bacciotti. *Stability and Control of Linear Systems*. Springer, 2019.
- [Bac61] John Backus. “Vibrations of the reed and the air column in the clarinet”. In: *The Journal of the Acoustical Society of America* 33.6 (1961), pp. 806–809.
- [Bac63] John Backus. “Small-vibration theory of the clarinet”. In: *The Journal of the Acoustical Society of America* 35.3 (1963), pp. 305–313.
- [Bac78] John Backus. “Multiphonic tones in the woodwind instruments”. In: *The Journal of the Acoustical Society of America* 63.2 (1978), pp. 591–599.
- [BD19] Stefano Bosi and David Desmarchelier. “Local bifurcations of three and four-dimensional systems: A tractable characterization with economic applications”. In: *Mathematical Social Sciences* 97 (2019), pp. 38–50.
- [BDK15] Serhii Brezetskyi, Dawid Dudkowski, and Tomasz Kapitaniak. “Rare and hidden attractors in Van der Pol-Duffing oscillators”. In: *The European Physical Journal Special Topics* 224.8 (2015), pp. 1459–1467.
- [Ben88] Arthur H Benade. “Equivalent circuits for conical waveguides”. In: *The Journal of the Acoustical Society of America* 83.5 (1988), pp. 1764–1769.
- [Ben90] Arthur H Benade. *Fundamentals of musical acoustics*. Courier Corporation, 1990.

- [Ber+13] Baptiste Bergeot et al. “Prediction of the dynamic oscillation threshold in a clarinet model with a linearly increasing blowing pressure”. In: *Nonlinear Dynamics* 73.1-2 (2013), pp. 521–534.
- [Bey+02] WJ Beyn et al. *Handbook of Dynamical Systems (Vol 2), chapter Numerical Continuation, and Computation of Normal Forms*. Elsevier, 2002.
- [BG68] Arthur H Benade and DJ Gans. “Sound production in wind instruments”. In: *Annals of the New York Academy of Sciences* 155.1 (1968), pp. 247–263.
- [BK88] AH Benade and SN Kouzoupis. “The clarinet spectrum: Theory and experiment”. In: *The Journal of the Acoustical Society of America* 83.1 (1988), pp. 292–304.
- [BL18] Barend Bentvelsen and Arnaud Lazarus. “Modal and stability analysis of structures in periodic elastic states: application to the Ziegler column”. In: *Nonlinear Dynamics* 91.2 (2018), pp. 1349–1370.
- [BL88] AH Benade and SJ Lutgen. “The saxophone spectrum”. In: *The Journal of the Acoustical Society of America* 83.5 (1988), pp. 1900–1907.
- [BNC09] Alistair CP Braden, Michael J Newton, and D Murray Campbell. “Trombone bore optimization based on input impedance targets”. In: *The journal of the Acoustical Society of America* 125.4 (2009), pp. 2404–2412.
- [Bri53] Leon Brillouin. “Wave propagation in periodic structures: electric filters and crystal lattices”. In: (1953).
- [BSS87] Richard H Byrd, Robert B Schnabel, and Gerald A Shultz. “A trust region algorithm for nonlinearly constrained optimization”. In: *SIAM Journal on Numerical Analysis* 24.5 (1987), pp. 1152–1170.
- [BSW20] Henri Boutin, John Smith, and Joe Wolfe. “Trombone lip mechanics with inertive and compliant loads (“lipping up and down”)”. In: *The Journal of the Acoustical Society of America* 147.6 (2020), pp. 4133–4144.
- [BTC15] Stefan Bilbao, Alberto Torin, and Vasileios Chatziioannou. “Numerical modeling of collisions in musical instruments”. In: *Acta Acustica united with Acustica* 101.1 (2015), pp. 155–173.
- [Bui+11] James M Buick et al. “Investigation of non-linear acoustic losses at the open end of a tube”. In: *The Journal of the Acoustical Society of America* 129.3 (2011), pp. 1261–1272.
- [BV04] Stephen Boyd and Lieven Vandenberghe. *Convex optimization*. Cambridge university press, 2004.
- [CDPF07] Bruno Cochelin, Nouredine Damil, and Michel Potier-Ferry. *Méthode asymptotique numérique*. Hermes Lavoissier, 2007.
- [CGC00] JS Cullen, Joël Gilbert, and DM Campbell. “Brass instruments: linear stability analysis and experiments with an artificial mouth”. In: *Acta Acustica united with Acustica* 86.4 (2000), pp. 704–724.
- [CGT00] Andrew R Conn, Nicholas IM Gould, and Ph L Toint. *Trust region methods*. Vol. 1. Siam, 2000.
- [Cha+19a] Vasileios Chatziioannou et al. “Inverse modelling of clarinet performance”. In: *Proc. 26th International Congress on Sound and Vibration (ICSV26), Montreal*. 2019.
- [Cha+19b] Vasileios Chatziioannou et al. “Investigating Clarinet Articulation Using a Physical Model and an Artificial Blowing Machine”. In: *Acta Acustica united with Acustica* 105.4 (2019), pp. 682–694.
- [CHPV17] Vasileios Chatziioannou, Alex Hofmann, and Montserrat Pàmies-Vilà. “An artificial blowing machine to investigate single-reed woodwind instruments under controlled articulation conditions”. In: *Proceedings of Meetings on Acoustics 174ASA*. Vol. 31. 1. Acoustical Society of America. 2017, p. 035003.
- [CK08] Antoine Chaigne and Jean Kergomard. *Acoustics of Musical Instruments (Acoustique des instruments de musique)*. Belin, 2008.

- [CL96] Thomas F Coleman and Yuying Li. “An interior trust region approach for nonlinear minimization subject to bounds”. In: *SIAM Journal on optimization* 6.2 (1996), pp. 418–445.
- [Col+19] Tom Colinot et al. “Influence of the “ghost reed” simplification of the bifurcation diagram of a saxophone model”. In: *Acta Acustica united with Acustica* 105.6 (2019), pp. 1291–1294.
- [Col+20] Tom Colinot et al. “Multiple two-step oscillation regimes produced by the alto saxophone”. In: *The Journal of the Acoustical Society of America* 147.4 (2020), pp. 2406–2413.
- [Coy+15] Whitney L Coyle et al. “Predicting playing frequencies for clarinets: A comparison between numerical simulations and simplified analytical formulas”. In: *The Journal of the Acoustical Society of America* 138.5 (2015), pp. 2770–2781.
- [CSW08] Jer Ming Chen, John Smith, and Joe Wolfe. “Experienced saxophonists learn to tune their vocal tracts”. In: *Science* 319.5864 (2008), pp. 776–776.
- [CSW09a] Jer-Ming Chen, John Smith, and Joe Wolfe. “Pitch bending and glissandi on the clarinet: roles of the vocal tract and partial tone hole closure”. In: *The Journal of the Acoustical Society of America* 126.3 (2009), pp. 1511–1520.
- [CSW09b] Jer-Ming Chen, John Smith, and Joe Wolfe. “Saxophone acoustics: introducing a compendium of impedance and sound spectra”. In: *Acoustics Australia* 37.1-19 (2009).
- [CSW11] Jer-Ming Chen, John Smith, and Joe Wolfe. “Saxophonists tune vocal tract resonances in advanced performance techniques”. In: *The Journal of the Acoustical Society of America* 129.1 (2011), pp. 415–426.
- [CTH82] PG Clinch, GJ Troup, and L Harris. “The importance of vocal tract resonance in clarinet and saxophone performance, a preliminary account”. In: *Acta Acustica united with Acustica* 50.4 (1982), pp. 280–284.
- [CV09] Bruno Cochelin and Christophe Vergez. “A high order purely frequency-based harmonic balance formulation for continuation of periodic solutions”. In: *Journal of sound and vibration* 324.1-2 (2009), pp. 243–262.
- [CW12] Vasileios Chatziioannou and Maarten van Walstijn. “Estimation of clarinet reed parameters by inverse modelling”. In: *Acta Acustica united with Acustica* 98.4 (2012), pp. 629–639.
- [Dal+05] Jean-Pierre Dalmont et al. “An analytical prediction of the oscillation and extinction thresholds of a clarinet”. In: *The Journal of the Acoustical Society of America* 118.5 (2005), pp. 3294–3305.
- [Dal07] Jean-Pierre Dalmont. “Analytical and experimental investigation of the dynamic range of conical reed instruments”. In: *Proceedings of the International Symposium on Musical Acoustics, Barcelona, Spain*. 2007.
- [Dal+95] Jean-Pierre Dalmont et al. “Some aspects of tuning and clean intonation in reed instruments”. In: *Applied acoustics* 46.1 (1995), pp. 19–60.
- [Das31] Panchanon Das. “Theory of the clarinet”. In: (1931).
- [DGK00] Jean-Pierre Dalmont, Joël Gilbert, and Jean Kergomard. “Reed instruments, from small to large amplitude periodic oscillations and the Helmholtz motion analogy”. In: *Acta Acustica united with Acustica* 86.4 (2000), pp. 671–684.
- [DGO03] Jean-Pierre Dalmont, Joël Gilbert, and Sébastien Ollivier. “Nonlinear characteristics of single-reed instruments: Quasistatic volume flow and reed opening measurements”. In: *The Journal of the Acoustical Society of America* 114.4 (2003), pp. 2253–2262.
- [DK94] JP Dalmont and J Kergomard. “Lattices of sound tubes with harmonically related eigenfrequencies”. In: *Acta acustica (Les Ulis)* 2.5 (1994), pp. 421–430.
- [DKK91] Eusebius Doedel, Herbert B Keller, and Jean Pierre Kernevez. “Numerical analysis and control of bifurcation problems (I): Bifurcation in finite dimensions”. In: *International journal of bifurcation and chaos* 1.03 (1991), pp. 493–520.

- [DLC+16] Patricio De La Cuadra et al. “Optimized redensing of the quena”. In: *EuroRegion, (Porto, Portugal)* (2016).
- [DLR08] Jean-Pierre Dalmont and Jean Christophe Le Roux. “A new impedance sensor for wind instruments”. In: *The journal of the Acoustical Society of America* 123.5 (2008), pp. 3014–3014.
- [DLR13] Jean-Pierre Dalmont and Jean-Christophe Le Roux. *Acoustic impedance sensor designed to measure the input acoustic impedance of a waveguide*. US Patent 8,544,327. 2013.
- [DLV14] J-P Dalmont and G Le Vey. “The irish Uilleann pipe: a story of lore, hell and hard D”. In: *International Symposium on Musical Acoustics*. 2014.
- [DMM04] D Dessi, F Mastroddi, and L Morino. “A fifth-order multiple-scale solution for Hopf bifurcations”. In: *Computers & structures* 82.31-32 (2004), pp. 2723–2731.
- [Doc+16] J-B Doc et al. “Sound production on a “coaxial saxophone””. In: *The Journal of the Acoustical Society of America* 140.5 (2016), pp. 3917–3924.
- [Doe81] Eusebius J Doedel. “AUTO: A program for the automatic bifurcation analysis of autonomous systems”. In: *Congr. Numer* 30.3 (1981), pp. 265–284.
- [Dou12] Vincent Doutaut. “An aid to innovation in instrument-making: a collaborative approach between workshops and research laboratories”. In: 2012.
- [DV15] Jean-Baptiste Doc and Christophe Vergez. “Oscillation regimes produced by an alto saxophone: Influence of the control parameters and the bore inharmonicity”. In: *The Journal of the Acoustical Society of America* 137.4 (2015), pp. 1756–1765.
- [DV17] J-P Dalmont and G Le Vey. “Discrete acoustical resonators with harmonic eigenfrequencies”. In: *Acta Acustica united with Acustica* 103.1 (2017), pp. 94–105.
- [DVM14] J-B Doc, Ch Vergez, and S Missoum. “A minimal model of a single-reed instrument producing quasi-periodic sounds”. In: *Acta Acustica united with Acustica* 100.3 (2014), pp. 543–554.
- [ELS00] Koen Engelborghs, T Luzyanina, and G Samaey. “DDE-BIFTOOL: a Matlab package for bifurcation analysis of delay differential equations”. In: *TW Report* 305 (2000), pp. 1–36.
- [Ern+20] A Ernout et al. “Woodwind instrument design optimization based on impedance characteristics with geometric constraints”. In: *Acta acustica* (2020 [submitted]).
- [Far+06] Snorre Farner et al. “Contribution to harmonic balance calculations of self-sustained periodic oscillations with focus on single-reed instruments”. In: *The Journal of the Acoustical Society of America* 119.3 (2006), pp. 1794–1804.
- [FBC00] Matteo Facchinetti, Xavier Boutillon, and Andrei Constantinescu. “Application of modal analysis and synthesis of reed and pipe to numerical simulations of a clarinet”. In: *The Journal of the Acoustical Society of America* 108.5 (2000), pp. 2590–2590.
- [Fer+10] Didier Ferrand et al. “High-precision regulation of a pressure controlled artificial mouth: the case of recorder-like musical instruments”. In: *Acta Acustica united with Acustica* 96.4 (2010), pp. 701–712.
- [Fer+14] Romain Feron et al. “The PAFI project: a collaborative approach for developing tools for instruments makers”. In: *Proceedings of International Symposium on Music Acoustics*. 2014.
- [FFK04] Claudia Fritz, Snorre Farner, and Jean Kergomard. “Some aspects of the harmonic balance method applied to the clarinet”. In: *Applied acoustics* 65.12 (2004), pp. 1155–1180.
- [Flo79] Gaston Floquet. “Sur la théorie des équations différentielles linéaires”. In: *Annales Scientifiques de L’École Normale Supérieure*. Vol. 8. 1879, pp. 3–132.
- [Fré+19] Vincent Fréour et al. “Numerical analysis and comparison of brass instruments by continuation”. In: *International Symposium on Musical Acoustics*. 2019.

- [Fri+05] Claudia Fritz et al. “Experimental study of the influence of the clarinetist’s vocal tract”. In: *Proc. Forum Acusticum*. 2005.
- [FS13] Vincent Fréour and Gary P Scavone. “Acoustical interaction between vibrating lips, downstream air column, and upstream airways in trombone performance”. In: *The Journal of the Acoustical Society of America* 134.5 (2013), pp. 3887–3898.
- [FS99] Leonardo Fuks and Johan Sundberg. “Blowing pressures in bassoon, clarinet, oboe and saxophone”. In: *Acta Acustica united with Acustica* 85.2 (1999), pp. 267–277.
- [Gaz94] Bruno Gazengel. “Caractérisation objective de la qualité de justesse, de timbre et d’émission des instruments à vent à anche simple”. PhD thesis. 1994.
- [GB04] Ludwig Gerhardt and Roger Blench. “The traditional music of the Jos Plateau in Central Nigeria: an overview”. In: (2004).
- [GCV19] Louis Guillot, Bruno Cochelin, and Christophe Vergez. “A Taylor series-based continuation method for solutions of dynamical systems”. In: *Nonlinear Dynamics* 98.4 (2019), pp. 2827–2845.
- [Gen+01] Oleg Gendelman et al. “Energy pumping in nonlinear mechanical oscillators: part I—dynamics of the underlying Hamiltonian systems”. In: *J. Appl. Mech.* 68.1 (2001), pp. 34–41.
- [GGA95] Bruno Gazengel, Joël Gilbert, and Noam Amir. “Time Domain Simulation of Single Reed Wind Instrument. From the Measured Input Impedance to the Synthesis Signal. Where are the Traps?” In: *Acta acustica (Les Ulis)* 3.5 (1995), pp. 445–472.
- [GGL06] Oleg V Gendelman, Emmanuel Gourdon, and Claude-Henri Lamarque. “Quasiperiodic energy pumping in coupled oscillators under periodic forcing”. In: *Journal of Sound and Vibration* 294.4-5 (2006), pp. 651–662.
- [GGL97] Noël Grand, Joël Gilbert, and Franck Laloë. “Oscillation threshold of woodwind instruments”. In: *Acta Acustica united with Acustica* 83.1 (1997), pp. 137–151.
- [GH88] David E Goldberg and John Henry Holland. “Genetic algorithms and machine learning”. In: (1988).
- [Gho38] RN Ghosh. “Theory of the Clarinet”. In: *The Journal of the Acoustical Society of America* 9.3 (1938), pp. 255–264.
- [GK11] Ph Guillemain and Jean Kergomard. “Generic resonator models for real-time synthesis of reed and brass instruments”. In: *Proceedings of the 6th Forum Acusticum*. 2011, pp. 515–520.
- [GKN89] Joël Gilbert, Jean Kergomard, and Edouard Ngoya. “Calculation of the steady-state oscillations of a clarinet using the harmonic balance technique”. In: *The journal of the Acoustical Society of America* 86.1 (1989), pp. 35–41.
- [GKV05] Philippe Guillemain, Jean Kergomard, and Thierry Voinier. “Real-time synthesis of clarinet-like instruments using digital impedance models”. In: *The Journal of the Acoustical Society of America* 118.1 (2005), pp. 483–494.
- [GMV19a] Joël Gilbert, Sylvain Maugeais, and Christophe Vergez. “From the bifurcation diagrams to the ease of playing of reed musical instruments. A theoretical illustration of the Bouasse-Benade prescription?” In: *International Symposium on Musical Acoustics*. 2019.
- [GMV19b] Joel Gilbert, Sylvain Maugeais, and Christophe Vergez. “From the bifurcation diagrams to the ease of playing of reed musical instruments. Application to a reed-like instrument having two quasi-harmonic resonances”. In: *7th International Conference on Nonlinear Vibrations, Localization and Energy Transfer*. 2019.
- [Gok79] Aleksandr Yakovlevich Gokhshtein. “On auto-oscillations of finite amplitude in a pipe with reed”. In: *Doklady Akademii Nauk*. Vol. 248. 3. Russian Academy of Sciences. 1979, pp. 556–560.
- [Gok81] A Ya Gokhshtein. “Role of the airflow modulator in the excitation of sound in wind instruments”. In: *Soviet Physics Doklady*. Vol. 26. 1981, p. 954.

- [GPP98] Joël Gilbert, Sylvie Ponthus, and Jean-François Petiot. “Artificial buzzing lips and brass instruments: Experimental results”. In: *The Journal of the Acoustical Society of America* 104.3 (1998), pp. 1627–1632.
- [GQT66] Stephen M Goldfeld, Richard E Quandt, and Hale F Trotter. “Maximization by quadratic hill-climbing”. In: *Econometrica: Journal of the Econometric Society* (1966), pp. 541–551.
- [Gro12] Timo Grothe. “Investigation of bassoon embouchures with an artificial mouth”. In: 2012.
- [Gui04] Ph Guillemain. “A digital synthesis model of double-reed wind instruments”. In: *EURASIP Journal on Advances in Signal Processing* 2004.7 (2004), p. 943842.
- [Gui+10] Ph Guillemain et al. “An instrumented saxophone mouthpiece and its use to understand how an experienced musician plays”. In: *Acta Acustica united with Acustica* 96.4 (2010), pp. 622–634.
- [Gui15] Alexis Guilloteau. “Conception d’une clarinette logique”. PhD thesis. Aix-Marseille Université, 2015.
- [Gui+15] Alexis Guilloteau et al. “The effect of the size of the opening on the acoustic power radiated by a reed woodwind instrument”. In: *Journal of Sound and Vibration* 343 (2015), pp. 166–175.
- [Gui+20] Louis Guillot et al. “A purely frequency based Floquet-Hill formulation for the efficient stability computation of periodic solutions of ordinary differential systems”. In: *Journal of Computational Physics* (2020), p. 109477.
- [GVC19] Louis Guillot, Christophe Vergez, and Bruno Cochelin. “Continuation of periodic solutions of various types of delay differential equations using asymptotic numerical method and harmonic balance method”. In: *Nonlinear Dynamics* 97.1 (2019), pp. 123–134.
- [Han06] Nikolaus Hansen. “The CMA evolution strategy: a comparing review”. In: *Towards a new evolutionary computation*. Springer, 2006, pp. 75–102.
- [HG14] Alex Hofmann and Werner Goebel. “Production and perception of legato, portato, and staccato articulation in saxophone playing”. In: *Frontiers in psychology* 5 (2014), p. 690.
- [Hir+90] A Hirschberg et al. “A quasi-stationary model of air flow in the reed channel of single-reed woodwind instruments”. In: *Acta Acustica united with Acustica* 70.2 (1990), pp. 146–154.
- [Hir95] A Hirschberg. *Mechanics of Musical Instruments (Chap. 6, J. Kergomard), chapter Elementary considerations on reed-instrument oscillations*. 1995.
- [HLC12] Thomas Helie, Nicolas Lopes, and René Causse. “Open-loop control of a robotized artificial mouth for brass instruments”. In: *The Journal of the Acoustical Society of America* 131.4 (2012), pp. 3470–3470.
- [Hol75] JH Holland. “Adaptation in Natural and Artificial Systems. Cambridge, MA: .” In: (1975).
- [Ido+93] Tohru Idogawa et al. “Nonlinear vibrations in the air column of a clarinet artificially blown”. In: *The Journal of the Acoustical Society of America* 93.1 (1993), pp. 540–551.
- [IL50] U Ingård and S Labate. “Acoustic circulation effects and the nonlinear impedance of orifices”. In: *The Journal of the Acoustical Society of America* 22.2 (1950), pp. 211–218.
- [Iro31] Eric J Irons. “On the fingering of conical wind instruments”. In: *The London, Edinburgh, and Dublin Philosophical Magazine and Journal of Science* 11.70 (1931), pp. 535–539.
- [Jac00] Leland B Jackson. “A correction to impulse invariance”. In: *IEEE Signal Processing Letters* 7.10 (2000), pp. 273–275.

- [Kau01] Wilfried Kausel. “Optimization of brasswind instruments and its application in bore reconstruction”. In: *Journal of New Music Research* 30.1 (2001), pp. 69–82.
- [KB49] Nikolai Mitrofanovich Krylov and Nikolai Nikolaevich Bogoliubov. *Introduction to non-linear mechanics*. 11. Princeton University Press, 1949.
- [Kee84] Douglas H Keefe. “Acoustical wave propagation in cylindrical ducts: Transmission line parameter approximations for isothermal and nonisothermal boundary conditions”. In: *The Journal of the Acoustical Society of America* 75.1 (1984), pp. 58–62.
- [Kel86] HB Keller. *Lectures on Numerical Methods In Bifurcation Problems*. Springer-Verlag, 1986.
- [Ker+16] Jean Kergomard et al. “Idealized digital models for conical reed instruments, with focus on the internal pressure waveform”. In: *The Journal of the Acoustical Society of America* 139.2 (2016), pp. 927–937.
- [KM71] J Kohut and MV Mathews. “Study of motion of a bowed violin string”. In: *The Journal of the Acoustical Society of America* 49.2B (1971), pp. 532–537.
- [KOG00] Jean Kergomard, Sébastien Ollivier, and Joel Gilbert. “Calculation of the spectrum of self-sustained oscillators using a variable truncation method: Application to cylindrical reed instruments”. In: *Acta Acustica united with Acustica* 86.4 (2000), pp. 685–703.
- [KOGV07] Bernd Krauskopf, Hinke M Osinga, and Jorge Galán-Vioque. *Numerical continuation methods for dynamical systems*. Springer, 2007.
- [Kuz95] Yuri A Kuznetsov. “Elements of applied bifurcation theory. 1998”. In: *Springer-Verlag, New York* (1995).
- [KVC10] Sami Karkar, Christophe Vergez, and Bruno Cochelin. “Toward the systematic investigation of periodic solutions in single reed woodwind instruments”. In: 2010.
- [KVC12a] Sami Karkar, Christophe Vergez, and Bruno Cochelin. “Numerical tools for musical instruments acoustics: analysing nonlinear physical models using continuation of periodic solutions”. In: 2012.
- [KVC12b] Sami Karkar, Christophe Vergez, and Bruno Cochelin. “Oscillation threshold of a clarinet model: A numerical continuation approach”. In: *The Journal of the Acoustical Society of America* 131.1 (2012), pp. 698–707.
- [LCL17] Steven M Lulich, Sherman Charles, and Benjamin Lulich. “The relation between tongue shape and pitch in clarinet playing using ultrasound measurements”. In: *The Journal of the Acoustical Society of America* 141.3 (2017), pp. 1759–1768.
- [Lev44] Kenneth Levenberg. “A method for the solution of certain non-linear problems in least squares”. In: *Quarterly of applied mathematics* 2.2 (1944), pp. 164–168.
- [LHC13] Nicolas Lopes, Thomas Hélie, and René Caussé. “Control of an artificial mouth playing a trombone and analysis of sound descriptors on experimental data”. In: *Proceedings of the Stockholm Music Acoustics Conference 2013*. 2013.
- [Li+16] Weicong Li et al. “The effect of blowing pressure, lip force and tonguing on transients: A study using a clarinet-playing machine”. In: *The Journal of the Acoustical Society of America* 140.2 (2016), pp. 1089–1100.
- [Lis83] George List. *Music and poetry in a Colombian village: A tri-cultural heritage*. Indiana University Press, 1983.
- [LS48] Harold Levine and Julian Schwinger. “On the radiation of sound from an unflanged circular pipe”. In: *Physical review* 73.4 (1948), p. 383.
- [LT10] Arnaud Lazarus and Olivier Thomas. “A harmonic-based method for computing the stability of periodic solutions of dynamical systems”. In: *Comptes Rendus Mécanique* 338.9 (2010), pp. 510–517.
- [LV15] Georges Le Vey. “Graph modelling of musical wind instruments: a method for natural frequencies computation”. In: *Acta Acustica united with Acustica* 101.6 (2015), pp. 1222–1233.

- [LV17] Georges Le Vey. “A Mathematical Model for Air Columns in a Class of Woodwinds”. In: *Acta Acustica united with Acustica* 103.4 (2017), pp. 676–684.
- [MA+16] Alberto Muñoz Arancón et al. “Estimation of saxophone reed parameters during playing”. In: *The Journal of the Acoustical Society of America* 139.5 (2016), pp. 2754–2765.
- [MA93] Joseph Derek Morrison and Jean-Marie Adrien. “Mosaic: A framework for modal synthesis”. In: *Computer Music Journal* 17.1 (1993), pp. 45–56.
- [MAGD18] Alberto Muñoz Arancón, Bruno Gazengel, and Jean-Pierre Dalmont. “Comparison of Human and Artificial Playing of a Single Reed Instrument”. In: *Acta Acustica united with Acustica* 104.6 (2018), pp. 1104–1117.
- [Man10] Paul Manneville. *Instabilities, chaos and turbulence*. Vol. 1. World Scientific, 2010.
- [Man+11] Ian R Manchester et al. “Regions of attraction for hybrid limit cycles of walking robots”. In: *IFAC Proceedings Volumes* 44.1 (2011), pp. 5801–5806.
- [Mar42] Daniel W Martin. “Lip vibrations in a cornet mouthpiece”. In: *The Journal of the Acoustical Society of America* 13.3 (1942), pp. 305–308.
- [Mas18] Hideki Masuda. “Research and development of a casual wind instrument: Venova(TM)”. In: *Congrès Français d’Acoustique*. 2018.
- [Mat84] Takashi Matsumoto. “A chaotic attractor from Chua’s circuit”. In: *IEEE Transactions on Circuits and Systems* 31.12 (1984), pp. 1055–1058.
- [MD11] Charles A Macaluso and Jean-Pierre Dalmont. “Trumpet with near-perfect harmonicity: Design and acoustic results”. In: *The Journal of the Acoustical Society of America* 129.1 (2011), pp. 404–414.
- [MG41] CS McGinnis and C Gallagher. “The mode of vibration of a clarinet reed”. In: *The Journal of the Acoustical Society of America* 12.4 (1941), pp. 529–531.
- [MK11] Elise Moers and Jean Kergomard. “On the cutoff frequency of clarinet-like instruments. geometrical versus acoustical regularity”. In: *Acta Acustica united with Acustica* 97.6 (2011), pp. 984–996.
- [MK95] Hideyuki Masuda and Toshifumi Kunimoto. *Wind type tone synthesizer adapted for simulating a conical resonance tube*. US Patent 5,438,156. 1995.
- [MS11] Hideyuki Masuda and Yuichiro Suenaga. *Pipe structure of wind instrument*. US Patent App. 13/023,793. 2011.
- [MS80] G Moore and A Spence. “The calculation of turning points of nonlinear equations”. In: *SIAM Journal on Numerical Analysis* 17.4 (1980), pp. 567–576.
- [MSW83] Michael E McIntyre, Robert T Schumacher, and James Woodhouse. “On the oscillations of musical instruments”. In: *The Journal of the Acoustical Society of America* 74.5 (1983), pp. 1325–1345.
- [NCG08] Michael J Newton, Murray Campbell, and Joël Gilbert. “Mechanical response measurements of real and artificial brass players lips”. In: *The Journal of the Acoustical Society of America* 123.1 (2008), EL14–EL20.
- [Ned98] CJ Nederveen. *Acoustical aspects of musical instruments*. Northern Illinois Univ. Press, 1998.
- [Nor+13] Daniel Noreland et al. “The logical clarinet: numerical optimization of the geometry of woodwind instruments”. In: *Acta Acustica united with Acustica* 99.4 (2013), pp. 615–628.
- [NV76] M Nakhla and Jiri Vlach. “A piecewise harmonic balance technique for determination of periodic response of nonlinear systems”. In: *IEEE Transactions on Circuits and Systems* 23.2 (1976), pp. 85–91.
- [NW06] Jorge Nocedal and Stephen Wright. *Numerical optimization*. Springer Science & Business Media, 2006.

- [ODK04] S Ollivier, J-P Dalmont, and J Kergomard. “Idealized models of reed woodwinds. Part I: Analogy with the bowed string”. In: *Acta acustica united with acustica* 90.6 (2004), pp. 1192–1203.
- [OKD05] S Ollivier, Jean Kergomard, and Jean-Pierre Dalmont. “Idealized Models of Reed Woodwinds. Part II: On the Stability of "Two-Step" Oscillations”. In: *Acta acustica united with acustica* 91.1 (2005), pp. 166–179.
- [Oll02] Sébastien Ollivier. “Contribution à l’étude des oscillations des instruments à vent à anche simple”. PhD thesis. Université du Maine, 2002.
- [Peg+00] Guido Pegna et al. “Experimental definition of the basin of attraction for Chua’s circuit”. In: *International Journal of Bifurcation and Chaos* 10.05 (2000), pp. 959–970.
- [Pet+19a] E Petersen et al. “The effect of the cutoff frequency on the sound production of a clarinet-like instrument”. In: *The Journal of the Acoustical Society of America* 145.6 (2019), pp. 3784–3794.
- [Pet+19b] E Petersen et al. “The link between the tonehole lattice cutoff frequency and woodwind sound radiation: a quantitative study applied to the clarinet”. In: *The Journal of the Acoustical Society of America* 145.6 (2019), pp. 3784–3794.
- [Pet+20] E Petersen et al. “On the tonehole lattice cutoff frequency of conical resonators: applications to the saxophone”. In: *Acta Acustica* (2020 [in press]).
- [Pet20] Erik Petersen. “Wave propagation in periodic structures applied to woodwind tonehole lattices: How the cutoff frequency balances sound production and radiation”. PhD thesis. Aix-Marseille Université, 2020.
- [PS81] Allan D Pierce and P Smith. *Acoustics: An introduction to its physical principles and applications*. Acoustical Society of America, 1981.
- [PVHC18] Montserrat Pàmies-Vilà, Alex Hofmann, and Vasileios Chatziioannou. “Analysis of tonguing and blowing actions during clarinet performance”. In: *Frontiers in psychology* 9 (2018), p. 617.
- [Ras89] S Neil Rasband. *Chaotic dynamics of nonlinear systems*. Courier Dover Publications, 1989.
- [Ric+09] Benjamin Ricaud et al. “Behavior of reed woodwind instruments around the oscillation threshold”. In: *Acta Acustica united with Acustica* 95.4 (2009), pp. 733–743.
- [Ros60] HoHo Rosenbrock. “An automatic method for finding the greatest or least value of a function”. In: *The Computer Journal* 3.3 (1960), pp. 175–184.
- [RPE14] Pablo E Riera, Martin Proscia, and Manuel C Eguia. “A comparative study of saxophone multiphonics: musical, psychophysical and spectral analysis”. In: *Journal of New Music Research* 43.2 (2014), pp. 202–213.
- [SB31] EG Shower and Rulon Biddulph. “Differential pitch sensitivity of the ear”. In: *The Journal of the Acoustical Society of America* 3.2A (1931), pp. 275–287.
- [SCH17a] Sebastian Schmutzhard, Vasileios Chatziioannou, and Alex Hofmann. “Parameter optimisation of a viscothermal time-domain model for wind instruments”. In: *Proceedings of the 2017 International Symposium on Musical Acoustics*. 2017, pp. 27–30.
- [SCH17b] Sebastian Schmutzhard, Vasileios Chatziioannou, and Alex Hofmann. “Parameter Optimisation of a Viscothermal Time-Domain Model for Wind Instruments”. In: *International Symposium on Musical Acoustics*. 2017.
- [Sch73] John C Schelleng. “The bowed string and the player”. In: *The Journal of the Acoustical Society of America* 53.1 (1973), pp. 26–41.
- [Sch81] RT Schumacher. “Ab initio calculations of the oscillations of a clarinet”. In: *Acta Acustica united with Acustica* 48.2 (1981), pp. 71–85.
- [Sey10] R Seydel. *Practical bifurcation and stability analysis*. 2010.

- [Sil+08] Fabrice Silva et al. “Interaction of reed and acoustic resonator in clarinetlike systems”. In: *The Journal of the Acoustical Society of America* 124.5 (2008), pp. 3284–3295.
- [Sil09] Fabrice Silva. “Émergence des auto-oscillations dans un instrument de musique à anche simple”. PhD thesis. Aix-Marseille Université, 2009.
- [Sil+09] Fabrice Silva et al. “Approximation formulae for the acoustic radiation impedance of a cylindrical pipe”. In: *Journal of Sound and Vibration* 322.1-2 (2009), pp. 255–263.
- [Sil+14] Fabrice Silva et al. “MoReeSC: a framework for the simulation and analysis of sound production in reed and brass instruments”. In: *Acta Acustica united with Acustica* 100.1 (2014), pp. 126–138.
- [Siv35] LJ Sivian. “Acoustic impedance of small orifices”. In: *The Journal of the Acoustical Society of America* 7.2 (1935), pp. 94–101.
- [SLS08] Gary P Scavone, Antoine Lefebvre, and Andrey R da Silva. “Measurement of vocal-tract influence during saxophone performance”. In: *The Journal of the Acoustical Society of America* 123.4 (2008), pp. 2391–2400.
- [Sta+17] Nataliya V Stankevich et al. “Scenario of the birth of hidden attractors in the Chua circuit”. In: *International Journal of Bifurcation and Chaos* 27.12 (2017), p. 1730038.
- [Sto72] Arnold Stokes. “On the approximation of nonlinear oscillations”. In: *Journal of differential equations* 12.3 (1972), pp. 535–558.
- [SW01] AL Schwab and M Wisse. “Basin of attraction of the simplest walking model”. In: *Proceedings of the ASME design engineering technical conference*. Vol. 6. 2001, pp. 531–539.
- [Tai+14] Pierre-André Taillard et al. “Statistical estimation of mechanical parameters of clarinet reeds using experimental and numerical approaches”. In: *Acta Acustica united with Acustica* 100.3 (2014), pp. 555–573.
- [Tai+18] P-A Taillard et al. “Modal analysis of the input impedance of wind instruments. Application to the sound synthesis of a clarinet”. In: *Applied Acoustics* 141 (2018), pp. 271–280.
- [Tai18] Pierre-André Taillard. “Theoretical and experimental study of the role of the reed in clarinet playing”. PhD thesis. 2018.
- [Tak+09] Kin’ya Takahashi et al. “Numerical study on multi-stable oscillations of woodwind single-reed instruments”. In: *Acta Acustica united with Acustica* 95.6 (2009), pp. 1123–1139.
- [Tea63] Larry Teal. *The art of saxophone playing*. Alfred Music, 1963.
- [Ter+12] Soizic Terrien et al. “Numerical resolution of a physical model of flute-like instruments: comparison between different approaches”. In: 2012.
- [Ter+15] Soizic Terrien et al. “Regime change thresholds in recorder-like instruments: Influence of the mouth pressure dynamics”. In: *Acta Acustica united with Acustica* 101.2 (2015), pp. 300–316.
- [THJC57] George B Thurston, Logan E Hargrove Jr, and Bill D Cook. “Nonlinear properties of circular orifices”. In: *The Journal of the Acoustical Society of America* 29.9 (1957), pp. 992–1001.
- [Tho79] Stephen C Thompson. “The effect of the reed resonance on woodwind tone production”. In: *The journal of the acoustical society of america* 66.5 (1979), pp. 1299–1307.
- [TK15] P-A Taillard and Jean Kergomard. “An analytical prediction of the bifurcation scheme of a clarinet-like instrument: Effects of resonator losses”. In: *Acta Acustica united with Acustica* 101.2 (2015), pp. 279–291.
- [Tou+17] Robin Tournemene et al. “Brass instruments design using physics-based sound simulation models and surrogate-assisted derivative-free optimization”. In: *Journal of Mechanical Design* 139.4 (2017).

- [TVF13] Soizic Terrien, Christophe Vergez, and Benoît Fabre. “Flute-like musical instruments: a toy model investigated through numerical continuation”. In: *Journal of sound and vibration* 332.15 (2013), pp. 3833–3848.
- [Vel+17] Lionel Velut et al. “How well can linear stability analysis predict the behaviour of an outward-striking valve brass instrument model?” In: *Acta Acustica united with Acustica* 103.1 (2017), pp. 132–148.
- [VFC13] Camille Vauthrin, Benoit Fabre, and Patricio de la Cuadra. “The design of a chromatic quena: How can linear acoustics help ?” In: *Stockholm Music Acoustics Conference*. 2013.
- [Vig+17] Pierre Vigué et al. “Regularized friction and continuation: Comparison with Coulomb’s law”. In: *Journal of Sound and Vibration* 389 (2017), pp. 350–363.
- [Vig+19] Pierre Vigué et al. “Continuation of periodic solutions for systems with fractional derivatives”. In: *Nonlinear Dynamics* 95.1 (2019), pp. 479–493.
- [VR97] Christophe Vergez and XAVIER Rodet. “Model of the Trumpet Functioning: Real-time Simulation and Experiments with an Artificial Mouth”. In: *PROCEEDINGS-INSTITUTE OF ACOUSTICS* 19 (1997), pp. 425–432.
- [VVG16] Lionel Velut, Christophe Vergez, and Joël Gilbert. “Measurements and time-domain simulations of multiphonics in the trombone”. In: *The Journal of the Acoustical Society of America* 140.4 (2016), pp. 2876–2887.
- [VWA07] Maarten Van Walstijn and Federico Avanzini. “Modelling the mechanical response of the reed-mouthpiece-lip system of a clarinet. Part II: A lumped model approximation”. In: *Acta Acustica united with Acustica* 93.3 (2007), pp. 435–446.
- [VZ+90] J Van Zon et al. “Flow through the reed channel of a single reed music instrument”. In: *Le Journal de Physique Colloques* 51.C2 (1990), pp. 821–824.
- [WB74] Theodore A Wilson and Gordon S Beavers. “Operating modes of the clarinet”. In: *The Journal of the Acoustical Society of America* 56.2 (1974), pp. 653–658.
- [Wis+05] Martijn Wisse et al. “How to keep from falling forward: Elementary swing leg action for passive dynamic walkers”. In: *IEEE Transactions on robotics* 21.3 (2005), pp. 393–401.
- [WLC09] Lili Wang, Wenlian Lu, and Tianping Chen. “Multistability and new attraction basins of almost-periodic solutions of delayed neural networks”. In: *IEEE Transactions on Neural Networks* 20.10 (2009), pp. 1581–1593.
- [Woo14] Jim Woodhouse. “The acoustics of the violin: a review”. In: *Reports on Progress in Physics* 77.11 (2014), p. 115901.
- [Wor71] Walter Elliott Worman. “Self-Sustained Nonlinear Oscillations of Medium Amplitude in Clarinet-Like Systems.” PhD thesis. Case Western University, 1971.
- [WSH04] Martijn Wisse, Arend L Schwab, and Frans CT van der Helm. “Passive dynamic walking model with upper body”. In: *Robotica* 22.6 (2004), pp. 681–688.

Abstract

This work links features of sound production in woodwinds to the action of the musician, through numerical simulation of a physical model supported by experiments. It focuses on the nonlinear dynamics of the model, as one of the missing links between the acoustical features of the instrument, and how easy it is to play. The results are intended to facilitate future instrument development endeavors that would use a physical model as a virtual prototype.

Two fundamentally different simulation methods are used conjointly to provide a robust understanding of the mechanisms governing sound production in woodwind instruments. On the one hand, time-domain synthesis allows large-scale direct investigations into the transients and steady-state oscillations, with the advantage of being interpretable directly in terms of musician actions. On the other hand, the Harmonic Balance Method associated with continuation (Asymptotic Numerical Method) provides a precise, in depth investigation of stable and unstable periodic solution branches throughout the parameter space. This method highlights bifurcations which signal the apparition or disappearance of oscillation regimes: Neimark-Sacker, period doubling, Hopf and fold. These last two are followed by continuation, in codimension 2.

Experimental results constitute the initial foundation and final validation of numerical simulations. Input impedance measurements allow simulations to be based on the acoustical parameters of real saxophones. This justifies subsequent comparisons of simulated dynamics with phenomena observed in playing situation using an instrumented saxophone mouthpiece. Archetypes of oscillating regimes are explored and connected to musician control parameters, such as the blowing pressure and action on the reed. The so-called standard, inverted and double two-step regimes are revealed and analyzed both experimentally and numerically.

The influence of geometrical and modal parameters of the resonator on the instrument's dynamics is detailed. The dynamic system is characterized globally, by mapping out its oscillation thresholds and regime production regions. Maps representing types of oscillation regimes produced depending on the control parameters constitutes a more detailed way to compare two instruments or fingerings. They are applied to compare two alto saxophones, demonstrate the effect of the register key, and assess sound production on a virtual prototype of bicylindrical resonator. This virtual prototype's geometry is optimized based on the input impedance of a saxophone, using a differentiable cost function well-suited to gradient-based optimization procedures.

A more fundamental investigation of woodwind dynamics tackles multistability (different regime being stable for the same control parameter values), which is shown to be ubiquitous on saxophones. The initial conditions leading to different regimes are grouped as attraction basins. Multistability is also characterized in a more musically interpretable way, via a variable blowing pressure transient affecting the obtained steady-state regime. These considerations are applied to improve the regime maps and avoid bias that may be due to overlooking multistable regimes. Improved regime maps are used to demonstrate that the ratio between the first two resonance frequencies leading to the most first register production is not exactly 2, but a slightly higher value.

The results of this dissertation and the related analysis tools further the understanding of a complex dynamic, that of the saxophone, and open the door to quantitative studies and direct application in virtual prototyping.

Résumé

Cette thèse lie la production de son par les instruments à anches aux actions du musicien, à travers des simulations numériques appliquées à un modèle physique et soutenues par des expériences. On se concentre sur la dynamique non linéaire du modèle, comme l'un des chaînons manquants entre les caractéristiques acoustiques de l'instrument et sa jouabilité. Les résultats doivent faciliter de futurs projets de développement d'instrument qui utiliseraient un modèle physique en tant que prototype virtuel.

Deux méthodes de simulation fondamentalement différentes sont utilisées conjointement pour améliorer notre compréhension des mécanismes régissant la production du son dans les instruments à anches. D'un côté, la synthèse temporelle permet des études à grande échelle des phénomènes transitoires et des régimes établis, avec l'avantage d'être interprétable directement en termes d'actions du musicien. D'un autre côté, la Méthode d'Équilibrage Harmonique associée avec la continuation (Méthode Asymptotique Numérique) permet d'explorer l'espace des paramètres de contrôle en suivant les branches de solutions périodiques stables et instables. Cette méthode met en évidence des bifurcations qui marquent l'apparition ou la disparition de régimes oscillants : Neimark-Sacker, doublement de période, Hopf et fold. Ces deux dernières sont suivies par continuation, en codimension 2.

Les résultats expérimentaux constituent à la fois un préalable et une validation finale des simulations numériques. Des mesures d'impédance d'entrée permettent de fonder les simulations sur les paramètres acoustiques de vrais saxophones. Ceci justifie les comparaisons ultérieures entre la dynamique simulée et les phénomènes observés en situation de jeu effectuées à l'aide d'un bec instrumenté.

Des formes archétypales de régimes d'oscillations sont étudiés et liés aux paramètres de contrôle du musicien que sont la pression d'alimentation et l'appui de la lèvres sur l'anche. Les régimes à deux états dits standard, inversé, et double, sont exhibés et analysés expérimentalement et numériquement. L'influence des paramètres géométriques et modaux du résonateur sur la dynamique de l'instrument est détaillée. Le système dynamique est caractérisé de manière globale, en cartographiant les seuils d'oscillations et les régions de production de régimes. Des cartes représentant les types de régimes oscillants permettent de comparer en détail deux instruments ou deux doigtés d'un même instrument. Ainsi, on compare deux saxophones altos, on illustre l'effet de la clé de registre, et on évalue un prototype virtuel de résonateur bicylindre. La géométrie de ce prototype virtuel est optimisée à partir de l'impédance d'entrée d'un saxophone, à l'aide d'une fonction de coût dérivable adaptée aux méthodes d'optimisations basée sur le gradient.

Une étude plus fondamentale de la dynamique des instruments à anches traite du phénomène de multistabilité (plusieurs régimes stables pour une seule valeur des paramètres de contrôle). Sur les saxophones, ce phénomène s'avère très important. Les conditions initiales menant à chaque régime sont regroupées en bassins d'attraction. La multistabilité est aussi caractérisée d'une manière plus proche du jeu musical, via un transitoire variable de pression d'alimentation qui affecte le régime final obtenu. Ces considérations sont appliquées à l'amélioration des cartographies de régimes afin d'éviter les biais qui peuvent apparaître si la multistabilité est négligée. Ces cartographies améliorées démontrent que le rapport entre les deux premières fréquences de résonance du saxophone qui mène à la production la plus importante de premier registre ne vaut pas exactement 2 mais une valeur légèrement plus élevée.

Les résultats de cette thèse et les outils d'analyse afférents permettent d'avancer dans la compréhension d'une dynamique complexe, celle du saxophone, et ouvrent la porte à des études quantitatives et à des applications directes de prototypage virtuel.